

THE TOMS PHENOMENON -  
TURBULENT PIPE FLOW OF DILUTE POLYMER SOLUTIONS

by

Preetinder Singh Virk

B. Tech., Indian Institute of Technology, Kharagpur  
(1962)

Submitted in Partial Fulfillment  
of the Requirements for the  
Degree of Doctor of Science

at the

MASSACHUSETTS INSTITUTE OF TECHNOLOGY

November, 1966

Signature of Author . . . . .  
Department of Chemical Engineering  
November 15, 1966

Certified by H. S. Mickley, Thesis Supervisor . . . . .

E. W. Merrill, Thesis Supervisor . . . . .

K. A. Smith, Thesis Supervisor . . . . .

E. L. Mollo-Christensen, Thesis Supervisor . . . . .

Accepted by G. C. Williams, Chairman, Departmental  
Committee on Graduate Theses . . . . .

THE TOMS PHENOMENON -  
TURBULENT PIPE FLOW OF DILUTE POLYMER SOLUTIONS

by

Preetinder Singh Virk

Submitted to the Department of Chemical Engineering on November 15, 1966, in partial fulfillment of the requirements for the degree of Doctor of Science.

ABSTRACT

Drag reduction caused by dilute, distilled water solutions of five polyethylene oxides, molecular weights from 80,000 to 6,000,000, in turbulent pipe flow was studied experimentally in 0.292 cm and 3.21 cm ID pipes. It was found that:

The Onset of drag reduction occurs at a well-defined wall shear stress related to the random coiling effective diameter of the polymer by the Onset Hypothesis.

Laminar to turbulent transition is not, in general, delayed.

The extent of drag reduction induced by a homologous series of polymers in a given pipe is a universal function of concentration, uniquely related to flow rate and molecular weight.

The maximum drag reduction possible is limited by a universal asymptote that is independent of polymer and pipe diameter.

The mean flow structure obtained when drag reduction is exhibited follows an "effective slip" model; in this, the mean velocity profile consists of a "Newtonian plug" convected along at an additional, "effective slip" velocity.

The turbulent flow structure follows the "effective slip" model towards the pipe wall, but is significantly different from Newtonian towards the pipe axis; in particular, the inertial subrange observed in isotropic Newtonian turbulence is entirely absent in polymer solution energy spectra taken on the pipe axis.

In polymer solution, both the stagnation pressure attained with Pitot tubes and the heat transfer from cylinders in cross flow are drastically different from Newtonian; in general, both are lower.

Thesis Supervisors: Harold S. Mickley  
Professor of Chemical Engineering

Edward W. Merrill  
Professor of Chemical Engineering

Kenneth A. Smith  
Assistant Professor of Chemical  
Engineering

Erik L. Mollo-Christensen  
Professor of Meteorology

Department of Chemical  
Engineering  
Massachusetts Institute  
of Technology  
Cambridge, Massachusetts 02139

November 15, 1966

Professor William C. Greene  
Secretary of the Faculty  
Massachusetts Institute of Technology  
Cambridge, Massachusetts 02139

Dear Professor Greene:

In accordance with the regulations of the Faculty, I herewith submit a thesis, entitled "The Toms Phenomenon - Turbulent Pipe Flow of Dilute Polymer Solutions," in partial fulfillment of the requirements for the degree of Doctor of Science in Chemical Engineering at the Massachusetts Institute of Technology.

Respectfully submitted,

Preetinder Singh Virk

## Acknowledgement

The author is especially indebted to his supervisors, Professors Mickley, Merrill, Smith and Mollo-Christensen, for suggesting the problem and for their interest, advice and encouragement in tackling it.

Too, it is a pleasure to thank:

Axel Erikson, Schuyler Holbrook and Harold Carter for help in constructing the equipment,

Dmitri Matiatos, Hyunkook Shin, Steve Paradis, Pat Fowles and Roy Levitch for stimulating discussions not always technical,

Andrew Goldsmith for a summer's assistance,

David Bourke for more than standard manufacturers' information on the Moyno pump,

the M.I.T. Computation Center and Physical Plant for use of their facilities,

Miss Angela Carbone for typing the thesis,

the Office of Naval Research for grant Nonr - 3963(10) under which this work was performed, and

my wife, Usha, for reasons too numerous to record.

## Table of Contents

	<u>Page</u>
I. SUMMARY	16
1.1 Introduction	16
1.2 Apparatus and Procedure	18
1.3 Scope of Investigation	20
1.4 Results and Discussion	20
1.4.1 Gross Flow	20
1.4.2 Flow Structure	32
1.4.3 The Over-all Picture	40
1.4.4 Anomalous Pitot Tube and Hot Film Measurements	45
II. INTRODUCTION	49
2.1 The Toms Phenomenon	49
2.2 Object of Thesis	51
2.3 Significance of Problem	52
2.4 Previous Work	53
2.5 Shortcomings of Prior Work	61
2.6 The Present Approach	62
III. APPARATUS	68
3.1 General Description	68
3.2 Detailed Descriptions	71
3.3 The Small System	72
3.4 The Big System	76
3.5 Measuring Instruments	85
3.6 Auxilliary Equipment	88

IV.	PROCEDURE	90
4.1	General Procedure	90
4.2	Detailed Procedure	97
4.3	Polymer Master Batch Makeup	98
4.4	Small System Runs	100
4.5	Big System Runs	102
V.	RESULTS	108
5.1	Scope of Investigation	108
5.2	Polymer Characterization	110
5.3	Gross Flow Measurements	111
5.4	Mean Velocity Measurements	113
5.5	Turbulence Measurements	115
VI.	DISCUSSION OF RESULTS	117
6.1	Chapter Organization	117
Part A.	Description of Results	118
6.2	Polymer Characterization	119
6.3	Gross Flow Measurements	120
6.4	Mean Velocity Measurements	130
6.5	Turbulence Measurements	136
Part B.	Analysis and Proposed Correlations	145
6.6	Gross Flow	146
6.6.1	The Laminar Regime	146
6.6.2	The Onset of Drag Reduction	147
6.6.3	Transition	169
6.6.4	The Extent of Drag Reduction	172

6.7	Anomalous Pitot Tube and Hot Film Measurements	200
6.7.1	Pitot Tube	200
6.7.2	Hot Film	209
6.8	Flow Structure	217
6.8.1	Mean Flow	217
6.8.2	Turbulence Structure	225
Part C.	The Over-all Picture	243
6.9	Evaluation of Earlier Explanations	245
6.10	Prediction and Estimation of the Toms Phenomenon	252
6.10.1	Gross Flow	252
6.10.2	Flow Structure	259
6.10.3	An Illustrative Example	261
VII.	CONCLUSIONS	267
VIII.	RECOMMENDATIONS	277
	FIGURES	280
IX.	APPENDICES	357
A.	Filmed Hot Film Analysis	358
B.	Spectrum Scaling Rules	374
C.	Current Onset Data	386
D.	Polyethylene oxide - Water Data	389
E.	Equipment Details	390



F.	Calibrations	402
G.	Summary of Data and Calculated Values	407
H.	Sample Calculations	429
I.	Location of Data	437
J.	Nomenclature	438
K.	Literature Citations	445
L.	Biographical Note	453

## TABLES

	<u>Page</u>	
1.4.1	Comparison of Flow Rates	48
1.4.2	Spectrum Parameters	48
5.1.1	Range of Variables	109
5.4.1	Comparison of Flow Rates	114
6.3.1	Drag Reduction Parameters	129
6.5.1	Shedding Frequencies	142
6.6.1	Onset of Drag Reduction Data	158
6.6.2	"Time" vs. "Length" Onset Hypotheses	166
6.6.3	Intrinsic Drag Reduction	176
6.7.1	Pitot Tube vs. Apparent Velocities	206
6.7.2	Accuracy of Turbulence Measurements	216
6.8.1	Spectrum Parameters	229
6.8.2	Solvent Spectrum Scaling Constants	234
6.10.1	Polymer Solution Flow Paths	258
6.10.2	Predicted vs. Experimental Results	266
A.2.1	Turbulent Signal Attenuation Ratio	371
B.1	Conditions for Experimental Spectra	378
B.2	Universal Dissipation Wave Numbers	382
B.3	Macroscales and Dissipation Integrals	385
C.1	Current Onset of Drag Reduction Data	386
D.1	Polyethylene oxide - Water Data	389
E.3.1	Pump Drive Gear Ratios	392
E.4.1	Anemometer Instability	398
E.5	Equipment Vendors and Manufacturers	399

G.1	Polymer Intrinsic Viscosities	411
G.2.1	Index of 0.292 cm System Runs	412
G.2.2	Full Range Runs	413
G.2.3	High Flow Runs	417
G.2.4	Specific Drag Reduction	421
G.3.1	Index of 3.21 cm System Runs	422
G.3.2	Gross Flow Runs	423
G.4	Mean Velocity Profiles	424
G.5	Hot Film Static Calibrations	425
G.6	rms Turbulent Intensity Profiles	426
G.7	Turbulent Energy Spectra	427

## FIGURES

		<u>Page</u>
2.1.1	Flow Diagram, Data of Toms	281
3.1.1	0.292 cm System Schematic	282
3.1.2	3.21 cm System Schematic	283
3.1.3	Micrometer Traverse	284
3.3.1	0.292 cm System Details	285
3.4.1	3.21 cm System Details	286,287
5.2.1	Intrinsic Viscosity Measurements	288
5.3.1	Pressure Gradients, 0.292 cm Pipe	289
5.3.2	Pressure Gradients, 3.21 cm Pipe	290
5.3.3	Solvent Flow Diagrams, Both Pipes	291
5.3.4 - 14	Polymer Solutions Flow Diagrams:	
	Polymer          Pipe, cm	
5.3.4	N10                0.292	292
5.3.5	N10                3.21	293
5.3.6	N80                0.292	294
5.3.7	N80                0.292 with Trigger	295
5.3.8	N750               0.292	296
5.3.9	N750               0.292 with Trigger	297
5.3.10	N3000              0.292	298
5.3.11	N3000              0.292 with Trigger	299
5.3.12	N3000              3.21	300
5.3.13	W301                0.292	301
5.3.14	W301                3.21	302
5.3.15	The Laminar Regime	303

5.3.16	Transition Reynolds Numbers	304
5.3.17 - 20	Specific Drag Reduction, 0.292 cm Pipe:	
5.3.17	All Polymers, 0.050 litres/sec	305
5.3.18	All Polymers, 0.040 litres/sec	306
5.3.19	N3000, Effect of Flow Rate	307
5.3.20	All Polymers, Error Limits as $c \rightarrow 0$	308
5.3.21	Comparison of Fractional Drag Reduction	309
5.3.22	Polymer Degradation, 3.21 cm System	310
5.4.1 - 3	Mean Velocity Results in Solvent:	
5.4.1	Mean Velocity Profiles	311
5.4.2	Velocity Defect Law	312
5.4.3	The Law of the Wall	313
5.4.4 - 8	Mean Velocity Results in Polymer Solution:	
5.4.4	Apparent Velocity Profiles	314
5.4.5	Apparent Centre Line Velocities	315
5.4.6	Mean Velocity Profiles	316
5.4.7	Velocity Defect Law	317
5.4.8	The Law of the Wall	318
5.5.1 - 3	Hot Film Static Calibrations	
5.5.1	Solvent	319
5.5.2	Polymer Solution	320
5.5.3	Check: Profile vs. Centre Line	321
5.5.4	rms Turbulent Intensity Profiles, Solvent	322
5.5.5	rms Turbulent Velocity Profiles, Polymer Solution	323

5.5.6 - 8	Axial Turbulent Energy Spectra:	
5.5.6	Solvent, "Low" Flow Rate	324
5.5.7	Solvent, "High" Flow Rate	325
5.5.8	Polymer Solution, "High" Flow Rate	326
6.3.1	Asymptotic Slopes	327
6.5.1	Turbulent Energy Dissipation	328
6.6.1	Comparison of Intrinsic Viscosities	329
6.6.2	Onset Wall Shear Stress Error Limits	330
6.6.3	The Onset Hypothesis, Polyethylene oxides	331
6.6.4	The Onset Hypothesis, All Available Data	332
6.6.5	The Transition Criterion	333
6.6.6	The Universal Drag Reduction Curve	334
6.6.7	Relation Between Superposing Parameters	335
6.6.8	Effect of Flow Rate on $[R]$	336
6.6.9	Correlation of Drag Reduction Parameters	337
6.6.10	The Maximum Drag Reduction Asymptote	338
6.7.1	The Pitot Tube Discrepancy	339
6.7.2	Heat Transfer Coefficient Ratio	340
6.8.1	The "Effective Slip" Model	341
6.8.2	The Wall Law in "Newtonian Plug"	342
6.8.3	rms Turbulent Intensity Profiles in Polymer Solution	343
6.8.4	Comparison of Turbulent Energy Spectra	344
6.10.1	General Toms Phenomenon Flow Diagram	345

A.3.1	Turbulent Signal Attenuation Ratio	346
B.1	Experimental Turbulent Energy Spectra	347
B.2	Universal Turbulent Energy Spectra	348
D.1	Polyethylene oxide - Water Data	349
E.2.1	3.21 cm System Layout (to scale)	350
E.2.2	Control Panel Connections	351
E.2.3	Micrometer Traverse (to scale)	352
E.3.1	Pump Pressure Ripple	353
F.1.1	Pressure Transducer Calibration	354
F.2.1	Pump Calibration	355
F.3.1	Variable Filter Calibration	356

## CHAPTER I

## Summary

## 1.1 Introduction

It is observed experimentally that, under certain conditions of turbulent pipe flow, dilute polymer solutions require a smaller specific energy expenditure than the pure solvent. Thus, with the polymer solutions, a lower pressure gradient is needed to maintain the same flow rate, or a higher flow rate can be attained for the same pressure gradient as solvent. This specific energy - or drag - reduction exhibited by dilute polymer solutions in turbulent pipe flow is termed the Toms Phenomenon, after Toms (1), who was the first to recognize it. Compared to the solvent, Toms typically reported drag reductions of 50% with 0.01 wt% solutions of polymethylmethacrylate, molecular weight  $2.3 \times 10^6$ , in monochlorobenzene.

The observations of Toms have been confirmed in many subsequent "gross flow" (pressure gradient vs. flow rate) studies, (4, 8, 17, 20, 26, 29), with several different polymer-solvent systems in turbulent flow through pipes ranging from 0.1 to 5.0 cm ID. From these, two general aspects have been recognized. First, that the onset of drag reduction occurs in a fairly well-defined fashion (25, 26, 20); the Onset Hypothesis developed in the present



work to relate this to the polymer is presented in Section 1.4, following. Second, that, qualitatively, the extent of drag reduction induced increases with increasing flow rate, increasing polymer molecular weight and, within limits, increasing concentration. Also, torque reductions relative to solvent have been reported in turbulent Couette flow (21,23) and with discs spinning in dilute polymer solutions (26,40), indicating that the Toms Phenomenon occurs generally in any turbulent shear flow.

Four types of explanations, all unconfirmed and essentially speculative, have been proposed for the Toms Phenomenon.

(1) "Effective" slip (1,2) induced by an abnormally mobile, oriented, layer of macromolecules near the pipe wall.

(2) Inherently delayed laminar-to-turbulent transition (8,20) where, in analogy to dusty gases (11), the macromolecules in solution are assumed to stabilize the flow, damping disturbances and thereby restricting turbulent energy production.

(3) "Anisotropic viscosity" (21) in which the macromolecules are supposed to elongate in the direction of flow under shear, thereby impeding the radial transport of momentum, reducing the turbulent shear stress and thence the drag.

(4) Visco-elasticity, (8,20,29), is by far the most popular in current literature. Polymer solutions are known to be visco-elastic, but this explanation vis-a-vis the Toms Phenomenon, in which case an elastic "interaction" between the macromolecules and the turbulence is envisaged, is essentially intuitive.

At present, no consistent, quantitative, set of experimental facts about the Toms Phenomenon can be established, because the work done to date suffers from:

- (1) a lack of adequate polymer characterization,
- (2) unavailability of systematic gross flow data over a wide enough grid of pipe diameter, flow rate, polymer molecular weight and concentration,
- (3) the total absence of flow structure measurements.

With a view to fulfilling these specific shortcomings, the object of this thesis was to study the Toms Phenomenon in pipe flow with respect to:

- (1) the gross effect of macromolecular additive, i.e., the relation of polymer to the drag reduction induced,
- (2) the flow structure, mean and turbulent, prevailing when the phenomenon was exhibited and how this differed from that in the solvent.

## 1.2 Apparatus and Procedure

The two experimental pipe flow systems employed are

shown schematically on Figs. 3.1.1 and 3.1.2. The majority of gross flow measurements were made in the one-pass 0.292 cm system in which the wall shear stress (pressure gradient) could be measured to  $\pm 1\%$  of its absolute value and the flow rate to  $\pm 1/2\%$ . Critical Reynolds numbers for both "natural" and artificially "triggered" transition could also be ascertained. Corroborative gross flow and all flow structure measurements were made in the recirculating 3.21 cm system. In this, the wall shear stress was measured to  $\pm 1\%$ , the volumetric flow rate controlled to  $\pm 1/2\%$  and determined from the positive displacement pump characteristics. Pitot tubes were used for mean velocity profiles and a constant temperature anemometer with cylindrical, quartz coated, hot film sensors for turbulent intensity and energy spectrum measurements. The test pipe was probed at its downstream end with a micrometer traverse capable of simultaneously holding a Pitot tube and a hot film probe in an "over and under" arrangement; this permitted in situ static calibration of the latter before and after each set of turbulence measurements, greatly enhancing their accuracy.

For each polymer, various concentrations were prepared by dilution from a concentrated "master" solution which was characterized before and after each series of runs.

### 1.3 Scope of Investigation

Five homologous polyethylene oxides, which are linear, random coiling polymers, were used with distilled water for solvent. All experiments were performed at  $25.0 \pm 0.5^\circ\text{C}$ . In all cases polymer solution density were identical with that of the solvent, and the maximum relative viscosity reached was around two. Table 5.1.1 is a summary of the range of variables and the types of measurements made.

### 1.4 Results and Discussions

#### 1.4.1 Gross Flow

In both systems, flow rate vs. wall shear stress results with solvent agreed well with established Newtonian friction factor relations, Poiseuille's in laminar and Prandtl's in turbulent flow, and were highly reproducible - the 99% confidence belt on the wall shear stress was everywhere within  $\pm 1\%$  of the absolute value. In the 0.292 cm system the critical Reynolds number was  $3150 \pm 230$  for "natural" and  $2025 \pm 70$  for "triggered" transition.

Figures 5.3.8, 5.3.9 and 5.3.14 show typical polymer solution gross flow diagrams. Four distinct regimes are observed:

- (1) the laminar regime,

- (ii) the transition region,
- (iii) turbulent flow, without drag reduction,
- (iv) turbulent flow, with drag reduction.

A striking feature is the sharp division between regions (iii) and (iv). For a given polymer-solvent combination, the wall shear stress,  $T_w^*$ , at this point, which marks the onset of drag reduction, is constant over large ranges of concentration; further, it appears independent of pipe diameter.  $T_w^*$  decreases with increasing polymer molecular weight. Region (iv) is characteristic of the Toms Phenomenon; throughout it, polymer solution flow lines lie to the left of the solvent line, indicative of lower specific power consumption. At constant concentration, the flow lines diverge from the solvent line so that drag reduction increases with flow rate. For a given polymer this divergence increases progressively with increasing concentration until rather high concentrations where it asymptotes to a constant. Correspondingly, the fractional drag reduction,  $R_F = (1 - (T_{wp}/T_{ws}))_Q$ , increases initially with increasing concentration, but tends to a constant, maximum value,  $R_{F,max}$ , at high concentrations. Two asymptotes limit the maximum drag reduction that can be attained. One is the high concentration asymptote noted above; its slope,  $N_p$ , is a function of polymer and approaches unity with increasing molecular weight. The

other is a polymer independent asymptote beyond which the wall shear stress could never be reduced; its slope,  $N_m$ , is about  $3/2$  in both pipes. This latter can be observed for 2000 and 3000 ppm N750, Fig. 5.3.8, and 500 ppm W301, Fig. 5.3.14; in both cases there is a marked change in slope from  $N_p$  to  $N_m$  as the flow lines switch asymptotes. The maximum values of  $R_F$  achieved were about 0.65 in the 0.292 cm and 0.80 in the 3.21 cm systems.

#### 1.4.11 The Laminar Regime

All polymer solutions tested were Newtonian, i.e., obeyed Poiseuille's law, in laminar flow. Also, for each polymer the relative viscosities for various concentrations yielded a "high shear" ( $\approx 10^3 \text{ sec}^{-1}$ ) intrinsic viscosity which was the same as that obtained, independently, in the low shear ( $\approx 10^0 \text{ sec}^{-1}$ ) GDM viscometer.

#### 1.4.12 The Onset of Drag Reduction

The observed onset behaviour suggests that a necessary condition exists, explicitly connecting the macromolecule causing the Toms Phenomenon to the turbulent shear flow in question, which must be satisfied for drag reduction to occur. Thus onset should be ascertained by parameters characteristic of:

- (1) the macromolecule causing drag reduction,

(2) the turbulence pertaining in the flow.

From two standpoints (42,49), the thermodynamic "excluded volume" and the hydrodynamic "equivalent Einsteinian sphere", the effective diameter,  $D_M$ , of a random coiling macromolecule in dilute solution is about twice its rms radius of gyration,  $R_G$ , independent of concentration.

So

$$D_M = 2R_G \quad (1.4.1)$$

Polymer solutions are considered dilute as long as the conformation of an individual macromolecule is unaffected by its neighbours; this corresponds, roughly, to the volume fraction of macromolecules based on  $D_M$  being less than that for random spherical packing.

Drag reduction is an "energetic" phenomenon, and Laufer (43) showed that the energy action in a turbulent pipe flow occurs very close to the pipe wall - all energy rates reach sharp maxima at  $y^+ \simeq 10$ . Therefore, the parameter chosen to characterize the turbulence was a "dissipation wave number",  $k_d$ , dimensions  $(\text{length})^{-1}$ . This, derived from a turbulent energy spectrum close to the wall, was defined as the wave number where the dissipation,  $k^2 E(k)$ , is a maximum; thus  $k_d$  is a measure of the "fine" scale of turbulence at which the dissipation of turbulent energy occurs. By invoking existing turbulence

theory (44,45) and experiments (43), it can be shown that

$$k_d = Ku_\tau/\gamma \quad (1.4.2)$$

where  $K$  is a constant, order  $10^{-1}$ , that depends only on  $y^+$ ; at  $y^+ \simeq 10$ , the best estimate is  $K \approx 0.2$ .

#### 1.4.121 The Onset of Drag Reduction Hypothesis

The onset of drag reduction in the turbulent flow of dilute polymer solutions occurs at a constant value of the product  $D_M k_d^*$  which is a ratio of the dimensions of the macromolecule and the fine scale of the turbulent shear flow. Mathematically,

$$D_M k_d^* = C \quad (1.4.3)$$

where  $C$  is a universal, dimensionless, constant, and the asterisk,  $*$ , indicates a value taken at onset. Using (1.4.2),

$$D_M (u_\tau^*/\gamma) = C' ; C' = C/K \quad (1.4.4)$$

from which, for a given polymer homologous series and solvent,

$$(T_w^*)^{1/2} = C''/R_G ; C'' = C' \nu \rho^{1/2}/2 \quad (1.4.5)$$



The onset hypothesis has the following consequences which provide means of testing its validity:

(1) From (1.4.1), for a given macromolecule-solvent,  $(T_w^*)^{1/2}$  should be independent of concentration for dilute solutions.

(2) From (1.4.2), for a given macromolecule-solvent,  $(T_w^*)^{1/2}$  should be independent of pipe diameter.

(3) In any pipe, from (1.4.4),  $(u_t^*/\nu)$  should vary as  $(1/D_M)$ , or, from (1.4.5), for a given homologous series and solvent,  $(T_w^*)^{1/2}$  should vary inversely as  $R_G$ .

(4) The onset constant,  $C$  (and  $C'$ ), should be universally constant, regardless of pipe, solvent and macromolecule.

The validity of consequence (1) has already been noted; error analysis of the present results shows that, typically,  $(T_w^*)^{1/2}$  is constant within  $\pm 10$  to 20% over 100 fold ranges of concentration. Figure 6.6.3  $(T_w^*)^{1/2}$  vs.  $(1/R_G)$ , indicates that both consequences (2) and (3) hold; results from both pipes, differing 11 fold in diameter, straddle the same straight line over an 8 fold range of  $R_G$  and, within experimental error, the line passes through the origin as predicted by (1.4.5). Verification of consequence (4) requires considerably more data than currently available in the literature. Adequate existing onset data is summarized in Table 6.6.1 from which  $C' = (D_M u_t^*/\nu)$  is

$0.015 \pm 0.005$ . Considering the diverse polymers, solvents and pipes, the constancy is mildly remarkable. Note that (1.4.4) is the "engineering" form of the Onset Hypothesis, and this value of  $C'$  is all that is required, empirically, to predict the onset wall shear stress for any characterized polymer-solvent pair. Values of  $C'$  and  $K$  give an onset constant,  $C$ , of  $0.003 \pm 0.001$  which would suggest that the macromolecule is about  $(1/300)$  the size of the dissipative "eddies" at onset. No good physical interpretation can be given for this low value, but it is intuitively disturbing and indicates that the physical motivation of the Onset Hypothesis is still open to question despite its empirical, experimental, validity.

Note, finally, that the Onset Hypothesis is based on "length" scales. On entirely analogous grounds, one may postulate a "time" based hypothesis, substituting macromolecular relaxation time,  $\tau_M$ , for  $D_M$  and a dissipation frequency,  $\omega_d$ , for  $k_d$ . However, application to existing data shows that the time based hypothesis fails, yielding "time" onset products  $(\tau_M \omega_d^*)$  that vary 100 fold over the ranges that the "length" product  $(D_M k_d^*)$  is constant within  $\pm 30\%$ .

### 1.4.13 Transition

With and without the trigger, the majority of solutions tested did not delay transition. Only those polymer solutions delayed transition for which the wall shear stress,  $T_{w,T}$ , corresponding to the normal transition Reynolds number, exceeded that,  $T_w^*$ , for the onset of drag reduction. In such cases region (iii), turbulent flow without drag reduction, was absent. This transition criterion - a delay when  $T_{w,T} > T_w^*$  - is illustrated in Fig. 6.6.5. It is broadly in accord with the Onset Hypothesis since  $T_w^*$  marks the beginning of polymer-turbulence interaction in a manner that decreases the dissipation.

### 1.4.14 The Extent of Drag Reduction

#### 1.4.141 Polymer Dependent Factors

The fractional drag reduction is defined by

$$R_F = (1 - (T_{wp}/T_{ws}))_Q \quad ; \quad (1.4.6)$$

the specific drag reduction is

$$R = \rho F_F / c \quad (1.4.7)$$

which, at infinite dilution, yields the intrinsic drag reduction,

$$[R] = \lim_{c \rightarrow 0} O(R) \quad (1.4.8)$$

In region (iv), for a given polymer and flow rate, the specific drag reduction decreases monotonically with increasing concentration. These R - c curves have a characteristic shape bounded by two asymptotes:

$$\begin{aligned} R &= [R], \quad c \rightarrow 0 \\ R &= R_{F,max}/c, \quad c \rightarrow \infty \end{aligned} \quad (1.4.9)$$

The intersection of these defines a characteristic intrinsic concentration,

$$[C] = R_{F,max}/[R] \quad (1.4.10)$$

Normalization of the coordinates of the R - c curves obtained in the 0.292 cm pipe by their respective parameters  $[R]$  and  $[C]$  results, irrespective of polymer and flow rate, in their superposition on to a single universal drag reduction curve, Fig. 6.6.6. On it,  $\alpha \equiv [C]$  and  $\beta \equiv [R]$  respectively, and the universal coordinates are

$$\begin{aligned} \gamma &= c/[C] \\ \delta &= R/[R] \end{aligned} \quad (1.4.11)$$

$[R]$  and  $[C]$  are themselves uniquely related, and each can be decomposed into flow rate and polymer dependent terms. Invoking the approximate logarithmic linearity of the flow lines and noting that the onset point  $(Q^*, T_w^*)$  is common to both the solvent and polymer, it can be shown that

$$[R] = \psi \ln(Q/Q^*) ; \quad \psi = - (dn_p/dc)_c \rightarrow 0 \quad (1.4.12)$$

where  $\psi$  depends only on the polymer, and  $\ln(Q/Q^*)$  expresses the "distance" beyond onset. Also,

$$[C] = (1 - (Q/Q^*)^{(N_p - n_s)}) / [R] \quad (1.4.13)$$

The two polymeric extent-of-drag-reduction parameters in (1.4.12 and 13) are  $\psi$ , characteristic of low, and  $N_p$ , characteristic of high concentrations, respectively. Experimental values of both correlate well with polymer intrinsic viscosity,  $[\eta]$ , as shown on Figs. 6.6.9 (a) and (b), though no physical significance can be attributed to either of the relations. The correlation cannot, at present, be extended to include the effect of pipe diameter,  $D$ ; but it is suspected that the numerical constants in the  $[\eta]$  vs.  $\psi$  and  $N_p$  relations are functions of  $D$ . In general, at flow rates corresponding to equal solvent wall shear stress, it was found that the fractional drag reduction

induced by a given concentration of polymer decreased with increasing pipe diameter.

For region (iv), the foregoing permits the entire drag reducing behaviour of a homologous series and solvent in a given pipe to be synthesized from a universal  $\delta$  vs.  $\gamma$  curve, such as Fig. 6.6.6,  $[\eta]$  vs.  $\psi$  and  $N_p$  relations, such as on Fig. 6.6.9, and a knowledge of the onset point, available from Section 1.4.121. No adequate literature data exist to test the correlations developed.

#### 1.4.142 Polymer Independent Limitations

The maximum drag reduction asymptote, slope  $N_m \approx 3/2$ , noted in both pipes is shown plotted in the Prandtl form on Fig. 6.6.10; its universality, independent of pipe, polymer and concentration, is evident. Figure 6.6.10 sets the limits within which the Toms Phenomenon is exhibited - the solvent line prior to onset and the asymptote which supercedes all flow lines eventually - both of which are independent of polymer and universal in Newtonian coordinates,  $f$  and  $N_{Re}$ . Between these limits the flow lines depend on  $f$ ,  $N_{Re}$  and the polymer. The equivalent "power law" form of the asymptote is

$$f = 0.42 N_{Re}^{-0.55} \quad (1.4.14)$$

which, on comparison with laminar and turbulent friction factors

$$f = 16 N_{Re}^{-1}, \text{ laminar (Poiseuille)}$$

$$f = 0.08 N_{Re}^{-\frac{1}{4}}, \text{ turbulent (Blasius)}$$

establishes that the ultimate condition of drag reduction in the Toms Phenomenon is definitely not laminar flow.

The maximum drag reduction asymptote has not hitherto been reported, and positive literature confirmation is lacking, though both Toms (1) and Metzner and Park (20) appear to have attained it.

#### 1.4.143 Degradation

Drag reduction by dilute polymer solutions is invariably accompanied by a decrease in polymer molecular weight - termed degradation. In the 0.292 cm pipe without the trigger - from which most gross flow data were derived - polymer degradation was found, by intrinsic viscosity measurements, to be negligible. In the 3.21 cm system degradation was slight before onset,  $(Q/Q^*) < 1$ , and very severe for  $(Q/Q^*) > 10$ ; thus onset data were essentially unaffected, but extent of drag reduction data were not entirely suitable for correlation. Degradation does not affect asymptote data as long as the concentration of undegraded polymer remains high enough for the asymptote to be followed; further, departure from this condition is readily discerned - see the 4 highest flow rate points for

500 ppm W301 on Fig. 5.3.14.

#### 1.4.15 The Newtonian Solvent

Onset and extent of drag reduction relations were developed with respect to the pure solvent. So long as the polymer solutions remain dilute, it is found that the viscosity buildup with increasing concentration can be accounted for by referring all relations to the "Newtonian" rather than the pure solvent. The Newtonian solvent is defined as having the same viscosity as the polymer solution in question, but obeying Newtonian flow relations. Its relative viscosity is, from the Flory-Huggins expansion,

$$\eta_r = 1 + c[\eta] + k'(c[\eta])^2 + \dots \quad (1.4.15)$$

#### 1.4.2 Flow Structure

##### 1.4.21 Mean Flow

Mean velocity profiles were measured in polymer solution at two flow rates: the "low" flow rate was at onset,  $(Q/Q^*) = 1$ ,  $R_F \simeq 0$ , while the "high" flow rate was well into region (iv),  $(Q/Q^*) = 5$ ,  $R_F \simeq 0.35$ . The results, compared with identical measurements in solvent, are shown in Figs. 5.4.7 and 5.4.8. Flow rates obtained by integration of the velocity profiles,  $Q_1$ , are compared with those



from the independent pump calibration,  $Q$  (with both solvent and polymer solution, the pump calibration was the same), in Table 1.4.1. At both flow rates,  $Q_1$  and  $Q$  check comparably in polymer solution and solvent. A larger Pitot tube was experimentally necessary at the "high" flow rate for reasons given in Section 1.4.4; with it the results were less precise, 1 to 2% lower, than with the 0.025 cm Pitot but, more importantly, the error was the same in polymer solution and solvent so comparisons are not impaired.

At the low flow rate the solvent velocity defect and wall laws are obeyed quite precisely in polymer solution. At the high flow rate the solvent defect law is obeyed closely, but the law of the wall is not - polymer solution results are "parallel-shifted" upwards such that the slope (i.e., the mixing length constant) is essentially unchanged. Obedience of the defect law is surprising since  $u_\tau$  in polymer solution is about 20% lower, which indicates that values of  $(U - U_{CL})$  must everywhere be 20% lower than in solvent, and therefore that a distinctly "blunter" profile prevails when drag reduction is exhibited. Further, this shows that  $u_\tau$  is a velocity scale in polymer solution also which, combined with the constancy of the mixing length constant, indicates that the profile is Newtonian when considered relative to  $U_{CL}$  - crudely speaking, when

looked at from the top. This motivates the "effective slip" model.

#### 1.4.211 The "Effective Slip" Model

At any point  $(Q, T_w)$  in fully developed turbulent flow, the mean velocity profile,  $U(\xi)$ , in dilute polymer solution consists of two additive portions or "plugs":

(1) The profile,  $V(\xi)$ , that would exist in the Newtonian solvent at the prevailing wall shear stress,  $T_w = \rho u_\tau^2$ .

(2) The constant "effective slip" velocity,  $V_S$ , required to make up the difference between the actual average velocity,  $U_{Av}$  (or flow rate,  $Q$ ), and that,  $V_{Av}$  (or flow rate,  $Q_N$ ), obtained from integration of the Newtonian plug.

Thus at any radial position,  $\xi$ ,

$$U(\xi) = V(\xi) + V_S \quad (1.4.16)$$

where

$$V_S = U_{Av} - V_{Av} \quad (1.4.17)$$

and average velocities are defined in the usual way,

$$U_{Av} = \int_0^1 U(1 - \xi)^2 = 4Q/\pi D^2 \quad (1.4.18)$$

In the present case,  $U(\xi)$ ,  $U_{Av}$  and  $u_\tau$  are known, so if the model holds,  $V(\xi)$  should obey all Newtonian (i.e., solvent) laws. By definition, (1.4.16),  $V(\xi)$  will identically obey the same defect law as  $U(\xi)$  which has already been noted to be Newtonian. Obedience of the wall law is tested as follows. If  $V(\xi)$  is Newtonian, then  $V_{Av}$  is available from  $u_\tau$  via the Prandtl friction factor relation. From  $V_{Av}$ , (1.4.17) and (1.4.16), the  $V(\xi)$  profile is obtained, point by point, from the  $U(\xi)$  profile, and  $v^+ (= V/u_\tau)$  vs.  $y^+ (= \xi Du_\tau/2\nu)$  should be the same as for solvent. At the low flow rate, in general before onset,  $V_S = 0$  so  $V(\xi) \equiv U(\xi)$ , and a purely Newtonian profile is predicted - as observed.  $v^+$  vs.  $y^+$  at the high flow rate is shown on Fig. 6.8.2 (compare Fig. 5.4.8) - the polymer solution points come within 1% of the solvent, indicating good agreement with the model.

Physically, an actual slip at the wall is, by dint of precedence, highly unlikely. The "effective slip" is best considered the net result of processes occurring extremely close to the pipe wall, an interpretation made in direct analogy to Clauser's "two layer" concept for turbulent boundary layers (57). By this, the mean flow consists of an "inner" region, say  $0 < \xi < 0.15$ , which is directly governed by the wall processes and an "outer" region, say  $0.05 < \xi < 1.00$ , which is controlled only by conditions

at its boundaries and is, therefore, only "loosely" coupled to the wall processes in as much as they determine its inner boundary condition. In a fully developed pipe flow, the shear stress profile is linear in radius, so the shear stress "seen" by the outer region at its inner edge is very close to the wall shear stress,  $T_w$ , hence, in it,  $u_\tau$  is the velocity scale. Obedience of the "effective slip" model indicates, therefore, that the outer region remains Newtonian even in flows exhibiting drag reduction. The outer region typically extends down to  $y^+ \simeq 50$  so, by inference, the central differences between drag reducing Toms Phenomenon flows and honest-to-goodness Newtonian flows must lie in a region  $0 < y^+ < 50$ , extremely close to the pipe wall. This is also the region one would expect, intuitively, to be altered when drag reduction occurs since it is where most of the energy action in a pipe occurs (43).

Observe finally that the outer region comprises the entire flow save for a thin wall region; thus the "effective slip" model is very satisfactory for practical mean velocity profile prediction.

#### 1.4.22 Turbulence Structure

Turbulence measurements in polymer solution were made only at the "high" flow rate; their absolute accuracy is

poorer than in solvent, because the Newtonian heat transfer laws that the anemometer was designed for do not hold in polymer solution - see Section 1.4.4.

#### 1.4.221 Intensity Profiles

In solvent, the rms axial turbulent velocity,  $u$ , could be measured to  $\pm 10\%$  and intensity profiles,  $(u/u_\tau)$  vs.  $\xi$ , agreed within that with the results of Laufer (43). In polymer solution, Fig. 6.8.3, intensities (absolute value good to  $\pm 20\%$ ) are essentially the same as solvent for  $\xi < 0.4$ , but are higher for  $0.4 < \xi < 1.0$ , a maximum difference of  $+40\%$  on the pipe axis; also, there is a "plateau" for  $0.4 < \xi < 0.7$ .

From the integrated momentum equation in a Newtonian flow,

$$\rho(1 - \xi)T_w = \overline{\rho u'v'} + (2\eta/D)(dU/d\xi) \quad (1.4.19)$$

so the local shear stress (LHS) is composed of turbulent,  $\overline{\rho u'v'}$ , and direct viscous components. From the mean flow, for  $y^+ > 50$ , the viscous term,  $(2\eta/D)(dU/d\xi)$ , is that which would prevail in the Newtonian solvent at the same  $T_w$ ; therefore,  $\overline{\rho u'v'}$  must also be. Thus both  $(u/u_\tau)$  and  $\overline{\rho u'v'}$  in polymer solution follow Newtonian rules for  $y^+ > 50$ ,  $\xi < 0.4$ . In the central core,  $0.4 < \xi < 1.0$ , which is relatively isotropic, one would expect  $v'$  to behave as

$u'$  so that, since  $\overline{u'v'}$  is still the same but  $u'$  considerably higher, the correlation coefficient between  $u'$  and  $v'$  in polymer solution must be reduced relative to the Newtonian plug - i.e.,  $u'$  and  $v'$  are more "out of phase". The physical significance of the intensity plateau observed from  $0.4 < \xi < 0.7$  is uncertain.

#### 1.4.222 Energy Spectra

Axial, one-dimensional turbulent energy spectra in solvent and polymer solution are shown on Figs. 5.5.7 and 5.5.8. Considerable confidence can be placed in spectra shapes - the distortion is about  $\pm 5\%$  - but the absolute value of the ordinate is  $\pm 25\%$  in solvent and  $\pm 50\%$  in polymer (this latter must be compared, however, with the 8 decade range spanned). Spectrum parameters are listed in Table 1.4.2;  $\Lambda_f$  is the macroscale, characteristic of the large "energy containing" eddies;  $\epsilon_1 = 15\nu \int_0^\infty k_1^2 E_1(k_1) dk_1$  is the dissipation rate assuming isotropy, and  $k_d$  is the dissipation wave number defined in connection with the Onset Hypothesis.

On the pipe axis,  $\xi = 1.00$ , there is a distinct difference in spectra shapes; in particular, the "inertial subrange" with slope  $-5/3$  that occurs for  $2 < k_1 < 20 \text{ cm}^{-1}$  in solvent is entirely absent in polymer solution in which, instead, there is an abrupt change in slope from  $-2/3$  to

-4 at  $k_1 = 6 \text{ cm}^{-1}$ . Ideally, the inertial subrange is observed when the regions of turbulent energy production (predominantly low wave numbers) and dissipation (predominantly high wave numbers) are far enough separated, so its absence is indicative of smaller separation or stronger "coupling" between these regions. From the experimental equality of the macroscales,  $\Lambda_f$ , the lower, energetic, wave numbers are the same in polymer solution so the stronger coupling must result in the dissipative wave numbers moving towards them - i.e., towards the origin - which, since dissipation varies as  $k_1^2$ , must result in lower dissipation. Both these consequences are observed: from Table 1.4.2,  $k_d$  decreases from 16 to  $6 \text{ cm}^{-1}$  and the dissipation in polymer solution is 40% lower despite the turbulent kinetic energy,  $u^2$ , being 40% higher than solvent.

Near the pipe wall,  $y^+ = 0.033$ , there is essentially no difference in the spectra; the shapes are remarkably similar, the ordinates only slightly different, and the dissipation about 10% less in polymer solution. This radial location corresponds to  $y^+ \simeq 100$  which is still in the "outer region", relatively remote from the energy action ( $y^+ \simeq 10$ ).

Both intensity profiles and spectra present the same picture. Near the wall (but still in the outer region),  $y^+ > 50$ ,  $y^+ < 0.4$ , the intensity,  $(u/u_\tau)$ , turbulent shear

stress,  $\overline{\rho u'v'}$ , and axial spectra indicate a Newtonian turbulence structure in polymer solution, strongly reinforcing the notion of a Newtonian plug convected along intact at an additional, "effective slip," velocity. Towards the pipe axis,  $0.4 < \zeta < 1.0$ , the turbulence structure is distinctly different from Newtonian. Note, however, that the Newtonian scaling fails only at the highest echelon of detail - turbulence structure - and then only in the central core, which region is the most independent of (strictly, the least dominated by) the energy processes occurring near the wall. Thus it is entirely possible that the turbulence structure in the central core is due to causes not directly related to those causing the Toms Phenomenon, though both must, eventually, be traced to the addition of macromolecules.

Flow structure measurements, mean and turbulent, have not hitherto been reported in the literature, so no comparisons can be made.

### 1.4.3 The Over-all Picture

#### 1.4.31 Evaluation of Earlier Explanations

The four types of explanations cited in Section 1.1 were:

- (1) "effective slip"
- (2) inherently delayed transition



- (3) anisotropic viscosity
- (4) visco-elasticity .

Of these, (2) is definitely not valid since transition is delayed only in certain specific cases dictated by the Onset Hypothesis. (1) is well obeyed, which shows that the significant differences between Toms Phenomenon and plain Newtonian flows lie in the immediate vicinity of the wall,  $0 < y^+ < 50$ , but "effective slip" remains an "engineering" notion, and its causes are likely encompassed within the remaining two explanations, (3) and (4). Because experimental measurements were not made in the immediate wall region,  $0 < y^+ < 50$ , no conclusive distinction can be made between the anisotropic viscosity and visco-elasticity explanations, but some peripheral evidence is available.

(a) On the pipe axis, roughly isotropic conditions prevail so a mechanism like (3) cannot be operative. Thus in the central core of the pipe, the observed differences in turbulence structure - notably the energy spectrum - are almost certainly due to a visco-elastic "interaction".

(b) Macromolecular elongation in (3) depends only on the mean shear rate; in the limit this should result in effectively laminar flow as all radial turbulent momentum transport is blocked by the extended macromolecules. But a visco-elastic mechanism would imply excitation of the macromolecules by the turbulence which, in the limit, would

result in a standoff at some turbulent condition where the turbulence was reduced to the extent that it failed to excite the macromolecules. The observed limiting case - the maximum drag reduction asymptote - is definitely not a laminar flow.

(c) If radial momentum transport were indeed impeded as in (3), one would expect the mixing length constant in the law of the wall to be altered which is not so.

(a) to (c) all tend to favour the visco-elastic viewpoint.

#### 1.4.32 Prediction of the Toms Phenomenon

The present findings are summarized in the form of a generalized Toms Phenomenon flow diagram, Fig. 6.10.1.

1. The three limiting lines are:

AB Poiseuille's law

$$f = 16 N_{Re}^{-1} \quad (1.4.20)$$

DG Prandtl's universal turbulent friction factor law

$$f^{-\frac{1}{2}} = 4.0 \text{Log}_{10}(N_{Re} f^{\frac{1}{2}}) - 0.4 \quad (1.4.21)$$

EH The maximum drag reduction asymptote

$$f^{-\frac{1}{2}} = 23 \text{Log}_{10}(N_{Re} f^{\frac{1}{2}}) - 43. \quad (1.4.22)$$

2. The most general flow path is ATFOMH with segments:

AT laminar flow (1.4.20)

TF transition region with T, the transition point, at the same  $N_{Re,T}$  as solvent.

FO fully developed turbulent flow, without drag reduction, (1.4.21).

O Onset point  $(Q^*, T_w^*)$  at which  $T_w^*$  is related to the polymer by the Onset Hypothesis

$$(D_M u_T^* / \gamma) = 0.015 \quad (1.4.23)$$

OM turbulent flow, with drag reduction, controlled by polymer parameters - concentration, molecular weight, species - as described in Section 1.4.14.

MH turbulent flow along maximum drag reduction asymptote, (1.4.22), independent of polymer

3. Special Cases

(a)  $c \rightarrow 0$ , ATFG (the solvent line) is followed.

(b)  $c \rightarrow \infty$ , ATFOKH is followed, the polymer solution flow line OM tending to asymptote OK, the slope of which,  $N_p$ , depends on

polymer. (Note:  $c \rightarrow \infty$  implies concentrated solutions)

- (c)  $T_w^* < T_{w,T}$ , transition is delayed to  $T'$  and segment TF is absent, drag reduction being attained as soon as turbulent flow is established. The path is AT'F'MH.
- (d)  $T_w(M) < T_w(C)$ , if the point M is predicted to lie to the left of point C, i.e., in a "virtual" region, then transition will be delayed to C and the maximum drag reduction asymptote followed immediately thereafter - path ACH.

4. Mean Velocity Profiles. At any point  $P(Q, T_w)$  in fully developed turbulent flow, the corresponding Newtonian "plug" refers to point  $N(Q_N, T_w)$  on the Newtonian solvent line. The "effective slip" velocity is

$$V_S = U_{Av} - V_{Av} = 4(Q - Q_N) / \pi D^2 \quad (1.4.24)$$

Equally,  $V_{Av}$  is available from  $T_w$  and (1.4.21). The Newtonian "plug" profile,  $V(\xi)$ , at N is obtained from standard  $u^+$  vs.  $y^+$  relations (see, e.g., (44)). The required velocity profile is  $U(\xi)$  given by

$$U(\xi) = V(\xi) + V_S, \quad y^+ > 50 \quad (1.4.25)$$

#### 1.4.4 Anomalous Pitot Tube and Hot Film Measurements

Two previously unreported phenomena were observed in the course of flow structure measurements.

##### 1.4.41 Pitot Tube

In polymer solutions the Pitot tube ceases to be the "absolute" instrument it is in Newtonian fluid flow. The stagnation pressure attained - hence the apparent velocity,  $U_a$ , indicated - is a function of:

- (a) absolute velocity,  $U_1$
- (b) Pitot tube diameter,  $d$
- (c) polymer molecular weight
- (d) polymer concentration .

The "discrepancy" between apparent and true velocities increases with increasing (a), (c) and (d) and with decreasing (b). The effects of velocity and Pitot tube diameter are shown on Fig. 5.4.5 on which apparent velocities in polymer solution are referred to identical solvent measurements. This is why the 0.025 cm tube was adequate at the "low", but a 0.168 cm Pitot had to be employed at the "high" flow rate, Section 1.4.21. If the Pitot face is modelled as a small disc normal to the flow, the discrepancy can qualitatively be explained by an energy argument whereby the macromolecules elongate according to the shear rate,

$(2U_1/d)$ , at the stagnation point, thereby abstracting energy from the mean flow and detracting from the stagnation pressure attained.

#### 1.4.42 Hot Film

The heat transfer from cylinders in cross flow in polymer solutions is a function of:

- (a) absolute velocity,  $U_1$
- (b) ambient strain rate,  $(dU_1/dr)$
- (c) polymer molecular weight
- (d) polymer concentration
- (e) cylinder diameter,  $d$ .

The (polymer solution/solvent) heat transfer coefficient ratio,  $(h_p/h_s)$ , at essentially zero strain rate is shown vs.  $U_1$  in Fig. 6.7.2. In terms of the cylinder Reynolds number,  $N_{Re,d}$ , three regions exist:

- (1)  $N_{Re,d} < 40$  ( $U_1 < 100$  cm/sec) the ratio is essentially unity.
- (2)  $40 < N_{Re,d} < 300$ , the ratio decreases sharply to a minimum of about 0.3 before increasing back to about unity. Since  $h_s \propto U_1^{1/2}$ , in the initial stage of this region,  $h_p$  is relatively insensitive to mean velocity,  $U_1$ .
- (3)  $N_{Re,d} > 300$ , the ratio drops abruptly to about 1/3 and becomes fairly insensitive to velocity.

Regions (2) and (3) overlap for  $250 < N_{Re,d} < 350$  where the heat transfer is unstable, and  $h_p$  may fluctuate by threefold.

The heat transfer improves with polymer degradation - i.e., decreasing molecular weight - and with increasing ambient strain rate.

Experimental turbulence results in polymer solution - which are always obtained via a mean velocity calibration - were independent of the heat transfer regime the sensor was operating in. But, since Newtonian laws were not obeyed, the calibrations were appreciably curved, which resulted in poorer absolute accuracy than in solvent.

Table 1.4.1  
Comparison of Flow Rates

Flow Rate	Pitot tube, cm	Solvent		Polymer Solution	
		$Q_1$	$Q$	$Q_1$	$Q$
"Low"	0.025	1.158	1.151	1.137	1.148
"High"	0.168	5.45	5.71	5.55	5.71

All flow rates in litres/sec.

$Q_1$  - Flow rate from integration of mean velocity profile

$Q$  - Flow rate from pump calibration

Table 1.4.2  
Spectrum Parameters

Spectrum	$\mathcal{F}$	$u_\tau$ cm/sec	$\nu$ cm <sup>2</sup> /sec	$\Lambda_f$ cm	$\mathcal{E}_1$ cm <sup>2</sup> /sec <sup>3</sup>	$k_d$ cm <sup>-1</sup>
Solvent	1.00	28.4	0.00894	0.73	8100	16
Polymer	1.00	26.5	0.0127	0.77	4800	6
Solvent	0.033	28.4	0.00894	1.15	26000	16
Polymer	0.033	26.5	0.0127	1.50	23000	21



## Chapter II

## INTRODUCTION

## 2.1 The Toms Phenomenon

The Toms Phenomenon concerns the reduction of specific power consumption obtained by the addition of minute amounts of macromolecular solute to a micromolecular solvent in turbulent flow. For a pure, Newtonian, solvent in a turbulent shear flow, for example in a pipe, a certain energy expenditure, reflected by the pressure gradient, is required to maintain a given flow rate. It is observed experimentally that very small amounts, of the order of parts per million, of soluble high polymer added to the solvent result in drastic reductions of the specific energy expenditure; thus a lower pressure gradient is required to maintain the same flow rate, or a higher flow rate can be attained for the same pressure gradient as the solvent.

This effect is best illustrated by a hydraulic flow diagram, a plot of flow rate,  $Q$ , versus wall shear stress,  $T_w$ ; the latter is directly proportional to the pressure gradient in a pipe flow. Figure 2.1.1 is such a plot of the data of Toms (1) for solutions of poly-methylmethacrylate in monochlorobenzene. No difference can be observed in the laminar regime, but in turbulent flow the flow lines for polymer solutions lie to the left of the solvent line,

indicative of a specific power (or drag) reduction. The fractional drag reduction,  $R_{F,Q}$ , at a given flow rate,  $Q$ , is defined by

$$R_{F,Q} = (1 - T_{wp}/T_{ws})Q \quad (2.1.1)$$

On Fig. 2.1.1 the fractional drag reduction increases with flow rate and concentration, a maximum value of about 60% being attained.

## 2.2 Object of Thesis

Two factors are essential to the occurrence of the Toms Phenomenon: the addition of a macromolecular solute and the turbulent flow of the solvent. The object of this thesis was to study the Toms Phenomenon in pipe flow with respect to:

(1) The gross effect of macromolecular additive as regards the relation of polymer to the drag reduction induced.

(2) The flow structure, mean and turbulent, prevailing when the phenomenon was exhibited and how it differed from that in the pure solvent.

### 2.3 Significance of the Problem

An understanding of the Toms Phenomenon is of interest from both practical and theoretical standpoints.

Practically it might be employed for:

(1) Reduction of hydrodynamic drag for both surface and submersible vessels, with consequent gains in speed and economy.

(2) More economic pumping of liquids, e.g., petroleum and petroleum products.

(3) Increasing the capacity of existing pipelines.

Theoretically, the interaction between the polymeric additive and the turbulence involves two fields of intense current interest:

(1) The rheology of dilute polymer solutions.

(2) Turbulent shear flow.

The experimental observations are stimulating also, because they run quite contrary to expectation; the addition of polymeric solute increases the solution viscosity whence one would expect a corresponding increase in specific power consumption.

## 2.4 Previous Work

A brief review of previous work is presented in approximately chronological sequence.

The work of Toms (1), for whom the phenomenon is named, was reported in 1948. He was the first to recognize clearly the drag reduction induced in turbulent flow by the addition of polymer. The flow of solutions of one linear, random coiling polymer, poly-methylmethacrylate, molecular weight about  $2 \times 10^6$ , in monochlorobenzene was studied in two pipes, 0.404 cm and 0.128 cm internal diameter. The only minor shortcoming of this work was that the highest Reynolds Numbers attained were modest - 10,000 in the 0.404 cm. pipe and 3,000 in the 0.128 cm. pipe - which cast some doubt on the establishment of fully turbulent flow. In a companion work, Oldroyd (2) proposed a "wall effect" explanation for the drag reduction observed. This envisaged an abnormally mobile layer of macromolecules near the pipe wall, oriented by the prevailing shear rate, which caused an "effective slip". It is fairly obvious that a slip at the wall would yield qualitatively the same results as observed experimentally.

The phenomenon had probably been encountered earlier during World War II work on the flow of "Napalm", which was noted (3) to be easier to pump than the solvent, gasoline. In these cases the effect observed was probably much less

pronounced, because the aluminium soaps then used in Napalm were relatively low molecular weight compared to polymers.

Further work was a by-product of investigations of the turbulent flow of "pseudoplastic" fluids (4,5,6). These studies, of which the work of Shaver and Merrill (4) is typical, were conducted with rather concentrated solutions of low molecular weight polymers. Pseudoplastic fluids obey the so-called "power law" rheological model over limited ranges of shear rate. On the basis of this model, a generalized "power law" Reynolds Number can be derived (7), and the object of these studies was the generation of generalized friction factor charts based on it with the power law index as a parameter. These studies encountered the Toms Phenomenon only inadvertently and did not pursue it, even though Shaver (7) foresaw increasing flow rate by the "judicious addition of polymer". The correlations obtained failed entirely to predict drag reduction in dilute, and therefore negligibly pseudoplastic, polymer solutions.

A paper by Savins (8) in 1963 was notable in many respects. In it the Toms Phenomenon was differentiated clearly from the "Non-Newtonian" flows of the preceding paragraph. Two new types of explanations were advanced as to its cause. First, in analogy to dusty gases, it was suggested that drag reduction might be a result of delayed

laminar to turbulent transition. Second, that drag reduction might result from the visco-elasticity introduced by the addition of polymer. While the mechanism of the visco-elastic hypothesis is unclear, it is perhaps the most popular hypothesis to date. In addition to the theorizing, experiments covering a wide range of laminar and turbulent flow rates in three pipes were reported, illustrating differences in the drag reducing ability of several polymers. Interpretation of the experimental results was, however, seriously hampered by the entire lack of polymer characterization.

The delayed transition hypothesis was based on the experimental observation (9,10) that dusty gases show lower pressure drops in turbulent flow than clean gases, for example in cyclone separators. To explain this Saffman (11) conducted a stability analysis which indicated that under certain conditions the dust would stabilize the flow, although a subsequent computer solution for plane Poiseuille flow (12) based on this analysis was not conclusive. Nevertheless, a delay in transition is in the same direction as drag reduction, and there is some physical similarity between dust particles in air and macromolecules in dilute solution, so a reasonable analogy exists. Related to dusty gases are turbulent flow investigations of fine particle slurries (13,14), where drag reduction has

been claimed but is very slight, and of fibre suspensions (15) which exhibit significant drag reduction. It has also been proposed, with little confirmation, that "Non-Newtoniancy" inherently delays transition (16).

A series of blowdown experiments in a 1.0 cm. pipe, using a number of homologous polyethylene oxides dissolved in water, was reported by Fabula (17). Although only a limited range of turbulent flow rates was covered, these experiments were notable for the careful characterization of polymers, the recognition that the Toms Phenomenon was associated with dilute solutions and the observation that drag reduction decreased at very high flow rates due to polymer degradation. Polymer degradation under shear had been reported earlier (18).

Attempts have been made to relate drag reduction to visco-elasticity (19,20). Unfortunately, experimental visco-elastic measurements, e.g., of the first normal stress difference, are possible only for concentrated solutions for which the viscosity buildup neutralizes considerably the drag reduction obtained with respect to the solvent. Further, the application of visco-elastic measurements in concentrated polymer solutions, in which the polymer molecules are extensively intertwined, to dilute solutions, in which each macromolecule is essentially on its own, is questionable.



Shin (21) studied the Toms Phenomenon in turbulent Couette flow with a view to finding the effect of the polymer used. Two homologous series were studied, polyethylene oxides and polyisobutylenes. The polymers were very carefully characterized using viscometry and light scattering to relate intrinsic viscosity to molecular weight and rms radius of gyration. The major findings were that for a given molecular weight, polymers with more mers and more flexible bonds were more effective in reducing drag, and that the concentration of polymer required to attain a given fractional drag reduction varied inversely with its terminal relaxation time, as calculated from the theory of Rouse (22). It was also proposed that drag reduction might result from an "anisotropic viscosity". This explanation assumes that the macromolecules are elongated under shear and align themselves in the direction of flow. Thus they impede the transfer of momentum in a transverse direction, reducing the turbulent shear stress and thence the drag. This work was extended in a subsequent thesis by Lee (23) to other polymers, polyacrylamides and polysodiumstyrenesulphonate, the latter a polyelectrolyte. An attempt was made to relate drag reduction to macromolecular extension under shear as predicted by Peterlin (24).

In the course of the present work, it was observed that

for a given polymer-solvent system and pipe the onset of drag reduction by the Toms Phenomenon occurred at a well-defined point, independent of concentration. The "Onset Hypothesis" developed to relate this to the polymer is discussed in detail later. It was shown to hold (25) for the pipe flow data of several investigators (1,8,17,26,27,28), as well as for experiments reported in this work.

Hershey (29) studied the flow of relatively high concentrations of polyisobutylene in cyclohexane and of polymethylmethacrylate in toluene in a recirculating system using pipes from 0.025 cm to 5.0 cm internal diameter. The onset of drag reduction, termed "incipient turbulence suppression", was correlated approximately with terminal relaxation times calculated from the theory of Zimm (30). Despite the two different polymer-solvent systems used, the radii of gyration of the polymers were nearly identical, as were their relaxation times. Further, variations in relaxation time were obtained by increasing polymer concentration considerably beyond limits where the linear visco-elasticity theory of Zimm, derived for dilute polymer solutions, is expected to hold.

The visco-elastic analog to the Navier-Stokes equations has been derived (31) using a simple one-parameter constitutive equation to describe the polymer solution. This was used to analyze transition in terms of the Weissenberg

Number, a ratio of elastic to viscous forces that is frequently referred to in a visco-elastic context (e.g., 32). The form of drag reduction at infinite dilution was also predicted. Experimental confirmation of these predictions are lacking, but this work represents an analytical advance in the study of the Toms Phenomenon, possibly the first such.

Very recently experimental velocity profiles have been reported in turbulent flows exhibiting drag reduction (33), but there is some question as to their validity since Pitot tube measurements in polymer solutions are anomalous (34,35). Pitot tube anomalies were anticipated by both Savins (36), who attributed them to normal stress effects, and Boggs and Thompsen (31), who attributed them to the curvature of the flow over the Pitot tube. The discrepancy observed experimentally does not agree with the predictions of either.

Concluding this section, miscellaneous Toms Phenomenon studies with polymer solutions are listed. Turbulent flow noise was found to be higher than in solvent (37). No striking conclusions were reached regarding the effect of sudden expansions (38). Drag reduction was observed in rough pipes (39) comparable in extent to that in smooth pipes. Torque reduction for spinning discs has been noted (26,40).

#### 2.4.1 Summary of Proposed Explanations

Explanations proposed for the Toms Phenomenon, as mentioned in Section 2.4, fall into four categories:

(1) A "wall effect" causing "effective slip" at the wall (1,2).

(2) Delayed laminar-to-turbulent transtion (8,20).

(3) Visco-elasticity (8,19,20,29).

(4) Anisotropic viscosity (21,23).

All of these are somewhat speculative since the state of the art precludes the enunciation of precise mechanisms. None of the above have been conclusively disproved or substantiated, but the visco-elastic type of explanation is definitely the most popular at present.

## 2.5 Shortcomings of Prior Work

The work done to date suffers from three major shortcomings:

(1) The failure to adequately characterize the polymers used. This impairs meaningful comparisons with other work and the full interpretation of experimental results.

(2) The complete lack of turbulence measurements and hence of the flow structure in the Toms Phenomenon. All of the work to date concerns pressure gradient versus flow rate relationships which provide too gross a picture of turbulent flows.

(3) There is no systematic experimental data available over an adequate grid of pipe diameter, flow rate, polymer molecular weight and concentration. Available data cover scattered ranges.

These shortcomings are understandable: the first is probably a consequence of the unfamiliarity of fluid mechanics investigators with polymer chemistry, the second because turbulence measurements in liquids are difficult and have only recently (41) become possible, the third because of the novelty of the effect. However, they do prevent the establishment of a consistent set of experimental facts that might serve as the basis for the future understanding of the Toms Phenomenon.

## 2.6 The Present Approach

The objectives of the present work were stated in Section 2.3. Their relevance to the understanding of the Toms Phenomenon and their experimental fulfillment is discussed in this section with respect to:

- (1) the polymers used
- (2) the gross effect of macromolecular additive and
- (3) the structure of turbulent flow.

### 2.6.1 The Polymers Used

A homologous series of polyethylene oxides were the polymers used for the reasons below.

(1) A homologous series removes the effect of molecular structure as a variable. This was considered important for an initial study; other homologous series might be studied in the future to evaluate the effect of molecular structure.

(2) Polyethylene oxides are commercially available in a wide range of molecular weights,  $10^4$  to  $10^7$ .

(3) They were known to have good drag reducing ability.

(4) They are conveniently water soluble.

(5) They are random coiling polymers, not polyelectrolytic. Polyelectrolytes are subject to severe configurational changes in dilute solution which makes them difficult to characterize.

The intrinsic viscosity of each polymer was determined

experimentally, before and after use. The relation of this to other polymeric properties was carried out in another work (21).

#### 2.6.2 The Gross Effect of Macromolecular Additive

This was obtained by flow rate versus pressure gradient measurements to ascertain the effect of polymer molecular weight and concentration on the laminar flow regime, transition, and the onset and extent of drag reduction in turbulent flow in two pipes, 0.292 cm and 3.21 cm internal diameter. In laminar flow the smaller pipe served as a high shear capillary viscometer to detect "shear thinning" or changes in intrinsic viscosity that might reflect changes in polymer configuration. The study of transition was important both because it figures in proposed explanations and because it is a very singular - and therefore interesting - point. Results from the turbulent regime served to establish systematically the manner in which the Toms Phenomenon occurs. This led to the recognition of parameters characteristic of the phenomenon and their correlation to polymeric properties. These parameters might, hopefully, be useful in comparing and predicting the onset and extent of drag reduction induced by polymers.

Experimentally, a wide range of variables was covered. Two pipes were used, 0.292 cm and 3.21 cm ID. Flow rates were varied to provide wall shear stresses from 1 to

2000 dynes/cm<sup>2</sup> in both pipes. Five molecular weights were used, covering a range from 80,000 to 6,000,000. Concentrations varied from 0.1 to 10,000 parts per million; the lowest concentration for any polymer was limited by the accuracy of the measuring instruments and the highest by the approximate criterion that the solution remain thermodynamically "dilute" (42), so that the maximum relative viscosity of the polymer solutions was about two.

Most of these measurements were made in the 0.292 cm pipe, because the smaller system permitted convenient, rapid, once-through operation without the use of prohibitively large amounts of solvent - distilled water. The recirculation necessary in the larger system caused polymer degradation with time and precluded accurate relation to polymer properties; thus only a few corroborative gross flow measurements were made in it.

### 2.6.3 The Structure of Turbulent Flow

The Toms Phenomenon is an "energetic" effect, resulting in the reduction of the specific power requirement. Since turbulent dissipation accounts for almost all the power required to sustain a turbulent flow, the turbulent energy balance is the natural place to start looking for an explanation of the mechanism of the Toms Phenomenon. To strike this balance (43), a detailed knowledge of the structure of turbulence is required. Some idea of this



was obtained from measurements in fully developed pipe flow of

- (1) the mean velocity profile ,
- (2) the axial turbulent intensity profile,
- (3) the axial one-dimensional turbulent energy spectrum,

at two radial positions, the pipe axis and very close to the pipe wall. These measurements are insufficient for the complete description of the turbulence, but the current accuracy of turbulence measurements in liquids did not warrant any greater complexity. Their major purpose was to compare the turbulence pertaining in the polymer solutions to that in the solvent at the same flow rate. Two flow rates were studied: one just before the onset of drag reduction and the other well into the drag reducing regime.

The relevance of the mean velocity and turbulent intensity profiles to any detailed study of flow structure is obvious. The turbulent energy spectrum, obtained from a Fourier analysis of the turbulent (fluctuating) velocity (44) gives the distribution of turbulent energy by wave-numbers. From the spectrum, and its moments, information can be derived regarding the "flow" of turbulent energy from its production to eventual dissipation at a point (see, for example, (45)). Measurements on the pipe axis and close to the wall are significant because these two positions represent contrasting extremes. On the pipe axis

the flow is unstrained and almost isotropic; it accounts for very little of the energy dissipation. Near the wall the flow is highly strained (high mean shear rate), highly anisotropic, and responsible for the major fraction of the production and dissipation of turbulent energy. In Newtonian fluids the shape and magnitude of energy spectra at these two positions differ markedly (43).

All flow structure measurements were made by traversing a cross section at the end of the 3.21 cm pipe. Pitot tubes were used for the mean velocity measurements and a hot film anemometer for the turbulence measurements. The two flow rates studied corresponded to solvent Reynolds Numbers of 50,000 and 250,000. Measurements in the solvent provided a basis for comparison with polymer as well as a means to establish the accuracy of the instruments used.

#### 2.6.4 Summary of Approach

In summary the approach used in this work was:

(1) To use a homologous series of linear random coiling polymers and to characterise them thoroughly.

(2) Conduct small scale pressure gradient versus flow rate experiments over a wide grid of polymer molecular weight and concentration in both laminar and turbulent flow. These established the basic manner in which the Toms Phenomenon occurred.

(3) Using information derived in (2) to make a few detailed studies of the flow structure in a system large enough to probe. These, conducted in both solvent and polymer solution at equal flow rates, would detect any changes in the flow structure obtained when the Tom's Phenomenon was exhibited.

## Chapter III

## APPARATUS

## 3.1 General Description

Two experimental pipe-flow systems, constructed around 0.292 cm and 3.21 cm ID test pipes, were employed.

## 3.1.1 The Small System

This system, Fig. 3.1.1, consisted of a 5 gallon blowdown tank from which liquid was forced under a constant gas pressure for one pass through a smooth, precision bore, stainless steel tube, 0.115 in. (0.292 cm) ID x 0.187 in. OD x 26.5 in. long. The tube had 4 pressure taps--one every 35 diameters beginning 110 diameters from the entrance. The pressure differential between any two taps was measured by a transducer, accurate to about 1% of the absolute value. The volumetric flow rate was measured directly with a "bucket and stop watch" arrangement at the system exit, accurate to about 1/2%. In addition to the pressure drop versus flow rate measurements, the critical Reynolds Number for transition could be measured by introducing a disturbance at the pipe entrance. When the flow was critical, the disturbance was amplified and could be detected downstream as a "hiccup" from the pressure transducer.

### 3.1.2 The Big System

This recirculating system, Fig. 3.1.2, centered around a seamless, stainless steel test pipe, 1.264 in. (3.21 cm) ID x 1.50 in. OD x 475 in. long, with its entire inside surface polished smooth. The pipe was composed of 5 sections, each 75 diameters long with a wall static pressure tap at its downstream end. The first 4 upstream sections were identical; the last "test" section had a machined window at its downstream end giving access to the inside of the pipe. A micrometer traverse, Fig. 3.1.3, capable of simultaneously holding a Pitot tube and a hot film probe in an "over and under" arrangement, was mounted positively on the window and permitted radial probing up to the far inside wall of the pipe. The flow entered the test pipe through a nozzle preceded by a 6 in. diameter, 39 in. long calming chamber and exited through a 5° conical diffuser which expanded up to a 3 in. IPS polvinylchloride pipe that returned via a filter to the pump. A two-stage, variable speed, Moyno "progressing cavity" pump was used for its gentle liquid handling and metering (positive displacement) action. A standpipe on its suction port and a surge tank downstream of its discharge port effectively eliminated pressure fluctuations, "ripple", emanating from the pump. The liquid temperature was controlled to  $\pm 0.2^{\circ}\text{C}$  by a sensor in the return line

that regulated the flow of city water to the shell side of a shell and tube heat exchanger between the pump and the calming chamber.

The pressure differential between the furthest downstream tap and any other was measured by a transducer, accurate to about 1% of the absolute value. The volumetric flow rate could be varied over a 100 fold range, up to a maximum of 9 litres/sec, and was controlled to  $\pm 1/2$  %.

Mean velocity profiles were obtained by traversing a Pitot impact tube and measuring the stagnation pressure with respect to a wall static pressure tap.

A constant temperature hot film anemometer with a cylindrical quartz coated hot film sensor was used for turbulence measurements. The simultaneous use of a Pitot tube with the hot film probe enabled in situ static calibration of the latter before and after each set of measurements, greatly enhancing their accuracy. Turbulent intensity and energy spectra were obtained by operating on the anemometer (electrical) signal with the usual instruments: a rms random signal voltmeter alone, for intensity, and in conjunction with a variable filter, for spectra.

### 3.2 Detailed Descriptions

In the sections following, fairly detailed descriptions of the components of each system and the measuring instruments used are presented under the headings:

- 3.3 The Small System
- 3.4 The Big System
- 3.5 Measuring Instruments
- 3.6 Auxilliary Equipment

Further details, scale drawings, and a list of vendors are given in Appendices E and F.

### 3.3 The Small System

The components of this system were:

- (1) the test pipe
- (2) the blowdown tank
- (3) the static pressure and flow control modules
- (4) the flowmeter
- (5) solution makeup equipment.

#### (1) The Test Pipe

The test pipe was made of smooth, seamless, precision bore, type 321 stainless steel tubing, 0.115 in. (0.292 cm) ID x 0.187 in. OD x 26.5 in. long. The tolerance on the inside diameter,  $\pm 0.0010$  in., was checked with an optical microscope and found to hold. The entrance to the pipe from the tank is shown in Fig. 3.3.1(a). A machined, burr free, square edged entrance was used to minimize the entrance length without unduly disturbing the flow. The flow could be "triggered" artificially by inserting a short concentric circular plug, 0.057 in. ID, into the pipe entrance, Fig. 3.3.1(b). The sudden expansion following this "trigger" continuously disturbed the flow, ensuring transition at the lowest possible Reynold's number. The pipe had 4 wall static pressure taps, one every 4.00 in., beginning 12.5 in. (110 diameters) from the entrance. These, Fig. 3.3.1(c), were made by milling a small flat on the outside of the tube



and drilling a radial 0.020 in. ID hole through the tube wall without letting the drill bit hit the far wall. The small burr resulting on the inside was entirely removed by alternate reaming and filing with a very smooth file. A bored out 3/16th inch "Swagelok" Tee, slipped over the tube with the 90° leg directly above the tap, served as a pressure take-off. All fittings downstream of the test pipe were of considerably larger inside diameter and offered, in comparison, negligible flow resistance.

#### (2) The Blowdown Tank

This was a vertical 5 gallon tank, approximately 8 in. OD x 26 in. high, made of 18 gauge type 304 stainless steel and tested to 100 psig. Cylinder nitrogen, reduced through a gas regulator, was used to pressurize the tank up to a maximum of 35 psig. Liquid was charged to the tank through a 4 in. ID mouth at the top, sealed by an O-ring cap. It left at the very bottom through the test pipe.

#### (3) The Static Pressure and Flow Control Modules

The static pressure module consisted of 4 ball valves connected on one side to each of the 4 pressure tap take-offs. The other side of the valve associated with the furthest downstream tap was connected directly to the low pressure port of a differential pressure transducer, while

the other three valves had a common header connected to the high pressure port. This permitted direct measurement of the pressure differential between the last tap and any other tap, and, by difference, the differential between any pair of taps.

The flow control module at the end of the test pipe consisted of a needle valve in parallel with a ball valve and a second ball valve downstream of these and in series with them. The valves in parallel complimented each other: the needle valve permitted fine flow control at low flow rates, but had a high resistance, limiting the maximum flow rate; the ball valve, with negligible flow resistance, permitted much high flow rates to be achieved with modest, but adequate, control. The second ball valve in series served to shut off the flow without altering the settings of the upstream valves.

#### (4) The Flowmeter

The flowmeter, Fig. 3.3.1(d), was a "bucket and stop watch" arrangement made up of a microswitch, an electric timer and a graduated cylinder. Liquid from the flow control module flowed through a flexible tube into a 4 in. length of copper tube and out. The copper tube, fixed to a movable block, could be rotated through a  $20^{\circ}$  arc in a vertical plane. Normally this exit tube was angled and the flow drained into a circular funnel leading to the sink.

To measure flow rate the tube was made vertical, thereby draining into a graduated measuring cylinder. A setscrew on the tube block was adjusted such that the same motion depressed a microswitch, which turned on the electric timer, at the instant that the flow entered the cylinder. The reverse process stopped the timer the instant flow into the cylinder ceased. Both liquid volume and time were read directly. Graduated cylinders of various capacities, 50 ml to 2000 ml, were used for accurate measurements over the entire range of flow rates.

#### (5) Solution Makeup Equipment

This consisted of common, miscellaneous units: a constant temperature bath, a filter, an extended shaft stirrer, a balance, several polypropylene containers. These served two functions:

- (a) To maintain the temperature of all solutions tested within acceptable limits,  $25.0 \pm 0.5^{\circ}\text{C}$ .
- (b) To make up uniform polymer solutions of prescribed, accurately known, concentration.

### 3.4 The Big System

A schematic diagram was presented earlier, Fig. 3.1.2. Scale drawings of the system layout and of secondary equipment, as well as details about control line connections, are presented in Appendix E.

The components of this system were:

- (1) the test pipe
- (2) the micrometer traverse and probes
- (3) the pump
- (4) discharge end equipment
- (5) the return line
- (6) suction end equipment
- (7) the control panels.

#### (1) The Test Pipe

The test pipe was made from commercial 1 1/2 in. OD, 0.120 in. wall, seamless, type 316 stainless steel tubing, with the inside specially polished. It was  $1.264 \pm 0.007$  in. ID x 1.50 in. OD x 475 in. long and was suspended horizontally 8 feet above the floor. It consisted of 5 equal flanged sections connected by a "male-female" arrangement, Fig. 3.4.1(a), in which the machined square pipe ends butted, compressing an O-ring between the machined flange faces without having them touch. This ensured positive alignment and a clean concentric joint. Each section had a wall static pressure tap, 1/32 in. ID drilled radially and

deburred on the inside, 2 in. from its downstream end. The farthest downstream, "test", section had a platform at its downstream end, onto which the traversing mechanism was mounted, with a rectangular window giving access to the inside of the pipe.

## (2) The Micrometer Traverse and Probes

The micrometer traverse provided for traversing the pipe with a Pitot tube and a hot film probe, individually or simultaneously.

Photographs of the traverse and the platform it is mounted on were given in Fig. 3.1.3; scale drawings are presented in Appendix E. When assembled, the arrangement resulted in almost no disruption of the inside surface of the pipe. It permitted positive location of the probes with respect to a common datum - the plane of contact between the traverse base and the pipe platform. The probes traversed in a radial plane up to the far wall. The ball bearing that fixed the micrometer shaft to the base had some axial play, resulting in 0.002 in. of lost motion when micrometer rotation was reversed. This was immaterial if all measurements were made with the same direction of rotation. Probe settings were maintained by friction between the probe shafts and the O-rings that sealed their entry into the pipe; in addition, a micrometer lock was provided. The static pressure tap on the test

section was located upstream of the probes and normal to the traversing plane. This way, static pressure readings were unaffected by the probes, and the flow at the wall was not disturbed by the tap. When the traverse was not in use, the pipe window was sealed by a matching lucite plug.

The probes used, Fig. 3.4.1(b), were built to specifications. All Pitot tubes had the same size tubular stainless steel shafts, 0.066 in. OD by 4 in. long. The impact tips varied from 0.020 in. OD, flattened to 0.010 x 0.030 in., to 0.066 in. OD. Cylindrical, quartz coated, hot film sensors, 0.001 or 0.002 in. OD x 0.020 in. sensing length were used. The cylindrical form was used for its symmetrical directional properties and the small flow disruption relative to other shapes, e.g., wedges and cones. The quartz coating insulated the platinum film from the liquid, greatly enhancing stable operation by the elimination of shunt electrical paths, electrolysis, scaling and bubble formation. However, the frequency response of the hot film is adversely affected by the coating. A linearized heat transfer analysis of this problem is given in Appendix A; for the sensors and experimental conditions employed in this work, the effect was negligible. L-shaped probes, with the sensor at the extreme upstream end, were used to minimize the effect of probe induced flow disturbances on

the sensor. The prongs on which the sensor mounted were bent slightly to permit probing very close to the wall. Electrical connections to the sensor were carried inside, but insulated from, the 0.061 in. OD tubular stainless steel casing. The nominal sensor resistance was 7 ohms.

### (3) The Pump

A two-stage Moyno "progressing cavity" pump (type 2L10, SSQ) with a stainless steel rotor and a synthetic rubber stator was used. It had a rated capacity of 140 gpm against a differential pressure of 75 psi. The pump was driven, via a gearbox, by a 10 hp variable speed, eddy current coupled, drive. The output shaft speed of the drive could be varied from 1670 to 100 rpm and was controlled to  $\pm 5$  rpm over the range. The drive was connected to the gearbox by a timing belt that effected a 26:84 speed reduction. The gearbox had 5 output-input ratios, ranging from 1:4.11 to 1.69:1, and its output shaft was coupled directly to the pump rotor. The precise rotational speed of the pump rotor at each gear ratio was calculated from the frequency of an 18 pole a-c generator tachometer mounted on the output shaft of the drive as an integral part of the electronic control system.

The eccentric rotor caused considerable mechanical vibration. To prevent the transmission of this to the rest of the system, the pump was bolted to the floor and connected

through flexible pipe. The pump also introduced a troublesome pressure fluctuation into the system, having a frequency approximately 4 times the pump rotational speed and an amplitude that varied with frequency but attained a maximum of 100 cm of water. This "ripple" was practically eliminated (attenuated 15 to 150 fold) by a 6 in. IPS standpipe over the suction port and a surge tank downstream of the discharge port. Pump details are given in Appendix E.3.

The pumping characteristic, flow rate versus rotational speed, determined by a "bucket and stop watch" calibration, was remarkably linear (Appendix F.2) over the entire range and was independent of both the pressure differential (up to 50 psi) and the liquid pumped (water or polymer solution).

#### (4) Discharge End Equipment

This comprised the units between the pump discharge and the entrance to the test pipe, all made of stainless steel, described in flow sequence.

(a) Ascending Pipe. Sections of 3 in. IPS pipe ascended from the pump to the level of the test pipe. These included two flanged flexible pipe sections: a horizontal 51 in. length bolted to the pump discharge port and a vertical 60 in. length following this, the free ends of both being connected to massive steel supports.



(b) Heat Exchanger. The one pass heat exchanger, with a 6 in. OD x 18 in. long shell and 280 1/4 in. OD, 18 BWG tubes, was axially in line with the test pipe. The flow of cold, filtered city water to the shell side was regulated by a motorized valve, actuated by a sensor placed in the return line. For steady flow, temperature regulation was  $\pm 0.2^{\circ}\text{C}$  around the set point (about  $25^{\circ}\text{C}$ ).

(c) Calming Chamber. The calming chamber, a 6 in. OD, 11 BWG by 39 in. long flanged tube, mounted directly onto the tube sheet at the exit of the heat exchanger. The surge tank was mounted onto the calming chamber about 8 in. from its entrance. A circular section of 1/8 in. cell aluminium honeycomb, 8 in. thick, was placed at the downstream end of the chamber, ending 4 in. from the exit. The flow exited from the calming chamber into the test pipe through a nozzle.

(d) Surge Tank. A vertical 7 1/2 gallon, 8 in. OD, 18 gauge wall, 36 in. long surge tank mounted, by a short flanged 4 in. IPS neck, onto the calming chamber. It was pressure tested to 100 psig, but never operated above 50 psig. It could be vented or pressurized with nitrogen through the pump end control panel to control liquid level, visible through a lucite level gauge. The surge tank was located on the calming chamber for two reasons: the pressure drop in the heat exchanger and pipe preceding it

enhanced its damping effectiveness, and the honeycomb downstream of it eliminated flow disturbances from the large 4 in. ID radial hole through which it communicated with the calming chamber.

(e) Nozzles. Either of two concentric, machined, lucite nozzles could be attached to the calming chamber exit. With a smooth elliptical nozzle, the calming system worked embarrassingly well; the flow remained laminar throughout the test pipe up to a Reynolds Number of 10,000, and turbulence was not fully developed in the test section up to 30,000. A square edged nozzle used in all the runs reported resulted in fully developed turbulent flow at the lowest flow rate, Reynolds Number about 4,000.

#### (5) The Return Line

The flow exited from the test pipe through a lucite diffuser which expanded in a  $5^\circ$  subtended angle cone from the 1.26 in. ID of the test pipe to the 3.07 in. ID of the return line. The cone angle was designed to prevent separation in the diffuser and the associated pressure drop and fluctuations.

The return line was made from 3 in. IPS Sched 40 polyvinylchloride pipe. It consisted of a wide, 20 in. diameter, reverse curve directly after the diffuser, followed by two 190 in. long straight sections parallel to and lying alongside the test section. A  $0-50^\circ\text{C}$  mercury

thermometer, graduated in tenths of a degree, was mounted in the return bend to indicate fluid temperature. The second straight section had two 1/32 in. ID wall taps 4 in. from its ends. The temperature control sensor that regulated the heat exchanger was mounted in an elbow near the end of the return line. Apart from the test pipe, 3 in. IPS pipe was used everywhere because of the low shear rate in it, thereby minimizing pressure drop and polymer degradation.

#### (6) Suction End Equipment

This comprised a filter, several 3 in. IPS ball valves, two 55 gallon tanks and a mixer.

(a) Filter. The filter was necessary to clean the system adequately for stable operation of the hot film anemometer. With 5 micron elements it could handle 100 gpm of water with a pressure drop of about 9 psi.

(b) Valves. The valve network permitted routine operations: by-passing the filter, charging and offloading liquid to and from the system, isolating the run tank or permitting flow through it. Only "full flow" ball valves were used for the purely on-off service because of their negligible flow resistance.

(c) Tanks. One 55 gallon stainless steel tank, the run tank, was permanently connected to the suction end of the system. During operation it was kept brim full and in communication with the system, but without net flow

through it. It served both as a reservoir to maintain the system full of liquid, despite venting and surge tank filling, and to provide a liquid seal over the suction port with the NPSH necessary to prevent cavitation in the pump. The second tank was a spare, used occasionally.

(d) Mixer. A portable, 1/3 hp, variable speed mixer could be mounted on the run tank; it aided polymer solution makeup.

#### (7) Control Panels

Two control panels assisted operation of the system.

One, at the downstream end of the test pipe, consisted of 1/4 in. ball valves connected to all the pressure taps in the system. The other ends of the valves were connected to permit, by switching, measurement of the differential pressure between any two taps with a single transducer. All panel lines were filled with water; vents between the pressure taps and the valves prevented air from remaining in the connections or entering the panel.

The second panel, at the pump end of the system, had three sections: one permitted venting the system at various points, the heat exchanger, calming chamber, return line; the second allowed measurement of the differential pressure between various points - pump suction and discharge, across the heat exchanger, surge tank to atmosphere - on a 1/2% 100 psi differential gauge; the third controlled surge tank level by venting or nitrogen pressurization.

### 3.5 Measuring Instruments

The measuring instruments used were:

- (1) a pressure transducer
- (2) a strip chart recorder
- (3) a hot film anemometer
- (4) an oscilloscope
- (5) an rms random signal voltmeter
- (6) a variable filter, and
- (7) a frequency counter.

All of these were commercial instruments, fully described with performance specifications in manufacturer literature. Only especially relevant points are listed below.

#### (1) The Pressure Transducer

The differential pressure transducer, with an accompanying amplifier-indicator, had a range from 1 to 800 cm of water with an accuracy about 1% of the absolute value (calibration, Appendix F.1). The calibration was independent of absolute pressure level up to 25 psig though a slight, monotonic, zero shift occurred. Its response, rated 120 cps, was practically instantaneous because of the small hydraulic capacitance, 0.018 cc for maximum deflection.

## (2) The Strip Chart Recorder

This was a standard, 1/4%, potentiometric volt-ohm-milliamp recorder with a 1 sec pen, and chart speeds from 0.05 to 20 in. per minute. It was connected to the transducer output through a simple, homemade, voltage divider that synchronized full scales.

## (3) The Hot Film Anemometer

This was a constant temperature unit with a linearized output, developed by Ling (41). It was modified slightly to operate the 7 ohm probes used (it was designed for 15 to 20 ohms), and the overheat and bridge balance potentiometers were replaced with 10 turn pots for finer, more reproducible, settings. A short description of the circuit and some of its operational idiosyncracies is given in Appendix E.4.

## (4) The Oscilloscope

A dual beam oscilloscope was used routinely to observe visually the anemometer and variable filter signals to ensure satisfactory operation.

## (5) The RMS Random Signal Voltmeter

This was a true rms meter (no shaping circuits) using thermocouple blocks to average input power over either of two time periods, 15 and 60 seconds. Signals with frequencies of 2 cps to 250 kc could be measured over the range from 0.5 mv to 250 v rms with an accuracy of  $\pm 1\%$ .

### (6) The Variable Filter

This was a rechargeable, battery-operated, proportional bandwidth filter with a range from 2.5 cps to 25 kc. Somewhat better accuracy than the rated  $\pm 1$  db over the whole range was obtained by calibration with white noise at fixed points in each frequency decade (Appendix F.3).

### (7) The Frequency Counter

The frequency counter had three gate times, 0.1, 1.0 and 10 seconds, and a four figure register. It was used to compute the flow rate in the big system from the frequency of the drive tachometer via the gear ratio and pump calibration.

### 3.6 Auxilliary Equipment

In this category were:

- (1) polymer dissolving vessels
- (2) a viscometer, and
- (3) a hot film calibrator.

#### (1) Polymer Dissolving Vessels

Concentrated polymer solutions, "master batches", were made up in baffled stainless steel vessels, agitated by relatively large diameter, low speed, six-bladed turbine impellers. Their capacity, 1 1/2 or 8 gal, depended on the system. In both cases impeller diameter was about half and baffle width about one eighth of the vessel diameter.

#### (2) The Viscometer

The low shear GDM viscometer (46) was used to ascertain the intrinsic viscosity of the polymers used. It was a laminar Couette flow viscometer with an accuracy of about  $\pm 2\%$  in the shear rate range ( $\sim 1 \text{ sec}^{-1}$ ) used.

#### (3) The Hot Film Calibrator

This was a small recirculating water tunnel built to test the operation of the hot film anemometer. The micrometer traverse (Section 3.4 (2)), mounted on a



rectangular lucite channel with both probes in the potential flow region of a free jet issuing from a 3/8 in. nozzle that was preceded by a honeycombed 4 in. x 4 in. x 16 in. long calming chamber. The velocity at the nozzle exit could be varied from 0 to 1000 cm/sec by a set of valves. A 1/2 hp centrifugal pump was used, an in line 5 micron filter kept the system clean and the water temperature was controlled to  $\pm 0.1^{\circ}\text{C}$ .

## Chapter IV

### PROCEDURE AND CHEMICALS

#### 4.1 General Procedure

In both systems the procedure involved makeup of a concentrated polymer master batch, its characterization, a series of runs with polymer solutions prepared by dilution from the master batch and, finally, the reduction of experimental data by a computer. All experimental measurements made in polymer solutions were preceded by identical measurements in the solvent. All experiments were performed at  $25.0 \pm 0.5^{\circ}\text{C}$ .

##### 4.1.1 Chemicals

All five polyethylene oxide polymers obtained commercially were used as received. Distilled water was the solvent throughout.

##### 4.1.2 Master Batch Makeup

A weighed amount of polymer was rapidly and evenly dispersed in the solvent with vigorous agitation, then permitted to dissolve slowly with gentle stirring to prevent mechanical degradation. 0.5 wt % of formaldehyde was added as a preservative. Final polymer concentration was obtained gravimetrically; intrinsic viscosity was derived from relative viscosity versus concentration measurements on the GDM viscometer.

#### 4.1.3 Small System Runs

Two series of flow rate versus wall shear stress runs were made in this system. "Full range" runs covered the entire system range, laminar flow, transition and turbulent flow, with a data density of 10 to 20 points per wall shear stress decade. These included some runs with the "trigger" installed. "High flow" runs covered only the highest 1/3 decade of wall shear stress with a 30 to 40 points per decade density; they were performed with the more dilute solutions.

The procedure for both series was essentially the same. A 6 or 12 gallon batch of polymer solution was made by mixing measured amounts of master batch and solvent. The solution was transferred to the blowdown tank, its temperature noted and the tank pressurized to 15 psig. For each data point the flowmeter was operated for about 30 sec with the appropriate measuring cylinder, and both liquid volume and time were recorded alongside the corresponding transducer (pressure drop) reading traced on the strip chart recorder. Normally the transducer was connected across the extreme pressure taps for the greatest accuracy; it was switched between intermediate taps occasionally to check pressure gradient constancy. Transition was observed by externally tapping the pipe entrance while cautiously increasing flow rate until a tap first caused an upward

spike in the transducer output; at that point the flow rate was measured. With the "trigger", except that tapping was unnecessary and had no effect, the procedure was the same.

#### 4.1.4 Big System Runs

Two series of runs were made in the big system also. "Mean flow" runs involved flow rate versus pressure gradient measurements (10 points per decade) with, in select cases, Pitot tube traverses at fixed flow rates. "Hot film" runs at fixed flow rates included measurement of turbulent intensity profiles and turbulent energy spectra.

Initially the system was filled with distilled water and run with the filter on at 100 gpm for about 4 hours, during which time all air was vented, pressure lines filled, the water brought to run temperature and thoroughly cleaned. Meanwhile, the Pitot tube was mounted on the micrometer traverse, aligned and located with a cathetometer. The pump was then stopped and the traverse installed on the test section window. Polymer solution was made up by directing the flow through the run tank, with the filter bypassed and the mixer on, adding a measured amount of polymer master batch and running the system, at a flow rate low enough to prevent degradation for enough time to attain uniform concentration. The run

tank was then bypassed and the 50 gallons of solution held in the recirculating loop used for experiments. When this was degraded it was remixed with the (relatively) fresh 50 gallons remaining in the run tank and the procedure repeated successively until the whole batch was degraded beyond acceptable limits.

At each flow rate, pump speed and the pressure differentials between the rear section static pressure tap and all upstream taps were measured. For velocity profiles, a constant selected flow rate was maintained and the Pitot tube traversed, about 30 points per profile, with the radial interval decreasing near the wall. At each radial position the pressure differential between the Pitot tube and the test section static pressure tap, as well as the micrometer reading, were recorded. Micrometer reading was related to Pitot tube position in the pipe by two independent methods: first from cathetometer readings taken during mounting, second from the position versus stagnation pressure trace near the wall - a plateau in the rapidly decreasing trace indicated the impact tube resting on the wall. The two methods always agreed within 0.001 in. (out of a 0.631 in. pipe radius). The pressure drop in the test section was measured before, after and during velocity profile measurement.

For "hot film" runs the preliminary and solution

makeup procedure was the same, except that the hot film probe was also mounted, with about  $1/4$  in. radial clearance from the Pitot tube, on the micrometer traverse. The anemometer was calibrated by having the Pitot tube and the hot film sensor exactly straddle the pipe axis, varying the system flow rate and recording corresponding Pitot tube and mean hot film signal readings. Turbulent intensity profiles were measured by the same procedure as velocity profiles; in addition, at each radial position the mean signal and rms turbulent signal were recorded. Micrometer setting was related to sensor position both from installation cathetometer readings and by observing when the sensor touched the wall - the electrical signal displayed on an oscilloscope changed drastically. Agreement between these two methods was precise at low flow rates, but at high flow rates, due to probe deflection, constant differences up to 0.005 in. occurred. Intensity profiles were sandwiched between calibrations. The turbulent energy spectrum was measured, at a fixed flow rate and radial position, by having the turbulent anemometer signal go through a variable filter into an rms random signal voltmeter. At each frequency, with 10 points per frequency decade, the rms value of the filtered signal was measured; initially and every decade thereafter the unfiltered, "all pass", rms signal value was also measured. Spectra were sandwiched between intensity measurements and calibrations.

#### 4.1.5 Data Reduction

All experimental data was reduced on an IBM 7094 computer.

Small system runs were reduced from volume, time transducer readings to a flow rate versus wall shear stress format. Where possible polymer solution data were compared with corresponding best fit solvent values to put them on a relative, system independent, basis. The latter were obtained by regression analysis of all solvent-only runs which served also to establish system accuracy.

In the big system, primary mean flow data were reduced to flow rate versus wall shear stress and velocity versus radial position formats. Solvent data were also converted into the traditional friction factor, velocity defect, and universal law of the wall forms to compare with literature and estimate system accuracy. Velocity profiles were integrated numerically to check flow rate against that from the independent pump calibration. Hot film calibrations were reduced to a mean signal versus mean velocity form and the slope of these curves used to reduce the intensity profiles from rms turbulent signals to rms turbulent velocities. Spectrum measurements were reduced to a one dimensional turbulent energy spectrum by a two-stage program that accounted for the proportional bandwidth filter: first, frequencies were converted to wave

numbers through the mean velocity and a normalized spectrum obtained with arbitrary ordinate; second, the ordinate was ratioed to make the integral equal to the mean square turbulent velocity, i.e., the mean turbulent kinetic energy per unit volume.



## 4.2 Detailed Procedures

Step-by-step experimental procedures are listed in the sections following

4.3 Master Batch Makeup

4.4 Small System Runs, and

4.5 Big System Runs

In Sections 4.4 and 4.5, frequent reference is made to the corresponding schematic diagrams, Figs. 3.1.1 and 3.1.2.

Data reduction programs are not discussed, because they were simple and routine. Further, all programs were checked out by hand calculations of the type illustrated in Appendix H, Sample Calculations.

#### 4.3 Master Batch Makeup

1. The small (big) makeup vessel was filled with 5 (27) litres of distilled water.
2. Enough polymer to give an eventual solution viscosity of about 10 poise was weighed out.
3. The turbine mixer was run at 600 (200) rpm for intense agitation.
4. Polymer was added to the vessel over 2 to 5 min. Agglomerates were broken up manually.
5. After 5 to 10 min. mixer speed was cut to 200 (60) rpm.
6. After 30 min., 50 (300) ml of 40% formaldehyde solution were added. Also, solution pH was lowered to 5.5 with nitric acid.
7. Stirring was stopped after 90 to 120 min. By this time solution was complete in the small system; the big system was let stand for 12 hr. for complete dissolution.
8. Polymer concentration was determined gravimetrically. Three aluminum cups were weighed empty, with about 20 gm of master batch solution and finally with the solid residue remaining after 20 hr. in a vacuum oven at 60°C and 25 mm Hg abs.
9. A known amount of master batch was diluted to 100 ml. This was further cut back to 5 (or 6) solutions, of equi-spaced concentrations, with relative viscosities from 1.3

to 2.0 and their viscosity measured at constant speed on the GDM viscometer. Solvent viscosity was also measured before and after the polymer solutions. From these measurements polymer intrinsic viscosity was computed.

10. All batches were used with 7 days of makeup. For the small system, step 9 was repeated after each series of runs.

#### 4.4 Small System Runs

1. Six or 12 gal of solvent, controlled to 25°C by the constant temperature bath, were weighed into the makeup container.

2. A 2 in. diameter impeller on an extended shaft stirrer was installed into the container and started at 800 rpm.

3. A measured volume of master batch was added to the solvent, along with a small amount of makeup solvent to attain the precise concentration desired.

4. Stirrer speed was cut to 200 rpm after 5 min. Stirring was stopped after 60 min.

5. The solution was transferred to the blowdown tank, filling it in 2 to 4 minutes, through a 1 in. tygon line by pressurizing the makeup container to about 3 psig.

6. Solution temperature was noted, the blowdown tank capped and pressurized to 15 psig

7. Prior to the run all pressure lines and the transducer were filled with water. The transducer amplifier and the recorder were warmed up for 4 hr. and synchronized.

8. The transducer was connected across T1-T4. The chart was started at 5 in./min. and shutoff valve B2 opened. Valves B1 and N1 were still closed.

9. N1 was opened to the desired amount. For successive points N1 was opened further.

10. The flow was diverted into an appropriate measuring cylinder for about 30 sec.; at very low flow rates this was upped to 100 sec, while at very high flow rates it was cut to 20 sec. Liquid volume and flow time were recorded on the chart alongside the transducer trace.

11. Every fifth point, the high pressure side of the transducer was switched between T3, T2 and T1 during step 10. For "high flow" runs, this was done at every point.

12. Towards the end of the laminar regime, the pipe entrance was tapped while step 9 was cautiously performed. When the first upward spike appeared on the transducer trace, step 10 was performed to measure the flow rate at transition. With the trigger, tapping was not necessary.

13. For reproducibility, N1 was closed somewhat and step 12 repeated.

14. For the higher flow rates, N1 and B1 were kept wide open, the tank was pressurized in increments from 15 to 35 psig, and steps 10 and 11 carried out between opening and closing B2.

15. At the end of each run the 500 ml of solution remaining in the tank were aspirated out; all valves being shut, the surface tension kept the test pipe and all lines full. After each series of runs, the system was filled with distilled water and thoroughly purged.

#### 4.5 Big System Runs

1. The test section window was blocked with the lucite plug. With valves B1,B3 shut, B2,B4,B5,B6 open, the run tank was filled with distilled water. The pump was started and run at 15 gpm until water emerged from B4 back into the tank. More water was added to the run tank, filling it, making a total of about 100 gal. in the system.

2. The temperature control system was turned on with a set point of  $25.0^{\circ}\text{C}$ .

3. B3 was opened, bypassing the tank, and the pump speeded up to 100 gpm.

4. After 1 hr. the pump was slowed to 20 gpm, B3 shut for 2 to 3 min. and the water in the run tank loaded into the system.

5. Steps 3 and 4 were repeated for about 4 hr. In that period all system vents, except the surge tank, were kept open, all pressure lines were filled with water, the whole 100 gal. batch thoroughly filtered and brought to run temperature.

6. In the above period the Pitot tube was mounted on the micrometer traverse and aligned with a cathetometer. The hot film probe position was plugged by a short 0.061 in. OD rod, one end of which was radiused to the pipe ID. With the micrometer locked at a given setting, the position of the impact tip with respect to the traverse base was located with the cathetometer.

7. With the surge tank full of water, the pump was stopped. B2 was shut and the surge tank vent opened, putting the system under atmospheric pressure.

8. The lucite plug was removed from the traverse window, the micrometer traverse mounted instead and Pitot tube connections made. Steps 7 and 8 served two purposes: preventing unnecessary wear on the probes (especially hot film probes) during preliminary operations and permitting prob. installations while keeping the system full.

9. With B2, B3 and all vents shut, B1, B4, B5, B6 open and the tank mixer on, the pump was restarted. The flow rate depended on the polymer; it was kept just below that for the onset of drag reduction in the test pipe to prevent degradation during solution makeup.

10. A measured amount of polymer master batch was added to the run tank in a 5 min. period.

11. Makeup was continued for about 5 run tank "hold times" ( $\text{tank volume}/\text{flow rate}$ ). Simple calculations, confirmed experimentally, showed that this would result in entirely uniform polymer concentration throughout the batch.

12. Terminating the makeup operation, B3 was opened, bypassing the tank, and the solution held in the recirculating loop used for experiments.

13. At intervals, steps 9, 11, and 12 were repeated to

remix the degraded batch in the loop with the (relatively) fresh batch in the run tank. This was continued until all the solution was degraded beyond acceptable limits.

14. At each flow rate the high pressure port of the transducer was switched between T<sub>4</sub>, T<sub>3</sub>, T<sub>2</sub>, T<sub>1</sub> and T<sub>0</sub>; the low pressure port was permanently connected to T<sub>5</sub>. Beside the pressure differential traces, recorded at 1 in./min., transducer amplifier-indicator attenuation and sensitivity, liquid temperature, pump gear ratio and drive tachometer frequency were also recorded.

15. For Pitot tube traverses, the pump speed potentiometer was set to give the desired flow rate and the transducer was connected across P<sub>1</sub>-T<sub>5</sub>.

16. Initially the Pitot tube was moved as close to the near wall as its construction would allow. The micrometer was then rotated by fixed amounts, moving the Pitot tube radially towards the far wall in 30 to 40 increments. The radial interval was decreased as the wall was approached. Micrometer reading and tachometer frequency were recorded alongside the transducer trace at each position.

17. Very close to the wall, the micrometer was rotated in 0.001 in. increments and the rapidly decreasing transducer trace observed. A plateau indicated the impact tube resting on the far wall, as close as it could get. The



micrometer was then backed off and the process repeated for reproducibility.

18. Step 16 was repeated, going away from the wall.

19. Before, after and several times during the traverse, the transducer was switched to T4-T5 to record test section pressure drop. Also the transducer was switched, every 10 readings, to T5-T5 to check on zero drift. Finally, the Pitot tube could, if necessary, be flushed with distilled water through the test section control panel.

20. For hot film runs, the procedure was identical up to step 14, except that in step 6 the hot film traverse was also mounted, aligned and located on the traverse. About 1/4 in. radial clearance was kept between the hot film probe and the Pitot tube to keep them well out of each others boundary layers. Also, the hot film sensor was kept a little ahead of the Pitot tip.

21. Liquid temperature was allowed to stabilize at the chosen flow rate. The hot film overheat, 1.025 for 0.002 in. and 1.050 for 0.001 in. diameter sensors, was set and the electrical hookup checked for noise.

22. For calibrations the micrometer was adjusted to position the Pitot tube and hot film sensor in the central core of the pipe, precisely astride and equidistant from the axis. The pump speed was then varied and the mean hot film signal at each speed recorded alongside the

corresponding Pitot tube trace. Ten to 20 mean velocity points were taken, covering the range encountered in the pipe at the traverse flow rate chosen. Calibrations were taken quickly - extended operation at other than the set flow rate caused slight temperature changes because the heat load changed, causing an offset of the temperature controller set point. Even though these changes were trivial, of the order of  $0.1^{\circ}\text{C}$ , they could be significant at the low overheats used. To keep track of this source of error, each calibration was taken at identical ascending and descending flow rates. If the results differed significantly, the calibration was rejected.

23. Intensity profiles were obtained in analogy to steps 15 through 19 for Pitot tube traverses, with the turbulent anemometer signal fed directly into the rms random signal voltmeter. In step 16, in addition to the micrometer reading and the Pitot tube trace, the mean hot film signal and the rms turbulent signal were recorded at each point. In step 17 instead of the transducer trace, the anemometer output was observed on an oscilloscope - it changed drastically upon the sensor touching the wall. Finally, step 22 was repeated before and after each profile.

24. For energy spectrum measurements at a fixed flow rate, the micrometer was locked with the hot film sensor at the desired radial position. The turbulent anemometer

signal was fed through the variable filter into the rms random signal voltmeter. Initially, and every 10 readings thereafter, the unfiltered, "all pass", rms signal value was recorded. The filter was then switched to a 1/10th octave bandwidth and, beginning at the highest frequency (25 kc), the rms filtered value was measured at each of 10 equi-spaced frequencies per decade, down to 2.5 cps. Meter time constants of 15 and 60 sec, respectively, were used for frequencies above and below 25 cps. In all cases rms readings were taken only after 6 to 8 time constants had elapsed. The filter gain was constant throughout a spectrum. Corresponding to each rms value, the mean anemometer signal was also recorded to keep track of drift, if any. At the end of a complete frequency scan, spot checks were made at random frequencies to check reproducibility. Before and after each spectrum, the intensity at that radial position (or a profile in its neighborhood) was obtained, step 23, preceded and followed, as always, by a calibration, step 22.

25. In the case of solvent only runs, the procedure was identical except that the solution makeup steps, 9 through 14, were omitted.

## Chapter V

## RESULTS

## 5.1 Scope of Investigation

Table 5.1.1 is a summary of the range of variables covered and the types of measurements made in each of the two systems. In all of the following, the test pipes are referred to by their inside diameters.

For gross flow measurements, polymer concentrations in the logarithmic series ... 1,2,5,10 ... were employed for the most part and are reported in weight parts per million. On figures nominal concentrations are listed; exact values (usually very close to nominal) are given in Appendix G. In all cases, polymer solution density was identical to that of the solvent.

In the 3.21 cm pipe, mean velocity and turbulence measurements in solvent and in polymer solution were made at equal volumetric flow rates. The polymer solution used for these was 1000 ppm of N3000.

All measurements were made at  $25.0 \pm 0.5^{\circ}\text{C}$ .

Unless stated otherwise, all error limits refer to the 99% confidence belt obtained from a "t" test.

A complete tabulation of experimental data is given in Appendix G.

Table 5.1.1.1

## Range of Variables

Polymer Designation	Intrinsic Viscosity $[\eta]$ dl/gm	Molecular Weight M	Concentration, ppm, vs. Measurement			
			0.292 cm		3.21 cm	
			Gross Flow	Gross Flow	Mean Velocity	Turbulence
N 10	0.73	92000	100-7500	1000-5000	--	--
N 80	1.8	280000	5-5000	-	--	--
N 750	3.4	630000	0.5-3000	-	--	--
N 3000	3.9	760000	0.5-2000	50-1000	1000	1000
W 301	20.0	6100000	2-100	5-500	--	--
Solvent: Distilled Water		All Measurements				

## 5.2 Polymer Characterization

Typical intrinsic viscosity measurements for all five of the polyethylene oxides used are presented in Fig. 5.2.1, a plot of  $\eta_{sp}/c$  and  $(\ln \eta_r)/c$  versus  $c$  from which extrapolation to  $c = 0$  yields the intrinsic viscosity. A listing of the intrinsic viscosities of all master batches is given in Appendix G.1. A plot from Shin (21), relating  $[\eta]$  to polymer molecular weight,  $M$ , and rms radius of gyration,  $R_G$ , is given in Appendix D.

### 5.3 Gross Flow Measurements

This section contains the results of flow rate versus pressure drop measurements in solvent and polymer solutions in both systems.

Figures 5.3.1 and 5.3.2 are plots of the pressure gradient at various flow rates in the solvent and typical polymer solutions in the 0.292 cm and 3.21 cm systems, respectively. In the  $(x, \Delta P)$  coordinates used, the farthest downstream static pressure tap is considered the origin,  $(0,0)$ , with  $x$  positive in the direction of flow.

Figures 5.3.3 to 5.3.14 are double logarithmic flow diagrams with ordinates volumetric flow rate,  $Q$ , in litres/sec and wall shear stress,  $T_w$ , in dynes/cm<sup>2</sup>. For each polymer, results of "full range" runs in the 0.292 cm pipe, the 0.292 cm pipe with the "trigger", and the 3.21 cm pipe are presented in sequence, preceded by results for the solvent alone. "High flow" runs in the 0.292 cm pipe, with very dilute polymer solutions, are not shown graphically to prevent crowding, but are listed with the others in Appendix G.2 and are referred to later.

Figures 5.3.15 to 5.3.20 are derived from gross flow measurements in the 0.292 cm pipe. Figure 5.3.15 is a Cartesian plot of  $Q$  versus  $T_w$  in the laminar flow regime. Figure 5.3.16 is a plot of the Reynolds number at transition,  $N_{Re,T}$ , versus polymer concentration,  $c$ , for all polymers

both with and without the "trigger". Figures 5.3.17 to 5.3.20 have the same coordinates, specific drag reduction,  $R (= R_F/c$ , where  $R_F = (1 - T_{wp}/T_{ws})_Q$  is the fractional drag reduction at a constant flow rate,  $Q$ ), versus concentration,  $c$ , reported in gm/dl - the units common to the polymer literature. They illustrate the extent of drag reduction as a function of flow rate and polymer concentration. Figures 5.3.17 and 5.3.18 cover the entire concentration range studied at flow rates of 0.05 and 0.04 litres/sec, respectively. Figure 5.3.19 shows the effect of flow rate for a typical polymer. Figure 5.3.20, with Cartesian coordinates, illustrates the 99% confidence limits on  $R$  for very dilute solutions.

Figure 5.3.21 is a comparison of the fractional drag reduction,  $R_F$ , obtained by various concentrations of three polymers at flow rates corresponding to equal solvent wall shear stress,  $T_{ws}$ , in the 0.292 cm and 3.21 cm pipes.

Finally, Fig. 5.3.22, in the 3.21 cm system, illustrates the decrease in the fractional drag reduction,  $R_F$ , with time due to degradation in the case of the polymer solution used in all detailed measurements.



#### 5.4 Mean Velocity Measurements

Solvent mean velocity profiles are presented in Figs. 5.4.1 to 5.4.3. Figure 5.4.1 has coordinates of  $(U/U_{CL})$  versus  $\xi - \zeta$  is the fractional pipe radius from the wall,  $(1-(2r/D))$  - and compares values of flow rate obtained from the pump calibration with an integration of the velocity profiles. Figure 5.4.2 is a velocity defect plot,  $(U_{CL} - U)/u_{\tau}$  versus  $\xi$ ; the solid line represents the semi-empirical defect law for Newtonian fluids with the wake correction for pipes as given in Hinze (44). Figure 5.4.3 is a law of the wall plot,  $u^+$  versus  $\ln y^+$ , the solid line being the best fit for the linear portion.

In the polymer solution, the apparent velocity indicated by a Pitot tube was a function of Pitot tube diameter, absolute velocity and polymer molecular weight. Figure 5.4.4 is a four part figure, at a constant volumetric flow rate, showing apparent velocity,  $U_a$ , versus  $\xi$  for three Pitot tubes in solvent and polymer solution. The pump calibration was identical in polymer solution and solvent (Appendix F, Fig. F.2). The flow rates obtained by integration of the apparent velocities are compared in Table 5.4.1. Under the conditions of Fig. 5.4.4, the fractional drag reduction,  $R_F$ , in the polymer solution was  $0.35 \pm 0.05$ ; the discrepancy between polymer solutions and solvent decreased with polymer degradation (as did  $R_F$ ).

Table 5.4.1  
Comparison of Volumetric Flow Rates

Pitot Diameter cm.	Solvent		Polymer Solution	
	$Q_1$	$Q$	$Q_1$	$Q$
0.025	5.66	5.70	5.20	5.71
0.055	5.54	5.70	5.49	5.71
0.168	5.45	5.71	5.55	5.71

All flow rates are in litres/sec.

- $Q_1$  - Flow rate from integration of velocity profile  
 $Q$  - Flow rate from pump speed and calibration

Figure 5.4.5 shows the ratio of apparent to solvent velocities obtained on the pipe centre line as a function of the solvent velocity at various flow rates for the three Pitot tubes. Apparent velocity profiles were unchanged when Pitot readings were referenced to a static pressure tube at the same radial position (rather than a wall tap which was the usual case).

Figures 5.4.6 to 5.4.8 are the polymer solution analogues to Figs. 5.4.1 to 5.4.3 for the solvent, with the same coordinates. At the lower flow rate, a 0.025 cm Pitot was used; at the higher flow rate, results with a 0.168 cm Pitot are reported for reasons discussed in Chapter VI, directly following. In both cases corresponding results in the solvent are also shown.

## 5.5 Turbulence Measurements

Figures 5.5.1 to 5.5.3 present typical hot film anemometer static calibrations:  $E$ , the mean anemometer signal, vs.  $U$ , the mean velocity. Figure 5.5.1 shows typical static calibrations in the solvent, obtained in the central core of the pipe. Figure 5.5.2 shows analogous calibrations in polymer solution. Figure 5.5.3 is a static calibration check, comparing  $E$  vs.  $U$  measurements obtained in the central core of the pipe (by varying flow rate) with those obtained by traversing the pipe diameter (using the existing velocity profile) at a constant flow rate.

Figure 5.5.4 shows turbulent intensity profiles in the solvent, plotted, after the manner of Laufer (43), as  $(u/u_\tau)$ , the rms turbulent velocity,  $u$ , normalized by the friction velocity,  $u_\tau$ , versus  $y$ . Figure 5.5.5, in polymer solution, has coordinates  $u$  (without normalization) versus  $y$ ; in addition, values of  $u$  for the solvent at the same volumetric flow rate, obtained from Fig. 5.5.4(b), are shown as a dashed line. Figure 5.5.5 is presented in two parts, to differentiate between the static calibrations used, for reasons that will be fully explained in Chapter VI. The accuracy of turbulent velocity measurements is estimated at  $\pm 10\%$  and  $\pm 15\%$  in solvent and polymer solutions, respectively.

Finally, Figs. 5.5.6 to 5.5.8 present axial, one

dimensional, turbulent energy spectra at two radial positions, the centre line,  $\zeta = 1.0$ , and near the wall,  $\zeta = 0.033$ . Spectra have double logarithmic coordinates of  $E_1(k_1)$  (the fractional axial turbulent kinetic energy per unit wave number contained between wave numbers  $k_1$  and  $k_1 + \Delta k_1$ ) vs.  $k_1$  (the axial wave number,  $2\pi f/U$ ). Figure 5.5.6 in the solvent at the lower flow rate shows replicated spectra at both radial positions and indicates the inherent accuracy obtained. Figures 5.5.7 and 5.5.8 are for the solvent and polymer solution, respectively, at the higher flow rate, at which the fractional drag reduction,  $R_F$ , in the latter was  $0.25 \pm 0.05$ . Tabulated values of the spectra and spectral functions are given in Appendix G.7.

The values of  $\zeta$  used throughout this section are those obtained from cathetometer measurements on the traverse; at the lower flow rate these are identically equal to values obtained by noting when the hot film sensor touched the wall, but at the high flow rates the probe deflected slightly, touching the wall at  $\zeta \approx 0.01$  on this basis. The change in values of  $\zeta$  due to the deflection is given in Appendix G.6; there is very little change for  $\zeta > 0.1$ . Further, the deflection for both polymer solution and solvent was about the same so that comparison is unaffected.

## Chapter VI

### DISCUSSION OF RESULTS

#### 6.1 Chapter Organization

This chapter is divided into three parts.

Part A is purely a description of the experimental results that were presented in Chapter V, with the same subheadings:

- 6.2 Polymer Characterization
- 6.3 Gross Flow Measurements
- 6.4 Mean Velocity Measurements
- 6.5 Turbulence Measurements .

Part B is an analysis of the results with, where possible, proposed correlations. It is divided into 3 sections:

- 6.6 Gross Flow
- 6.7 Anomalous Pitot Tube and  
Hot Film Measurements
- 6.8 Flow Structure

Part C is the over-all picture, obtained by a general application of the results of the present work, in areas of theoretical and practical interest:

- 6.9 Evaluation of Earlier  
Explanations
- 6.10 Prediction and Estimation  
of the Toms Phenomenon .

Part A  
Description of Experimental Results

## 6.2 Polymer Characterization

Intrinsic viscosity measurements, Fig. 5.2.1, were plotted in the form of the Flory-Huggins equation,

$$(\eta_{sp}/c) = [\eta] + k' [\eta]^2 c \quad (6.2.1)$$

and its complement,

$$(\ln \eta_r/c) = [\eta] + k'' [\eta]^2 c; k'' = k' - 0.5 \quad (6.2.2)$$

In all cases the two forms of plotting gave straight lines with the same zero concentration intercept,  $[\eta]$ , within 99% confidence limits. Values of the intrinsic viscosity were accurate to  $\pm 5\%$  of the absolute value. The Flory-Huggins constant,  $k'$ , was typically  $0.35 \pm 0.05$  which is the usual, empirical value (42).

### 6.3 Gross Flow Measurements

Figures 5.3.1 and 5.3.2, showing pressure gradients in the solvent and polymer solutions in both pipes, indicate the linearity of the static pressure,  $P$ , in axial distance,  $x$ , characteristic of fully developed flow. This justifies the conversion of pressure gradient to wall shear stress by the fully-developed flow force balance

$$T_w = 0.25 D(-dP/dx) \quad (6.3.1)$$

The wall shear stress is the variable exclusively employed hereafter.

Figures 5.3.3 to 5.3.14 are hydraulic flow diagrams,  $Q$  vs.  $T_w$ , for the solvent and polymer solutions. This form of plotting was preferred to the conventional friction factor - Reynolds number form because it permits direct comparisons and avoids manipulations of the data into what might, for polymer solutions, be irrelevant groupings.

Figure 5.3.3 shows results for the solvent, distilled water, in both pipes. In the 3.21 cm pipe, only the turbulent regime was covered; the lowest Reynolds number attained was 4000. Over the two decades of flow rate, experimental values of the wall shear stress agreed to within 1% of those calculated from Prandtl's (or von Karman's) universal law (47),



$$(1/f)^{1/2} = 4.0 \log_{10} N_{Re} (f)^{1/2} - 0.40 \quad (6.3.2)$$

In the 0.292 cm pipe both the laminar and the turbulent regimes were covered. Comparison with established laws - Poiseuille's in laminar and Prandtl's in turbulent flow - shows that the slopes of the logarithmic  $Q$  vs.  $T_w$  lines are as predicted, but values of the experimental wall shear stress are uniformly about 5% too low; this could partly be due to a small error in the value used for the pipe inside diameter, magnified by the high power dependence of the wall shear stress on diameter (at constant flow rate  $T_w \propto D^{-3}$  in laminar and  $D^{-3.8}$  in turbulent flow). However, the same pipe was used in all experiments, and the results were highly reproducible - the 99% confidence belt on the wall shear stress was everywhere better than 1% of the absolute value - so that an accurate datum was established with solvent results. With the trigger installed, the Reynolds number for laminar-to-turbulent transition decreased from  $3150 \pm 230$  to  $2025 \pm 70$  and fully developed turbulent flow was established somewhat sooner (i.e., at lower flow rate), but the solvent flow diagram was unchanged in both laminar and turbulent regimes; see Run 94 on Fig. 5.3.3.

Figures 5.3.4 to 5.3.14 are flow diagrams for polymer solutions, arranged by ascending polymer molecular weight.

All of them follow the same qualitative pattern. In general, 4 distinct regions exist:

- (i) the laminar regime
- (ii) the transition region
- (iii) turbulent flow, without drag reduction, and
- (iv) turbulent flow, with drag reduction .

In the 3.21 cm pipe, the first two regions are not present - they were experimentally inaccessible.

#### (i) The Laminar Regime

In this region a linear relationship exists between  $Q$  and  $T_w$  as shown both by the  $45^\circ$  slopes on the logarithmic flow diagrams and by the straight lines on Fig. 5.3.15, a Cartesian plot. The laminar flow lines shift to the right with increasing polymer concentration, reflecting an increase in viscosity. In no case is shear thinning observed. With the trigger, the laminar regime was unchanged.

#### (ii) The Transition Region

This region, initiated by the transition point at which the laminar flow first becomes unstable, appears as a blank in the flow diagrams since stable readings could not be obtained in it. With polymer solutions the effect of the trigger was the same as for solvent; the Reynolds number for transition was decreased, the extent

of the transition region curtailed and fully developed turbulent flow established earlier. Figure 5.3.16 compares the transition Reynolds number,  $N_{Re,T}$ , in polymer solutions with that in the solvent, both with and without the trigger. The majority of cases exhibit no discernible delay in transition. Solutions of N10 never delayed transition; only the most concentrated solutions of N80, N750 and N3000 delayed transition markedly without the trigger, but of these several caused no delay with the trigger, while even relatively dilute solutions of W301, the highest molecular weight, delayed transition. Some very concentrated solutions, e.g., 2000 ppm N3000, 20 and 100 ppm W301, exhibited no distinct transition point, the flow lines curved gradually away from the laminar line and faired into the turbulent line.

(iii) Turbulent Flow, Without Drag Reduction

In this region, which starts immediately following the establishment of fully developed turbulent flow, the polymer solutions follow lines on or parallel to the solvent line. For a given polymer the flow lines for various concentrations are brought much closer together than in the laminar regime because of the greatly reduced dependence on the viscosity - from a 1.0 power law in laminar to a 0.23 power law in turbulent flow. No drag

reduction is obtained in this regime. In fact, at a given flow rate, the wall shear stresses for polymer solutions are slightly higher than for solvent, corresponding to their increased viscosity. In this region, too, the flow lines are unaffected by the trigger.

(iv) Turbulent Flow, With Drag Reduction

This region is characteristic of the Toms Phenomenon; throughout it the specific power consumption for polymer solutions is lower than for the solvent, as indicated by the flow lines lying to the left of the solvent line.

The division between regions (iii) and (iv) is quite sharp and is marked by a discontinuity in the slope of the  $Q$  vs.  $T_w$  curves for polymer solutions. For a given polymer, the wall shear stress at this break point, which marks the onset of drag reduction, is remarkably constant over large ranges of concentration and appears to be independent of pipe diameter. This is illustrated by all Figs. 5.3.4 to 5.3.14; values of the onset (of drag reduction) wall shear stress,  $T_w^*$ , are summarized in Table 6.3.1 at the end of this section. They were obtained by observing, in each case, where the totality of data diverged from the solvent line; the method is good to about  $\pm 10\%$  (as can be verified by trying it on any of Figs. 5.3.4 to 5.3.14) and yields the same results as averaging, for each polymer, values of  $T_w^*$  for each

concentration. The error limits for  $T_w^*$  given in Table 6.3.1 are in excess of the observed  $\pm 10\%$  accuracy of this method for analytical reasons discussed in Sec. 6.6.2.

In the 0.292 cm pipe, results with and without the trigger were essentially identical. In the 3.21 cm pipe,  $T_w^*$  for N10 is  $\pm 25\%$  because of the small effect, and the value for W301 is based on the three higher concentrations (20, 100, 500 ppm), because the 5 ppm solution was degraded during solution makeup. The onset wall shear stress decreases with increasing polymer molecular weight; thus higher molecular weights begin to reduce drag - exhibit the Toms Phenomenon - at lower wall shear stresses than lower molecular weights.

The extent of drag reduction is described with the aid of three parameters: the fractional drag reduction at constant flow rate,

$$R_F = (1 - T_{wp}/T_{ws}) \quad (6.3.3)$$

the specific drag reduction,

$$R = R_F/c \quad (6.3.4)$$

and the slope,  $n$ , of the logarithmic flow diagram of the form

$$T_w = A Q^n \quad (6.3.5)$$

At constant concentration the flow lines for polymer solutions diverge from the solvent so that drag reduction increases with flow rate. In some cases the lines curve markedly back towards the solvent at high flow rates, indicative of polymer degradation, e.g., 2 ppm W301, Fig. 5.3.13. The divergence between the polymer and solvent lines increase progressively with concentration until rather high concentrations where it asymptotes to a constant. This asymptotic slope,  $N_p$ , is a function of polymer and approaches unity with increasing molecular weight. At constant flow rate the specific drag reduction,  $R$ , varies with concentration as shown in Figs. 5.3.17 and 5.3.18. For a given concentration, the specific drag reduction increases greatly with molecular weight. All the  $R - c$  curves have a similar shape and exhibit two asymptotes. At low concentrations,  $c \rightarrow 0$ , the curves tend to zero slope and  $R$  tends to a constant, while at high concentrations,  $c \rightarrow \infty$ , the curves tend to a  $-1$  slope and  $R$  varies inversely as concentration. Corresponding to this the fractional drag reduction,  $R_F$ , increases linearly with concentration at low concentrations, while at high concentrations it asymptotes to a constant, maximum value, corresponding to the limiting slope  $N_p$ . The effect of flow rate on the  $R - c$  curves is shown on Fig. 5.3.19. The specific drag reduction increases with increasing flow

rate, as is evident also from the geometry of the polymer solution flow lines.

Two asymptotes limit the maximum drag reduction that can be attained in a pipe: one is the polymer-dependent limiting slope,  $N_p$ , referred to earlier; the other is a polymer-independent asymptote, slope  $N_m$ , beyond which the wall shear stress could not be reduced in either pipe. The latter is illustrated in Fig. 6.3.1, derived from the higher polymer concentrations shown in Figs. 5.3.4 to 5.3.14. In the 0.292 cm pipe, N10 and N80 did not attain the second asymptote; N750 and N3000 can be seen clearly to follow their limiting slope asymptote at first, then switch to the second, maximum drag reduction, asymptote with a marked change in slope from  $N_p$  to  $N_m$ , W301 follows the second asymptote all along. In the 3.21 cm pipe only W301 reached the second asymptote, and again the marked change in slope from  $N_p$  to  $N_m$  is evident. The slope  $N_m$  is about 1.5, independent of pipe diameter. While only a few concentrations are shown for clarity on Fig. 6.3.1, the following solutions also attained the second asymptote:

Fig. 5.3.8	1000, 2000 ppm	N750
Fig. 5.3.10	500, 2000 ppm	N3000
Fig. 5.3.11	2000 ppm	N3000
Fig. 5.3.13	5, 100 ppm	W301

Table 6.3.1 is a summary of characteristic drag reduction parameters,  $T_w^*$ ,  $N_p$  and  $N_m$ , in both pipes.

Finally, one curious observation. On Fig. 5.3.14 for 500 ppm W301 in the 3.21 cm system, a few points scatter wildly. All of these were taken directly after flow was started from rest; a short time after startup, they reverted to the normal curve followed. This startup transient occurred only in this single case.



Table 6.3.1

## Characteristic Drag Reduction Parameters

Pipe	0.292 cm			3.21 cm		
	$T_w^*$	$N_p$	$N_m$	$T_w^*$	$N_p$	$N_m$
N10	$350 \pm 50$	$1.45 \pm 0.03$	-	$400 \pm 100$	-	-
N80	$80 \pm 10$	$1.20 \pm 0.02$	-	-	-	-
N750	$70 \pm 10$	$1.10 \pm 0.02$	$1.48 \pm 0.02$	-	-	-
N3000	$50 \pm 10$	$1.07 \pm 0.02$	$1.50 \pm 0.02$	$55 \pm 10$	-	-
W301	-	-	$1.48 \pm 0.02$	$3.5 \pm 1.0$	$1.00 \pm 0.03$	$1.50 \pm 0.03$

#### 6.4 Mean Velocity Measurements

Figures 5.4.1 to 5.4.3 presented solvent mean velocity profiles in the 3.21 cm pipe, plotted in conventional forms. Figure 5.4.1,  $U/U_{CL}$  vs.  $\xi$ , shows the axial symmetry of the profiles and the good agreement between flow rates computed by integrating the velocity profiles (referred to hereafter as integrated flow rates) and from the independent pump calibration. Figure 5.4.2 shows the good agreement between the experimental profiles and the semi-theoretical velocity defect law,

$$(U_{CL} - U)/u_{\tau} = -2.44 \ln(\xi) + 0.8 + h(\xi) \quad (6.4.1)$$

in which  $h(\xi)$  is a wake correction as given in Hinze (44). Figure 5.4.3 indicates the universality of the law of the wall. The best fit straight line, of the form

$$u^+ = A \ln(y^+) + B, \quad (6.4.2)$$

through the linear portions has constants (A,B) of  $(2.42 \pm 0.03, 5.51 \pm 0.16)$  which are close to the values of Clauser  $(2.44, 4.9)$  and of Nikuradse  $(2.5, 5.5)$ , quoted by Hinze (44).

Figure 5.4.4(s) compares solvent mean velocity profiles taken with 3 Pitot tubes, 0.025, 0.055 and 0.168 cm OD,

at the same flow rate,  $5.7 \pm 0.01$  litres/sec (the measurements used in Figs. 5.4.1 to 5.4.3 were all made with the 0.025 cm Pitot). Mean velocities obtained with the 0.055 cm Pitot are essentially identical with those from the 0.025 cm Pitot, but with the 0.168 cm Pitot the mean velocities obtained are about 1% low in the central core and about 2% low near the wall. This is caused by two factors: the relatively large size of the tube (5% of the pipe diameter) and the short nose length (7 stem diameters as opposed to the regulation 14), both of which were experimentally necessary. Table 5.4.1 compared integrated flow rates obtained with the three Pitots. In solvent, despite the identical velocities, the integrated flow rate obtained from the 0.055 cm Pitot is slightly lower than that from the 0.025 cm Pitot due to a truncation type of error in the numerical integration, caused because the larger tube could not get as close to the wall (see Appendix H, Sample Calculations). This can be shown by integrating the 0.025 cm Pitot profile only up to the lowest  $z$  obtained by the 0.055 cm Pitot. The result,  $Q_i = 5.55$  litres/sec, is identical to that obtained by integrating the 0.055 cm Pitot profile. Similar reasoning, coupled with the lower velocities recorded by the 0.168 cm Pitot accounts for its integrated flow rate, being about 3% lower than that from the 0.025 cm Pitot.

In summary, mean velocity measurements in the solvent with the 0.025 cm Pitot tube are well in accord with accepted pipe flow relations. With larger Pitot tubes, the results are slightly less precise, but for reasons that are adequately understood. Further, all measurements in polymer solutions will be referred to corresponding ones in solvent so that comparisons are unimpaired.

Figures 5.4.4(a)-(c) showed apparent velocity profiles at the same volumetric flow rate and with the same Pitot tubes as in Figure 5.4.4(s) but for a 1000 ppm polyethylene oxide solution of relative viscosity 1.4. Under these conditions, this solution exhibits a fractional drag reduction,  $R_F$ , of  $0.35 \pm 0.05$ . Table 5.4.1 presented a comparison of the integrated apparent flow rates for polymer solution and for distilled water, the solvent. It is clear that the profiles depend strongly on the diameter of the Pitot tube used. Close to the centre line, the apparent velocity in the polymer solution approaches that of the solvent as the Pitot tube diameter is increased. Close to the wall, the smallest Pitot tube behaves much the same as it does on the centre line; but for the larger Pitot tubes, the apparent velocity can equal or exceed that obtained with water. As a result, an integration of the apparent velocities as obtained with the smaller Pitot tube yields a flow rate that is 10% lower, whereas the corresponding

integration for the largest tube yields one that is 2% higher than for solvent.

Figure 5.4.5 shows the ratio of apparent to solvent velocities obtained on the pipe centre line as a function of the solvent velocity at various flow rates for the three Pitot tubes. It is seen that for a given Pitot tube, the difference between the solvent velocity and the apparent velocity in the polymer solution decreases as the flow rate decreases. In fact, at a centre line velocity of about 180 cm/sec for the solvent, corresponding to a flow rate of 1.15 litres/sec ( $N_{Re} = 50,000$ ), where the polymer solution exhibits no drag reduction, velocity profiles taken with the .025 cm Pitot tube behaved normally and yielded integrated flow rates which checked with those of the solvent and the pump. In all cases, the apparent velocity approached that of the solvent as the polymer degraded.

Mean velocity measurements in polymer solution, presented in Figs. 5.4.6 to 5.4.8, were made at two flow rates, 1.15 and 5.70 litres/sec, just before the onset of drag reduction (region (iii)) and well into the region of drag reduction (region (iv)), respectively. At the lower flow rate measurements with the 0.025 cm Pitot are presented, because they were consistent - the integrated and pump flow rates agreed. At the higher flow rate,

apparent velocities indicated by the 0.168 cm Pitot were used as the best estimate of the true velocities, because the Pitot tube discrepancy observed in polymer solutions at the high flow rate diminished with increasing Pitot tube size, Fig. 5.4.5. However, it must be emphasized that these are only reliable to within the 2% agreement between integrated and pump flow rates (it was noted earlier that the pump calibration was unchanged in polymer solution), because in polymer solution the Pitot tube ceases to be an "absolute" device. The Pitot tube discrepancy is further considered in Section 6.7.1.

Figure 5.4.6,  $U/U_{C1}$  vs.  $\xi$ , shows little difference between profiles in the solvent, Fig. 5.4.1, and in polymer solution; at the higher flow rate (see also Fig. 5.4.4(d)), the profile appears to be slightly blunter than the solvent; the difference in velocities is from -1% on the axis to +3% near the wall. The Reynolds numbers in polymer solution are lower than in the solvent at the same flow rate because of the increased viscosity ( $\eta_r = 1.42$ ) of the former. At the lower flow rate, there is good agreement between integrated flow rates in polymer solution and solvent at the same pump flow rate - 1.14, 1.16 and 1.15 litres/sec respectively. At the higher flow rate, the integrated flow rate in polymer solution, 5.55, exceeds that in the solvent, 5.45, by about 2%, but both are lower than the pump flow rate, 5.70 litres/sec,

due to the large Pitot tube diameter and the attendant truncation error in the integration.

Figure 5.4.7 shows that the Newtonian velocity defect law is obeyed in polymer solution at both flow rates. At the higher flow rate this obedience is mildly remarkable because, compared to the solvent,  $u_{\tau}$  is 17% lower, whereas  $U_{CL}$  is about the same in the polymer solution. At the lower flow rate, near the wall, the velocity defects in polymer solution are very slightly higher than for solvent, corresponding to a less blunt than Newtonian profile, but the difference is small enough to lack significance.

Figure 5.4.8 shows that the Newtonian (i.e., solvent) law of the wall holds well in polymer solution at the low flow rate, but fails at the high flow rate where the results are roughly parallel to, but displaced upward from, it. Comparison of the latter with corresponding solvent results (taken with the 0.168 cm Pitot at the higher flow rate) shows that, referring to Equation (6.4.2), the slope,  $A$ , i.e., the "mixing length" constant, is essentially unchanged, but the wall constant,  $B$ , is increased by about 7.

## 6.5 Turbulence Measurements

Turbulence measurements in solvent and polymer solution are presented in the sequence: calibrations, intensities, and spectra. In each case the preceding measurement is required for the computation of the succeeding one and influences its accuracy as shown in Appendix H.

### 6.5.1 Static Calibrations

Static calibrations in the solvent, Fig. 5.5.1, show that the mean anemometer signal,  $E$ , is reasonably linear in mean velocity,  $U$ .  $E$  is approximately proportional to the square of the heat transfer coefficient (see Appendix E.4, Hot Film Anemometer Details).

In polymer solution, static calibrations indicate markedly different - and hitherto unreported - heat transfer characteristics. At the lower velocities, 30 to 200 cm/sec, Fig. 5.5.2(a), two regimes exist with a transition region from 60 to 160 cm/sec. The approximate solvent calibration line shown indicates that around 40 cm/sec, i.e., in the lower velocity regime, the heat transfer in polymer solution is roughly the same as solvent; in the second, higher velocity, regime it is considerably poorer and also is relatively insensitive to velocity. Because the transition between the two regimes occurs squarely at the mean velocities encountered in the 3.21 cm pipe at the low flow rate (see Fig. 5.4.6), turbulence measurements at



this flow rate were not pursued in polymer solution. At velocities between 350 to 900 cm/sec, Fig. 5.5.2(b), static calibrations are shown with solvent, fresh polymer solution and degraded polymer solution at identical operating conditions. The solvent calibration is linear. With fresh polymer solution, two distinct heat transfer regimes exist: one, prevailing at lower velocities, in which the heat transfer in polymer solution improves with velocity and approaches that in the solvent until, at about 800 cm/sec, an abrupt transition takes place to the second regime, which prevails at higher velocities and exhibits much poorer heat transfer. On going from high to low velocities the process is reversed, and at about 600 cm/sec an abrupt transition occurs from the second to the first regime with an improvement in heat transfer. As the polymer degrades the heat transfer improves, seen by the calibration curve shifting upward toward the solvent, and the second regime is not observed, though it may merely have been delayed to higher than the maximum experimental velocity. The calibrations in polymer solution are markedly curved, because the anemometer linearizer depends on a Newtonian type of heat transfer relationship which, evidently, is not followed.

Figures 5.5.1 and 5.5.2 showed calibrations obtained in the central core of the pipe by varying flow rate,

referred to as "centre line" calibrations. Static calibrations, called "profile" calibrations, using the mean velocity profile existing at a given flow rate were also obtained by traversing the hot film radially across the pipe and plotting the mean anemometer signal,  $E$ , at each radial position versus the mean velocity at that position as indicated by the 0.168 cm Pitot tube. In centre line calibrations the ambient rate of strain,  $(dU/dr)$ , was essentially zero, but in profile calibrations each mean velocity is associated with the strain rate prevailing at that radial position. In pipe flow the strain rate increases towards the wall so that lower velocities, obtained closer to the wall, are associated with higher strain rates. Comparison between centre line and profile calibrations, as in Figs. 5.5.3(a) to (c), presumably detects, therefore, the dependence of heat transfer on strain rate. In solvent, (a), the two methods agree; in Newtonian fluids heat transfer is independent of strain rate. In fresh polymer solution, (b), the two methods agree at the higher velocities, but diverge at lower velocities, indicating that the heat transfer near the wall is better than in the central core at the same mean velocity, i.e., that heat transfer improves with ambient strain rate. As the polymer degrades the divergence decreases and eventually disappears, (c), when the

fractional drag reduction at the high flow rate drops from 0.40 for the fresh solution to about 0.25.

### 6.5.2 Intensity Profiles

In the solvent, Fig. 5.5.4, turbulent intensity profiles at both flow rates are in accord with the measurements of Laufer (43); the present experimental intensities are at most about 10% higher.

Figure 5.5.5, in polymer solution at the high flow rate with  $R_F = 0.30 \pm 0.10$ , is in two parts to distinguish the calibrations used. Figure 5.5.5(a) was compiled from calibrations and profiles which satisfied the static check, as in Fig. 5.5.3(c), and were therefore completely consistent. Figure 5.5.5(b) was compiled from calibrations and profiles which yielded static checks similar to Fig. 5.5.3(b) and thus is definitely valid only for the region,  $y^+ > 0.3$ , where the static check is satisfied. The difference in calibration checks is due to the degree of polymer degradation;  $R_F$  was  $0.25 \pm 0.05$  for Fig. 5.5.5(a) and  $0.35 \pm 0.05$  for Fig. 5.5.5(b). In both (a) and (b), despite the high scatter caused by curved calibrations, the trend is the same. Relative to the solvent the rms turbulent velocity,  $u$ , in polymer solution is increased in the central core,  $1.0 > y^+ > 0.5$ , but is lower near the wall,  $0.5 > y^+$ , although for  $y^+ < 0.05$  the scatter precludes good comparison. The shape of the profile is altered

too. Instead of increasing almost monotonically from the pipe axis to the wall as in solvent, the profile exhibits a plateau extending for a third of the radius,  $0.40 < \zeta < 0.70$ , over which  $u$  is roughly constant. Note, however, that while  $u$  near the wall is about 15-20% lower than the solvent, the friction velocity,  $u_\tau$ , in polymer solution is also down about the same amount so that  $(u/u_\tau)$ , the turbulent intensity of Laufer, is about the same in both polymer solution and solvent for  $\zeta < 0.4$ . On the axis,  $\zeta = 1.0$ ,  $u$  is about 20% higher than solvent, which corresponds to  $(u/u_\tau)$  being about 40% higher.

Finally, all hollow points on Fig. 5.5.5, the majority, were derived using calibrations in the first, better heat transfer, regime of Fig. 5.5.2(b) which was the one that normally prevailed at the velocities existing at the high flow rate. The few filled (solid) points were derived using calibrations in the second, poorer heat transfer, regime that prevailed on occasion at the higher velocities in the central core of the pipe. It can be seen that, despite the difference in the heat transfer laws, approximately the same results are obtained independent of the regime in which the hot film sensor was operating.

### 6.5.3 Energy Spectra

In the solvent, Figs. 5.5.6 and 6.6.7, centre line spectra at  $f_y = 1.0$  show small regions where the inertial sub-range relation,  $E_1(k_1) \propto k_1^{-5/3}$ , of isotropic turbulence is obeyed. Solvent "wall" spectra, at  $f_y = 0.033$ , exhibit considerable regions where  $E_1(k_1) \propto k_1^{-1}$  as predicted by Tchen, quoted in Hinze, (44). At both radial positions the spectra flatten out,  $E_1(k_1) \propto k_1^0$ , at low wave numbers  $k_1 \rightarrow 0$ . Finally, using the spectrum scaling rules developed in Appendix B, solvent spectra are in modest agreement with the spectra of Iaufer (43) in air at  $N_{Re} \simeq 500,000$ , as shown on Figs. B.1 and B.2.

One particular problem that occurs in using a cylindrical hot film sensor is that when the cylinder Reynolds number,  $N_{Re,d}$ , exceeds 40, periodic eddy shedding occurs behind it. This results in a corresponding small periodic variation being superimposed upon the over-all heat transfer coefficient, which latter reflects the instantaneous velocity past the cylinder. Thus Fourier analysis of the fluctuating anemometer signal - i.e., measurement of the turbulent energy spectrum - shows extraneous "spikes" at the shedding frequency and its harmonics. Shedding frequencies can be predicted from Roshko (48); those for conditions at which solvent spectra were measured in the present work are given in Table 6.5.1.

At the low flow rate, Fig. 5.5.6, no shedding was predicted - or observed - at  $\zeta = 0.033$ . At  $\zeta = 1.00$ , a small shedding peak was observed at  $\sim 9000$  cps; it did not affect the spectrum, because this is well above the frequency, 2500 cps, where the spectra were cut off owing to an adverse signal-to-noise ratio - i.e., the filtered anemometer signal was small compared to the electronic noise of the instrumentation. For this very reason, shedding was insignificant at the high flow rate, at both radial positions, since it occurred with frequencies, 21,000 at  $\zeta = 0.033$  and 32,000 cps at  $\zeta = 1.00$ , where the spectral energy density was so small as to be negligible. In polymer solution, shedding frequencies cannot be predicted, but no characteristic "spikes" were observed in the spectra.

Table 6.5.1

## Hot Film Sensor Shedding Frequencies

Spectra	Sensor Diameter cm.	$\zeta$	$N_{Re,d}$	Shedding Frequency cps
Low, Fig. 5.5.6	0.0025	0.033	31	No Shedding
		1.00	51	8600
High, Fig. 5.5.7	0.0051	0.033	290	21000
		1.00	440	31000

In polymer solution at the high flow rate,  $R_F = 0.25 \pm 0.05$ , Fig. 5.5.8, the change in the centre line spectrum is apparent upon comparison with Fig. 5.5.7, whereas the wall spectrum is not significantly different from the solvent. Polymer and solvent spectra were taken at slightly different flow rates, 7% lower in solvent, but the difference is trivial compared to the inherent  $\pm 50\%$  accuracy of the spectra (note, however, that  $\pm 50\%$  is about  $\pm 1/5$  of a decade and the spectra ordinates span 8 decades). The big difference between centre line spectra is that in the polymer solution a very abrupt change of slope, from  $E_1(k_1) \propto k_1^{-2/3}$  to  $E_1(k_1) \propto k_1^{-4}$ , occurs at  $k_1 \simeq 6 \text{ cm}^{-1}$ . The change in spectrum shape is similar to the action of a "low pass" filter, cutting off at (the frequency corresponding to)  $k_1 \simeq 6 \text{ cm}^{-1}$ ; in fact, observation of the fluctuating anemometer signal on an oscilloscope showed a distinct lack of high frequency "fuzz" in the case of the polymer solution. Finally, with polymer degradation the spectrum shifted towards the solvent -  $E_1(k_1)$  increased for  $k_1 > 10$ , but decreased for  $k_1 < 10$ .

Wall spectra, at  $\mathcal{E} = 0.033$ , are very similar in shape, including the small, unexplained, hump that occurs at  $k_1 \simeq 4$  (corresponding to a frequency of  $\sim 400$  cps) in both polymer solution and solvent. Differences in the ordinate -  $E_1(k_1)$  in polymer solution is somewhat lower

than in solvent at the same  $k_1$  - are small.

In Fig. 6.5.1 dissipation curves,  $k_1^2 E_1(k_1)$  vs.  $k_1$ , derived from the spectra shown on Figs. 5.5.7 and 5.5.8, in polymer solution are compared with those in solvent at both radial positions. On the centre line,  $\xi = 1.00$ , the curves are markedly different; in polymer solution, a sharp maximum occurs at  $k_1 \simeq 6 \text{ cm}^{-1}$ , whereas in solvent a rather shallow maximum occurs at  $k_1 \simeq 16 \text{ cm}^{-1}$ . Also, in polymer solution the area under the curve, i.e.,

$\int_0^{\infty} k_1^2 E_1(k_1) dk_1$ , is about 60% less than in solvent.

Near the wall,  $\xi = 0.033$ , the dissipation curves are not very different, though  $\int_0^{\infty} k_1^2 E_1(k_1) dk_1$  in polymer solution is about 30% less than in solvent.



Part B

Analysis of Results and Proposed Correlations

## 6.6 Gross Flow

Gross flow measurements are analysed in the sequence

- 6.6.1 The Laminar Regime
- 6.6.2 The Onset of Drag Reduction
- 6.6.3 Transition
- 6.6.4 The Extent of Drag Reduction.

### 6.6.1 The Laminar Regime

From results in the 0.292 cm pipe, it is evident that all polymer solutions tested, which caused definite drag reduction in turbulent flow, were Newtonian in the laminar regime. The relative viscosities of these solutions were ascertained from the flow diagrams by

$$\eta_r = (\eta_p / \eta_s) = (dT_w/dQ)_p / (dT_w/dQ)_s \quad (6.6.1)$$

These relative viscosities lead to high shear intrinsic viscosities for each polymer; shear rates in the laminar regime were of the order of  $10^3 \text{ sec}^{-1}$  which contrasts with  $10^0 \text{ sec}^{-1}$  in the GDM viscometer. Figure 6.6.1 is a typical example, comparing  $(\eta_{sp}/c)$  vs.  $c$  for N750 as obtained from the pipe flow with GDM viscometer measurements for the same master batch. There is no significant difference between the two sets, indicating no change in intrinsic viscosity and, by inference, no great change in macromolecular conformation at the high shear rates prevailing in the pipe.

Non-Newtonianity in polymer solutions is commonly attributed to molecular entanglements that occur in concentrated polymer solutions; thus the observed Newtonianity is probably due to the solutions being relatively dilute even at the highest polymer concentrations employed in the present work.

In no case was drag reduction observed in laminar flow even when the wall shear stress,  $T_w$ , was greatly in excess of that,  $T_w^*$ , which marked the onset of drag reduction in turbulent flow.

#### 6.6.2 The Onset of Drag Reduction

It was noticed, prior to the present experimental investigation, that the gross flow data of Toms (1) and Savins (8) exhibited one striking trend; namely that for dilute solutions of a given macromolecule-solvent combination, the onset of drag reduction occurred only after a certain value of the wall shear stress had been exceeded. This "critical" or "onset" wall shear stress depended on polymer molecular weight, but appeared independent of polymer concentration and pipe diameter. This trend is confirmed by and clearly illustrated in the flow diagrams, Figs. 5.3.4 to 5.3.14, of the present investigation. It is exhibited whenever the Toms Phenomenon occurs (1,8,26,27,28,29).

The above suggests that a necessary condition exists

which explicitly connects the macromolecule causing the Toms Phenomenon to the turbulent shear flow in question. Only when this condition is satisfied is it possible for the polymer solution to exhibit drag reduction. Thus it appears reasonable to assume that the onset of drag reduction would be ascertained by parameters characteristic of

- (1) the macromolecule causing drag reduction
- (2) the turbulence pertaining in the flow.

(1) The macromolecule can be characterized by a "diameter",  $D_M$ , derived from its excluded volume in dilute solution by the method of Tanford (49).

(2) The structure of turbulent pipe flow is not well enough understood to choose an entirely satisfactory scale. However, since drag reduction is an "energetic" type of phenomenon, and it is well known that the energy action in a pipe flow occurs close to the wall (43,50), the parameter chosen to characterize the turbulence was a wave number,  $k_d$ , with dimensions of inverse length, derived from the turbulent energy spectrum close to the wall.  $k_d$  was defined as the wave number where the dissipation,  $k^2 E(k)$ , is a maximum. This definition of the dissipation wave number,  $k_d$ , is reminiscent of, but different from, the so-called "microscale" and  $k_d$  is, likewise, a measure of the fine scale at which the dissipation of turbulent energy occurs.

With the background above, the following hypothesis was formulated.

#### 6.6.21 The Onset of Drag Reduction Hypothesis

The onset of drag reduction in the turbulent flow of dilute polymer solutions occurs at a constant value of the product  $D_M k_d^*$ , which is a ratio of the dimensions of the macromolecule and the fine scale of the turbulent shear flow. Mathematically,

$$D_M k_d^* = C \quad (6.6.2)$$

where  $C$  is a universal, dimensionless, constant and the asterisk,  $*$ , indicates a value taken at the onset of drag reduction.

#### 6.6.22 Tests for the Onset Hypothesis

To test this hypothesis, it is necessary to ascertain the values of  $D_M$  and  $k_d^*$ , and, in the absence of direct, experimental measurements, to devise rules for estimating them.

(1) Tanford (49) presents calculations for the "effective diameter" of a random coiling macromolecule in dilute solution. From two standpoints, the thermodynamic "excluded volume" and the hydrodynamic "equivalent Einsteinian sphere", this effective diameter comes to about twice (strictly, 1.8)

the rms radius of gyration,  $R_G$ , of the macromolecule. Thus in all that follows, macromolecular diameter,  $D_M$ , is taken as

$$D_M = 2R_G \quad (6.6.3)$$

In the above relation of Tanford,  $D_M$  is also a weak function of molecular weight,  $M$ . But for polyethylene oxides in water, for example, the ratio ( $D_M/2R_G$ ) varies by a factor of  $\sim 1.05$  when  $M$  changes from  $10^5$  to  $10^7$  so the molecular weight dependence will be neglected. The rms radius of gyration,  $R_G$ , is accessible directly from light scattering measurements. It can also be estimated from intrinsic viscosity-molecular weight relationships by the use of the Kirkwood-Riseman "equivalent sphere model" and Flory's universal constant,  $\Phi$ , (42) as shown by Kurata and Stockmeyer (51).

Polymer solutions are considered thermodynamically dilute if the conformation of an individual macromolecule is unaffected by its neighbours - enough intervening solvent separates them. A limiting value of this "separateness" occurs when the volume fraction of macromolecules,  $x_v$ , based on their effective diameter,  $D_M$ , corresponds to random spherical packing, i.e., to touching. The concentration at this point,  $c_c$  gm/dl, roughly separates dilute from concentrated polymer solutions. It is easily shown to be given by

$$\begin{aligned}
 c_c &= 100(x_v)(M/N_A)(6/\pi D_M^3) \\
 &= 250(M/D_M^3)
 \end{aligned}
 \tag{6.6.4}$$

(2) Experimental turbulent energy spectra are seldom available so spectrum scaling rules were derived, Appendix B, to relate spectra to more accessible quantities. These rules invoke the four following assumptions (a) and facts (f).

(a) The Reynolds number in the pipe flow is high enough for universal equilibrium to exist at the high wave number, in which region the controlling parameters are the dissipation,  $\mathcal{E}$ , and the kinematic viscosity,  $\nu$ . (a)

(b) At the high wave numbers there is local isotropy. (a)

(c) Near the pipe wall the dissipation,  $\mathcal{E}$ , is approximately equal to the production,  $\Gamma$ , of turbulent energy. (f)

(d) The normalized turbulent energy production,  $(\Gamma \nu / u_\tau^4)$ , is a function only of position,  $y^+$ , in the pipe. (f)

From this length and time scales can be derived and it can be shown that

$$k_d = Ku_\tau / \nu \tag{6.6.5}$$

where  $K$  is a constant that depends only on position,  $y^+$ , in the pipe. From Laufer (43), the dissipation rate,  $\epsilon$ , reaches a sharp maximum at  $y^+ \simeq 10$ , so this is the logical position at which to obtain  $k_d$ . At  $y^+ \simeq 10$ , from Laufer's spectra, it is estimated that  $K \approx 0.2$ .

Substitution of (6.6.5) into (6.6.2) yields

$$D_M(u_\tau^*/\nu) = C' ; C' = C/K , \quad (6.6.6)$$

which is the "engineering" form of the onset hypothesis; once  $C'$  is known,  $u_\tau^*$  can be predicted for any characterized polymer-solvent pair and solutions of it will reduce drag for  $u_\tau > u_\tau^*$ , i.e., when  $T_w > T_w^*$ . For polymers in a given solvent, a more convenient form of the hypothesis is

$$(T_w^*)^{1/2} = C''/R_G ; C'' = C'\nu\rho^{1/2}/2 \quad (6.6.7)$$

The onset hypothesis, (6.6.2, .6 and .7) has the following consequences which provide means of testing its validity.

(1) The value of  $(T_w^*)^{1/2}$  - the wall shear stress at the onset of drag reduction - should be independent of pipe diameter for a given macromolecule-solvent pair. This follows from (6.6.5) being independent of pipe diameter.

(2) For a given macromolecule-solvent combination,  $(T_w^*)^{1/2}$  should be independent of polymer concentration for



dilute solutions. This follows from (6.6.3) being valid and concentration independent only in thermodynamically dilute solutions.

(3) In any pipe from (6.6.6),  $u_T^*/\gamma$  should vary inversely as  $D_M$ , the effective diameter of the macromolecule in the solvent. From (6.6.7), for a given solvent,  $(T_W^*)^{1/2}$  should vary inversely as the rms radius of gyration,  $R_G$ , of the macromolecule.

(4) Finally, the value of the dimensionless onset group,  $(D_M k_d^*)$ , i.e., of constants  $C$  and  $C'$ , should be a constant, regardless of the pipe, solvent and macromolecule.

The onset hypothesis will now be applied to the present experimental results which are then compared with the results of other investigators.

Consequence (2), the concentration independence of  $(T_W^*)^{1/2}$ , can be observed on the flow diagrams. Very close scrutiny shows that experimental verification at very low concentration is difficult, because the polymer flow lines approach the solvent line in slope, making it hard to ascertain accurately their intersection with it. At very high concentrations, much in excess of the dilute solution limitation, (6.6.4),  $T_W^*$  appears to decrease slightly. Between these two extremes there is, typically, a 100 fold range of concentrations where  $T_W^*$  is indeed constant. Similar behaviour is exhibited by the measurements of

others; see, for example, Fig. 2.1.1, the data of Toms.

It is of interest here to analyse the uncertainty in a value of  $T_w^*$  derived from the intersection of a polymer flow line with the solvent line. Let these, respectively, be

$$T_w = A_p(Q)^{np} \quad (\text{polymer solution}) \quad (6.6.8)$$

$$T_w = A_s(Q)^{ns} \quad (\text{solvent}) \quad (6.6.9)$$

both of them being assumed logarithmically linear. (6.6.8) and (6.6.9) will intersect at a point,  $(Q^*, T_w^*)$ , marking the onset of drag reduction where, if  $N$  denotes the ratio  $(np/ns)$ ,

$$T_w^* = (\ln(A_p) - N \ln(A_s)) / (1 - N) \quad (6.6.10)$$

An error analysis of (6.6.10) shows that the fractional "standard error" in  $T_w^*$ ,  $\epsilon(T_w^*)$ , is given by

$$\begin{aligned} \epsilon(T_w^*) &= (V(T_w^*)/T_w^{*2})^{\frac{1}{2}} \\ &= (N/(1-N)) \left\{ (\ln(A_p/A_s)/(1-N))^2 \left[ (V(ns)/ns^2) \right. \right. \\ &\quad \left. \left. + (V(np)/np^2) \right] + V(\ln(A_s)) + V(\ln(A_p))/N^2 \right\}^{\frac{1}{2}} \end{aligned} \quad (6.6.11)$$

where the operator  $V(X)$  denotes the variance of  $X$ . (6.6.11) gives the standard error in  $T_w^*$  in terms of the standard errors (the terms of the form  $V(X)/X^2$ ) of the constants,  $A_p$ ,  $A_s$ ,  $n_p$  and  $n_s$ , of Equations (6.6.8 and .9) and the slope ratio,  $N$ . The former reflect the inherent accuracy of the experimental measurements and can be derived from statistical analysis of solvent runs in both 0.292 cm and 3.21 cm pipes; thus values of  $\epsilon(T_w^*)$  can be calculated as a function of  $N$ , or (since the solvent slope,  $n_s$ , is a constant)  $n_p$ , for any polymer. Results of such a calculation are presented on Fig. 6.6.2 for solutions of N3000 in the 0.292 cm pipe, assuming that experimental measurements in polymer solution and solvent are of equal accuracy. As is evident from inspection of (6.6.11),  $\epsilon(T_w^*)$  increases drastically as  $n_p \rightarrow n_s$ , ( $N \rightarrow 1$ ), but at lower values of  $n_p$ , corresponding to the concentrations shown on Figs. 5.3.10 and 5.3.11, it asymptotes to a standard error of about 10%, which, for 95% error limits, amounts to a confidence belt of  $\pm 20\%$ . This confidence belt will, of course, get better as more and more individual values of  $T_w^*$  are determined (for different concentrations), but the  $\pm 20\%$  values were quoted on Table 6.3.1 to err on the safe side. Presented also on Fig. 6.6.2, as solid points, are values of  $\epsilon(T_w^*)$  for all polymers at their respective limiting slopes,  $N_p$ , at which the uncertainty in the intersection with the solvent line is a minimum.

The foregoing analysis also illustrates the extreme accuracy required to obtain reliable values of the onset wall shear stress; for example, in the 0.292 cm system, values of  $(V(ns)/ns^2)$  and  $(V(\ln(As))/(\ln(As))^2)$  were  $0.03 \times 10^{-4}$  and  $3.1 \times 10^{-4}$ , respectively, which correspond to 99% confidence limits of  $\pm 0.45\%$  in the slope,  $ns$ , and  $\pm 1.1\%$  in the constant,  $As$ .

Figure 6.6.3 is a plot of  $(T_w^*)^{1/2}$  vs.  $(1/R_G)$ , as suggested by (6.6.7), for the 5 polyethylene oxide polymers tested in 2 pipes; on it are also tabulated values of macromolecular parameters. Some of the numbers on Fig. 6.6.3 are slightly different from those reported in Reference 25, an earlier publication arising from the present work, as a result of more precise data reduction. Values of  $R_G$  were obtained from the light scattering results of Shin (21), which are given in Fig. D.1 of Appendix D, a plot of  $[\eta]$  vs.  $M$  and  $R_G$  for polyethylene oxides in water. For the polymer N80, which lay outside the confidence envelope, Shin's experimental  $R_G$  value was used directly; in all other cases  $R_G$  was obtained from the best fit line. Figure 6.6.3 shows that both consequences (1) and (3) hold; results from both pipes, differing 11 fold in diameter, straddle the same line over an 8 fold range of  $R_G$ . The best straight line of the form

$$(\tau_w^*)^{1/2} = I + C''/R_G \quad (6.6.12)$$

has constants ( $I, C''$ ) of  $(0.04 \pm 1.97, 6500 \pm 1100)$ . The value of the intercept,  $I$ , indicates that within experimental error the line passes through the origin, as predicted by (6.6.7). The value of the slope,  $C''$ , can be used to predict, directly, the onset wall shear stresses for polyethylene oxides in water with an accuracy of  $\pm 20\%$ . Consequences (1) and (3) are also obeyed by the results of other investigators, a complete listing of which is given in Appendix C. In cases where the polymers were not adequately characterized, only (1) can be verified.

The verification of consequence (4), the universal constancy of the onset group,  $(D_M k_d^*)$ , requires considerably more experimental information than is currently available in the literature. Of the other data available, only in 3 cases (1, 17, 29) can  $R_G$  be reasonably estimated. Of these, Fabula (17) covered only an advanced stage of region (iv) (of Section 6.3) so  $(\tau_w^*)$  values are not directly available. The data which exist to test consequence (4) are summarized in Table 6.6.1 and plotted on Fig. 6.6.4; they are due to Toms (1), Hershey (29), and the present work.

From Table 6.6.1 the value of  $C' = D_M(u_\tau^*/\nu)$  is about  $0.015 \pm 0.005$ . Considering the diverse polymers, solvents and pipes, the constancy is mildly remarkable. Empirically,

Table 6.6.1

Summary of Experimental Onset of Drag Reduction Data

No.	Solvent	Polymer	$[\eta]$ dl/gm	Pipe Dia. cm	$R_G$ $^\circ A$	$u_r^*/\nu_s$ cm <sup>-1</sup>	$C'$	Ref.
1	MCB	PMMA	3.9	0.128	600	1030	0.0124	1
2	MCB	PMMA	3.9	0.404	600	1100	0.0132	1
3	CYC	PIB	3.44	0.081	445	2190	0.0195	29
4	CYC	PIB	3.44	0.177	445	2200	0.0196	29
5	CYC	PIB	3.44	1.29	445	2320	0.0206	29
6	CYC	PIB	3.44	2.54	445	1660	0.0148	29
7	BEN	PIB	0.82	1.29	275	3740	0.0206	29
8	BEN	PIB	0.82	2.54	275	2640	0.0145	29
9	Water	PEO	0.66	3.21	315	2240	0.0141	This Work
10	Water	PEO	0.73	0.292	350	2100	0.0147	
11	Water	PEO	1.75	0.292	795	1000	0.0159	
12	Water	PEO	3.38	0.292	835	940	0.0157	
13	Water	PEO	3.61	3.21	875	830	0.0145	
14	Water	PEC	3.90	0.292	910	790	0.0144	
15	Water	PEO	20.1	3.21	2350	210	0.0099	

Abbreviations used are:

MCB - Monochlorobenzene      PMMA - Polymethylmethacrylate  
 CYC - Cyclohexane            PIB - Polyisobutylene  
 BEN - Benzene                    PEO - Polyethylene oxide

 $R_G$  - for cases 1-8, estimated from Flory (42).

this value of  $C'$  is all that is required to predict, via (6.6.6), the onset wall shear stress for any solvent-polymer pair. Theoretically, however, it is interesting to find the value of the onset constant,  $C$ , of (6.6.2).

Using the value,  $K = 0.2$ , derived from Laufer's spectra at  $y^+ = 70$ ,

$$C = KC' = 0.2(0.015 \pm 0.005) = 0.003 \pm 0.001$$

This means that the ratio of macromolecular to turbulent scales at the onset of drag reduction is 0.003, i.e., the macromolecule is 1/330th the size of the dissipative eddies. Intuitively, one might expect that the onset of drag reduction would imply equality of the two scales and thence values of  $C$  of the order of unity. Three possible explanations for the small value of  $C$  are

(i) that the macromolecule might, at the onset of drag reduction, be extended to several times its zero shear dimension as measured by  $R_G$ ,

(ii) that  $1/k_d$  might be too large a scale to characterize the region of turbulent dissipation, and

(iii) that the scaling constant,  $K$ , is too small.

These are pursued briefly.

(i) No experimental measurements of the elongation of macromolecules under shear exist, although it is generally

suspected to occur. According to the (theoretical) calculations of Peterlin (24), for dilute solutions of flexible, random coiling macromolecules, the ratio of rms end to end distance at a shear rate  $G$  to that at zero shear is

$$L = (r_e/r_{e,0}) = (1 + 2\beta_0^2/3)^{1/2} \quad (6.6.13)$$

where

$$\beta_0 = (M[\eta] \eta_s G)/(N_A kT)$$

is a dimensionless shear rate. The extension ratio,  $L$ , is a function only of  $\beta_0$ . Since at the pipe wall the product  $\eta_s G$  is  $T_w$ , at the onset of drag reduction one has

$$\beta_0^* = (M[\eta] T_w^*)/(N_A kT) \quad (6.6.14)$$

Substituting relevant values into (6.6.14) for three polymers, N10, N3000, W301, gives

$$\beta_0^* = 0.086, 0.56, 1.73 \quad \text{respectively,}$$

which leads to extension ratios of

$$L^* = 1.00, 1.10, 1.73 \quad \text{respectively.}$$

This shows only slight elongation of the macromolecules at the onset of drag reduction, eliminating (i) as a possible



cause for the low onset constant. It is interesting to note that the onset product,  $C'$ , for W301 (No.15 on Table 6.6.1) was about 60% lower than for the other polyethylene oxides; if this were multiplied by the onset extension ratio calculated above ( $L^* = 1.73$ ), i.e., if a calculated correction were applied for the increase in the macromolecular length scale,  $D_M$ , the value of  $C'$  would come within 10% of the others.

(ii)  $k_d$  would be a good measure of the dissipative region if the maximum in  $k^2E(k)$  were sharp. As seen on Fig. 6.5.1, experimental solvent spectra yield  $k^2E(k)$  vs.  $k$  curves which exhibit relatively shallow maxima. It might, therefore, be better to re-define the dissipative scale as the wave number,  $k_e$ , beyond which only a certain, small fraction, say 5%, of the dissipation occurs, i.e., by a relation such as

$$\left[ \int_{k_e}^{\infty} k^2E(k)dk / \int_0^{\infty} k^2E(k)dk \right] = 0.05 \quad (6.6.15)$$

$k_e$  thus represents the highest wave number that might be associated with dissipation - for  $k > k_e$  only a negligible fraction of the total dissipation occurs. Reference to measured spectra (see Table 6.8.1 later) shows that, order of magnitude wise,  $k_e \simeq 10(k_d)$ .

(iii) While  $u_\tau$  and  $\nu$  are well known to be the controlling parameters in a turbulent pipe flow, the scaling constant,  $K$ , which permits a numerical value to be assigned (through (6.6.5)) to the dissipation wave number,  $k_d$ , is subject to considerable uncertainty; see Appendix B. From an energy viewpoint the outer edge of the so-called laminar sublayer,  $y^+ \approx 10$ , is the most important radial position since both the turbulent energy production and dissipation rates reach a sharp maximum at it. Unfortunately, turbulent energy spectra have never been reported at this vital position, because it is too close to the wall to be experimentally accessible. The closest Laufer got was  $y^+ = 72$ , at which point the dissipation rate is about a tenth of that at  $y^+ = 10$ , and the trend of Laufer's spectra indicates that  $k_d$  increases rapidly as the wall is approached. Thus it is conceivable that the value  $K = 0.2$ , derived from Laufer's spectrum at  $y^+ = 72$ , might be an order of magnitude lower than the value of  $K$  at  $y^+ = 10$  which we actually want. However, this is speculation; until relevant spectra are measured, the value 0.2 is the best available, although it must be recognized that it is derived from a spectrum at a radial position relatively remote from where the energy action in a pipe actually is.

From the foregoing, it is apparent that the low value of the onset constant,  $C$ , is not due to an erroneous

magnitude being assigned to the macromolecular scale. On the other hand, the numerical value of the turbulent scale is uncertain; while the value used might, conceivably, be too low (it may be increased one order by using  $k_e$  for  $k_d$  and possibly another from obtaining  $K$  at  $y^+ = 10$  instead of 100), this must await further clarification of the structure of turbulent pipe flow. Thus, full physical interpretation of the  $0.003 \pm 0.001$  value of the onset constant,  $C$ , which implies that the macromolecule is  $10^2$  smaller in size than the dissipative eddies, is not currently possible. Therefore, the physical motivation of the Onset Hypothesis is open to question, and the Hypothesis must, for the present, be accepted from a purely empirical standpoint.

#### 6.6.23 "Time" Based Onset Hypotheses

Finally, in regard to the onset of drag reduction, it is interesting to note that the Onset Hypothesis of Sections 6.6.21 and .22 is a "length" based hypothesis, since that is the dimension scaled. Similar to it, and on entirely analogous grounds, one might postulate a "time" based onset hypothesis, relating the macromolecular relaxation time,  $\tau_M$ , to the dissipation frequency,  $\omega_d^*$ , at the onset of drag reduction. This would give

$$\tau_M \omega_d^* = C_t \quad (6.6.16)$$

No experimental methods exist to ascertain relaxation times in dilute polymer solutions, but they may be calculated from the linear viscoelasticity theories of Rouse (22) or Zimm (30). From Zimm, for a "non free-draining" macromolecule in solution at infinite dilution, the terminal relaxation time,  $\tau_1$ , is

$$\tau_1 = 0.422(M [\eta] \eta_s)/(N_A kT) \quad (6.6.17)$$

The terminal relaxation time is the longest in the spectrum of polymer relaxation times and represents the highest value that might be used for  $\tau_M$ .

$\omega_d$  can be scaled using the same rules as for  $k_d$ , from which

$$\omega_d = W(u_\tau^2/\nu) \quad (6.6.18)$$

where  $W$  is a constant of order  $10^1$  near the wall; from Laufer, at  $y^+ = 10$ ,  $W$  is estimated about 4 (Appendix B).

The "time" hypothesis, (6.6.16), reduces to its "engineering" form,

$$\tau_M(u_\tau^*/\nu) = C_t^I; \quad C_t^I = C_t/W \quad (6.6.19)$$

and, for a given solvent, to

$$(T_w^*) = C_t^{II}/\tau_M; \quad C_t^{II} = C_t^I \eta \quad (6.6.20)$$

with consequences analogous to the earlier onset hypothesis. However, application of (6.6.19) to experimental results shows poor constancy of the product  $\tau_M(u_\tau^{*2}/\gamma) = C'_t$  as shown on Table 6.6.2 for the same data used in Table 6.6.1 presented earlier. For example, for the polyethylene oxides used in the present work, values of  $C'_t$  differ by 20 fold over the range covered (whereas values of  $C'$ , the corresponding "length" constant, were  $\pm 30\%$ ). Multiplication of  $C'_t$  values on Table 6.6.2 by the scaling constant,  $W$ , would yield "time" based onset products from  $10^{-1}$  to  $10^1$ , contrasting with (and subject to the same limitations as) the "length" based value of  $(3 \pm 1)10^{-3}$ .

Two "time" hypotheses have recently been proposed, in somewhat different forms, by Hershey (29) and Fabula (52).

Hershey "showed" that macromolecule terminal relaxation times, calculated from the Zimm theory (30), were of the same order of magnitude as the shear rate,  $u_\tau^{*2}/\gamma$ , at the onset of drag reduction, i.e.,  $C'_t$  was of order  $10^0$ . This conclusion was based on results in several pipes for several concentrations of 2 polymer-solvent systems (of the 5 systems apparently tested): namely, polyisobutylene ( $M = 0.72 \times 10^6$ ) in cyclohexane and polymethylmethacrylate ( $M = 1.5 \times 10^6$ ) in toluene. Although the Zimm theory is for infinite dilution, in analogy to the equivalent Rouse theory, a small concentration dependence of  $\tau_1$  might be

Table 6.6.2

Comparison of "Time" and "Length" Onset Hypotheses

No.	Solvent	Polymer	$M \times 10^{-6}$	Pipe Dia. cm	$\tau_1 \times 10^3$ sec	$u_t^2 / \gamma_s \times 10^{-3}$ sec <sup>-1</sup>	$c_t'$	$c_t'$ from Table 6.6.1
1	MCB	PMMA	2.3	0.128	0.17	7.3	1.21	0.0124
2	MCB	PMMA	2.3	0.404	0.17	8.3	1.38	0.0132
3	CYC	PIB	0.72	0.081	0.054	54.5	2.97	0.0195
4	CYC	PIB	0.72	0.117	0.054	55.0	3.00	0.0196
5	CYC	PIB	0.72	1.29	0.054	61.0	3.33	0.0206
6	CYC	PIB	0.72	2.54	0.054	31.0	1.71	0.0145
7	BEN	PIB	0.72	1.29	0.0089	98.0	0.87	0.0206
8	BEN	PIB	0.72	2.54	0.0089	49.0	0.43	0.0145
9	Water	PEO	0.080	3.21	0.00081	45.0	0.036	0.0141
10	Water	PEO	0.092	0.292	0.0010	39.5	0.040	0.0147
11	Water	PEO	0.28	0.292	0.0074	8.9	0.066	0.0159
12	Water	PEO	0.63	0.292	0.033	7.9	0.256	0.0157
13	Water	PEO	0.69	3.21	0.038	6.2	0.235	0.0145
14	Water	PEO	0.76	0.292	0.045	5.6	0.254	0.0144
15	Water	PEO	6.1	3.21	1.86	0.39	0.733	0.0099

Abbreviations used are the same as in Table 6.6.1.

 $\tau_1$  - Calculated from Zimm Theory, Equation (6.6.17).

permitted, as Hershey pointed out, by substituting polymer solution viscosity,  $\eta_p$ , for the solvent viscosity,  $\eta_s$ , in (6.6.17), so long as the polymer solutions may be considered "dilute". From the Flory-Huggins expansion,

$$\eta_r = (\eta_p / \eta_s) = (1 + c[\eta] + k'(c[\eta])^2 + \dots) \quad (6.6.21)$$

it is easily shown, by putting  $c = c_c$  from (6.6.4), that polymer solutions might be considered dilute only when  $\eta_r < 1.2$  - at most  $\eta_r < 1.5$ . For the region of validity of the Zimm theory, therefore, the concentration dependence of  $\tau_1$  must be small, 50% at most. Thus, reverting to (6.6.17), the product  $(M[\eta]\eta_s)$  determines the relaxation time. For the two cases Hershey cited, the product  $(M[\eta])$  was identical so the only difference in relaxation times was due to solvent viscosities,  $\eta_s$ , which were about 50% different. Therefore, the equality of scales observed by Hershey was due to the fact, in essence, that the relaxation time was not varied in the two cases used as a basis for his conclusions. Had the relaxation time been varied, his "time" hypothesis would almost certainly have failed in a manner similar to that illustrated in Table 6.6.2 for the polyethylene oxides.

In passing, it was noted by Hershey that for a given polymer solution, the Reynolds number at the onset of drag

reduction was proportional, "approximately", to the pipe diameter, so that

$$N_{Re}^* \propto D \quad (6.6.22)$$

from which, by invoking the Blasius friction factor relation, it can be shown that, for a given polymer solution,

$$T_w^* \propto D^{-\frac{1}{4}} \quad (6.6.23)$$

whereas for our "length" based hypothesis,  $T_w^*$  was independent of pipe diameter. The diameter dependence of (6.6.23) is, however, small enough to be considered "approximate"; it can easily be shown that if the exponent of the Diameter,  $D$ , in (6.6.22) were changed from 1 to  $8/7$ ,  $T_w^*$  would become independent of  $D$  in (6.6.23). In fact, as was shown earlier in Table 6.6.1, the data of Hershey followed our length based onset hypothesis quite well.

The second "time" hypothesis, that of Fabula (52), will not be discussed; though purportedly derived from different, "non-particulate", physical considerations, it reduces to the form of (6.6.16). Also, it was tested in the original article with ( $T_w^*$ ) data supplied (25) from the present work, which, as has already been shown, could not be so correlated.



#### 6.6.24 Summary

It is observed experimentally that the onset of drag reduction in the Toms Phenomenon is well defined. The Onset Hypothesis, Section 6.6.21, is an attempt to relate macromolecular to turbulent length scales at this point. The consequences of the Onset Hypothesis are well followed by the experimental results of the present work as well as those of other investigators, as shown on Figs. 6.6.3 and 6.6.4 and Table 6.6.1. From data presently available the best absolute value of the onset constant,  $C$ , (Equation (6.6.2)), which is the ratio of macromolecular to dissipative turbulence dimensions at onset, is  $0.003 \pm 0.001$ . This low value of  $C$ , while it does not impair the empirical use of the Onset Hypothesis, is intuitively disturbing; and its physical significance cannot, at present, be explained. It appears, however, that the low value of  $C$  is not due to an erroneous macromolecular scale, but rather to the great numerical uncertainty in scaling the turbulence.

Finally, it was shown that "time" based hypothesis, relating macromolecular relaxation time to the frequency of turbulence, fail to correlate the onset of drag reduction.

#### 6.6.3 Transition

It was seen on Fig. 5.3.16 that laminar-to-turbulent transition was not, in general, delayed by the addition of

polymer. From Poiseuille's law, the wall shear stress at transition,  $T_{w,T}$ , is

$$T_{w,T} = 8N_{Re,T} \eta^2 / \rho D^2 \quad (6.6.24)$$

which, for polymer solutions in a given pipe, reduces to

$$(T_{w,T})_p / (T_{w,T})_s = (\eta_p / \eta_s)^2 = (\eta_r)^2 \quad (6.6.25)$$

Values of the transition wall shear stress for polymer solutions, calculated from (6.6.25), using experimental relative viscosities derived from the laminar regime, are plotted on Fig. 6.6.5. Comparison with Fig. 5.3.16 shows that, within experimental error, transition is delayed only when  $T_{w,T} > T_w^*$ , the onset wall shear stress. Thus, without the trigger, solutions of N80, N750 and N3000 delay transition only after the viscosity has built up sufficiently for  $T_{w,T}$  to exceed  $T_w^*$ , whereas even dilute solutions of W301,  $T_w^* \sim 3.5$  dynes/cm<sup>2</sup>, delay transition, while N10 solutions,  $T_w^* \sim 350$  dynes/cm<sup>2</sup>, never do. This also explains why some solutions, e.g., 1000 ppm of N3000, which delay transition without the trigger, do not with the trigger; in the latter case,  $T_{w,T}$  is lower by the ratio of respective transition Reynolds numbers (2025/3150), and the value of  $T_w^*$  falls between the two  $T_{w,T}$  values.

The above criterion, that transition is delayed only

when the wall shear stress at transition exceeds the onset wall shear stress, is broadly in accord with the Onset Hypothesis, because  $T_{w,T}^*$  represents incipient interaction between the macromolecule and the turbulence in a manner that decreases the energy dissipation and a delay in transition reflects just such a trend.

The transition criterion is also consistent with the gross flow pattern observed in polymer solutions. When  $T_{w,T} < T_w^*$ , the polymer solutions follow the general pattern described in Section 6.3. But when  $T_{w,T} > T_w^*$ , the laminar regime is prolonged and drag reduction occurs immediately on the establishment of turbulent flow. Thus region (iii) - turbulent flow without drag reduction - is masked entirely and the onset point is not observed since the flow following transition goes into an advanced state of region (iv). This behaviour is illustrated by several cases in the 0.292 cm pipe, e.g., 500 ppm N3000, Fig. 5.3.10. In some cases where  $T_{w,T} \gg T_w^*$ , transition is delayed so greatly that no break is observed in the flow lines, and region (ii) consists of a gradual shift away from the laminar line of region (i) into the final turbulent flow line of region (iv), e.g., 2000 ppm N3000, Figs. 5.3.10 and 11 and 20,100 ppm W301, Fig. 5.3.13.

From (6.6.24),  $T_{w,T} \propto D^{-2}$ , so, if  $N_{Re,T}$  stays

constant (traditionally 2100) then in the 3.21 cm pipe,  $T_{W,T}$  will be about 0.2 dynes/cm<sup>2</sup>. Thus  $T_{W,T} < T_W^*$  for both N3000 and W301, and they exhibit both regimes (iii) and (iv) separated by the normal onset point, Figs. 5.3.12 and 5.3.14.

For polymer solutions where  $T_{W,T} > T_W^*$ , it would appear that  $T_W^*$  might be obtained by back extrapolation of the flow lines obtained in region (iv) to their intersection with the solvent line. This is the case, generally, as seen by comparing results with and without the trigger, e.g., Figs. 5.3.8 and 5.3.9 or Figs. 5.3.10 and 5.3.11, provided that the flow lines are characteristic of the polymer. The extrapolation would, clearly, fail if the flow lines had attained the polymer independent limiting asymptote,  $N_m$ , as is the case with 2000 ppm N3000, Fig. 5.3.10 and 20 and 100 ppm W301, Fig. 5.3.13.

#### 6.6.4 The Extent of Drag Reduction

The extent of drag reduction induced by a macromolecular additive has been shown experimentally to be a function of several variables - polymer concentration and molecular weight, flow rate and pipe diameter - and to be limited both by polymer dependent and polymer independent asymptotes.

In this section the extent of drag reduction is analysed with respect to

- (1) polymer dependent factors
- (2) polymer independent limitations and
- (3) polymer degradation.

#### 6.6.41 Polymer Dependent Factors

In this part polymer independent limitations and polymer degradation are assumed absent; the conclusions affected by these assumptions are suitably modified in the respective, succeeding parts.

Drag reduction in a given pipe will initially be compared at equal polymer solution and solvent flow rates; this represents an energy reduction per unit volume per unit time basis. (Comparison at equal wall shear stresses would yield equivalent results, altered only by the constants of coordinate transformation.) The effects of flow rate and polymer molecular weight will be examined next and, finally, the effect of pipe diameter will be considered.

The fractional drag reduction induced by a concentration  $c$  dl/gm of polymer at a flow rate  $Q$  is

$$R_{F,Q} = (1 - (T_{wp}/T_{ws}))_Q \quad (6.6.26)$$

where the  $Q$  subscript will be dropped in future use.

By the Onset Hypothesis,

$$\begin{aligned}
 R_F &= 0, & T_{wp} &\leq T_w^*, & \text{and} \\
 R_F &> 0, & T_{wp} &> T_w^*.
 \end{aligned}
 \tag{6.6.27}$$

The specific drag reduction is

$$R = R_F/c \tag{6.6.28}$$

which, on going to infinite dilution, yields the intrinsic drag reduction,

$$[R] = \lim_{c \rightarrow 0} (R) \tag{6.6.29}$$

for a given polymer and flow rate in a given pipe. In analogy to the intrinsic viscosity,  $[\eta]$ , the intrinsic drag reduction,  $[R]$ , is a measure of the inherent drag reducing ability of a macromolecule in dilute solution.

On the specific drag reduction vs. concentration curves of Figs. 5.3.17 and 5.3.18, it was noticed that as  $c \rightarrow 0$ ,  $R$  tended to a constant, recognized now as  $[R]$ . Experimental values of  $[R]$ , derived from Cartesian  $R - c$  plots like Fig. 5.3.20 to prevent the uncertainty of logarithmic extrapolation to infinite dilution, are given in Table 6.6.3 for 4 polymers at two flow rates in the 0.292 cm pipe. At high concentrations,  $c \rightarrow \infty$ , the polymer flow lines asymptote to the limiting slope,  $N_p$ , and consequently  $R_F$  asymptotes to a constant,  $R_{F,max}$ .

while the  $R - c$  curves tend to an asymptote with a  $-1$  slope. The intersection of the two asymptotes of the  $R - c$  curves, i.e.,

$$\begin{aligned} R &= [R] , & c \rightarrow 0 \\ R &= R_{F,\max}/c , & c \rightarrow \infty \end{aligned} \quad (6.6.30)$$

occurs at  $( [C] , [R] )$  where  $[C] (= R_{F,\max}/[R])$  might be considered a characteristic concentration. Two conclusions can be drawn from the  $R - c$  curves. First, for any polymer, the initial increments accomplish the greatest unit drag reduction and the "efficiency" of drag reduction,  $dR_F/dc$ , decreases with increasing concentration - from  $[R]$  at low to 0 at high concentrations. Second, the intrinsic drag reduction,  $[R]$ , which is the "efficiency" of drag reduction at infinite dilution, increases drastically with polymer molecular weight.

$R$  has units of inverse concentration; in this section concentration is expressed in gm/dl, the units common to the polymer literature.  $R$  can, however, be used to measure the energy reduction per macromolecule by converting concentrations from  $c$ , gm/dl, to  $m$ , molecules/cm<sup>3</sup>, so that

$$R' = R_F/m = R (100M/N_A)$$

Table 6.6.3  
Intrinsic Drag Reduction,  $[R]$

Flow Rate, litres/sec.	0.050	0.040
Polymer		
N10	$1.3 \pm 0.2$	$0.8 \pm 0.2$
N80	$45 \pm 5$	$35 \pm 5$
N750	$300 \pm 30$	$200 \pm 30$
N3000	$350 \pm 50$	$300 \pm 30$
All values in 0.292 cm pipe. Units of $[R]$ are (dl/gm)		

Now if  $\mathcal{E}_T$  is the rate of energy dissipation per unit volume to maintain the solvent in turbulent flow at the flow rate  $Q$ , then

$$\mathcal{E}_T = U_{AV}(-dP/dx) = 16QT_w/\pi D^3$$

and the product ( $\mathcal{E}_T R'$ ) is the decrease in the dissipation rate per macromolecule. Similarly, ( $\mathcal{E}_T [R]$ ) is the intrinsic decrease in dissipation rate - that caused, so to speak, by the first macromolecule. Normalization of these products by a "natural" molecular energy rate - e.g.,



$kT/\tau_M$  - would yield a dimensionless group, characteristic of drag reducing ability, that might be useful in comparing polymeric species. The molecular viewpoint will not be pursued here.

The remarkable similarity of the shapes of the  $R - c$  curves suggests their superposition by suitable  $x$  and  $y$  shifts (which are multiplicative, the curves on Figs. 5.3.17 and 18 being double logarithmic). Figure 6.6.6 is such a "universal" drag reduction curve, prepared from Figs. 5.3.17, 18 and 19 by visual superposition, with coordinates of dimensionless concentration,  $\gamma$ , and dimensionless specific drag reduction,  $\delta$ , where

$$\begin{aligned}\delta &= c/\alpha \\ \delta &= R/\beta\end{aligned}\tag{6.6.31}$$

The superposing constants,  $\alpha$  and  $\beta$  (i.e., the  $x$  and  $y$  shifts) are listed alongside. They may immediately be identified with the parameters  $[C]$  and  $[R]$  defined by (6.6.30) and comparison between the values of  $\beta$  on Fig. 6.6.6 and the independently derived values of  $[R]$  on Table 6.6.3 shows modest agreement. In addition, over the range of flow rates and polymers covered,  $\alpha$  and  $\beta$  (or  $[C]$  and  $[R]$ ) are related as shown on Fig. 6.6.7. The foregoing suggests a powerful possibility - namely that the entire drag reducing behaviour of a member of the

homologous series of polyethylene oxides might be ascertained from a knowledge of the superposing parameters  $[R]$  and  $[C]$ .

In relating the superposing parameters to flow rate and polymer, we shall work with the intrinsic drag reduction,  $[R]$ , although either  $[C]$  or their product,  $[R][C] = R_{F,max}$ , may equally well be used (the last named has the advantage of easy experimental accessibility).

The effect of flow rate is obtained by invoking the experimentally observed, approximate, logarithmic linearity of the polymer solution flow lines, both before and after the onset of drag reduction. Since the onset point,  $(Q^*, T_w^*)$ , is common to both regions of turbulent flow (regions (iii) and iv) of Section 6.3)

$$T_{ws} = T_{wp} = T_w^* (Q/Q^*)^{ns}, \quad T_{wp} \leq T_w^* \quad (6.6.32)$$

$$T_{wp} = T_w^* (Q/Q^*)^{np}, \quad T_{wp} > T_w^* \quad (6.6.33)$$

The solvent line is always given by (6.6.32) so that, using (6.6.26),

$$R_F = (1 - (Q/Q^*)^{np-ns}) \quad (6.6.34)$$

from which, using (6.6.29) and L'Hospital's rule,

$$[R] = (-dnp/dc)_c \rightarrow 0 (\ln(Q/Q^*)) \quad (6.6.35)$$

Equation (6.6.35) gives  $[R]$  as a product of two terms: the  $\ln(Q/Q^*)$  term which is the flow rate dependence and the  $(-dn_p/dc)_c \rightarrow 0$  term which is independent of flow rate and a function only of polymer. The flow rate dependence can be tested by plotting  $[R]$  vs.  $\ln(Q)$  for a given polymer; Fig. 6.6.8 for N3000 indicates approximate agreement, yielding a straight line, passing through the point  $(0, Q^*)$ , over an eight fold range of flow rate as predicted. It must be noted, however, that this agreement attests to the extreme linearity of the N3000 flow lines and would not be quite so good for, say, N80, the flow lines of which have some curvature.

The intrinsic function  $(-dn_p/dc)_c \rightarrow 0$ , denoted hereafter by  $\Psi$ , is difficult to ascertain directly, because at low concentrations the slopes of the polymer solutions approach that of the solvent, and derivatives are subject to high percentage uncertainty. The value of  $\Psi$  can, however, be inferred from values of  $[R]$  at known flow rates,  $Q$ , and the experimental value of  $Q^*$  for a given polymer. Figure 6.6.9(a) is a plot of  $\Psi$  vs.  $[\eta]$  (both of which, incidentally, have the same dimensions of inverse concentration) derived from experimental values of  $[R]$  and  $Q^*$  for 4 polymers. Since for polyethylene oxides in water the Mark-Houwink relation is

$$[\eta] = 1.05 \times 10^{-4} (M)^{0.78} \quad (6.6.36)$$

the relation of Fig. 6.6.9(a),

$$\Psi = 3.6 [\eta]^3 \quad (6.6.37)$$

implies a square to cubic dependence of  $\Psi$  on molecular weight. The physical significance of this is, as yet, obscure, but the good correlation between  $\Psi$  and  $[\eta]$  makes it an attractive empirical way to relate intrinsic drag reducing ability to a polymeric parameter.

Form inspection of Table 6.3.1, the polymer limited asymptotic slope,  $N_p$ , would appear to follow the limiting forms

$$\begin{aligned} N_p \rightarrow n_s \quad , \quad [\eta] \rightarrow 0 \\ N_p \rightarrow 1 \quad , \quad [\eta] \rightarrow \infty \end{aligned} \quad (6.6.38)$$

which suggest a relationship of the form

$$\ln((N_p - 1)/(n_s - 1)) = A[\eta] \quad (6.6.39)$$

where  $A$  is a negative constant. A plot of  $\ln(N_p - 1)$  vs.  $[\eta]$  is shown on Fig. 6.6.9(b) and results in a fair straight line for 4 polymers with a value of  $-0.65$  for  $A$ . As with the  $\Psi - [\eta]$  relation of (6.6.37), no physical interpretation can be given for the  $N_p - [\eta]$  relation.

Elimination of  $[\eta]$  between (6.6.37) and (6.6.39) gives

$$\ln((N_p - 1)/(n_s - 1)) = -0.42 \psi^{\frac{1}{3}} \quad (6.6.40)$$

which links the drag reducing behaviour of a polymer at low concentration,  $\psi$ , to that at high concentrations,  $N_p$ .

Finally, the superposing parameters  $[R]$  and  $[C]$  are related, in general, through (6.6.30) applied in (6.6.34) which gives,

$$R_{F,max} = [R] [C] = (1 - (Q/Q^*)^{N_p - n_s}) \quad (6.6.41)$$

so that

$$[C] = (1 - (Q/Q^*)^{N_p - n_s}) / [R] \quad (6.6.42)$$

which cannot coincide with the simple power law  $[R] - [C]$  relationship of Fig. 6.6.7. Applying limiting conditions to (6.6.41) and invoking (6.6.35), it can easily be shown that

$$\begin{aligned} [C] &= (n_s - N_p) / \psi, \quad (Q/Q^*) \rightarrow 1 \\ [C] &= 1 / [R], \quad (Q/Q^*) \rightarrow \infty \end{aligned} \quad (6.6.43)$$

so that for a given polymer the power dependence of  $[C]$  on  $[R]$  will vary from 0 to -1, depending on flow rate. This effect can only just be observed by the decreasing flow rate points for N3000 on Fig. 6.6.7. Thus, while superposition can always be effected on a universal curve

such as Fig. 6.6.6, regardless of polymer and flow rate, the relation between the superposing parameters is, in general, one such as (6.6.42) rather than the polymer and flow rate "independent" power law of Fig. 6.6.7, which latter is valid only within the range of conditions noted on the figure.

The extent of drag reduction analysis presented so far might be summarized as follows for a homologous series of polymers exhibiting the Toms Phenomenon in a given pipe.

(1) At any flow rate the specific drag reduction versus concentration curves are bounded by two asymptotes; at infinite dilution,  $c \rightarrow 0$ ,  $R$  tends to a constant,  $[R]$ , the intrinsic drag reduction, while at high concentrations,  $c \rightarrow \infty$ ,  $R$  varies inversely as  $c$ , because the fractional drag reduction reaches a constant, maximum value,  $R_{F,max}$ , corresponding to the polymer limited asymptotic slope,  $N_p$ , being attained by the polymer flow lines. The intersection of the two asymptotes defines two characteristic parameters,  $[R]$  and  $[C]$ .

(2) All of the  $R - c$  curves are similar in shape and may be superposed onto a single, "universal", curve when  $R$  and  $c$  are normalized by their corresponding characteristic parameters  $[R]$  and  $[C]$ .

(3) The parameters  $[R]$  and  $[C]$  are uniquely related and each depends on both flow rate and polymer.

(4)  $[R]$ , for example, can be decomposed into the product of a flow rate term,  $(\ln(Q/Q^*))$ , and an intrinsic polymeric term,  $\Psi$ , as in equation (6.6.35).

(5) Both  $\Psi$ , an intrinsic function characteristic of low concentrations, and  $N_p$ , the asymptotic slope characteristic of high concentrations, correlate well with polymer intrinsic viscosity,  $[\eta]$ , although the physical significance of these relationships is, as yet, obscure.

The foregoing developments relate to a single polymer homologous series - solvent combinations (polyethylene oxides - water) in a single pipe (0.292 cm).

The use of different polymer-solvent systems is not expected to alter the form of the relations derived, so long as the polymers remain random coiling. Other combinations would be very useful in relating drag reduction to the structure (configuration) and deployment (conformation) of the macromolecule.

The effect of pipe diameter could not be studied thoroughly in this work because of polymer degradation - a problem that plagues all large scale work where polymer solutions must be recirculated. It was observed on Fig. 5.3.21 that, at flow rates corresponding to equal solvent wall shear stresses,  $T_{ws}$ , the fractional drag reduction,  $R_F$ , induced by a given polymer concentration decreased with increasing pipe diameter: since onset,  $T_w^*$ , is independent

of pipe diameter, this means that the corresponding polymer flow line slope,  $n_p$ , decreases with diameter. However, both the 3.21 cm pipe data and those of Fabula (17), in a 1.0 cm pipe appear to superpose on Fig. 6.6.6 - the universal curve for polyethylene oxides in water in the 0.292 cm pipe. Since the flow rate dependence of drag reduction depends only on the logarithmic linearity of the flow lines which is, roughly, observed, the superposition of larger pipe data on Fig. 6.6.6 suggests only simple changes in drag reduction - polymer relations like (6.6.37) and (6.6.39), hopefully only in the constants, which might all be considered functions of pipe diameter.

No adequate literature data exist, at present, with which the relations developed might be compared and checked.

This section on polymer dependent factors is concluded with two concepts of engineering interest.

(a) The "Newtonian" Solvent

The "Newtonian" solvent for any polymer solution is defined as an imaginary solvent having the same viscosity as the polymer solution, but exhibiting no drag reduction - i.e., following Newtonian flow relations. The relative viscosity of a polymer solution with respect to its actual solvent is given by the Flory-Huggins equation,

$$\eta_r = (1 + c[\eta] + k'(c[\eta])^2 + \dots) \quad (6.6.21)$$



and from the Newtonian friction factor relation, it can be shown that, at the same flow rate, the wall shear stress for the Newtonian solvent is

$$(T_{wns}/T_{ws}) = (\eta_r)^{2-ns} \quad (6.6.44)$$

from which a generalized fractional drag reduction,  $R_{FN}$ , defined by

$$R_{FN} = (1 - (T_{wp}/T_{wns})) \quad (6.6.45)$$

may be calculated. At low concentrations  $R_{FN}$  reduces to  $R_F$  because  $\eta_r \rightarrow 1$ ; at high concentrations it corrects for the buildup of polymer solution viscosity. In the present work the correction was always small, a maximum difference of 7% between  $R_{FN}$  and  $R_F$ , so the concept was not employed. But it could be useful in correlating high concentration data like that of Toms (1), in which polymer solution viscosity is greatly increased. Also, it can easily be shown that in region (iii), turbulent flow without drag reduction,  $R_{FN}$  is precisely 0 (whereas  $R_F$  is slightly negative since  $T_{wp} > T_{ws}$  due to the increased viscosity).

(b) The "Optimum" Concentration

This is defined as the concentration at which, for a given flow rate, the maximum drag reduction is obtained,

i.e.,  $R_F$  is a maximum. It was seen earlier that with increasing concentration, the flow lines attain an asymptotic slope,  $N_p$ , and  $R_F$  tends to a constant, maximum value. As concentration is increased still further, the flow lines maintain the slope  $N_p$ , but shift to the right (toward the solvent line) as the increased viscosity overwhelms the drag reduction. Thus some "optimum" concentration exists beyond which  $R_F$  decreases slowly. Very close scrutiny of the data of Toms (1) and those of the present work shows that while  $R_F$  exhibits the shallow maximum described above,  $R_{FN}$  asymptotes monotonically to a constant, although the absolute difference between the two is trivial so long as the polymer solutions might, even remotely, be considered dilute.

#### 6.6.42 Polymer Independent Limitations

It was seen in Fig. 6.3.1 that a polymer independent asymptote limited the maximum drag reduction attainable in a pipe and that its slope,  $N_m$ , was independent of pipe diameter. If this asymptote in each pipe is back extrapolated to its intersection with the corresponding turbulent flow solvent line, this occurs at a point  $(Q_m, T_{wm})$  where the Reynolds number,  $N_{Re,m}$ , is roughly the same,  $500 \pm 200$ , which, considering the difference in pipe diameters and the decades of extrapolation, implies that the asymptote is

independent of both polymer and pipe. The asymptote is

$$\left(\frac{T_w}{T_{wm}}\right) = \left(\frac{Q}{Q_m}\right)^{Nm} \quad (6.6.46)$$

algebraic manipulation of which gives

$$f = f_m(N_{Re,m})^{(2-Nm)} (N_{Re})^{-(2-Nm)} = Am N_{Re}^{-nm} \quad (6.6.47)$$

The exponent  $nm$  is a constant since  $Nm$  is constant and  $f_m$  and  $N_{Re,m}$  are related by the solvent friction factor relation, so  $Am$  is a constant since  $N_{Re,m}$  is constant. Thus (6.6.47) is the friction factor relation for the maximum drag reduction asymptote, independent of pipe and polymer. Its universality can be tested by plotting  $f$  vs.  $N_{Re}$  for the points of Fig. 6.3.1, but a somewhat better form of plotting is that of Prandtl,  $f^{-1/2}$  vs.  $\text{Log } N_{Re} (f)^{1/2}$ , which, for Newtonian fluids, yields a truly universal straight line. This latter was applied to all the points in Fig. 6.3.1 which lay on the maximum drag reduction asymptote in each pipe, using solution viscosities as experimentally measured. The results are shown on Fig. 6.6.10, along with representative solvent points. For both pipes and all solutions, the points lie on a common curve over a 10-fold range of  $N_{Re} f^{1/2}$  - corresponding to

an  $N_{Re}$  range from 5000 to 150,000 - and points from the small pipe fair into those from the larger one. For  $N_{Re} f^{1/2} > 500$ , the asymptote is well represented by a straight line,

$$f^{-\frac{1}{2}} = 23 \text{Log}_{10}(N_{Re} f^{\frac{1}{2}}) - 43 \quad (6.6.48)$$

which intersects the solvent line,

$$f^{-\frac{1}{2}} = 4.0 \text{Log}_{10}(N_{Re} f^{\frac{1}{2}}) - 0.4 \quad (6.6.49)$$

at a Reynolds number of about 1500. For  $N_{Re} f^{1/2} < 500$ , the asymptote points diverge from the line (6.6.48) in a manner similar to that of solvent points from the solvent line, (6.6.49), possibly for the same reason - that the Reynolds numbers are too low for "universality" - in both cases.

The points of Fig. 6.6.10 also follow a unique curve when plotted in the double logarithmic  $f$  vs.  $N_{Re}$  form with a slope close to  $-\frac{1}{2}$ ; the best fit power law is

$$f = 0.42 N_{Re}^{-0.55}, \quad 4000 < N_{Re} < 150,000 \quad (6.6.47)$$

The difference between the Reynolds numbers at the intersection of the solvent line, 500 from (6.6.46) and 1500 from (6.6.48), is due to the incompatibility of the two forms of plotting. It is easily seen that the forms (6.6.46 and 47)

yield an upward concave curvature on  $f^{-\frac{1}{2}}$  vs.  $\text{Log}(N_{\text{Re}} f^{\frac{1}{2}})$  coordinates, especially at low  $N_{\text{Re}}$ , as occurs on Fig. 6.6.10. Practically, the disagreement for  $N_{\text{Re}} f^{1/2} < 500$  is of little consequence, because most of it occurs at "virtual" Reynolds numbers where the flow is actually laminar so that the question of drag reduction does not arise. For higher than experimental values,  $N_{\text{Re}} f^{1/2} > 4000$ , modest agreement exists between extrapolations of (6.6.48) and the power law forms (6.6.46, 47) (similar to that between (6.6.49) and the Blasius equation), but (6.6.48) is to be preferred, in analogy to the solvent.

The correlation of the maximum drag reduction asymptote by the same parameters - friction factor and Reynolds number - as the solvent shows that the Toms Phenomenon is always exhibited within the bounds of the two lines of Fig. 6.6.10, equations (6.6.48) and (6.6.49).

Theoretically, this is very stimulating, because it suggests the existence of a polymeric parameter, say  $\pi$ , such that a pair of conditions like

$$\begin{aligned} \pi &< \pi_1 \\ \pi &> \pi_2 \end{aligned} \quad (6.6.50)$$

result, respectively, in either the solvent line or the asymptote being followed, both of which are independent of  $\pi$ . The onset of drag reduction is possibly a particular case of the first condition, because prior to onset, the

solvent line is always followed. Further, both  $\pi_1$  and  $\pi_2$  are quite well defined, judging from the abruptness with which both the onset of drag reduction and the switch to the maximum drag reduction asymptote occur. For values of  $\pi$  intermediate between  $\pi_1$  and  $\pi_2$ , the polymer solution flow lines depend on the coordinates of Fig. 6.6.10 as well as on  $\pi$ , as is evidenced by the dependence of drag reduction on polymer and flow rate. No good candidate for  $\pi$  can be advanced in the present work, but its delineation would, clearly, be central to the understanding of the Toms Phenomenon.

Also, from the form of the asymptote, it is clear that the ultimate condition of drag reduction in the Toms Phenomenon is not laminar flow. Comparison of the respective friction factor relationships

$$f = 16.0(N_{Re})^{-1} \quad \text{Laminar (Poiseuille)}$$

$$f = 0.08(N_{Re})^{-0.25} \quad \text{Turbulent (Blasius)}$$

$$f = 0.42(N_{Re})^{-0.55} \quad \text{Asymptote (6.6.47)}$$

shows a curious progression of the Reynolds number exponent: that for the asymptote is roughly the geometric mean of the laminar and turbulent exponents.

Engineering wise, this asymptote is valuable, because

it sets the limits to which drag can be reduced in any pipe. The fractional drag reduction on the asymptote - and therefore the maximum possible - is

$$R_{F,m} = (1 - (Q/Q_m)^{Nm-ns}) \quad (6.6.51)$$

At flow rates corresponding to the same solvent shear stress,  $T_{ws}$ , it can be shown that

$$(Q/Q_m)^{Nm-ns} \propto D^{-\frac{2}{7}}$$

because from Blasius,

$$(Q)_{T_{ws}} \propto D^{\frac{15}{7}},$$

$N_{Re,m}$  is a constant, so

$$Q_m \propto D^1$$

and

$$Nm - ns = 1 \frac{1}{2} - 1 \frac{3}{4} = -\frac{1}{4}$$

Thus the second term in the bracket of (6.6.51) diminishes with increasing pipe diameter so that at flow rates corresponding to the same solvent shear stress, the maximum drag reduction possible increases with increasing pipe

diameter. This is also evident from the geometry of Fig. 6.3.1 and was illustrated in Fig. 5.3.21 by solutions of W301 in both pipes.

The developments of this section modify the preceding, polymer oriented, analysis of the Toms Phenomenon in a simple way. Namely, that in the region between the solvent line, (6.6.49), and the maximum drag reduction asymptote, (6.6.48 or 6.6.47), all polymer solutions obey the previous relations until their flow lines intersect the asymptote; after this intersection, the flow lines are superceded by the asymptote and the latter is universally followed.

The maximum drag reduction asymptote has not hitherto been reported. Fabula (17) observed "breaks", similar to those in Fig. 6.3.1, in the flow lines for polyethylene oxide - water solutions in a 1.0 cm pipe, but operated at very high wall shear stresses where degradation was severe; Metzner and Park (20) appear to have attained the asymptote with a polyacrylamide in water in 1/2 and 1 in. pipes, but the solution was so concentrated that it was appreciably non-Newtonian (a "power law" exponent of 0.55) and their results, presented in terms of the power law Reynolds number, are difficult to decipher; Toms (1) may have reached the asymptote in his 0.128 cm. pipe, but had too few points in the turbulent regime. Thus, while these are



in qualitative agreement, no adequate data are available in the literature to really test the form and universality of (6.6.48) and its confirmation must await further experimental information. Also, only polyethylene oxides in water were used in the present work, and though the asymptote was independent of molecular weight - which strongly suggests its independence of polymer - other polymer homologous series-solvent combinations remain to be tested.

#### 6.6.43 Polymer Degradation

Polymer degradation refers to a decrease in the molecular weight of the polymer, i.e., a decrease in its degree of polymerization, with consequent attenuation of related macromolecular properties. Degradation may stem from biological (bacterial) or mechanical causes.

Polyethylene oxides dissolved in water are subject to biological degradation on standing. In the present work this was eliminated entirely by adding 1/2% by weight of formaldehyde to all polymer master batches.

Mechanical degradation occurs when polymer solutions are subjected to shear. It has been reported in the literature, (17,18,53), both in laminar and turbulent flow. In the present work mechanical degradation could occur during

- (1) master batch makeup
- (2) polymer solution makeup
- (3) pipe flow experiments.

- (1) Master Batch Makeup

Degradation during this step was minimized by the procedure of Chapter IV. Also, it introduced no error, because all master batches were characterized after makeup.

- (2) Polymer Solution Makeup

This step caused negligible degradation in polymer solutions run in the 0.292 cm pipe which were made up in batches with gentle stirring for long periods. Intrinsic viscosities measured after solution makeup were identical with those of the corresponding master batches.

In the 3.21 cm system some degradation occurred during solution makeup, discussed more fully in (3). For N10 and N3000 solutions, from viscosity measurements, this was negligible; for W301 some degradation probably occurred, but the low concentrations, where it was most pronounced, were too dilute to characterize.

- (3) Pipe Flow

It appears that drag reduction in turbulent pipe flow is always associated with polymer degradation. For a given polymer, degradation increases both with the prevailing wall shear stress and the time of exposure. Because drag reduction depends strongly on polymer molecular weight

and degradation increases with wall shear stress, degradation can be detected on gross flow diagrams by the flow lines tending towards the solvent line at the higher flow rates with a concave downward curvature.

In the once-through 0.292 cm system, without the trigger, degradation was checked in two ways: by intrinsic viscosity measurements on solutions that had been run through the pipe at the highest flow rate (about 0.060 litres/sec) and by repeatedly running the same solution at this flow rate and noting changes in pressure gradient. The results showed that for 4 polymers, N10, N80, N750 and N3000, degradation was negligible. W301 solutions definitely degraded, as indicated by the 2 ppm flow line on Fig. 5.3.13, but were too dilute to characterize by viscosity measurements. W301 solutions also illustrate an interesting point. Suppose a concentration,  $c_a$ , is required to attain a drag reduction asymptote - in the case of Fig. 5.3.13, the maximum drag reduction asymptote,  $N_m$ . Then all solutions with  $c > c_a$  will follow the same asymptote which, aside from small viscosity changes, will be the same flow line. Thus, if these are run, and degrade, the flow lines will not change until enough macromolecules (a fraction  $(1 - c_a/c)$ ) degrade to make them leave the asymptote towards the solvent line. Therefore, more concentrated solutions will follow the asymptote up to higher

flow rates (wall shear stresses). On Fig. 5.3.13, flow lines for 5, 20 and 100 ppm are initially identical; at about 0.040 litres/sec, the 5 ppm line curves towards the solvent, while the other two remain on the asymptote up to the highest flow rates attained. The same reasoning explains why, in general, degradation is more readily apparent on low concentration flow lines. Suppose, at a given flow rate,  $Q$ , a polymer degrades at a rate of  $(dm/dt)$  molecules per unit time per unit volume and that degraded molecules are ineffective in reducing drag. Then this degradation corresponds, effectively, to a decrease in polymer concentration at a rate

$$(dc/dt) = (100)(dm/dt) M/N_A \quad (6.6.52)$$

where  $c$  is in gm/dl units. The rate of decrease of the fractional drag reduction,  $R_F$ , is

$$(dR_F/dt) = (dR_F/dc)(dc/dt) \quad (6.6.53)$$

We know from the  $R - c$  curves that  $(dR_F/dc)$  is greatest ( $= [R]$ ) at low and lowest ( $= 0$ ) at high concentrations so if  $dc/dt$  is constant, the time rate of change of drag reduction will be greatest for low concentrations.

In the recirculating 3.21 cm system, mechanical degradation could occur at several locations: the test pipe, pump, return line, fittings and, during solution makeup, the agitated run tank. Of these, the test pipe was by far the most important source. For any polymer, at flow rates below those corresponding to the onset of drag reduction in the 3.21 cm pipe ( $Q < Q^*$ ), degradation was slight. For example, 1000 ppm N3000 could be run for 2 hours at  $Q/Q^* \approx 1$  with little subsequent change in its drag reducing ability. The same solution run at  $Q/Q^* \approx 5$  degraded with time as shown on Fig. 5.3.22. For this reason, all polymer solutions were made up at  $Q/Q^* < 1$ , and subsequent gross flow measurements conducted as rapidly as possible. For W301 solutions,  $Q/Q^* \approx 1$  corresponded to very low flow rates, which necessitated long makeup times (Section 4.5, step 11) during which some degradation probably occurred at locations other than the test pipe, notably in the agitated run tank. This degradation would be most apparent in the flow lines of the lowest concentrations.

At the highest flow rates in the 3.21 cm pipe, all solutions degraded, as may be seen by the curvature in the flow lines. For W301, Fig. 5.3.14, degradation was very severe at  $Q > 3$  litres/sec ( $Q/Q^* > 10$ ); for example, on the 100 ppm flow line the two points at  $Q = 2.4$  litres/sec

were taken 2 minutes apart. On the same figure, the 500 ppm flow line deviated from the maximum drag reduction asymptote only at the 4 highest points. This was checked in two ways: first, by running fresh solution directly up to the high flow rates (i.e., before it had time to degrade), and second, by observation of pressure gradient vs. time. In the former case, the points on the asymptote were replicated, while those off it were different due to varying degrees of degradation. In the latter check, while the asymptote was followed the pressure gradient at a given flow rate was constant with time, despite degradation (by the reasoning of (6.6.53)); whereas when the asymptote was not followed, drag reduction became a function of concentration, and the pressure gradient increased with time as polymer degraded.

In summary, in the present work polymer degradation was negligible, or accounted for, in all measurements used as a basis for generalization.

In practical applications, all extent of drag reduction relations developed would be affected by degradation in the direction of less drag reduction. Because degradation is slight before the onset of drag reduction, an interim measure of the severity of degradation in any pipe is given by the ratio of operating to onset flow rates,  $Q/Q^*$ . For any polymer, degradation is slight for  $Q/Q^* < 1$  and very

severe for  $Q/Q^* > 10$ . Degradation increases with exposure time (residence time in once-through applications); at a given flow rate,  $Q (> Q^*)$ , for a given polymer, the fractional drag reduction decreases rapidly at first, but at long times tends to a value intermediate between the initial, undegraded value, and 0. From an engineering viewpoint, degradation would almost certainly be an important factor in the economic evaluation of applications of the Toms Phenomenon.

## 6.7 Anomalous Pitot Tube and Hot Film Measurements

It was observed that the two instruments classically used to measure fluid flow structure - the Pitot tube for mean and the hot film anemometer for fluctuating velocities - behaved anomalously in polymer solution. This behavior - not hitherto reported in the literature - will be discussed first to assess the uncertainties in flow structure measurements.

### 6.7.1 Pitot Tube Measurements

From Figs. 5.4.4 and 5.4.5 and the description in Section 6.4, it is evident that the velocity indicated by a Pitot tube in polymer solution is a function of:

- (a) the absolute velocity
- (b) Pitot tube diameter
- (c) polymer molecular weight
- (d) polymer concentration .

Of these, the concentration dependence, (d), was not experimentally ascertained, but appears obvious.

These observations might be attributed to the effect of the polymer molecules in solution on

(1) the stagnation pressure attained on the face of the Pitot tube (modelled as a small disc normal to the flow),

(2) the indicated static pressure, by virtue of normal stress effects.



Of these the second appears not to be the case because, from Section 5.4, apparent velocity profiles obtained from a Pitot-static tube by alternately referencing the Pitot to the static tube and to a wall static pressure tap were identical. According to the analyses of Savins (36), and Astarita and Nicodemo (34), normal stress effects depend strongly on radial position in the pipe, being greatest near the wall and negligible on the axis. Thus different profiles would be expected in the above case with little or no discrepancy on the axis, neither of which were the case. Therefore, the discrepancy in Pitot reading has to do with the stagnation pressure rather than the static pressure indicated.

Regarding stagnation effects, one can visualize macromolecules being elongated elastically under the strain rate prevailing at the stagnation point, thereby extracting energy and detracting from the stagnation pressure attained. Presumably, these elastic effects should increase with the rate of strain at the stagnation point which is, in turn, proportional to the free stream velocity and inversely proportional to the Pitot tube diameter, so the effect should increase with free stream velocity and decrease with increasing Pitot tube diameter. This is in accord with the observations. Recently, Boggs and Thompsen (31) have performed a theoretical analysis of

this phenomenon which, unlike the data, predicts that the fractional error is independent of velocity. Furthermore, their results would suggest that there should be no observable effect unless the solution is several orders of magnitude more elastic than is indicated by the theory of Rouse (22).

Alternatively, one can present a mechanical energy argument without resorting to specific constitutive equations, such that if subscripts 1 and 2 refer respectively to the free stream and to the stagnation point, then

$$P_1 + E_1 \frac{c}{100M} N_A + \rho \frac{U_1^2}{2} = P_2 + E_2 \frac{c}{100M} N_A \quad (6.7.1)$$

where E is the elastic energy per molecule and in an unstrained free stream, e.g., the axis of a pipe,  $E_1 = 0$ . Further, if  $P_2 - P_1$  is interpreted in terms of an apparent velocity,  $U_a$ , such that

$$P_2 - P_1 = \frac{\rho U_a^2}{2} \quad (6.7.2)$$

then, on the pipe centre line,

$$\frac{\rho}{2} (U_1^2 - U_a^2) = E_2 \frac{c}{M} N_A \quad (6.7.3)$$

where, as before,  $E_2$  is expected to increase with increasing free stream velocity,  $U_1$ , and decrease with increasing Pitot

tube diameter,  $2a$ . This explanation requires that in all cases exhibiting these anomalies, the polymer molecules must be significantly elongated by the rate of strain at the stagnation point; for this is the only way in which the molecules can store energy. By using the analysis of Peterlin (24), one can demonstrate that this requirement is fulfilled and that, for the shear rates of these experiments, the RMS end-to-end distance may be several times greater than that for zero shear rate. This is shown on Fig. 6.7.1, a plot derived from the data on Fig. 5.4.5, for three Pitot tubes. Both the kinetic energy discrepancy,  $\rho(U_1^2 - U_a^2)/2$ , from (6.7.3) and the corresponding extension ratio,  $L$ , calculated from (6.6.13) are given as functions of  $(U_1/a)$ , the rate of strain at the stagnation point. Note that in Figs. 5.4.5 and 6.7.1, both referring to the pipe axis, the solvent velocity is used for  $U_1$ , the "free stream" velocity in polymer solution, because there is no absolute way of determining the latter. While this choice need not, a priori, be correct, the solvent velocity is constant so no relative error is introduced in comparisons between the various Pitot tubes; also, the absolute error is small because, a posteriori, the centre line velocity in solvent is very close (within 1%) to the "best" value in polymer solution. The three Pitot tubes used were not geometrically similar; also  $(U_1/a)$  is the strain rate

only at the stagnation point itself (from potential flow theory), whereas the energy balance must be taken across the whole Pitot face. Therefore, only qualitative confirmation of the energy argument can be claimed.

Parenthetically, it would appear that an experimental Pitot tube having a hemispherical nose tip with a central pinhole would be the best to evaluate the strain rate - and hence the discrepancy - accurately (54).

Two consequences of the energy argument are, first, that it is a "time mean" argument, independent of any turbulence obtained in the flow, so that the discrepancy should be observed even in laminar flow so long as the mean strain rates are adequate. This remains to be experimentally proven. Second, if the argument is valid, then everywhere other than the pipe axis the macromolecules in the "free stream" are elongated to varying degrees according to the ambient strain rate. Thus, in (6.7.1),  $E_1$  is a function of radial position,  $r$ , so Pitot readings in polymer solution must also be. This also has still to be checked experimentally, though there are indications (see later) that the radial dependence might be weak.

The accuracy of Pitot tube measurements in polymer solution is considered next.

At the "low" flow rate, measurements with the 0.025 cm Pitot might be considered entirely accurate (as accurate

as the solvent), because integrated and pump flow rates agreed to 1% and Pitot readings were independent of Pitot size.

At the "high" flow rate, from the measurements made, there is no way of knowing what the true velocity profile in polymer solution is; it can only be inferred. First, since it was established that the pump calibration in polymer solution was the same as in the solvent, all profiles on Fig. 5.4.4 are at the same true volumetric flow rate (see  $Q$  on Table 5.4.1). Second, at all radial positions the apparent velocity indicated,  $U_{a,r}$ , increases with increasing Pitot size--Fig. 5.4.4, solid points. As a consequence, the integrated flow rate,  $Q_1$ , increases similarly. Now for both  $U_{a,r}$  and  $Q_1$ , the rate of change between the 0.025 and 0.055 cm Pitots is much higher than that between the 0.055 and 0.168 cm Pitots, shown on Table 6.7.1. This strongly suggests an asymptotic approach to the true velocity profile with increasing Pitot tube size; thus, measurements with the 0.168 cm Pitot are the "best" available.

The absolute accuracy of the 0.168 cm Pitot in polymer solution can, also, only be inferred. First, this can hardly be superior to that in the solvent, which was, Section 6.4, from -1% on the axis to -2% near the wall. This factor does not affect comparison between polymer

Table 6.7.1

## Rate of Change of Apparent Velocities

Pitot <u>d</u>	$\xi = 1.00$		$\xi = 0.055$		Flow Rate	
	$U_a$	$\frac{\Delta U_a}{\Delta d}$	$U_a$	$\frac{\Delta U_a}{\Delta d}$	$Q_1$	$\frac{\Delta Q_1}{\Delta d}$
0.025	767	1070	526	2270	5.20	9.7
0.055	809		594		5.49	
		97		89		0.53
0.168	820		604		5.55	

Units are:

$d$  - cm

$U_a$  - cm/sec

$Q_1$  - litres/sec

$\xi = 0.055$  represents the closest that the 0.168 cm Pitot could get to the pipe wall.

solution and solvent. Second, the integrated flow rate,  $Q_1$ , is about 2 1/2% lower than the pump, but 1 1/2% higher than the corresponding  $Q_1$  in solvent. Because of the large Pitot size and the attendant truncation error in integration,  $Q_1$  being lower than  $Q$  in both cases is understandable. However, the integrated value in polymer solution exceeding that in solvent is somewhat disturbing, even though the difference, 1 1/2%, is within the magnitude of the truncation error and therefore could be caused by small differences in velocity profiles in the (inaccessible) wall region. Third, measurements taken with the 0.168 cm Pitot cannot be appreciably dependent upon radial position. For, in order for this to happen, the macromolecules in the "free stream" must be elongated appreciably compared to their eventual elongation on the Pitot face - i.e., the strain rate in the free stream,  $(dU_1/dr)$ , must compare with that at the stagnation point,  $(U_1/a)$ . In a pipe, the greatest strain rate is at the wall so the "worst" radial position is with the Pitot resting on the wall. When this occurs the tube face is essentially all in the "law of the wall" region, from which

$$(dU_1/dr)/(U_1/a) = A/u^+ \quad (6.7.4)$$

where  $A$  is the (inverse of the) mixing length constant. Since  $A$  is practically unchanged in polymer solution

(Fig. 5.4.8), the ratio is of the order of  $10^{-1}$  so any radial dependence must be small. Thus the over-all accuracy of 0.168 cm Pitot measurements in polymer solution is of the same order as in the solvent.

#### 6.7.11 Summary

Pitot tubes in polymer solution indicate apparent velocities which are, in general, too low. The "discrepancy" between the apparent and true velocities increases with increasing absolute velocity and decreasing Pitot tube diameter. The experimental observations, which disagree with all current literature analyses, can tentatively be explained by a mechanical energy argument based on macromolecular extension at the stagnation point with a consequent abstraction of energy that detracts from the stagnation pressure attained. From the experiments and the energy analysis developed, it is strongly suspected, though not definitely proven, that, at the "high" flow rate, 5.70 litres/sec, studied in the present work, mean velocity measurements with the 0.168 cm Pitot are the best available and are as accurate as measurements taken with the same tube in solvent. Also, at the "low" flow rate, 1.15 litres/sec, where the discrepancy was negligible, measurements with a 0.025 cm Pitot are as accurate as in solvent.



## 6.7.2 Hot Film Measurements

From static calibrations, Figs. 5.5.1 to 5.5.3, it was evident that the mean heat transfer from cylinders in transverse flow in polymer solutions is a function of

- (a) mean velocity
- (b) ambient (free stream) strain rate
- (c) polymer molecular weight.

Although not experimentally tested, a dependence on

- (d) polymer concentration and
- (e) cylinder diameter

also appears likely.

The mean velocity dependence at zero strain rate - i.e., from centre line calibrations - was illustrated in Fig.

5.5.2. From these static calibrations of the hot film in the solvent and polymer solutions, it is possible via the anemometer circuit to infer the ratio of the heat transfer coefficients,  $h_p/h_s$ . This is shown as a function of the mean velocity,  $U_1$ , in Fig. 6.7.2. At very low velocities, the ratio is almost unity. This conclusion is approximate, because (see Fig. 5.5.2(a)) only a rough idea of the solvent calibration could be obtained. As the mean velocity exceeds that corresponding to a cylinder Reynolds number of about 40,  $h_p/h_s$  decreases sharply to about 0.4, then climbs back to about unity, around which

region it drops abruptly to about 0.3 and stays thereabouts up to the highest experimental mean velocity of about 900 cm/sec. Thus there is a range of higher velocities in which the heat transfer is unstable and may change by threefold between the two overlapping regimes.

As the polymer degrades the heat transfer improves, and the instability apparently vanishes--the drop at high velocities is not observed, though it may merely have been delayed to higher than the maximum experimental velocity.

From Fig. 5.5.3, at a given mean velocity, heat transfer improved with increasing strain rate, but the dependence on strain rate decreased with polymer degradation. Thus in all events degradation - i.e., decreasing polymer molecular weight - resulted in more solvent-like behaviour.

Three heat transfer regimes may be distinguished on Figs. 5.5.2 and 6.7.2. In terms of cylinder Reynolds number,  $N_{Re,d}$ , these are :

(i)  $N_{Re,d} < 40$ . In this, the first regime of Fig. 5.5.2(a), the heat transfer in polymer solution is about the same as in solvent.

(ii)  $40 < N_{Re,d} < 300$ . This is an intermediate regime comprising the second regime of Fig. 5.5.2(a) and the first regime of Fig. 5.5.2(b), in which the heat transfer coefficient ratio,  $(h_p/h_s)$ , goes through a minimum - decreasing initially before increasing up to about unity. In the

initial stages of this regime, the heat transfer coefficient in polymer solution,  $h_p$ , is quite insensitive to mean velocity.

(iii)  $N_{Re,d} > 300$ . This is the higher velocity, poorer heat transfer, regime of Fig. 5.5.2(b) which prevails following an abrupt transition from region (ii). In it ( $h_p/h_s$ ) is initially about 1/3 and increases slowly with mean velocity.

No explanation can be given for the heat transfer behaviour in polymer solutions, but two interesting facts emerge. First, there is a curious parallel between the three regions above and the regimes observed in the transverse flow of Newtonian fluids across cylinders. Thus, in the latter case,  $N_{Re,d} = 40$  marks the beginning of Karman street formation ("eddy shedding"), while  $40 < N_{Re,d} < 300$  is considered a transition region between the start of eddy shedding and the establishment of a fully turbulent wake (48). Second, heat transfer improves with ambient strain rate, which latter is associated with already extended macromolecules in the free stream. This suggests that the process of macromolecular extension - which is greatest when the free stream is unstrained - hinders heat transfer; this is in the same direction as the Pitot tube discrepancy. However, the flow around cylinders is too complex for any straightforward extension of the energy argument.

The accuracy of hot film measurements is considered next.

In hot film (wire) anemometry, it is always assumed that fluctuating velocity components are small compared to the mean component. Thus, if

$$E = f(U) \quad (6.7.5)$$

is the static (mean) response, then the dynamic response is obtained by considering the fluctuating components as "differentials" of the means such that, at any mean velocity,  $U_1$ ,

$$e' = \left( \frac{dE}{dU} \right)_{U_1} u' \quad (6.7.6)$$

Thus, in theory, only the instantaneous slope of the static calibration is required to convert fluctuating anemometer (electrical) signals to turbulent velocities. In practice, a linear static response greatly enhances the accuracy of turbulence measurements, because the slope is independent of velocity and can be ascertained with greater precision. To obtain this linear relation in (6.7.5), the electrical signal from the hot film sensor must be suitably operated upon. This process, carried out electronically in a "linearizer", requires a knowledge of the heat transfer relation between the fluid and the sensor. All commercial

"linear" anemometers are built on the assumption that this is a Newtonian relation of the form

$$N_{Nu,d} = A + B N_{Pr}^m N_{Re,d}^n \quad (6.7.7)$$

where (A,B,m,n) are constants - typically (0.43, 0.48, 0.31, 0.50) for cylinders in cross flow (55). With the hot film system used in the present work - that of Ling (41) - the static calibration was reasonably linear in water, as seen on Fig. 5.5.1, and the slope could be determined to  $\pm 5\%$ . This led to an accuracy of  $\pm 10\%$  for turbulent velocity measurements in solvent which is typical of the state of the art.

In polymer solutions, however, there are several sources of error:

(1) Most important, the heat transfer relation is not of the form of (6.7.7) so static calibrations are curved and slopes are difficult to obtain accurately -  $\pm 10\%$  at best.

(2) All mean velocities used in static calibrations were got with the 0.168 cm Pitot tube and are subject to the uncertainties discussed in Section 6.7.1; this error is believed small.

(3) Since heat transfer is a function of strain rate, so are static calibrations; they may differ in an unknown

way at each radial position. This was accounted for by matching profile and centre line calibrations and rejecting all points where these were not identical. However, this prohibited meaningful measurements in fresh polymer solutions in which strain rate dependence - and drag reduction - was greatest.

(4) Calibrations were dependent upon the state of polymer degradation and so changed continuously with time. This error was minimized by sandwiching turbulence measurements between calibrations and making the time interval between them short enough for the change to be small.

In view of all these, turbulent velocities in polymer solution are good to about  $\pm 20\%$ , and measurements are limited to relatively degraded polymer solutions where the heat transfer behaviour was less starkly anomalous. It is also clear from the foregoing that the successful use of hot film anemometers in polymer solutions - if it is at all possible - must await a thorough investigation of heat transfer therein - i.e., of the heat transfer analogue of the Toms Phenomenon.

Implicit in the derivation of the dynamic response, (6.7.6), from the static calibration is the assumption that the former is independent of frequency. In practice, frequency response is limited both by the hot film sensor itself and the anemometer electronics, of which the former

almost always controls. In the present case, quick and dirty tests using a small amplitude square wave superimposed on the sensor signal while the latter was operating showed that the frequency response was of the order of 10 kc; that is all frequencies up to 10 kc were faithfully followed by the system. This is in agreement with calculations from a heat conduction analysis of the quartz coated hot film sensor, Appendix A, and would be valid both in solvent and in polymer solution.

Finally, turbulent energy spectra measurements are subject to two kinds of errors. First, there are those stemming from the actual Fourier analysis of the fluctuating anemometer signal. These include errors in anemometer frequency response, variable filter calibration, rms meter readings, etc., all of which are small (of the order of 5% combined) and serve to distort the shape of the spectrum. These errors are the same in both polymer solution and solvent. Second, there are errors which occur in putting the spectra onto an absolute basis,  $E_1(k_1)$  vs.  $k_1$ : namely, errors in  $u^2$ , the turbulent kinetic energy, for the ordinate and errors in  $U$ , the mean velocity, for the abscissa. Of these the error in the mean velocity is small (of the order of 1% in solvent and 2% in polymer solution), but that in  $u^2$  is considerable -  $\pm 20\%$  in solvent and  $\pm 40\%$  in polymer solution. Thus, while confidence may be

placed in comparison of spectra shapes, the comparison of absolute magnitudes is subject to considerable uncertainty.

A summary of the approximate accuracies of various turbulence measurements is presented in Table 6.7.2.

Table 6.7.2

Approximate Accuracy of Turbulence Measurements

Measurement	(dE/dU)	u	Spectra		Frequency Response
			Shape	Absolute Magnitude	
Solvent	$\pm 5\%$	$\pm 10\%$	$\pm 5\%$	$\pm 25\%$	10 kc.
Polymer Solution	$\pm 10\%$	$\pm 20\%$	$\pm 5\%$	$\pm 50\%$	10 kc.



## 6.8 Flow Structure

Flow structure measurements consist of mean velocity profiles, turbulent velocity profiles and turbulent energy spectra. As noted previously, mean velocity measurements were made at two flow rates - one at the onset of drag reduction,  $(Q/Q^*) = 1$  and the other well into the region of drag reduction,  $(Q/Q^*) = 5$ . Turbulence measurements were made only at the higher flow rate,  $(Q/Q^*) = 5$ .

### 6.8.1 Mean Flow

At the "low" flow rate,  $(Q/Q^*) = 1$ ,  $R_F \simeq 0$ , it was seen on Figs. 5.4.7 and 5.4.8 that velocity profiles in polymer solution obeyed both the Newtonian velocity defect and wall laws quite precisely. It can therefore be concluded that before the onset of drag reduction, the mean flow structure is identical to that in the solvent. It will be recalled that the gross flow,  $Q$  vs.  $T_w$ , was, likewise, identical.

At the "high" flow rate,  $(Q/Q^*) = 5$ ,  $R_F \simeq 0.35$ , polymer solution velocity profiles obeyed the Newtonian velocity defect law, Fig. 5.4.7, but did not follow the law of the wall, Fig. 5.4.8. In the latter case, all points were displaced such that the mixing length constant,  $A$ , was essentially unchanged, but the wall constant,  $B$ , was increased by about 7; thus polymer solution points were

shifted upward roughly parallel to the Newtonian line. The polymer solution following the defect law is interesting, because  $(T_{wp}/T_{ws}) = (1 - R_F)$  so that  $u_\tau$  is nearly 20% lower than in solvent; thus values of  $(U_{CL} - U)$  must, at all radial positions, be 20% lower than corresponding values in solvent, which means that a distinctly "blunter" profile is obtained. Further, this indicates that  $u_\tau$  is the velocity scale in polymer solution - just as it is in solvent - so long as mean velocities are considered relative to the maximum,  $U_{CL}$ . Thus  $T_{wp}$  is the shear stress "seen" by, and therefore "controlling", the flow in the region covered - say  $0.05 < \xi < 1.00$ . If this is so, then, in suitable velocity coordinates,  $T_{wp}$  (or  $u_\tau$ ), should also scale the flow in the "law of the wall" region in a Newtonian manner. This latter is also suggested by the mixing length constant,  $A$ , remaining unchanged in polymer solution.

#### 6.8.11 The "Effective Slip" Model

Consider the following model, illustrated on Fig.

6.8.1. Assume an "effective slip",  $V_S$  cm/sec, at the pipe wall - equivalent to letting the wall move in the direction of flow with velocity  $V_S$ . We have, therefore,

$$\begin{aligned} \xi = 0, \quad U &= V_S \\ (dU/d\xi) &= DT_{wp}/2\eta = Du_\tau^2/2\gamma \end{aligned} \quad (6.8.1)$$

$$\begin{aligned} \xi = \xi, \quad U &= U \\ \xi = 1, \quad U &= U_{CL} \end{aligned}$$

Now, let

$$V = (U - V_S) \quad (6.8.2)$$

be the velocity which results in the polymer solution profile following all Newtonian laws. Then  $V$  is the coordinate we are looking for. In terms of it, (6.8.1) becomes,

$$\begin{aligned} \xi = 0, \quad V &= 0 \\ (dV/d\xi) &= (dU/d\xi) = Du_\tau^2/2\gamma \end{aligned} \quad (6.8.3)$$

$$\xi = \xi, \quad V = V$$

$$\xi = 1, \quad V = V_{CL} = U_{CL} - V_S$$

It is clear that  $(\xi, V)$  coordinates will follow the velocity defect law because

$$\begin{aligned} (V_{CL} - V)/u_\tau &= (U_{CL} - V_S - U + V_S)/u_\tau \\ &= (U_{CL} - U)/u_\tau \end{aligned}$$

and  $(\xi, U)$  coordinates have already been shown to. To test if  $(\xi, V)$  obey the same law of the wall as solvent, we need to determine the "effective slip" velocity,  $V_S$ . This can be done by integrating (6.8.2) across the pipe radius, so

$$\int_0^1 U d(1 - \xi)^2 = \int_0^1 V d(1 - \xi)^2 + \int_0^1 V_S d(1 - \xi)^2 \quad (6.8.4)$$

Defining average velocities in the usual way,

$$U_{AV} = 4Q/\pi D^2 = \int_0^1 U d(1 - \xi)^2 \quad (6.8.5)$$

gives, since  $V_S$  is independent of  $\xi$ ,

$$U_{AV} = V_{AV} - V_S \quad (6.8.6)$$

$U_{AV}$  is known from the flow rate. And if  $(\xi, V)$  obey Newtonian laws, then  $V_{AV}$  must be related to the prevailing  $u_\tau$  by the universal friction factor relation of Prandtl, (6.6.49). For the conditions at the "high" flow rate, we have

$Q$  - 5.71 litres/sec, so, by (6.8.5),

$U_{AV}$  - 705 cm/sec.

$u_\tau$  - 25.0 cm/sec., from which, using (6.6.49),

$V_{Av}$  - 545 cm/sec., and thus, from (6.8.6)

$V_S$  - 160 cm/sec.

Now, if  $V_S$  is subtracted from the mean velocity,  $U$ , recorded at each radial position, this gives the  $(\xi, V)$  profile which, if all of the foregoing reasoning is valid, should result in the same law of the wall,  $(V/u_\tau)$  vs.  $\ln(\xi Du_\tau/2\nu)$ , being followed as in solvent. On Fig. 6.8.1, it is seen that this is indeed the case; polymer solution points processed as above come very close to - within 1% - the corresponding solvent line (compare Fig. 5.4.8), implying that  $V$  is indeed the coordinate in which polymer solution velocity profiles follow all Newtonian laws. Parenthetically, note that Fig. 6.8.2 was prepared, for reasons discussed in Section 6.7.1, from 0.168 cm Pitot results. In solvent these were somewhat less precise than results with the 0.025 cm Pitot so the "law of the wall" on Fig. 6.8.2 is slightly different from that of Fig. 5.4.3. This, of course, is incidental to the central issue - that of polymer solution following the same rules, whatever they be, as solvent. Note also that this "effective slip" approach readily includes the flow prior to the onset of drag reduction; in that case the "slip" component is zero, and Newtonian velocity profiles are predicted - as observed.

The preceding suggests a very attractive, simple way to consider mean velocity profiles in polymer solution:

namely, as consisting of two additive portions or "plugs". Of these, the upper "plug" is the velocity profile that would be obtained in the "Newtonian" solvent at the wall shear stress prevailing in the polymer solution. The lower "plug", upon which the upper one is convected along, is the uniform "effective slip" velocity required to make up the difference between the actual volumetric flow rate and that obtained by integration of the upper, "Newtonian", portion. As a corollary, the volumetric flow rate,  $Q$ , (or the average velocity,  $U_{AV}$ ) might be thought of as comprising a "Newtonian" component,  $Q_N$  (or  $V_{AV}$ ), associated with the prevailing wall shear stress, and a "slip" component,  $Q_S$  (or  $V_S$ ). Of these,  $Q_N$  may naturally be associated with the energy consumption required to maintain flow, whereas  $Q_S$  may be considered as being free of any energy expenditure and so associated with drag reduction in the Toms Phenomenon.

The flow rate components are directly available from the gross flow diagrams, Figs. 5.3.5 to 5.3.14; drawing a vertical line at any wall shear stress,  $T_w$ , corresponding to  $u_\tau$ , gives  $Q_N$  at its intersection with the solvent line (strictly speaking, the "Newtonian" solvent line should be used) and  $Q$  at the intersection with the desired polymer solution flow line. These components are also available from a conventional friction factor plot as follows. At

any given flow rate,  $Q$ , and friction velocity,  $u_\tau$ , in polymer solution, let  $f_p$  be the actual friction factor,

$$f_p^{-\frac{1}{2}} = (U_{AV}/\sqrt{2} u_\tau) \quad (6.8.7)$$

and let  $f_N$  be the friction factor, calculated from, for example, (6.6.49), that would be expected in the Newtonian solvent at the prevailing  $u_\tau$ ,

$$\begin{aligned} f_N^{-\frac{1}{2}} &= (V_{AV}/\sqrt{2} u_\tau) \\ &= 4.0 \text{ Log}_{10}(\sqrt{2} u_\tau D/\nu) - 0.4 \end{aligned} \quad (6.8.8)$$

Then the fractional flow rate "components" are

$$\begin{aligned} (Q_N/Q) &= (V_{AV}/U_{AV}) = (f_N/f_p)^{-\frac{1}{2}} \quad (\text{Newtonian}) \\ (Q_S/Q) &= (V_S/U_{AV}) = 1 - (f_N/f_p)^{-\frac{1}{2}} \quad (\text{Slip}) \end{aligned} \quad (6.8.9)$$

The foregoing suggests comparison of drag reduction at equal wall shear stress rather than equal flow rate. This can be done in complete analogy with the work of Section 6.6.41; the conclusions derived therein will, of course, be unchanged. Thus a fractional slip,  $S_F$ , induced by a concentration  $c$  dl/gm of polymer at a given wall shear stress,

$T_w$ , is defined by

$$S_{F,T_w} = ((Q_p/Q_s) - 1)T_w \quad (6.8.10)$$

The fractional slip,  $S_F$ , and the fractional drag reduction,  $R_F$ , are directly related when the same reference solvent condition is used; i.e., when the constant wall shear stress,  $T_w$ , used in (6.8.10) is that in the solvent at the constant flow rate,  $Q$ , used in (6.6.27). As an example, from (6.8.10), using the approach of equations (6.6.32 to 6.6.35), the intrinsic slip,  $[S]$  dl/gm, is

$$\begin{aligned} [S] &= (1/ns)(-dnp/dc)_c \rightarrow 0 \ln(Q/Q^*) \\ &= [R] / ns \end{aligned} \quad (6.8.11)$$

All extent of drag reduction results can, similarly, be converted simply to an extent of slip basis if desired.

While the agreement between the effective slip model postulated and the experimental mean flow results obtained seems too good to be merely coincidental, it is based only on 2 velocity profiles - one before and one after the onset of drag reduction. And, unfortunately, no reliable velocity profiles are available in the literature to provide an "external" check. Therefore, the concept of an "effective slip" - originally proposed by Oldroyd (2) - will not be



pursued in any detail, pending further experimental evidence. However, one obvious question arises: namely, how can a "slip" be justified at all? All slip (and no slip) hypotheses are notoriously difficult to prove because of the experimental inaccessibility of the "interface" between the solid boundary and the flowing fluid. In micromolecular, Newtonian, fluids, the usual objection to slip - and the cornerstone of the accepted "no slip at solid boundaries" condition - is that, on a molecular scale, it is difficult to imagine any difference between the wall and the fluid in contact with it. For macromolecular solutions, this objection is not quite so serious because, on a molecular scale, macromolecules are, indeed, different. Also, in at least one case - melt fracture in the extrusion of bulk polymers - slip does occur. Thus for polymer solutions, slip at the wall is somewhat easier to imagine than in micromolecular fluids. But an actual, physical, slip remains dubious and the "effective" slip might best be considered the net result of the unknown processes occurring very close to the wall in the turbulent flow of polymer solutions, as shown in Section 6.8.23.

### 6.8.2 Turbulence Structure

The turbulence measurements made, axial rms turbulent velocity profiles and axial one-dimensional turbulent

energy spectra at two radial positions, give only a fragmentary picture of the structure of turbulence. Their main virtue lies, as pointed out in Chapter II, in comparison between solvent and polymer solution to indicate differences. Also, such turbulence measurements in polymer solutions have not hitherto been reported in the literature.

### 6.8.21 rms Turbulent Velocity Profiles

Laufer (43) showed that, for Newtonian fluids, rms turbulent velocity profiles in the central core of a pipe were universal when normalized by the friction velocity,  $u_\tau$ , - akin to the mean velocity defect law - and also, that very close to the wall,  $y^+ < 20$ , universality existed in  $(u/u_\tau)$  vs.  $y^+$  - akin to the mean velocity law of the wall. The second region was experimentally inaccessible in the present work.

In polymer solution, Fig. 5.5.5 and Section 6.5.2, the rms turbulent velocity profile was considerably different from solvent at the same flow rate. But normalization of the points on Fig. 5.5.5(a), for example, by the prevailing  $u_\tau$  gives results shown on Fig. 6.8.3, on which the experimental results for solvent, derived from Fig. 5.5.4(b), are shown as a dashed line. For  $y^+ < 0.4$ , the turbulent "intensity",  $(u/u_\tau)$ , in polymer solution is essentially the

same as in solvent, but for  $\xi > 0.4$ , it is considerably higher, + 40% at  $\xi = 1.00$ .

In a fully developed, Newtonian, turbulent pipe flow, the integrated momentum equation yields

$$\rho(1 - \xi)u_{\tau}^2 = \overline{\rho u'v'} + \frac{2\eta}{D} (dU/d\xi) \quad (6.8.11)$$

which states that, at any radial position,  $\xi$ , the local shear stress is composed of turbulent,  $\overline{\rho u'v'}$ , and viscous,  $\frac{2\eta}{D} (dU/d\xi)$ , shear stresses. We know, from the mean flow structure of Section 6.8.1, that the viscous term,  $\frac{2\eta}{D} (dU/d\xi)$ , is that which would prevail in the Newtonian solvent at the same  $u_{\tau}$ . Therefore, from (6.8.11),  $\overline{\rho u'v'}$  in polymer solution must coincide with the corresponding Newtonian  $\overline{\rho u'v'}$  at all radial positions. The turbulent shear stress,  $\overline{\rho u'v'}$ , comprises three elements:  $u'$  and  $v'$ , the axial and radial turbulent velocities, and the correlation, or "phase", between them. Of these only  $u'$  was experimentally determined so changes in the other two cannot, strictly, be differentiated. However, because both  $\overline{u'v'}$  and the intensity,  $(u/u_{\tau})$ , follow Newtonian rules, it appears very likely that in the region of the wall,  $\xi < 0.4$ , the turbulent flow structure in polymer solution is the same as in the Newtonian solvent at the same  $u_{\tau}$ . For the central core of the pipe,  $1.0 > \xi > 0.4$ ,  $\overline{u'v'}$  must

still be the same, but  $(u/u_r)$  is higher than Newtonian. Since this region is the most isotropic in the pipe, one might guess that  $u'$  and  $v'$  are similar whence, in it, the correlation coefficient between them must be lower in polymer solution than in solvent, i.e., the axial and radial components are more "out of phase" in polymer solution. This conclusion is considerably weaker than the previous one for  $\xi < 0.4$ , because Newtonian laws, for which 6.8.11 is valid, were not followed in the central core.

Finally, it will be noted that the "plateau" in turbulent intensity that occurs for  $0.4 < \xi < 0.7$ , starts at the radial position where the profile ceases to follow Newtonian laws. While this is a prominent feature of the polymer solution profile, which would imply physical significance, no interpretation can be given for it.

#### 6.8.22 Turbulent Energy Spectra

The spectra were presented - as taken - on Figs. 5.5.6 to 5.5.8. Table 6.8.1 is a tabulation of quantities characteristic of these spectra; the various columns are described briefly.  $\rho u_r$  and  $u_r/\rho$  are energy density and wave number scales with which  $E_1(k_1)$  and  $k_1$ , respectively, can be nondimensionalized.  $\Lambda_f$  is the "macro" or "integral" scale of the turbulence, defined by

$$\Lambda_f = \frac{1}{2} \pi E_1(k_1) k_1 \rightarrow \sigma/u^2 \quad (6.8.12)$$

Table 6.8.1

Spectrum Parameters

	Q	u	$\gamma u_T$	$u_T/\gamma$	$\xi$	$\Lambda_f$	$\lambda_f$	$\int_0^\infty k_1^2 E_1(k_1) dk_1$	$k_d$	$k_e$
Solvent	1.15	5.62	0.065	820	1.00	0.82	0.26	925	9	50
Solvent	5.30	27	0.25	3200	1.00	0.73	0.15	60500	16	80
Polymer	5.71	32	0.34	2100	1.00	0.77	0.20	25000	6	55
Solvent	1.15	16.2	0.065	820	0.033	0.90	0.19	15000	14	85
Solvent	5.30	59.5	0.25	3200	0.033	1.15	0.19	195000	16	125
Polymer	5.71	55	0.34	2100	0.033	1.50	0.22	120000	21	85

Units are:

Q - litres/sec

u - cm/sec

$u_T/\gamma$ ,  $k_d$ ,  $k_e$  -  $cm^{-1}$

$\Lambda_f$ ,  $\lambda_f$  - cm

$\gamma u_T$  -  $cm^3/sec^2$

$\int_0^\infty k_1^2 E_1(k_1) dk_1$  -  $sec^{-2}$

It may be identified, roughly, with the size of the larger, "energy containing" eddies existing in the flow. Division of  $\Lambda_f$  values on Table 6.8.1 by the pipe diameter, 3.21 cm, gives  $(\Lambda_f/D)$  ratios of roughly 1/4 - which is of the order expected in a pipe (43). Macroscales in polymer solution and solvent are essentially identical on the pipe axis,  $\xi = 1.00$ ; near the wall the value in polymer solution is somewhat higher.  $\lambda_f$  is the "microscale",

$$\frac{1}{\lambda_f^2} = \frac{1}{2u^2} \int_0^{\infty} k_1^2 E_1(k_1) dk_1 \quad (6.8.13)$$

classically considered characteristic of the dissipative eddies, although this interpretation, derived for isotropic turbulence at infinite Reynolds number, is highly suspect in anisotropic turbulence like pipe flow (see, e.g., 56). The integral  $\int_0^{\infty} k_1^2 E_1(k_1) dk_1$  has been loosely referred to earlier (and will be later) as the turbulent "dissipation". Strictly speaking, it is just one axial component of the several components of the turbulent dissipation,  $\mathcal{E}$ , and only in isotropic turbulence are the two synonymous, being related by a multiplicative constant (44),

$$\mathcal{E} = 15 \nu \int_0^{\infty} k_1^2 E_1(k_1) dk_1 \quad (6.8.14)$$

For this reason the dissipation integral is a better measure of the true dissipation on the pipe axis - which is the most isotropic location in a pipe - than near the wall. From Table 6.8.1, at the higher flow rate, the ratio of  $\int_0^{\infty} k_1 E_1(k_1) dk_1$  in polymer solution to that in solvent is 0.58 at  $\xi = 1.00$  and 0.88 at  $\xi = 0.033$ ; thus the dissipation is 40% lower on the axis, but only 10% lower near the wall.  $k_d$  and  $k_e$  are dissipation wave numbers, defined in connection with the Onset Hypothesis, in Section 6.6.2.  $k_d$  is the wave number at which the maximum occurs in the dissipation curves,  $k_1^2 E_1(k_1)$  vs.  $k_1$ , such as shown on Fig. 6.5.1.  $k_e$  is the wave number beyond which only a small fraction, 5%, of the dissipation occurs.  $k_e$  is about one order of magnitude higher than  $k_d$ , but both follow similar trends.

From the measurements made, polymer solutions and solvent can be compared only at the "high", drag reducing, flow rate. One question arises: namely, to what datum should polymer solution spectra be referred, considering that

- (a) solvent spectra, Fig. 5.5.7, were taken at a 7% lower flow rate and
- (b) the relative viscosity of the polymer solution - and its Newtonian solvent - was 1.4. There are several logical choices:

(1) Solvent spectra as measured. This avoids any manipulation of experimental results.

(2) Solvent spectra at the same flow rate as polymer solution.

(3) Newtonian solvent spectra at the same flow rate as polymer solution. This would account for the viscosity buildup.

(4) Newtonian solvent at the same friction velocity,  $u_\tau$ , as polymer solution. This is suggested by the reasoning of Section 6.8.1.

Choices (2), (3) and (4) require that the measured solvent spectra be translated to other conditions. There are no ironclad rules for doing this; the best available are the spectrum scaling rules of Appendix B, which, strictly, are valid only for the higher wave numbers, but, in view of the small changes required, hopefully do not introduce much error when applied throughout. Using these in the same pipe and at the same radial position, a point  $(k_1, E_1(k_1))$  on the measured spectra corresponds to the point  $(k_1', E_1'(k_1'))$  on spectra at condition ' where

$$k_1' = k_1 (u_\tau'/\nu)' / (u_\tau/\nu) = \alpha_w k_1$$

(6.8.13a)

$$E_1'(k_1') = E_1(k_1) (\nu u_\tau)' / (\nu u_\tau) = \beta_w E_1(k_1)$$



for "wall" spectra and

$$k_1' = k_1 \left[ (u_\tau/\gamma)' / (u_\tau/\gamma) \right]^{3/4} = \alpha_a k_1$$

$$E_1'(k_1') = E_1(k_1) \left[ (\gamma u_\tau)' / (\gamma u_\tau) \right] \left[ (u_\tau/\gamma)' / (u_\tau/\gamma) \right]^{-1/4}$$

$$= \beta_a E_1(k_1)$$

(6.8.13b)

for spectra on the pipe axis. Values of the scaling parameters,  $u_\tau$  and  $\gamma$ , and the multipliers,  $(\alpha, \beta)$ , derived from them for reference conditions (1) to (4) above, are given on Table 6.8.2. Considering the  $\pm 50\%$  accuracy of the spectral ordinates, it is clear from Table 6.8.2 that a precise datum is of marginal value, because the shifts required to convert the measured solvent spectra to other reference conditions are small - of the same magnitude as the error. Nonetheless, there is some difference between solvent (1 and 2) and Newtonian solvent (3 and 4) datums. Figures 5.5.7 and 5.5.8 and Table 6.8.1, as such, provide for (1) - direct comparison between solvent and polymer solution. Figure 6.8.4 compares the polymer solution spectra of Fig. 5.5.8 with reference condition (4), i.e., with the spectra which would prevail in the Newtonian solvent at the same  $u_\tau$ . The latter were got by multiplying

Table 6.8.2

## Solvent Spectrum Scaling Constants

Reference Condition	$u_\tau$ cm/sec	$\gamma$ cm <sup>2</sup> /sec	$u_\tau/\gamma$ cm <sup>-1</sup>	$\gamma u_\tau$ cm <sup>3</sup> /sec	Ordinate		Multipliers	
					Wall $\alpha_w$	$\beta_w$	Axis $\alpha_a$	$\beta_a$
(1)	28.4	0.00894	3180	0.254	1.00	1.00	1.00	1.00
(2)	30.6	0.00894	3430	0.273	1.08	1.08	1.06	1.06
(3)	31.5	0.0127	2428	0.400	0.78	1.58	0.83	1.68
(4)	26.5	0.0127	2080	0.335	0.65	1.32	0.72	1.47

Reference conditions for solvent spectra are, as in text,

- (1) Measured solvent spectra, Fig. 5.5.7.
- (2) Solvent at same flow rate, 5.70 litres/sec, as polymer solution spectra, Fig. 5.5.8.
- (3) Newtonian solvent at same flow rate, 5.70 litres/sec, with same relative viscosity, 1.42, as polymer solution, Fig. 5.5.8.
- (4) Newtonian solvent at same  $u_\tau$ , 26.5 cm/sec, as polymer solution spectra, Fig. 5.5.8.

solvent spectra of Fig. 5.5.7 by the relevant  $(\alpha, \beta)$  -  $(0.65, 1.32)$  at  $\xi = 0.033$  and  $(0.72, 1.47)$  at  $\xi = 1.00$  - given on Table 6.8.2. Figure 6.8.4 will be used in the discussion following, bearing in mind that, within the accuracy of the spectra, this is essentially the same as direct comparison with solvent or any of the other reference conditions listed above.

On the pipe axis,  $\xi = 1.00$ , the shape of the spectrum - in the fidelity of which great confidence can be placed - is distinctly different in polymer solution. The central difference is that the "inertial subrange", slope  $-3/2$  to  $-5/3$ , which occurs for  $2 < k_1 < 20 \text{ cm}^{-1}$  in solvent is entirely absent in polymer solution where, instead, an abrupt change of slope, from  $-2/3$  to  $-4$ , occurs at  $k_1 \sim 6 \text{ cm}^{-1}$ . In addition, with polymer degradation the change became less abrupt,  $E_1(k_1)$  decreased for  $k_1 < 10 \text{ cm}^{-1}$ , but increased for  $k_1 > 10 \text{ cm}^{-1}$ ; i.e., a spectral redistribution of energy occurred in the direction of a more solvent-like distribution. (Reversing the degradation process in the mind's eye suggests, in the limit, a curious idealized spectrum, having a square "cut off" at  $k_1 = 6 \text{ cm}^{-1}$  such that

$$E_1(k_1) = \text{Constant}, \quad k_1 < 6$$

$$= 0 \quad k_1 > 6).$$

Now, from classical turbulence theory (45), turbulent energy is produced, dissipated and transferred at all wave numbers. But the production occurs, or is associated with, the lower wave numbers - the region of the "energy containing eddies" - while dissipation is associated with the higher wave numbers. Thus there is a "cascade" of energy, a net flow, from the lower to the higher wave numbers. If the "energetic" and the "dissipative" regions are widely enough separated, then a region exists between them in which the production is small compared to that at lower wave numbers, and the dissipation is small compared to that at higher wave numbers. Thus, in effect, there is merely an inertial transfer of energy in this region, the flux through it being a constant as the turbulent energy proceeds from the low wave numbers, where it was produced, to the high wave numbers, where it will be dissipated. This is the inertial sub-range and Kolmogorov showed that in it  $E_1(k_1) \propto k_1^{-5/3}$  - for Newtonian, isotropic, turbulence. The shape of the centre line spectrum in polymer solution and its trend with degradation suggest a "shorting-out", or 'bypassing', of this inertial sub-range, which implies a much stronger interaction, or coupling, between the energy-containing and dissipative regions than exists in solvent. It would be extremely interesting to know how the macromolecules achieve this!

From the macroscales on Table 6.8.1, it is apparent that the energy-containing eddies - or wave numbers - in polymer solution are not very different from those in solvent. Therefore, a "stronger interaction" would imply the dissipative wave numbers should move towards the lower, energetic, wave numbers with, since dissipation varies as the square of the wave number, a decrease in dissipation. The resulting shift of the dissipation curve towards the origin, i.e., towards the energy-containing region, and the decrease in the total dissipation have already been shown on Figs. 6.5.1(a) and Table 6.8.1. In Fig. 6.5.1 polymer solution is compared with solvent; no particular purpose is served by comparison with Newtonian solvent, because the trend is the same. It is noteworthy that while the mean square turbulent kinetic energy,  $u^2$ , in polymer solution is 40% higher than solvent, the dissipation is 40% lower.

Near the pipe wall,  $\xi = 0.033$  ( $y^+ \approx 100$ ), there is no significant change in the spectrum. The ordinates are only slightly different, and spectra shapes in polymer solution and solvent are remarkably similar. Likewise, the dissipation curves, Fig. 6.5.1(b) were similar.

### 6.8.23 Summary

The following observations can be made from turbulence

measurements in polymer solution exhibiting the Toms Phenomenon.

(1) At all radial positions, the turbulent shear stress,  $\overline{\rho u'v'}$ , is that which would be obtained in the Newtonian solvent at the same friction velocity,  $u_\tau$  (or wall shear stress,  $T_w$ ).

(2) For  $\xi < 0.4$ , turbulent intensity profiles,  $(u/u_\tau)$  vs.  $\xi$ , follow Newtonian rules, but for  $1.0 > \xi > 0.4$ , intensities in polymer solution are higher than Newtonian.

(3) On the pipe axis,  $\xi = 1.00$ ; the axial turbulent energy spectrum is significantly different from solvent. Mainly, the "inertial subrange" is absent, and the total dissipation much lower.

(4) Near the wall,  $\xi = 0.033$ ; there is no significant difference between spectra in polymer solution and solvent.

Thus turbulent intensity profiles and turbulent energy spectra present the same picture - one of essentially Newtonian behaviour near the wall, but starkly different from Newtonian behaviour in the central core of the pipe. Specifically, the following conclusion can be culled from the observations above.

(1) In the region of the wall,  $\xi < 0.4$ , from (1), (2) and (4), it appears that the turbulence structure in polymer solution is the same as that in the Newtonian solvent at the same  $u_\tau$ .

(ii) In the central core of the pipe,  $1.0 > \xi > 0.4$ , from (1) and (2), the axial and radial turbulent velocity components are more "out of phase" in polymer solution, i.e., the correlation coefficient between  $u'$  and  $v'$  is lower than in solvent. Also, from (3), on the pipe axis, the absence of the inertial subrange indicates a stronger coupling between the wave numbers responsible for turbulent energy production and dissipation. Since the former are essentially unchanged, this results in dissipation occurring at lower wave numbers and therefore being less than in solvent. Both conclusions in this paragraph are based on "Newtonian" reasoning which may not be completely valid in this region.

(iii) Now the central region of the pipe is unimportant from an energy viewpoint, and the wall region, (1), - where the energy action occurs - has a turbulent structure which follows Newtonian laws. This strongly reinforces the notion of Section 6.8.1 that the flow structure prevailing in polymer solution is essentially that of the Newtonian "plug", corresponding to the prevailing  $u_\tau$ , convected along at an additional, "effective slip", velocity.

(iv) Note that we have proceeded in the direction of increasing detail - from gross to mean to turbulent flow. It has been shown that the relevant Newtonian gross flow parameters,  $u_\tau$  and  $\nu$ , completely scale the mean flow

structure, but only scale the turbulence structure in the region of the wall. However, the breakdown of Newtonian scaling occurs in the central core of the pipe which is the region least dominated by - i.e., most independent of - the energy processes that occur in a turbulent pipe flow. Also, the breakdown occurs only at the highest echelon of detail, namely turbulence structure. The Toms Phenomenon must, since it results in a reduction of specific energy consumption, be related to the energetic processes. Therefore, it is entirely conceivable that the turbulence structure in the central core of the pipe is due to causes not directly related to those causing the Toms Phenomenon - although both must, ultimately, be traced to the addition of macromolecules to the solvent.

(v) Finally, as has been mentioned earlier, from an energy viewpoint, one might expect that the behaviour in a region extremely close to the pipe wall would determine the Toms Phenomenon. Flow structure results confirm this expectation from a somewhat different angle.

In direct analogy to turbulent boundary layers, the flow in a pipe may be pictured as consisting of two portions: an "inner" region, say  $\xi < 0.15$ , which is directly dependent on processes occurring at the wall (or very close to it), and an "outer" region, say  $0.05 < \xi < 1.00$ , which is controlled only by conditions at



its boundaries and, therefore, is only "loosely" coupled to the wall processes in as much as the latter determine conditions at its inner boundary. It has been shown, both for untranspired and transpired turbulent boundary layers (Clauser (57), Smith (58)) that the flow structure in the outer region is completely scaled by the shear stress at its inner edge, i.e., by the shear stress it "sees", irrespective of the wall processes which brought this about. In a fully developed pipe flow, the shear stress profile is linear in radius, so at any  $\xi$  the shear stress,  $T_\xi$ , is

$$T_\xi = (1 - \xi)T_w \quad (6.8.14)$$

Thus the shear stress at the inner edge of the outer region is very close to the wall shear stress, which latter, we have seen, scales the flow structure in polymer solution. Therefore, the outer region in a pipe flow exhibiting the Toms Phenomenon is essentially the same as in a Newtonian pipe flow. Further, the inner and outer regions overlap below about  $\xi \simeq 0.15$  and, though our experimental results terminated at  $y^+ \simeq 150$ , it is safe to say, from the law of the wall being followed, that the overlap continues down to  $y^+ \simeq 50$ . Thus the difference between flow in the Toms Phenomenon and honest-to-goodness Newtonian pipe flow must lie in the region of  $0 < y^+ < 50$ , which is the "extremely close to the wall" region of the energetic processes.

The foregoing stresses - akin to Newtonian flow (43) - the importance of experimental measurements in the immediate vicinity of the wall. It is also the best rationale for the "effective slip" model, Section 6.8.11, since, independent of the mechanism very close to the wall, the outer region which comprises better than 95% of the flow is "effectively" controlled by the wall shear stress (i.e.,  $u_\tau$ ), just as in the Newtonian case.

PART C

THE OVER-ALL PICTURE

## Part C: The Over-all Picture

All the conclusions derived from the observations in Part A and the analysis in Part B are specifically listed in the next chapter. In this part, the findings are applied in a more general way for:

- 6.9 Evaluation of Earlier Explanations, and
- 6.10 Prediction and Estimation of the Toms Phenomenon.

## 6.9 Evaluation of Earlier Explanations

It will be recalled from Chapter II that four distinct types of explanations have been proposed for the Toms Phenomenon, viz.,

- (i) laminar turbulent transition delay
- (ii) "effective" slip
- (iii) an anisotropic viscosity in polymer solutions, and
- (iv) visco-elasticity.

Each of these will be examined in the light of the present findings.

### 6.9.1 Transition Delay

It has clearly been shown, Section 6.6.3, that polymer solutions exhibiting the Toms Phenomenon do not, in general, delay transition. Further, cases in which transition is delayed satisfy criteria derived from other, independent, sources (i.e., the Onset Hypothesis). Therefore, the delayed transition type of explanation for the Toms Phenomenon may safely be rejected. We venture, very briefly, to explain why, physically.

The explanation was proposed by Savins (8) in direct analogy to dusty gases, for the turbulent flow of which, slight drag reduction has been reported (9,10). To explain the latter, Saffman (11) conducted a stability analysis

which showed that "coarse" dust particles - which cannot respond quickly to velocity changes - would stabilize the flow, presumably because "disturbances" would have to flow around the particles with a frictional dissipation of their energy and a consequent reduction in their ability to trigger transition. The disturbances causing transition are associated with low wave numbers, i.e., large eddies, typically of order  $(D/4)$  in a pipe. For any reasonable pipe diameter and macromolecule, the ratio of particle to disturbance size is so small, less than say  $10^{-3}$ , that stabilization in the manner suggested is exceedingly unlikely. In fact, macromolecules in solution are more akin to Saffman's "fine" dust which, he showed, had no effect on transition.

### 6.9.2 "Effective" Slip

This explanation was first proposed by Oldroyd (2); the extent to which it is followed was demonstrated in Section 6.8.1 and attests to the remarkable insight of the original investigators - Toms and Oldroyd. While the effective slip model is well obeyed, it remains an "engineering" notion - entirely adequate for most practical purposes, but yielding little physical insight other than that the processes of interest in the Toms Phenomenon occur extremely close to the wall. An actual

slip at the wall, while somewhat more conceivable in macromolecular than in micromolecular fluids, is still, by dint of precedence, a dubious proposition. Therefore, the processes causing the "effective" slip are, very likely, encompassed within the two remaining types of explanations - anisotropic viscosity and visco-elasticity.

### 6.9.3 Anisotropic Viscosity vs. Visco-elasticity

From the inference that the processes of importance occur extremely close to the wall, in which region experimental measurements could not be made, no conclusive distinction can be made between the two remaining types of explanations. However, some circumstantial type of evidence can be derived from the present work, and this is presented after brief descriptions of the two explanations.

#### 6.9.31 Anisotropic Viscosity

It is strongly suspected that macromolecules elongate under shear (24); so, in a pipe flow, macromolecules will be elongated to varying degrees in the direction of flow, according to the mean shear rate - from zero on the pipe axis to a maximum at the wall. At high enough wall shear rates, this orientation could lead to an anisotropic viscosity, the viscosity "component" in the radial direction

being different from that in the axial and azimuthal directions. Physically, the stretched macromolecules would presumably impede eddy movement in the radial direction, normal to their elongation, thereby decreasing momentum transfer and hence the specific energy expenditure. This explanation is due to Merrill, first quoted in Shin (21). From this reasoning the radial turbulent velocity,  $v'$ , would be the most affected; in the present work only axial turbulence measurements were made so a good, direct, experimental test of the explanation cannot be made.

#### 6.9.32 Visco-elasticity

There is little question that macromolecules are elastic and that their addition to micromolecular solvent results in the solution becoming visco-elastic - even though solutions exhibiting the Toms Phenomenon are so dilute that their elasticity cannot be measured experimentally. The notion of macromolecules exchanging energy, "interacting", with the turbulent flow field is so appealing physically that, in the current literature, visco-elasticity is almost taken for granted as the cause of the Toms Phenomenon (8,20,21,28,29,31,33,34). But no mechanism, even remotely acceptable, has yet been proposed. And the more formal approach, using visco-elastic constitutive equations, is promising but, in view of the complexity,



such drastic simplifications have to be made that the results predicted (e.g., 31) do not agree with experiments. Thus, so far as the Toms Phenomenon is concerned, the major argument in favour of the visco-elastic explanation is, at present, intuitive.

### 6.9.33 Other Evidence

Peripheral evidence available from the present results to distinguish between the two remaining explanations is as below.

(1) On the pipe axis, roughly isotropic conditions can be expected to prevail. Therefore, the anisotropic viscosity - due to macromolecular extension - cannot be operative in this region. Thus the observed differences from Newtonian flow structure in the central core must be caused by visco-elasticity. Specifically, the absence of the inertial subrange in the turbulent energy spectrum, which is suggestive of closer coupling between the energetic and dissipative wave numbers, must be due to the elasticity of the unstrained macromolecules. Therefore, in isotropic turbulence, at any rate, there is a definite "interaction" between polymer and turbulence.

(2) Macromolecular elongation as in the anisotropic viscosity explanation depends only upon the mean shear rate. One would expect, therefore, that, in the limit, this would

result in effectively laminar flow as all turbulent radial momentum transport was blocked by the elongated macromolecules. On the other hand, a visco-elastic mechanism would imply excitation of the macromolecules by the turbulence, which, in the limit, would result in a stand-off at some turbulent condition when the turbulence was reduced to the extent where it failed to excite the macromolecules. The limiting case obtained in practice, the maximum drag reduction asymptote of Section 6.6.4, is definitely not a laminar flow; this favours the latter viewpoint.

(3) The anomalous Pitot tube and hot film behaviour, Section 6.7, shows that the stagnation pressure and heat transfer in polymer solution follow other than Newtonian laws. In both these cases, the process of macromolecular extension appeared to be important. This is an elastic process, with a change in internal energy, which can be associated with visco-elasticity, whereas anisotropic viscosity depends only upon the ultimate mean elongation, independent of how it was attained. Also, the anomalous effects are so dramatic that, intuitively, they suggest a drastic difference from Newtonian, such as visco-elasticity, rather than one of degree involving different viscosity components, such as anisotropic viscosity.

(4) If radial momentum transport were, in fact, impeded,

as visualized in the anisotropic viscosity explanation, one would expect a change in the mixing length constant,  $A$ , of the law of the wall. But it was seen in Section 6.8.1 that the Newtonian law of the wall was obeyed in polymer solution; even when the "effective slip" model is not used, the mixing length constant was much the same as in solvent, Fig. 5.4.8. The equivalence of turbulence structure for the wall region,  $y^+ < 0.4$ , in polymer solution and Newtonian solvent at the same  $u_\tau$ , is in the same vein; since, in the anisotropic case, we would expect significant changes in the radial component,  $v'$ , compared to the axial,  $u'$ , and consequently in the structure.

#### 6.9.34 Summary

Because experimental measurements were not obtained in the region very close to the pipe wall, no conclusive distinction can be made between the anisotropic viscosity and visco-elastic type of explanations for the Toms Phenomenon. Circumstantial evidence from the present investigation, however, favours the visco-elastic viewpoint. In the unlikely event that an anisotropic viscosity type of mechanism is important near the wall, the turbulent flow structure in the central core of the pipe will, in any case, be influenced by the visco-elasticity of polymer solutions.

## 6.10 Prediction and Estimation of the Toms Phenomenon

In this section the analyses used in Part B, in which the Toms Phenomenon was related to the polymer causing it, are reversed.

It will be assumed that the following are known or can be obtained,

- (1) pipe inside diameter,  $D$  (assumed smooth),
- (2) solvent physical properties,  $\rho_s$ ,  $\eta_s$ , and
- (3) polymer conformation in solvent,  $[\eta]$  and  $R_G$ .

For convenience, double logarithmic coordinates of flow rate,  $Q$ , vs. wall shear stress,  $T_w$ , will be used, as in the preceding.

### 6.10.1 Gross Flow

The Toms Phenomenon flow diagram in the most general case will first be constructed using solvent physical properties. This will subsequently be modified for certain specific cases encountered in practice. All geometric references are to Fig. 6.10.1.

(1) The phenomenon will always be exhibited within three, polymer independent, bounding lines which are drawn in initially, viz.,

- (i) Poiseuille's law for laminar flow, AB
- (ii) Prandtl's (6.6.49), or Blasius' laws for turbulent flow, DG

(iii) The maximum drag reduction asymptote, (6.6.47 or 6.6.48), EH.

The point T on AB is the transition point,  $N_{Re} \approx 2100$ . Fully developed turbulent flow is assumed established at F on DG. The intersection of (ii) and (iii), E, will occur at  $N_{Re} \approx 500$  and will always be in a "virtual" region, lying to the left of the laminar line AB, which is never physically attained. All "virtual" regions on Fig. 6.10.1 are shown by broken lines.

(2) From the rms radius of gyration of polymer,  $R_G$ , using (6.6.6) and the onset constant  $C'$  from Table 6.6.1, the wall shear stress at the onset of drag reduction,  $T_w^*$  ( $= \rho u_\tau^{*2}$ ), can be predicted. Thus,

$$(2R_G)(u_\tau^*/\nu) = 0.015 \quad (6.10.1)$$

using consistent units or

$$T_w^* = 56 \times 10^{10} \rho (\nu/R_G)^2 \quad (6.10.2)$$

with  $T_w^*$  in dynes/cm<sup>2</sup>,  $R_G$  in Angstroms,  $\rho$  in gm/cm<sup>3</sup> and  $\nu$  in cm<sup>2</sup>/sec.

Corresponding to  $T_w^*$  on the solvent line is the Onset Point, O, with coordinates  $(Q^*, T_w^*)$ ; it will serve as an origin for further construction.

(3) Estimation of the extent of drag reduction requires

three relations, each of which depends upon polymer homologous series and pipe diameter in a manner as yet unknown. However, these relations are of the form of

(i) the universal drag reduction curve,

Fig. 6.6.6

(ii) equation (6.6.37) for the intrinsic function,  $\Psi$ , vs.  $[\eta]$  as in Fig. 6.6.9(a)

(iii) equation (6.6.39) for the polymer limited asymptotic slope,  $N_p$ , vs.  $[\eta]$  as in Fig. 6.6.9(b).

All of these must be ascertained experimentally.

(4) The polymer flow line that yields the maximum drag reduction, OL, is drawn through O with a slope,  $(d \ln T_w / d \ln Q)$ , of  $N_p$ . From (6.6.39), for high molecular weights in small pipes,  $N_p$  is essentially 1.0.

(5) The general point P,  $(Q, T_w)$ , on the flow line, OJ, for polymer concentration  $c$ , is obtained as follows, assuming that flow rate,  $Q$ , has been selected and the wall shear stress,  $T_w$ , is desired.

(i) The intrinsic drag reduction,  $[R]$ , at the flow rate  $Q$  is got from  $(Q/Q^*)$  and the  $\Psi$  got in step 3, by using (6.6.35).

$$[R] = \Psi \ln(Q/Q^*) \quad (6.6.35)$$

(ii) The characteristic concentration,  $[C]$ , is

$$[C] = R_{F, \max} / [R] \quad (6.6.41)$$

and  $R_{F,max}$  at flow rate  $Q$  is directly available from line  $OL$  drawn in step 4.

(iii) Now the universal drag reduction curve, such as Fig. 6.6.6, is entered at  $\gamma$ ,

$$\gamma = c / [C] , \quad (6.6.33)$$

and the corresponding ordinate,  $\delta$ , read. From this the specific drag reduction,  $R$ , at point  $P$  is

$$R = \delta [R] , \quad (6.6.33)$$

the fractional drag reduction,  $R_F$ , is

$$R_F = cR , \quad (6.6.28)$$

and so, if  $T_{WS}$  is the solvent wall shear stress at flow rate  $Q$ , point  $S$ , the wall shear stress,  $T_w$ , in polymer solution is

$$T_w = T_{WS} (1 - R_F) \quad (6.6.26)$$

which defines the point  $P$ .

(6) It is evident that  $P$  will always lie between the solvent line,  $OG$ , and the polymer limited line,  $OL$ . However, should the wall shear stress predicted put  $P$  above the maximum drag reduction asymptote,  $EH$ , then in practice

P will lie on the asymptote at the flow rate Q; i.e., if  $T_{w,Q} > T_w(EH)_Q$ , then  $T_{w,Q} = T_w(EH)_Q$ .

(7) The foregoing assumes that polymer solutions are so dilute that their viscosity is that of the solvent. So long as the solutions remain thermodynamically "dilute", the viscosity buildup with concentration can be accounted for quite precisely by referring all relations to the corresponding "Newtonian" solvent and redrawing the flow diagram accordingly. Redrawing can be avoided by employing the more general  $f^{-1/2}$  vs.  $N_{Re} f^{1/2}$  coordinates and using corresponding polymer parameter - drag reduction relations. When polymer concentration exceeds that for "diluteness", i.e., roughly when  $\eta_r > 2$ , the behaviour will be less well defined, and the general dilute solution rules above will progressively bread down.

(8) Finally, the paths followed by polymer solutions exhibiting the Toms Phenomenon are summarized, referring again to Fig. 6.10.1.

(1) The most general path is ATFOMH, with segments

AT	laminar flow
T	transition point, same $N_{Re}$ as solvent
TF	transition region
FO	fully developed turbulent flow without drag reduction



- O onset of drag reduction, predicted by Onset Hypothesis
- OM turbulent flow with drag reduction, controlled by polymer parameters - concentration, molecular weight, species - and pipe diameter
- MH turbulent flow along maximum drag reduction asymptote, independent of polymer parameters and pipe diameter

(ii) At very low concentrations,  $c \rightarrow 0$ , the line OJ tends to the solvent line, OG, and the limiting flow line at 0 concentration is, of course, AFTG. At high polymer concentrations,  $c \rightarrow \infty$ , OJ tends to OL, the limiting polymer flow line (point M tends to K) and the path is ATFOKH.

(iii) If the onset wall shear stress is less than that at transition, i.e., if the point O lies to the left of T, then transition will be delayed, say to T'. For further prediction, the point O will still serve as a "virtual" origin from which the polymer flow lines will appear to emanate. Also, drag reduction will occur immediately following the establishment of turbulent flow so point F, renamed F', will lie on the polymer flow line, OJ, rather than the solvent line, DG. The path followed is thus AT'F'MH.

(iv) If the point M is predicted to lie to the left of C, in a "virtual" region, then transition will be delayed to C and the maximum drag reduction asymptote followed immediately thereafter. In this case, path ACH, the polymer flow line cannot be traced back to the onset point, because, independent of polymer, the turbulent segment, CH, is the same.

Several examples of all these paths can be observed on flow diagrams of Section 5.3. Specific cases, derived, for convenience, from just 2 polymers, are listed on Table 6.10.1

Table 6.10.1  
Examples of Polymer Solution Flow Paths

Case	Path	Figure	Pipe	Polymer	c, ppm
(1)	ATFOP	5.3.11	0.292	N3000	500
	PMH	5.3.10			
(2)*	ATF	5.3.11	0.292	N3000	20
	FOKH	5.3.14	3.21	W301	500
(3)	AT'F'MH	5.3.10	0.292	N3000	1000
(4)	ACH	5.3.10	0.292	N3000	2000
		5.3.13	0.292	W301	20

\*The region ATF is not observed in the 3.21 cm pipe because the laminar regime lay at lower than experimental flow rates.

### 6.10.2 Flow Structure

Visualize operation at the point P ( $Q, T_w$ ), on Fig. 6.10.1 with the relaxation that P may lie anywhere so long as it is in the region of fully developed turbulent flow - FOMH. Drop a perpendicular through P which cuts the Newtonian solvent line at N, ( $Q_N, T_w$ ). The solvent point, N, may, equally, be calculated from  $T_w$  by Newtonian laws, e.g., (6.6.49).

#### 6.10.2! Mean Velocity Profiles

Let  $(V, \xi)$  be the mean velocity profile in the Newtonian solvent at point N which can be predicted by the usual laws (44), from  $u_\tau = (T_w/\rho)^{1/2}$ , viz.,

$$(V/u_\tau) = 2.44 \ln\left(\frac{1}{2} \int Du_\tau/\gamma\right) + 4.9, \text{ law of the wall}$$

$$(V_{CL}-V)/u_\tau = -2.44 \ln\left(\frac{1}{2} \int\right) + 0.8 + h\left(\frac{1}{2} \int\right), \text{ velocity defect law}$$

Also let the "effective slip" velocity,  $V_S$ , be

$$V_S = \sqrt{(Q - Q_N)/\pi D^2} \quad (6.10.3)$$

Now, if U be the mean velocity in polymer solution, then for all radial positions in excess of  $y^+$  (i.e.,  $\frac{1}{2} \int Du_\tau/\gamma \approx 50$ ), it will be given by

$$U = V + V_S \quad (6.8.2)$$

which is the required  $(U, \xi)$  profile. For  $y^+ < 50$ , the mean velocity profile cannot, as yet, be predicted.

Note that if P,  $(Q, T_w)$ , lies before the onset of drag reduction, i.e., on FO, then  $Q = Q_N$  so  $U = V$ , and a purely Newtonian profile is predicted.

#### 6.10.22 Turbulent Flow Structure

Turbulence measurements were made only at a single flow rate; strictly, therefore, a generalization cannot be made. One would strongly suspect, however, that if P lies before the onset of drag reduction, the turbulence structure would be that in the solvent. After the onset of drag reduction, within the bounds  $y^+ > 50$ ,  $\xi < 0.4$ , the structure is expected to be the same as in the Newtonian solvent at the point N,  $(Q_N, T_w)$ . In the central core,  $0.4 < \xi < 1.0$ , the structure will be different from Newtonian; the turbulent intensity,  $(u/u_r)$ , will be higher and the spectrum shape altered such that the inertial subrange of isotropic turbulence is absent. The extent of this difference cannot be predicted, but it is expected to increase with increasing drag reduction.

## 6.10.3 Illustrative Example

Given:

Pipe: 0.292 cm ID

Solvent: Distilled water at 25.0°C

Polymer: Polyethylene oxide, N750

$$[\eta] = 3.40 \text{ dl/gm}$$

$$R_G = 840 \text{ \AA}$$

To Predict:

- (1) The wall shear stress at the onset of drag reduction,  $T_w^*$  dynes/cm<sup>2</sup>.
- (2) At a flow rate,  $Q$ , of 30 cm<sup>3</sup>/sec (0.030 litres/sec):
  - (a) the maximum fractional drag reduction,  $R_{F,max}$ , possible with the given polymer
  - (b) the wall shear stress,  $T_{wp}$ , for a 100 ppm solution
  - (c) the maximum fractional drag reduction possible,  $R_{Fm}$ , with any polymer.

Solution:

- (1) From Onset Hypothesis

$$(2R_G)(u_\tau^*/\nu) = 0.015 \quad (6.10.1)$$

$$2R_G = 1680 \times 10^{-8} \text{ cm}$$

$$\nu = 0.00895 \text{ cm}^2/\text{sec}$$

so

$$u_\tau^* = (0.015)(0.00895)/(1680 \times 10^{-8})$$

$$= 7.99 \text{ cm/sec}$$

whence

$$T_w^* = \rho u_\tau^{*2} = (0.997)(7.99)^2$$

$$= 64 \text{ dynes/cm}^2 \quad \underline{\text{ANSWER}} .$$

(2) To predict the extent of drag reduction, we require the turbulent flow solvent line.

From Blasius,

$$f = 0.0791 N_{Re}^{-0.25} \quad (6.10.4)$$

which, for the given pipe and solvent, becomes

$$T_{ws} = 1.87 Q^{1.75} \quad (6.10.5)$$

with  $T_{ws}$  in dynes/cm<sup>2</sup> and  $Q$  in cm<sup>3</sup>/sec.

The best fit experimental solvent line (Fig. 5.3.3) was

$$T_{ws} = 1.63 Q^{1.77} \quad 6 < Q < 60 \text{ cm}^3/\text{sec} \quad (6.10.6)$$

(6.10.6) will be used in what follows; compared to (6.10.5) it yields about 5% lower values of  $T_{ws}$  at a given  $Q$ .

We can now define the following with reference to Fig. 6.10.1:

(i) the Onset point,  $O(Q^*, T_w^*) \equiv (7.95, 64)$  using  $T_w^*$  and (6.10.6)

(ii) the solvent point,  $S(Q, T_{ws}) \equiv (30, 676)$  using the given  $Q$  and (6.10.6)

(iii) the parameter  $(Q/Q^*) \equiv (30/7.95) \equiv 3.77$ .

(a) From Fig. 6.6.9(b), the slope of the polymer-limited asymptote is

$$N_p = 1 + (n_s - 1)(\exp(-0.65[\eta])) \quad (6.6.39)$$

so

$$\begin{aligned} N_p &= 1 + (1.77 - 1)\exp(-0.65)(3.40) \\ &= 1.085 \end{aligned}$$

Recall that

$$R_{F, \max} = (1 - (Q/Q^*)^{(N_p - n_s)}) \quad (6.6.41)$$

$$(N_p - n_s) = -0.685$$

$$(Q/Q^*) = 3.77$$

so

$$R_{F,\max} = 0.60 \quad \underline{\text{ANSWER}}$$

(b) It is given that

$$c = 100 \text{ ppm} = 0.01 \text{ gm/dl}$$

From Fig. 6.6.9(a), the intrinsic polymeric parameter is

$$\psi = 3.6[\eta]^3 = (3.6)(3.4)^3 = 141 \text{ dl/gm} \quad (6.6.37)$$

and

$$[R] = \psi \ln(Q/Q^*) = (141)(\ln(3.77)) = 187 \text{ dl/gm} \quad (6.6.35)$$

so

$$[C] = R_{F,\max}/[R] = (0.60)/(187) = 0.00321 \text{ gm/dl} \quad (6.6.41)$$

We now enter the universal drag reduction curve at

$$\gamma = c/[C] = (0.01)/(0.00321) = 3.12$$

where, from Fig. 6.6.6,

$$\delta = R/[R] = 0.205$$

so



$$R = (0.205)(187) = 38.3 \text{ dl/gm}$$

$$R_F = cR = (0.01)(38.3) = 0.38 \quad (6.6.28)$$

whence

$$T_{wp} = (1 - R_F)(T_{ws}) \quad (6.6.26)$$

$$= (1-0.38)(676) = 420 \text{ dynes/cm}^2 \quad \underline{\text{ANSWER}}$$

(c) The maximum drag reduction possible is limited by the maximum drag reduction asymptote, the power law form for which is

$$f = 0.42 N_{Re}^{-0.55} \quad 4000 < N_{Re} < 150,000 \quad (6.6.47)$$

which, for our pipe and solvent, becomes

$$T_{wm} = 1.56 Q^{1.45} \quad (6.10.7)$$

so, at  $Q = 30$ ,

$$T_{wm} = (1.56)(30)^{-0.55} = 217 \text{ dynes/cm}^2$$

and

$$R_{Fm} = (1 - (217/676)) = 0.68 \quad \underline{\text{ANSWER}}$$

Table 6.10.2 is a comparison between predicted and experimental values; the  $\pm 10\%$  agreement is typical, but

it will be noted that this is an "internal" test, the object of which is to illustrate the prediction methods rather than to test the accuracy of the correlations developed.

Table 6.10.2

Comparison of Predicted and Experimental Values

Case	Predicted	Exptl.	Figure	c
(1) $T_w^*$	64	$70 \pm 10$	5.3.8,9	All
(2) (a) $R_{F,max}$	0.60	0.54	5.3.8	2000
(b) $T_{wp}$	420	460	5.3.8	100
(c) $R_{Fm}$	0.68	0.67	5.3.13	5

Note:  $T_w$  in dynes/cm<sup>2</sup>

c in ppm

Exptl.  $R_{F,max}$  is quoted without correction for viscosity; corrected value ( $R_{FN}$ ) is 0.59.

## Chapter VII

## CONCLUSIONS

1. Dilute polymer solutions exhibiting the Toms Phenomenon in pipes follow, in general, four gross flow regimes:

- (i) Laminar flow
- (ii) Transition from laminar to turbulent flow
- (iii) Turbulent flow, without drag reduction
- (iv) Turbulent flow, with drag reduction.

2. For a certain polymer-solvent combination, the onset of drag reduction, separating regimes (iii) and (iv), occurs at a well-defined wall shear stress,  $\tau_w^*$ , independent of pipe diameter and polymer concentration.

3. The onset wall shear stress,  $\tau_w^*$ , is related to the effective, random coiling, diameter of the macromolecule,  $D_M (= 2R_G)$ , by the Onset Hypothesis, Section 6.6.21. The engineering form of the Onset Hypothesis is

$$(2R_G)(\tau_w^*/\rho)^{1/2}/\gamma = C' ,$$

where the best value of the constant  $C'$  is  $0.015 \pm 0.005$ .

4. Physical interpretation of the onset constant,  $C (= KC')$ , see Section 6.6.2), as a ratio of macromolecular to dissipative eddy size, is as yet uncertain.

5. In all cases, Poiseuille's law is obeyed in laminar flow, (i). Irrespective of wall shear stress, drag reduction is never observed in the laminar regime.
6. In general, the critical Reynolds number for transition,  $N_{Re,T}$ , is the same as in solvent. Transition is delayed only when the wall shear stress,  $T_{w,T}$ , corresponding to  $N_{Re,T}$  exceeds the onset wall shear stress,  $T_w^*$ .
7. In region (iii), turbulent flow without drag reduction, polymer solutions obey the usual Newtonian laws. This region is masked when  $T_w^* < T_{w,T}$ , in which case transition is delayed and drag reduction obtained as soon as turbulent flow is established.
8. The extent of drag reduction in region (iv), characteristic of the Toms Phenomenon, depends upon
- (a) flow rate
  - (b) polymer concentration
  - (c) polymer molecular weight
  - (d) pipe diameter .
9. In region (iv), for a given polymer and pipe, polymer solution flow lines diverge progressively from the solvent line as concentration is increased until, at relatively high concentrations, an asymptotic limiting scope,  $N_p$ , is attained.  $N_p$  is characteristic of the polymer. Accordingly, at a given flow rate,  $Q$ , the fractional drag reduction,  $R_p$ ,

increases with concentration initially but ultimately asymptotes to a constant, maximum value,  $R_{F,max}$ , independent of concentration.

10. For a given polymer and flow rate, the specific drag reduction,  $R = R_F/c$ , decreases with increasing concentration according to a curve bounded by two asymptotes:

$$R = [R] , \quad c \rightarrow 0 ,$$

$$R = R_{F,max}/c , \quad c \rightarrow \infty .$$

At low concentrations,  $R$  tends to a constant, maximum value,  $[R]$ , termed the intrinsic drag reduction; at high concentrations,  $R$  varies inversely with concentration corresponding to the maximum fractional drag reduction,  $R_{F,max}$ , being attained. The intersection of the two asymptotes defines two characteristic drag reduction parameters,  $[R]$  and  $[C]$ .

11. For a given polymer homologous series - solvent combination in a given pipe, irrespective of flow rate and molecular weight, specific drag reduction versus concentration curves superpose onto a single, universal curve when the ordinates,  $R$  and  $c$ , are normalized by their respective characteristic parameters,  $[R]$  and  $[C]$ .

12.  $[R]$  and  $[C]$  are uniquely related to each other.  $[R]$ ,

for example, can be decomposed into the product of a flow rate term,  $(\ln(Q/Q^*))$ , which expresses the "distance" beyond the onset point, and an intrinsic polymeric term,  $\Psi$ , independent of flow rate.  $\Psi$  correlates well with polymer intrinsic viscosity,  $[\eta]$ ; from the present data, a relation of the form

$$\Psi = A' [\eta]^3$$

is obtained, where  $A'$  (and, possibly, the exponent 3) depends on pipe diameter and homologous series.

13. The maximum drag reduction that can be achieved is limited by two asymptotes:

(a) a polymer dependent asymptote, slope  $N_p$ , noted in conclusion 9 above, and

(b) a universal, maximum drag reduction asymptote, slope  $N_m$ , which is independent of polymer and pipe.

14.  $N_p$  correlates well with polymer intrinsic viscosity,  $[\eta]$ ; from the present data a relation of the form

$$\ln((N_p - 1)/(n_s - 1)) = A[\eta]$$

is obtained, where  $A$  depends upon pipe diameter and homologous series. For high molecular weights,  $N_p$  approaches unity; for low molecular weights,  $N_p$  tends towards the solvent slope,  $n_s$ .

15. The universal maximum drag reduction asymptote, slope  $Nm \approx 3/2$ , is defined by a unique friction factor vs. Reynolds number relation, analogous to but different from, Newtonian friction factor relations in turbulent flow. For comparison, these are

(a) power law forms

$$f = 0.08 N_{Re}^{-0.25} \quad - \quad \text{Newtonian (Blasius)}$$

$$f = 0.42 N_{Re}^{-0.55} \quad - \quad \text{Asymptote}$$

(b)  $f^{-\frac{1}{2}}$  vs.  $N_{Re} f^{\frac{1}{2}}$  forms

$$f^{-\frac{1}{2}} = 4.0 \text{Log}_{10}(N_{Re} f^{\frac{1}{2}}) - 0.4 \quad - \quad \text{Newtonian (Prandtl)}$$

$$f^{-\frac{1}{2}} = 23 \text{Log}_{10}(N_{Re} f^{\frac{1}{2}}) - 43 \quad - \quad \text{Asymptote}$$

This asymptote supercedes, and is followed by, all polymer flow lines after their intersection with it.

16. At flow rates corresponding to equal solvent wall shear stress,  $T_{ws}$ ,

(a) the fractional drag reduction,  $R_F$ , induced by a given polymer concentration,  $c$ , decreases with increasing pipe diameter, but

(b) the maximum drag reduction possible, given by the maximum drag reduction asymptote, increases with increasing pipe diameter.

17. So long as the polymer solutions remain thermodynamically dilute, the effect of polymer solution viscosity buildup with concentration can be accounted for in all gross flow relations by reference to the "Newtonian" instead of the actual solvent. The "Newtonian" solvent has the same viscosity as the polymer solution in question, but obeys Newtonian flow relations.

18. In fully developed turbulent flow, regions (iii) and (iv), mean velocity profiles in polymer solutions exhibiting the Toms Phenomenon obey the "effective slip" model. By this, for  $y^+ > 50$ , the velocity profile,  $(U, \xi)$ , at any operating point,  $(Q, T_w)$ , is composed of two additive portions:

(a) The velocity profile,  $(V, \xi)$ , which would exist in the Newtonian solvent at the same  $u_\tau (= (T_w/\rho)^{1/2})$ . This is available from the usual Newtonian laws; see, e.g., Hinze (44).

(b) The constant, "effective slip" velocity,  $V_S$ , at which the Newtonian portion, (a), is convected along to make up the difference between the actual flow rate,  $Q$ , and that  $Q_N$ , which would prevail in the Newtonian solvent at the same  $u_\tau$  ( $Q_N$  is, of course, the flow rate resulting from integrating the profile in (a) above and, as such, directly available from Newtonian friction factor relations).

Thus, at any radial position,  $\xi$ , the velocity,  $U$ , is



$$U = V + V_S, \quad y^+ > 50$$

If the operating point is prior to the onset of drag reduction,  $V_S = 0$  and  $U \equiv V$  so a purely Newtonian profile will prevail.

19. Obedience of the effective slip model indicates that the most significant differences between drag reducing, Toms Phenomenon, flows and Newtonian flows are confined to a region  $y^+ < 50$ , very close to the pipe wall. From Laufer (43), this is also the region most important from an energy viewpoint.

20. In region (iv) of conclusion 1, axial rms turbulent intensity profiles  $(u/u_\tau)$  vs.  $\xi$ , in polymer solution are the same as in solvent for the region towards the wall,  $0.05 < \xi < 0.40$ , but in the central core,  $0.4 < \xi < 1.0$ , the intensity is higher than in solvent, the difference being greatest on the axis,  $\xi = 1.0$ . The profiles show a curious plateau, with constant  $(u/u_\tau)$ , for  $0.4 < \xi < 0.7$ .

21. Also, in region (iv), axial one-dimensional turbulent energy spectra are essentially Newtonian in the wall region,  $\xi = 0.033$  ( $y^+ \cong 100$ ), but strikingly different on the pipe axis,  $\xi = 1.00$ . In the latter case, the inertial subrange is entirely absent and the dissipation,

$$\int_0^{\infty} k_1^2 E_1(k_1) dk_1, \text{ considerably lower than Newtonian.}$$

22. In the "wall" region,  $y^+ > 50$ ,  $\xi < 0.4$ , turbulence structure, measured by the axial intensity,  $(u/u_\tau)$ , the turbulent shear stress,  $\overline{\rho u'v'}$ , and axial turbulent energy spectra, is the same as in Newtonian solvent at equal  $u_\tau$ .

23. On the pipe axis, the turbulence structure is markedly different from Newtonian, but, because this region is little influenced by wall processes, this could be for reasons not directly connected with those causing the Toms Phenomenon.

24. Since essentially isotropic conditions prevail on the pipe axis, the absence of the inertial subrange in the turbulent energy spectrum indicates a stronger "coupling" of energetic and dissipative wave numbers in polymer solution - due, almost certainly, to visco-elasticity.

25. Of the four types of explanations proposed for the Toms Phenomenon, viz.,

- (a) delayed laminar to turbulent transition
- (b) "effective" slip
- (c) anisotropic viscosity
- (d) visco-elasticity

(a) is definitely not valid; (b) is an adequate engineering concept but, since an actual slip is unlikely, is encompassed within the remaining two, (c) and (d). Because measurements were not made in the region extremely close

to the pipe wall, no definite distinction can be made between (c) and (d). But circumstantial evidence derived from this work favours the visco-elastic type of explanation, (d), over the anisotropic viscosity type, (c).

26. In polymer solution, the stagnation pressure attained on the face of a Pitot tube is a function of

- (a) the absolute, free stream, velocity
- (b) Pitot tube diameter
- (c) polymer molecular weight
- (d) polymer concentration.

Thus the apparent velocity, obtained directly from the indicated stagnation pressure, differs from the true velocity: the difference or "discrepancy" increases with increasing absolute velocity, molecular weight and concentration and with decreasing Pitot tube diameter. The discrepancy can qualitatively be accounted for by an energy argument (Section 6.7.1) based on macromolecular elongation by the rate of strain at the stagnation point.

27. In polymer solution, heat transfer from cylinders in cross flow is a function of

- (a) the absolute, free stream velocity
- (b) cylinder diameter
- (c) polymer molecular weight
- (d) polymer concentration
- (e) ambient, free stream, strain rate .

The ratio of heat transfer coefficients in polymer solution and solvent,  $(h_p/h_s)$ , behaves as follows with increasing cylinder Reynolds number,  $N_{Re,d}$ :

$N_{Re,d} < 40$ , the ratio is essentially unity,

$40 < N_{Re,d} < 300$ , the ratio decreases sharply to a minimum of about 0.3 before increasing back up to about unity,

$N_{Re,d} > 300$ , the ratio drops abruptly to about  $1/3$  and remains thereabouts, increasing only slowly with  $N_{Re,d}$ .

At the higher Reynolds numbers, where the two latter regimes overlap,  $250 < N_{Re,D} < 350$ , the heat transfer is unstable, and the heat transfer coefficient may fluctuate between values differing by threefold. Heat transfer improves with polymer degradation, i.e., with decreasing molecular weight, and with increasing ambient strain rate.

## Chapter VIII

## RECOMMENDATIONS

1. Experimental measurements in the immediate vicinity of the pipe wall,  $0 < y^+ < 50$ , would be of extreme interest in differentiating between flows exhibiting the Toms Phenomenon and Newtonian flows. Quoting Laufer (43), "This is, of course, a very difficult experimental task."

2. All gross flow relations developed would benefit from further experiments with other, well-characterized, polymer homologous series - solvent combinations and pipe diameters. Specifically, this includes the testing of

(a) the Onset Hypothesis

(b) the universal specific drag reduction curve

(c) the correlation of basic extent of drag

reduction parameters,  $\psi$  and  $N_p$ , with polymer intrinsic viscosity.

(d) the maximum drag reduction asymptote.

Such a series of experiments would also indicate the influence of polymer structure (configuration) and deployment in solvent (conformation) in causing the Toms Phenomenon.

3. The physical significance of (a) to (d) above should be explored. A promising approach to this appears via an analytical analysis using idealized visco-elastic

constitutive equations, modelled, possibly, after the initial work of Boggs and Thompsen (31). Of particular interest would be an analysis of the response of a macromolecule in solution to a strained turbulent flow field.

4. A systematic study of the Pitot tube "discrepancy" in polymer solutions would be very useful in two respects:

- (a) in itself, as a previously unknown phenomenon and
- (b) with a view to future use of Pitot tubes in polymer solution.

Such a study might best be conducted with spherical nosed Pitot tubes having central pinholes over which stagnation pressure is measured. Operation in both laminar and turbulent flow would ascertain the importance of time - varying velocity and strain rate.

5. Similar to 4, a study of heat transfer in polymer solutions would be very interesting, specifically the heat transfer:

- (a) in pipe flows, exhibiting the Toms Phenomenon and
  - (b) from cylinders in cross flow.
- (a) Since pipe flow friction is all "skin" friction, the observed reduction in turbulent momentum transfer should, by analogy, lead to similar reductions in heat transfer to polymer solutions.

(b) This is of interest for future hot wire type of work and, more importantly, because the flow around cylinders appears to be significantly altered in polymer solution - notably the eddy shedding process.

**FIGURES**

Pp. 281 - 345 Figures for Text

Pp. 346 - 356 Figures for Appendices



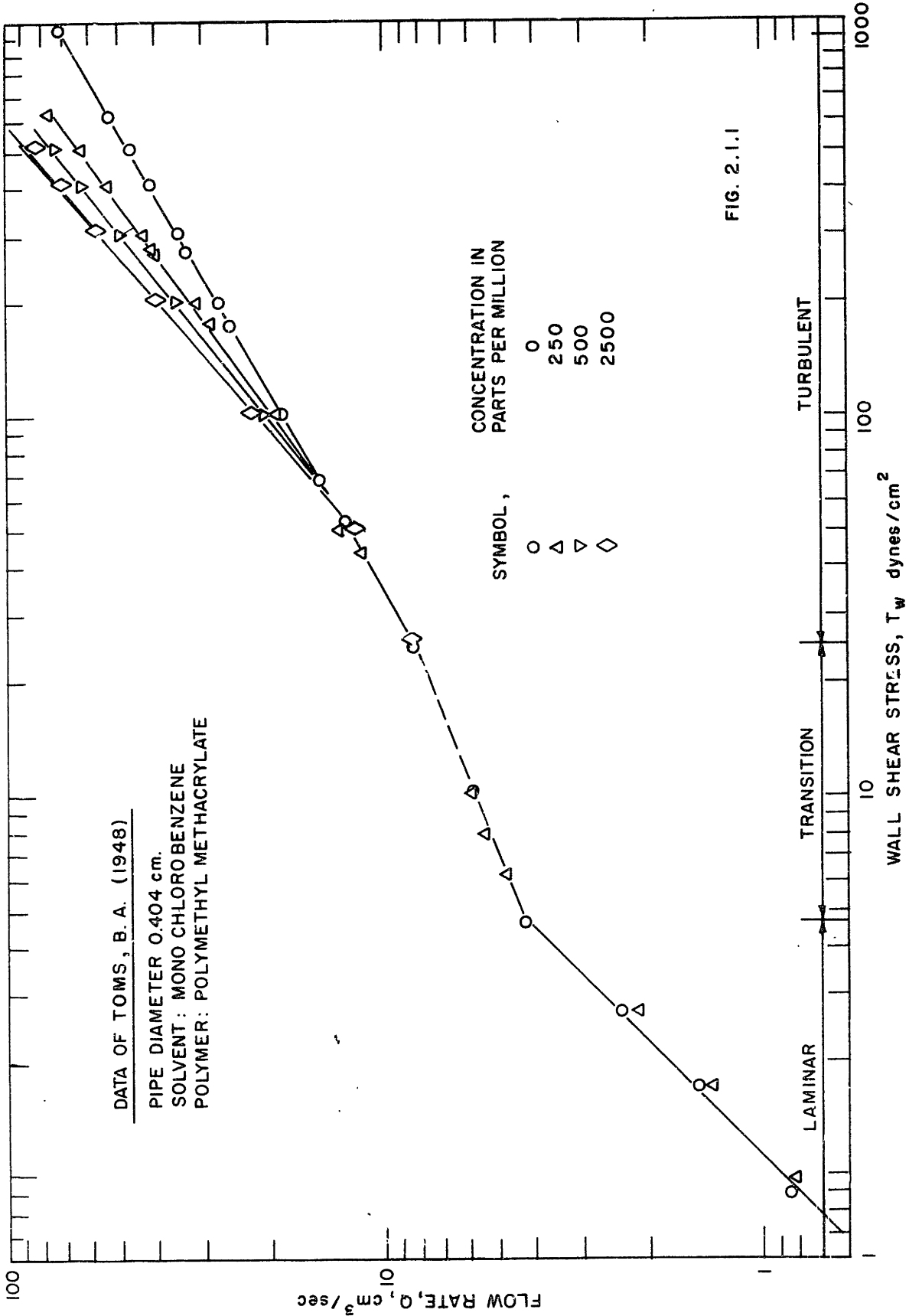


FIG. 2.1.1

0.292 cm SYSTEM SCHEMATIC

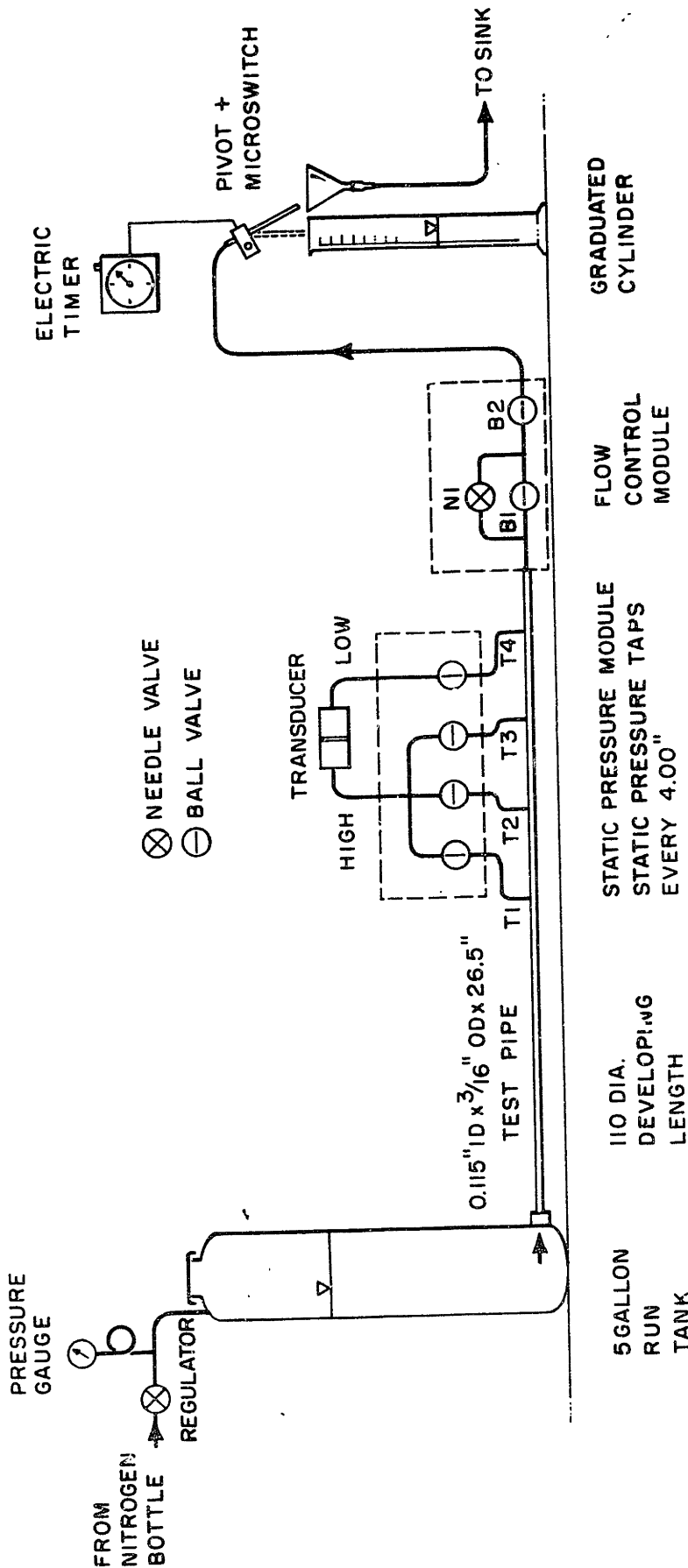
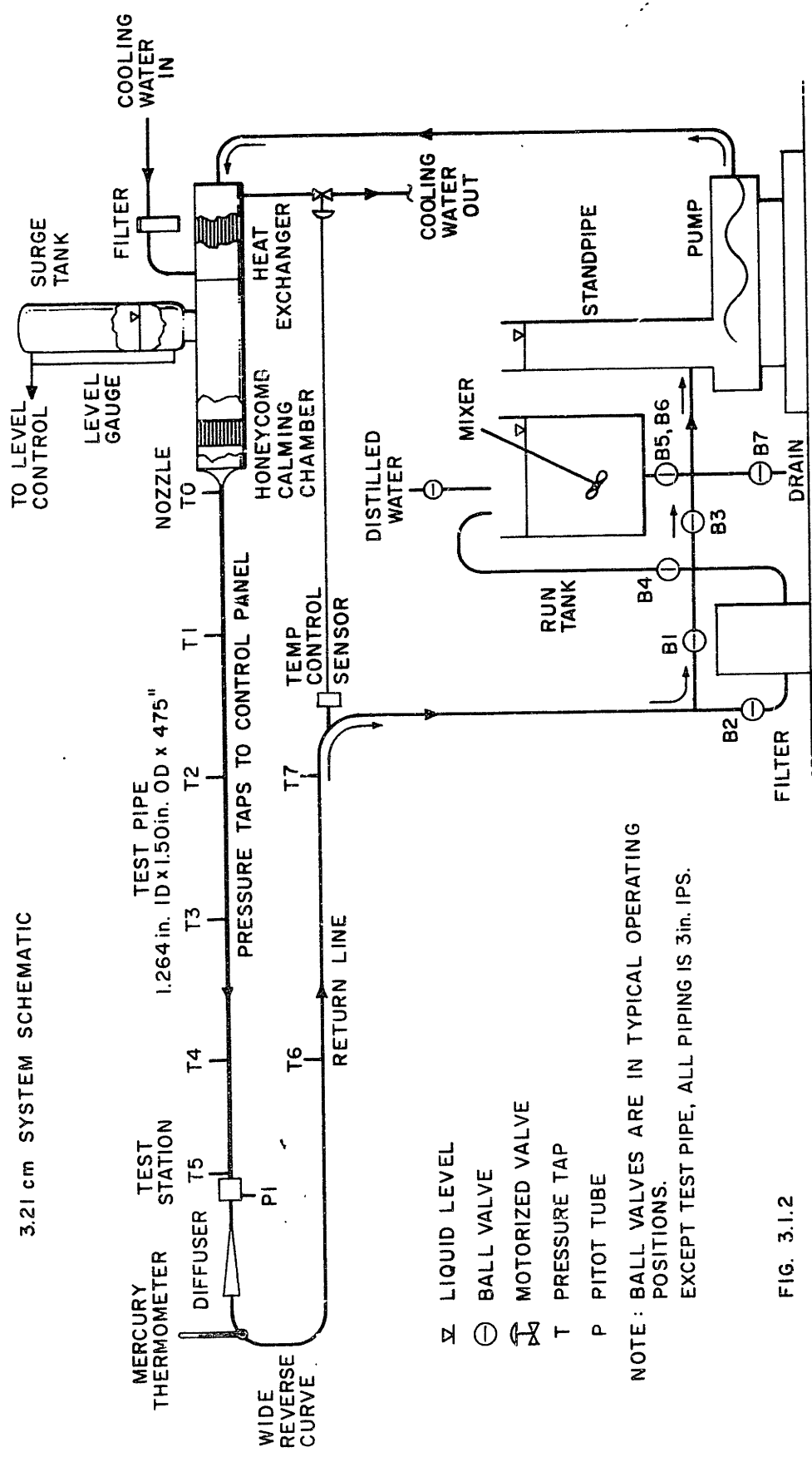


FIG. 3.1.1

3.21 cm SYSTEM SCHEMATIC



- ∇ LIQUID LEVEL
- ⊖ BALL VALVE
- ⊕ MOTORIZED VALVE
- T PRESSURE TAP
- P PITOT TUBE

NOTE: BALL VALVES ARE IN TYPICAL OPERATING POSITIONS.  
EXCEPT TEST PIPE, ALL PIPING IS 3 in. IPS.

FIG. 3.1.2

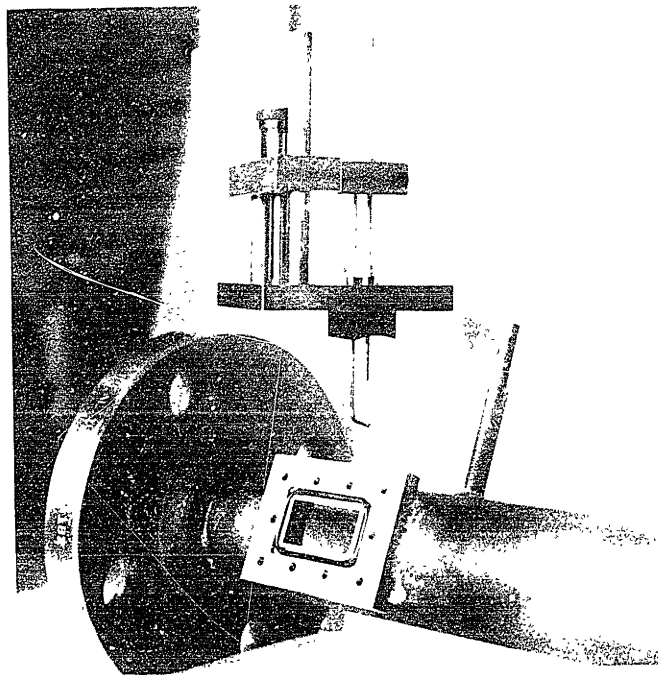
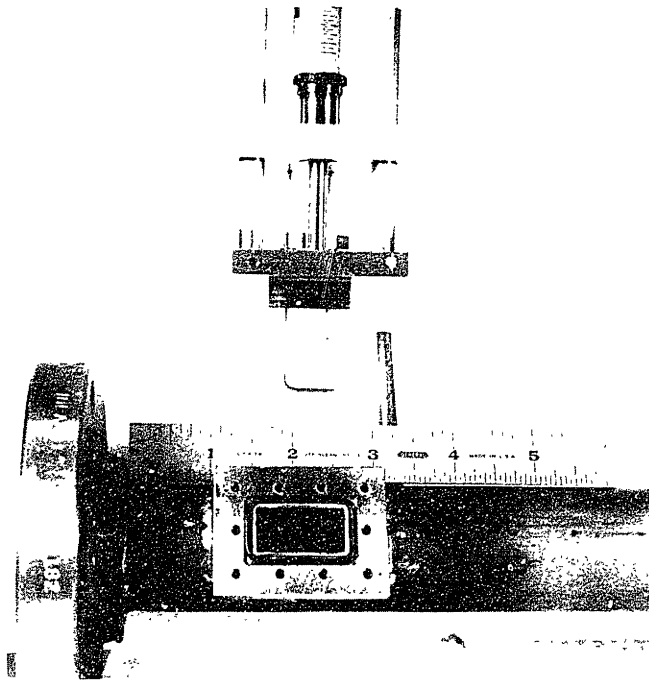
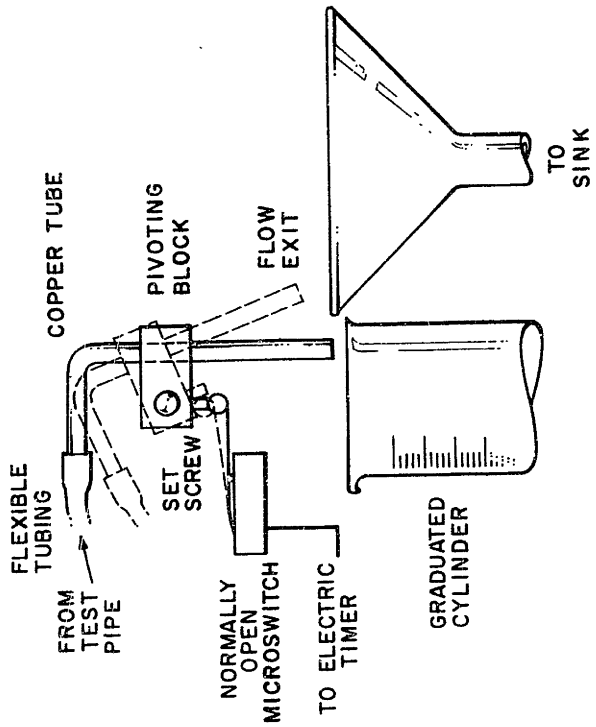
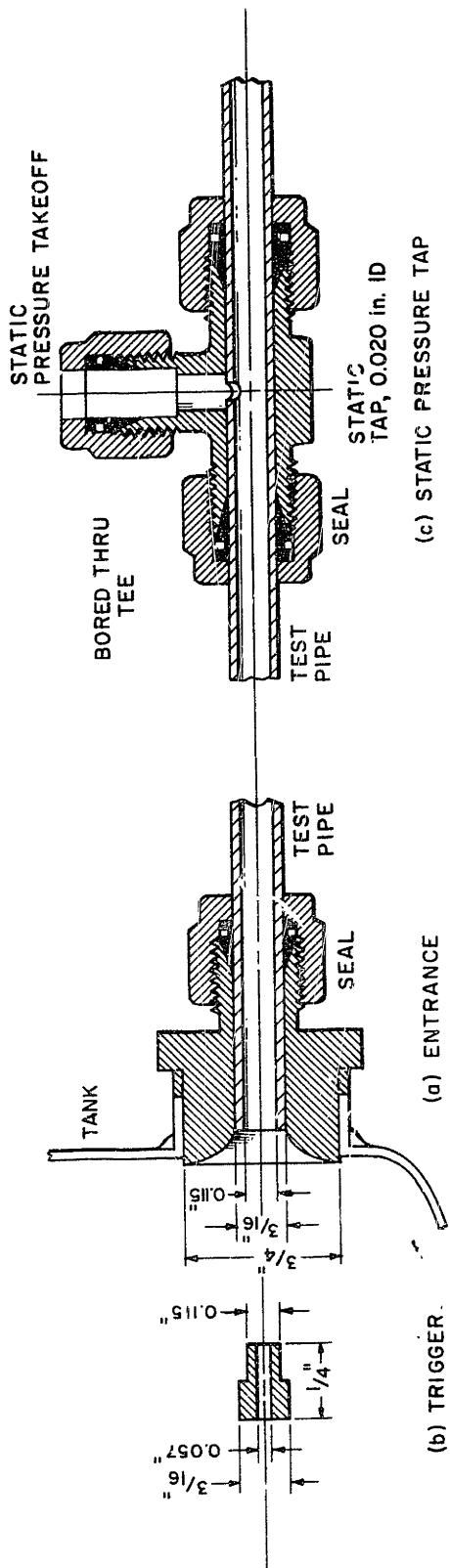
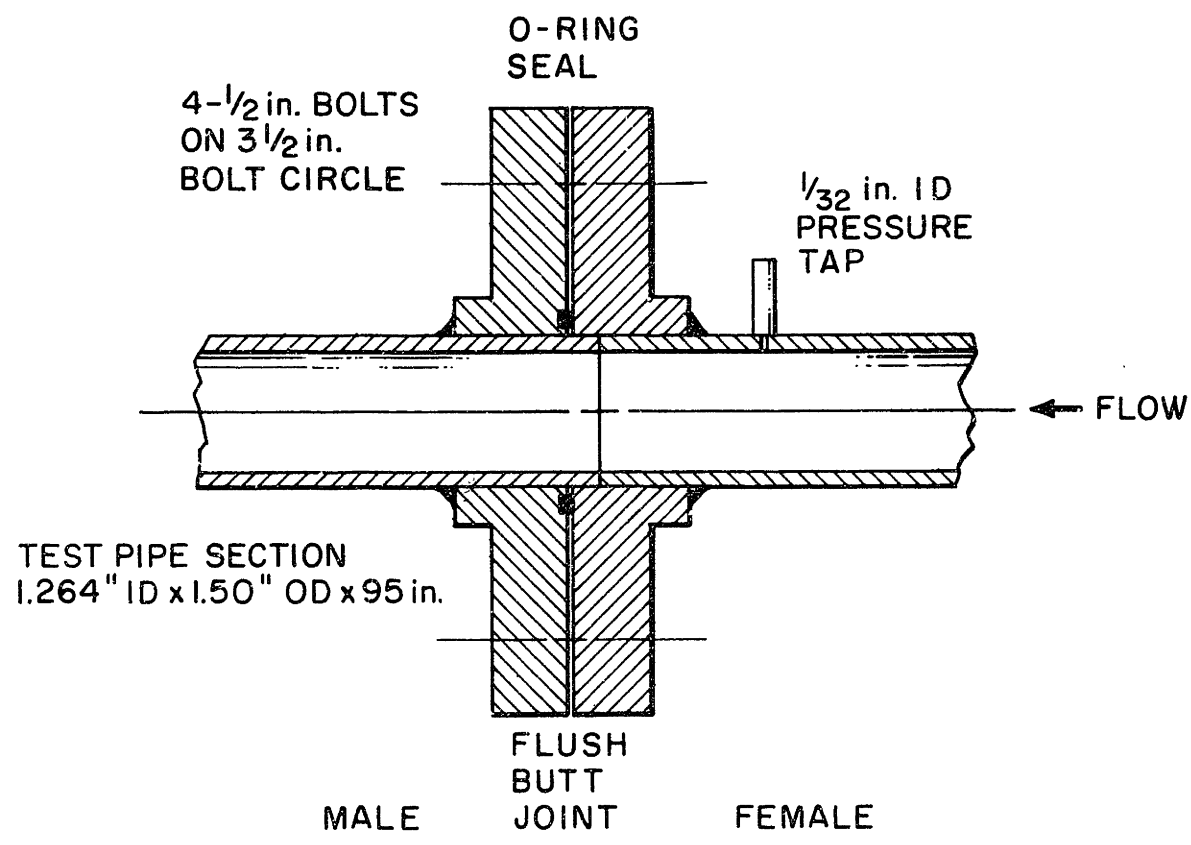


Fig. 3.1.3 Micrometer Traverse



(d) FLOWMETER

FIG. 3.31  
0.292 cm SYSTEM DETAILS



TEST SECTION JOINT

FIG. 3.4.1 (a)

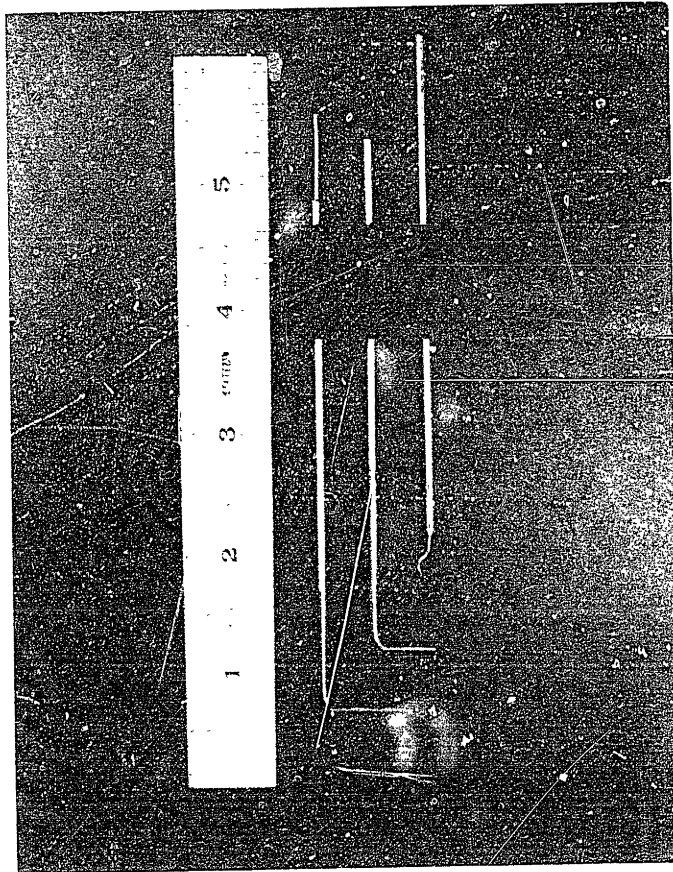
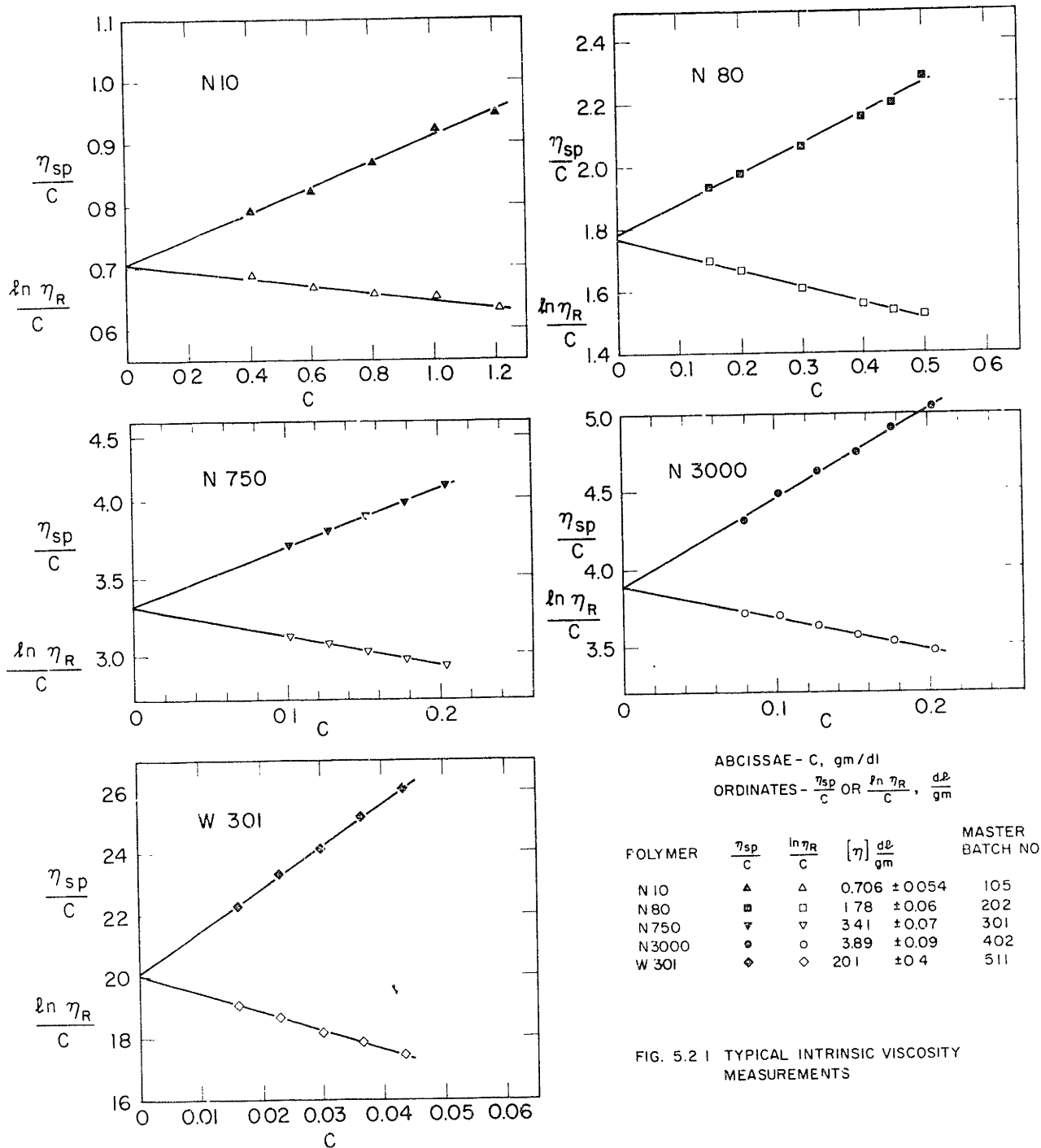


Fig. 3.4.1(b) Probes





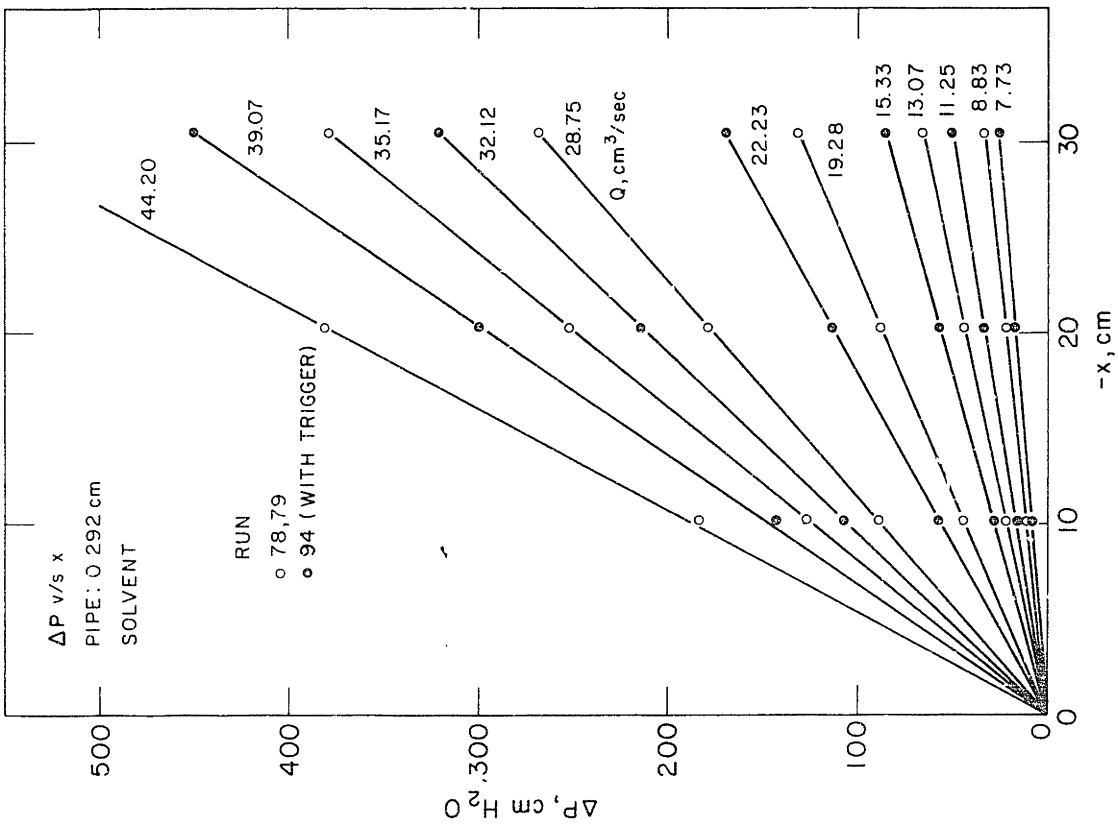
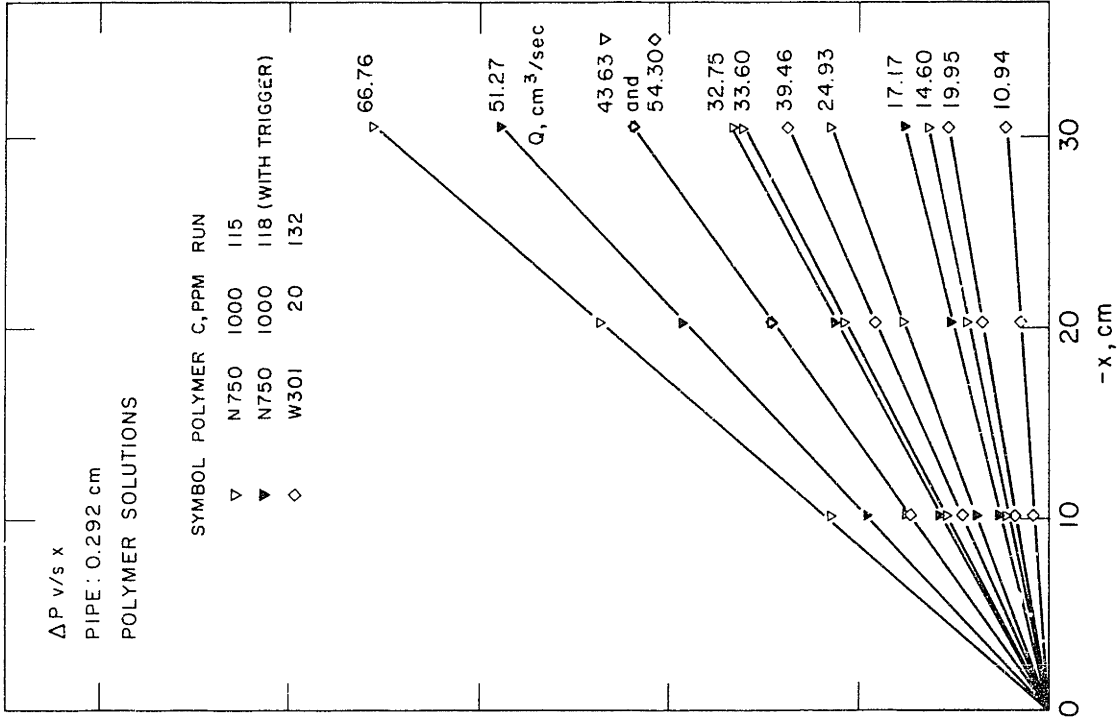


FIG. 5.3.1

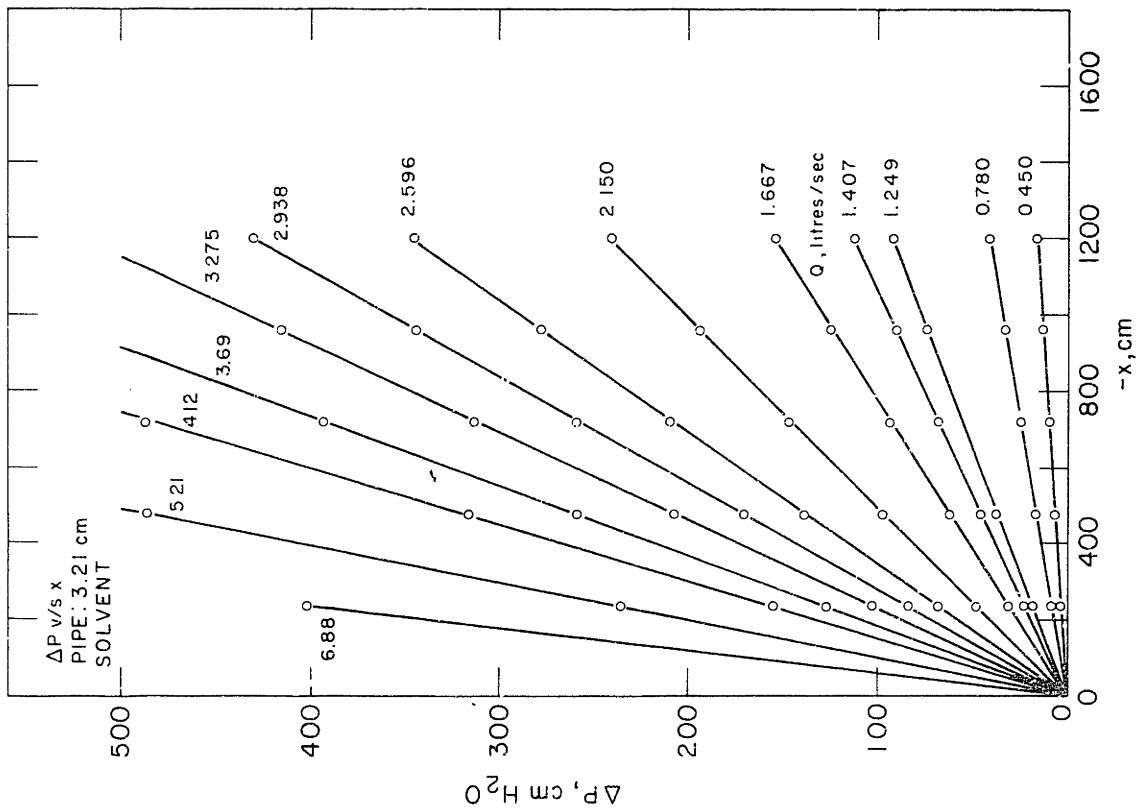
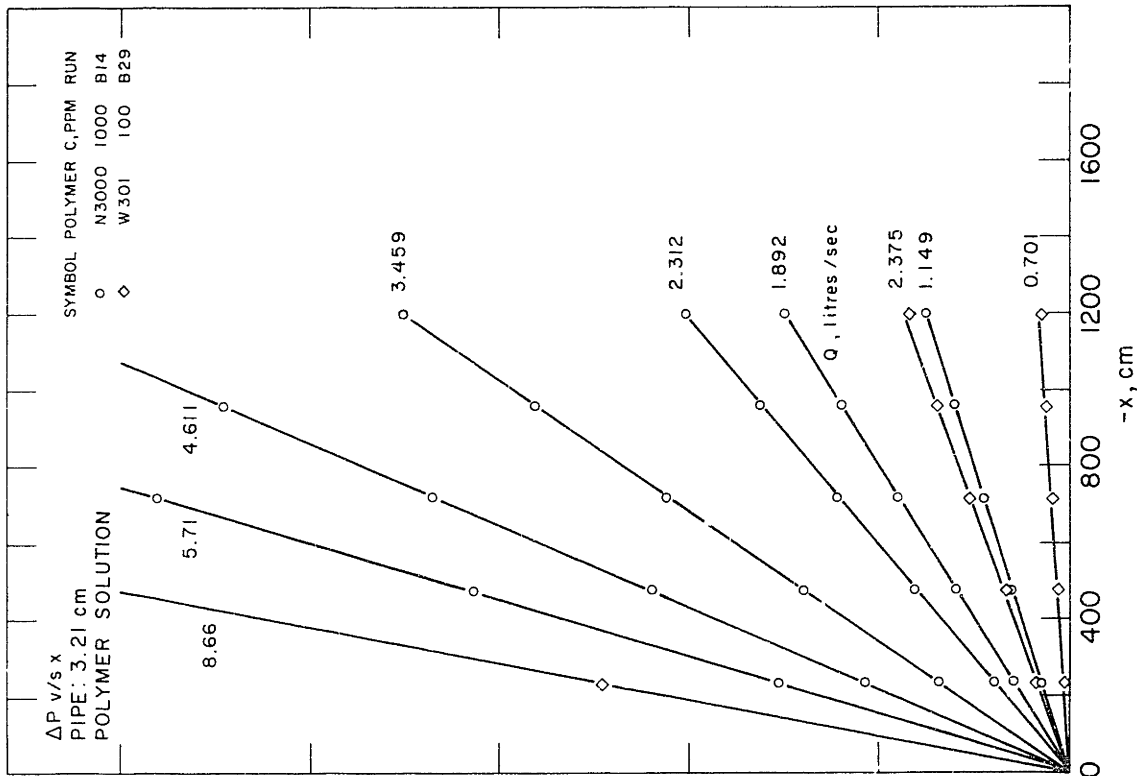


FIG. 5.3.2

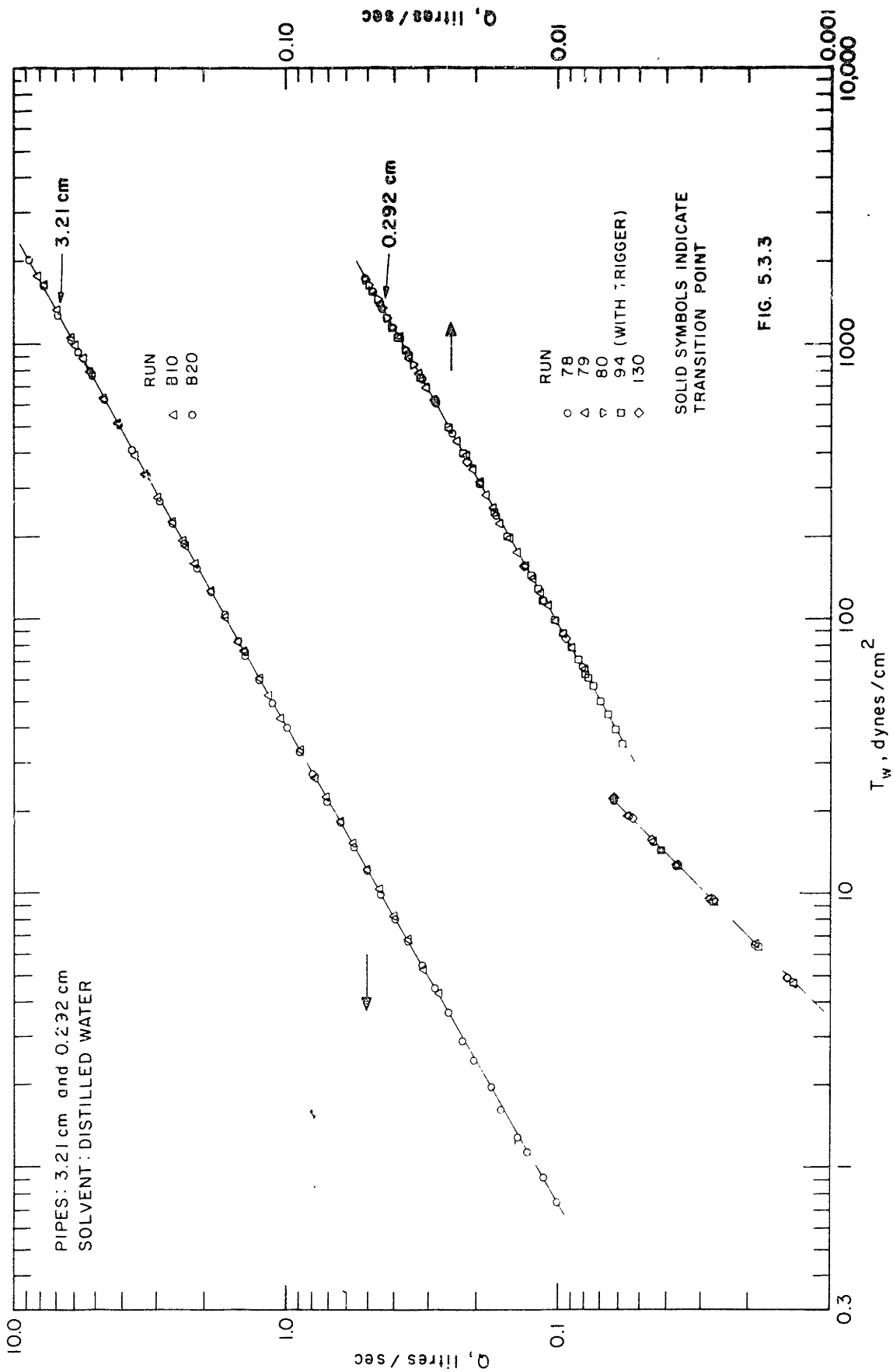
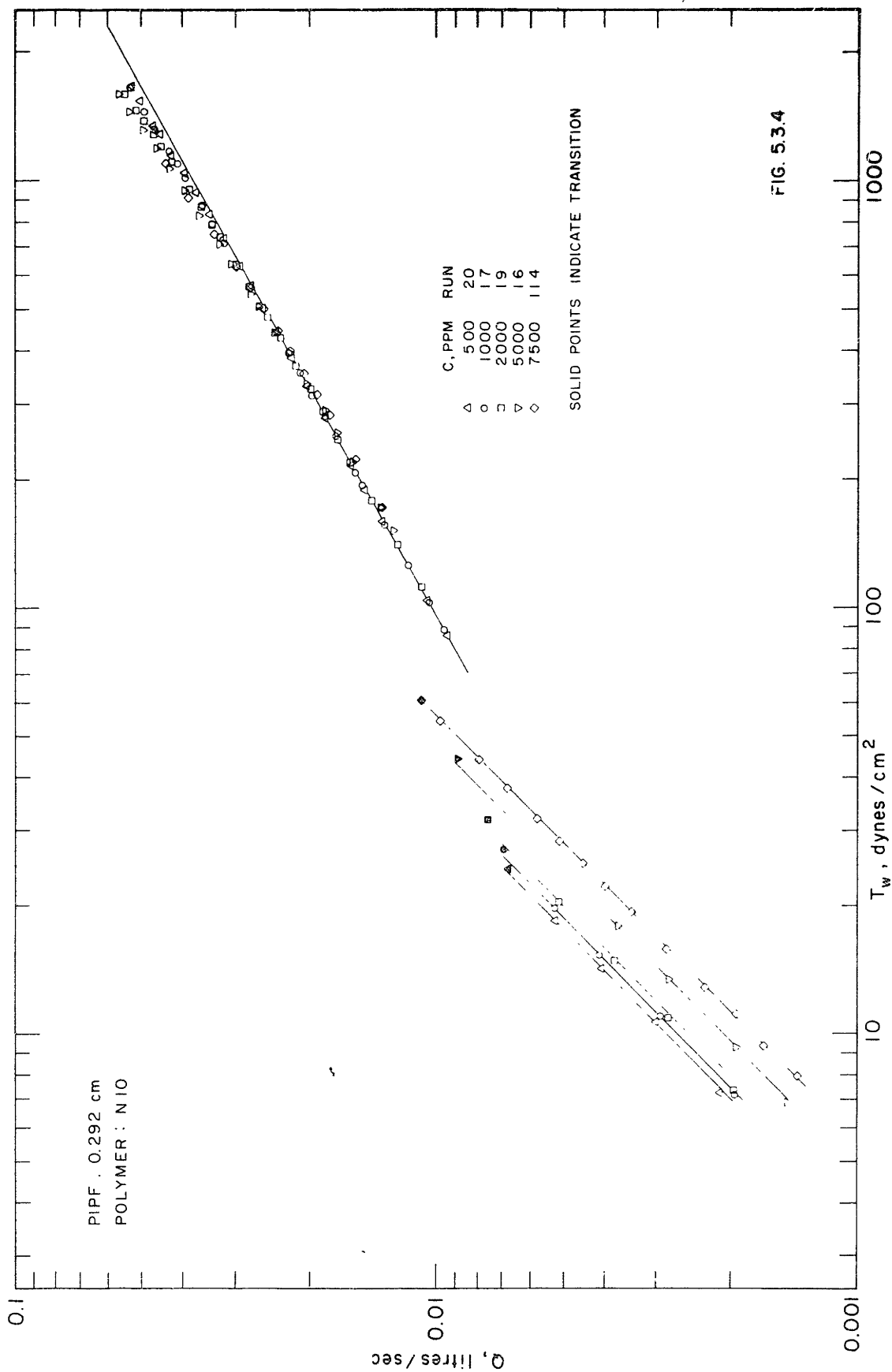


FIG. 5.3.3



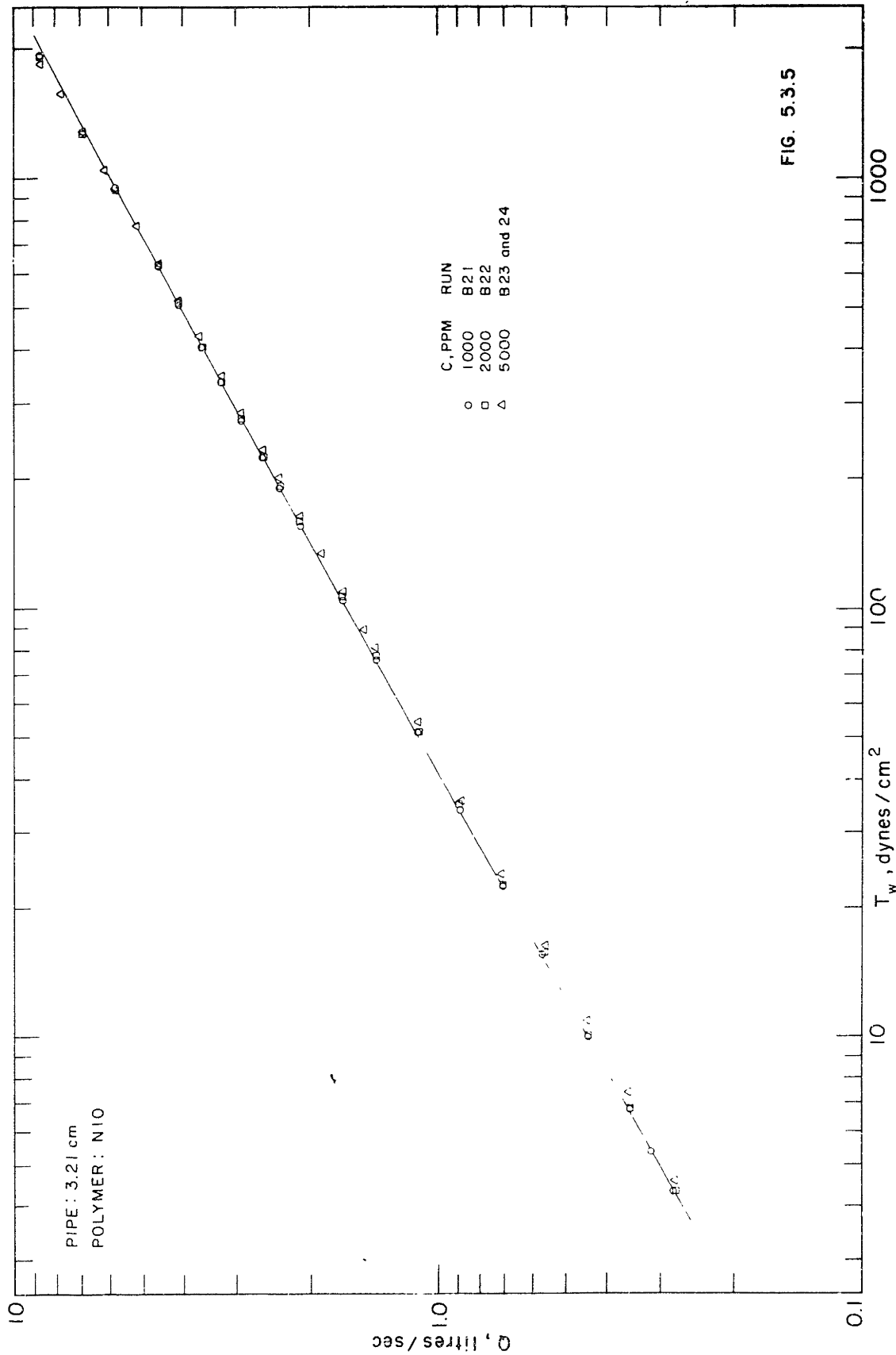
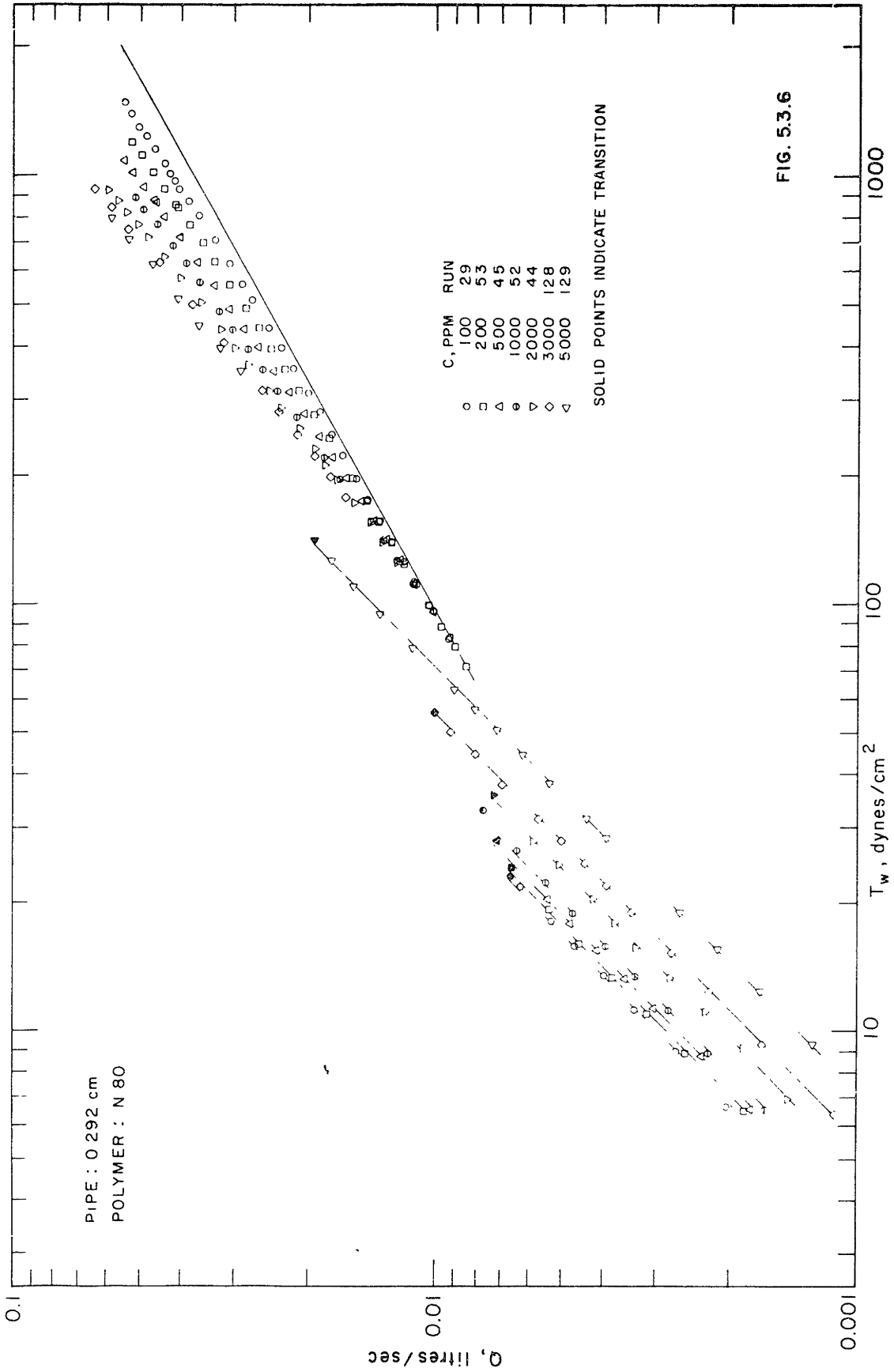
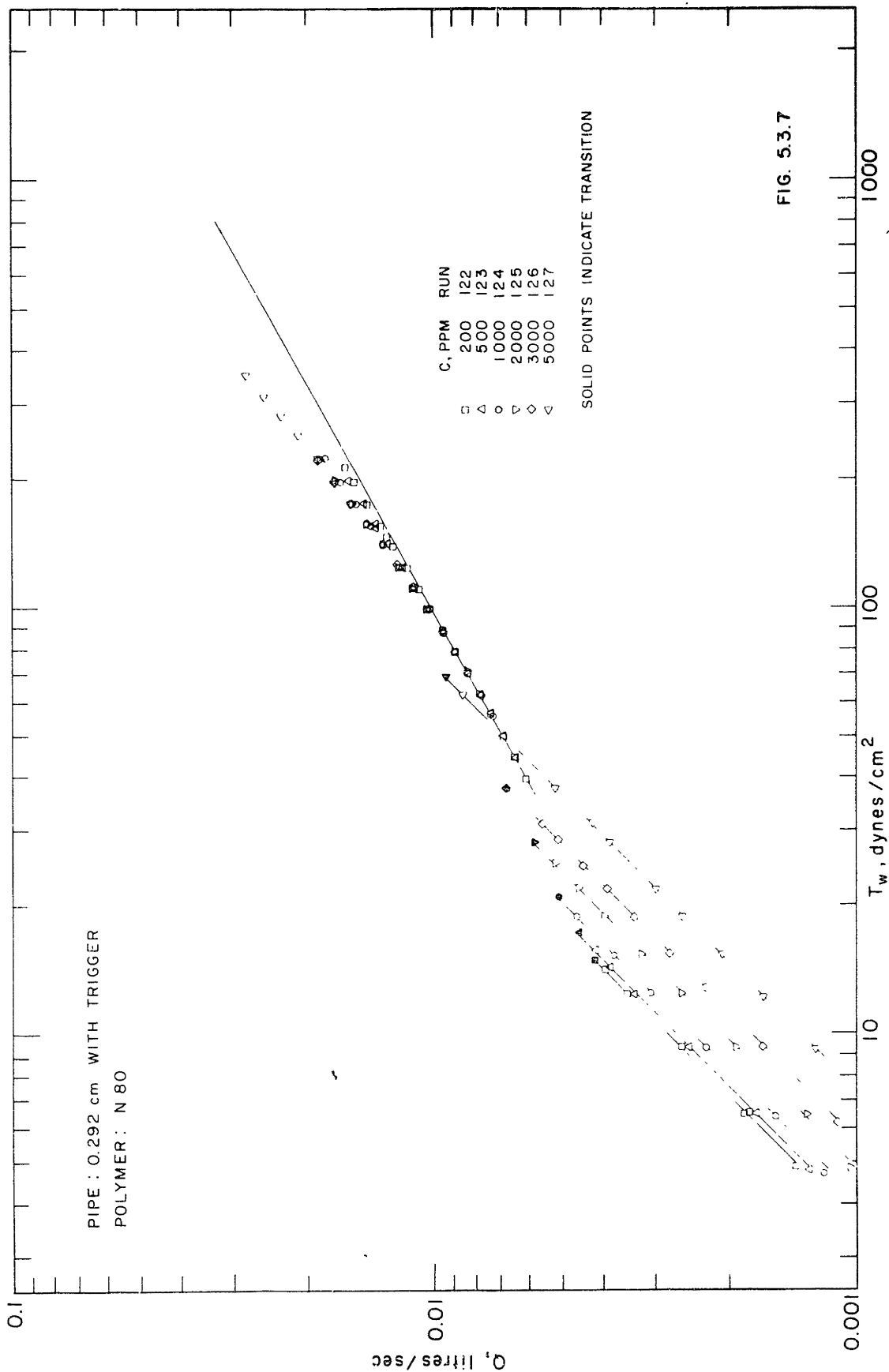


FIG. 5.3.5





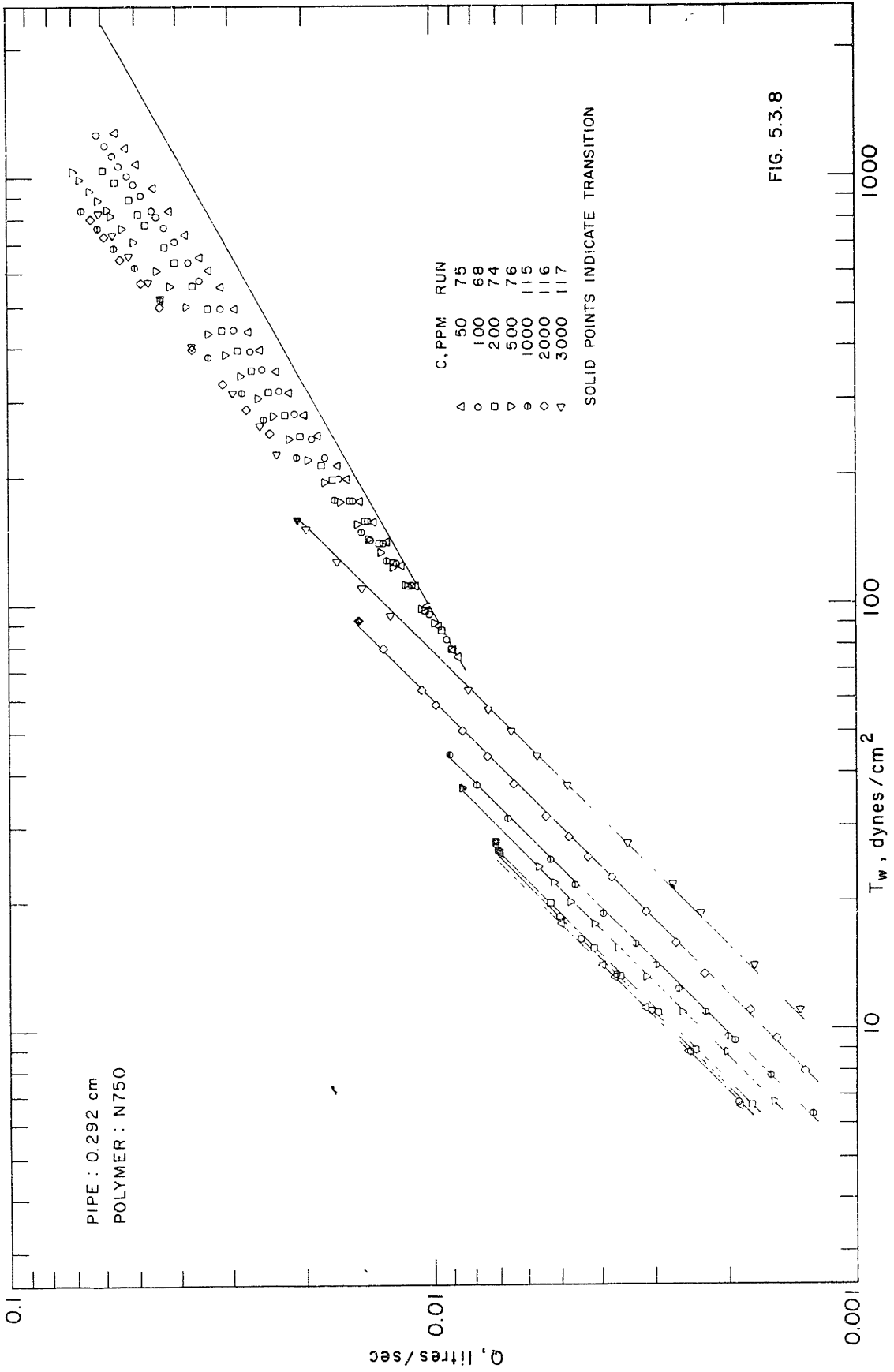


FIG. 5.3.8



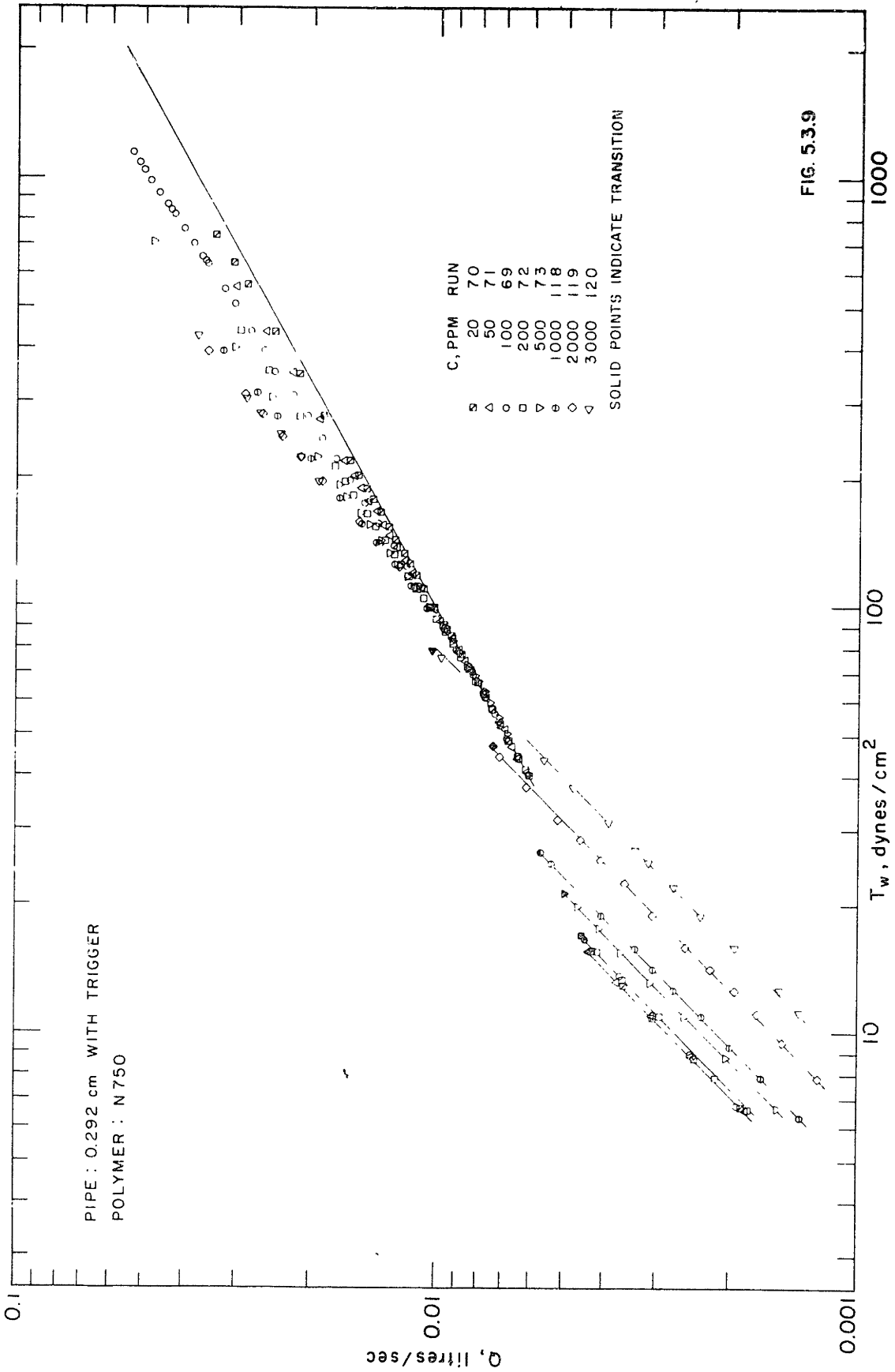


FIG. 5.3.9

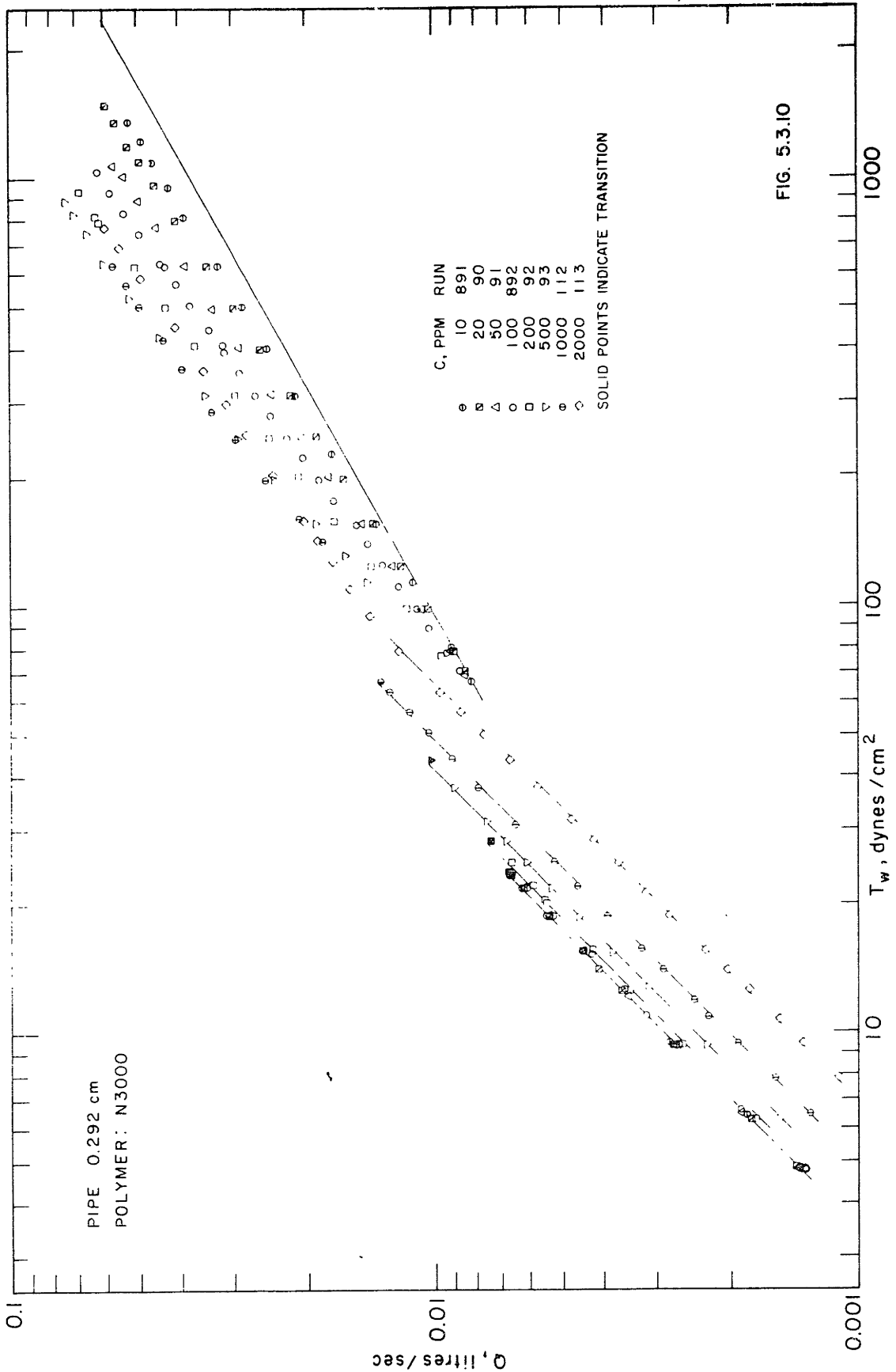
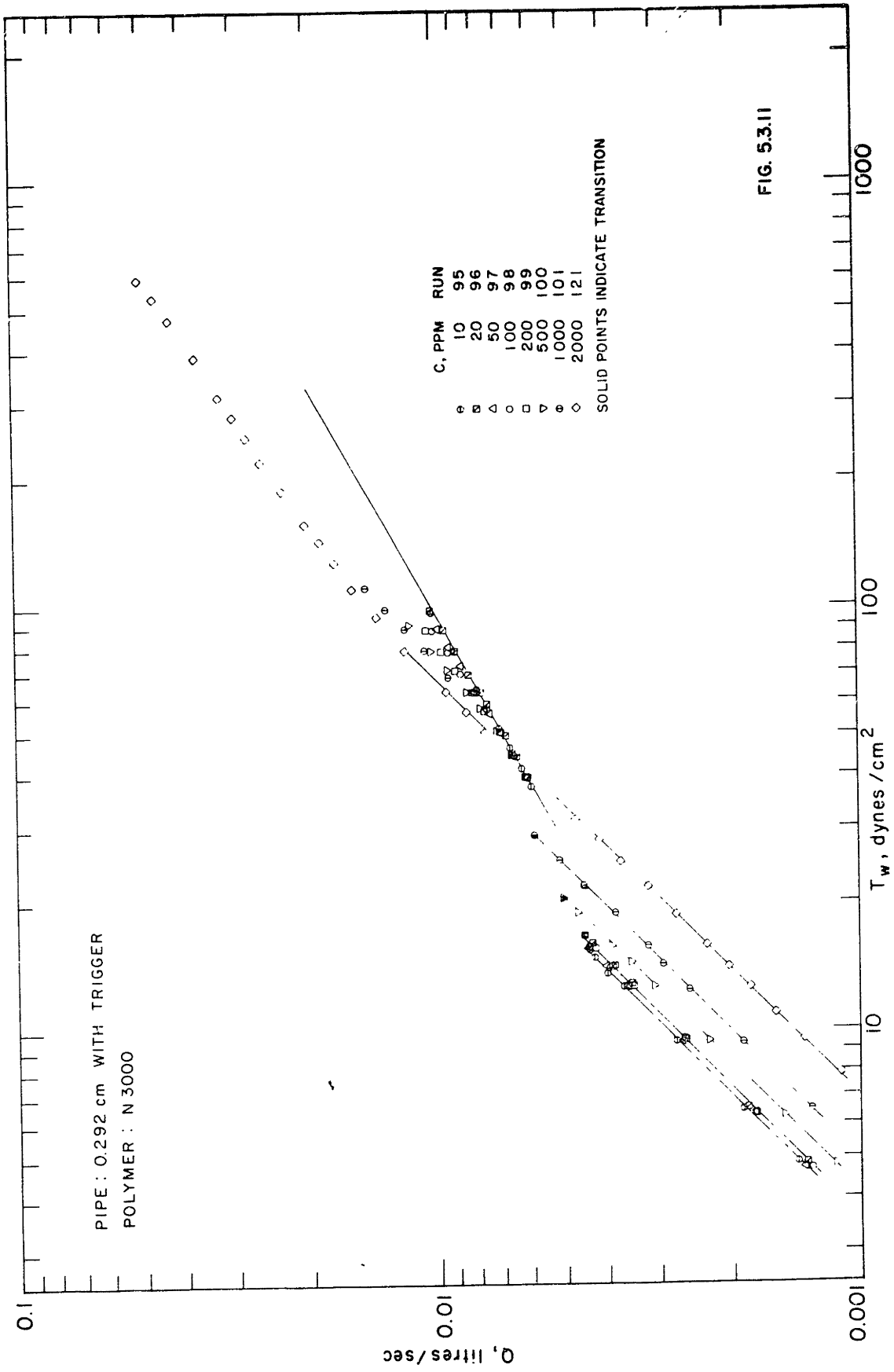
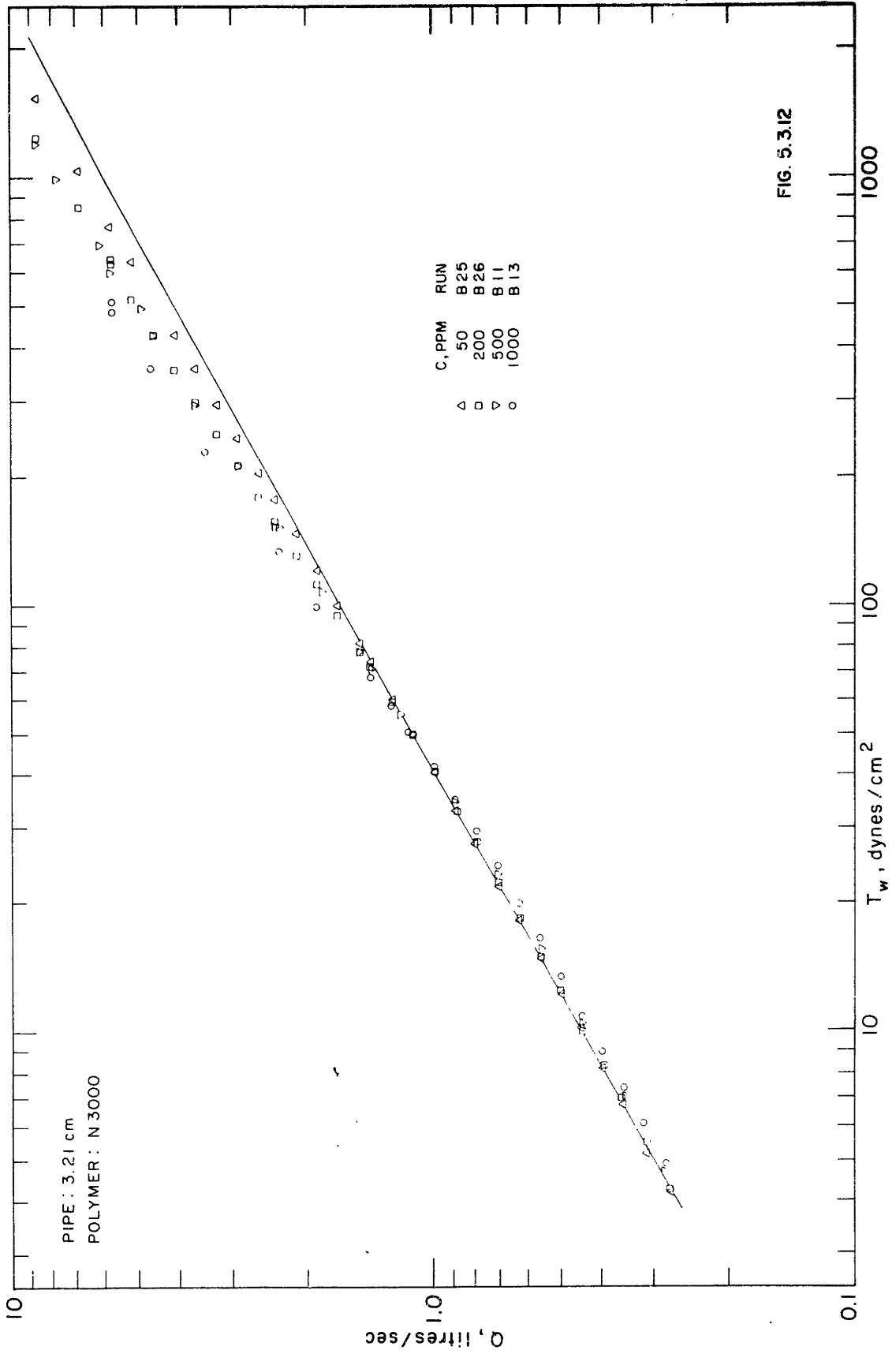


FIG. 5.3.10





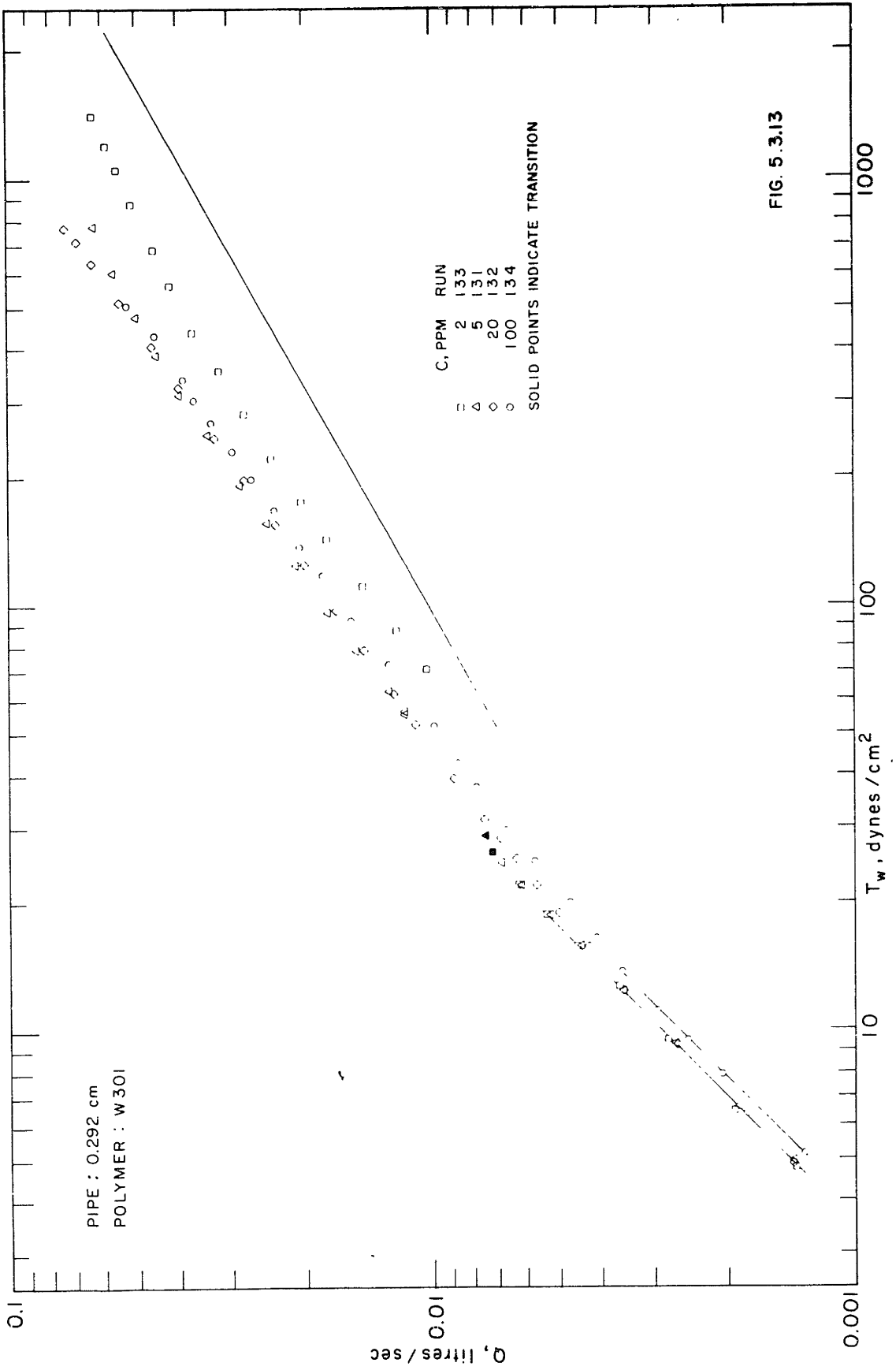


FIG. 5.3.13

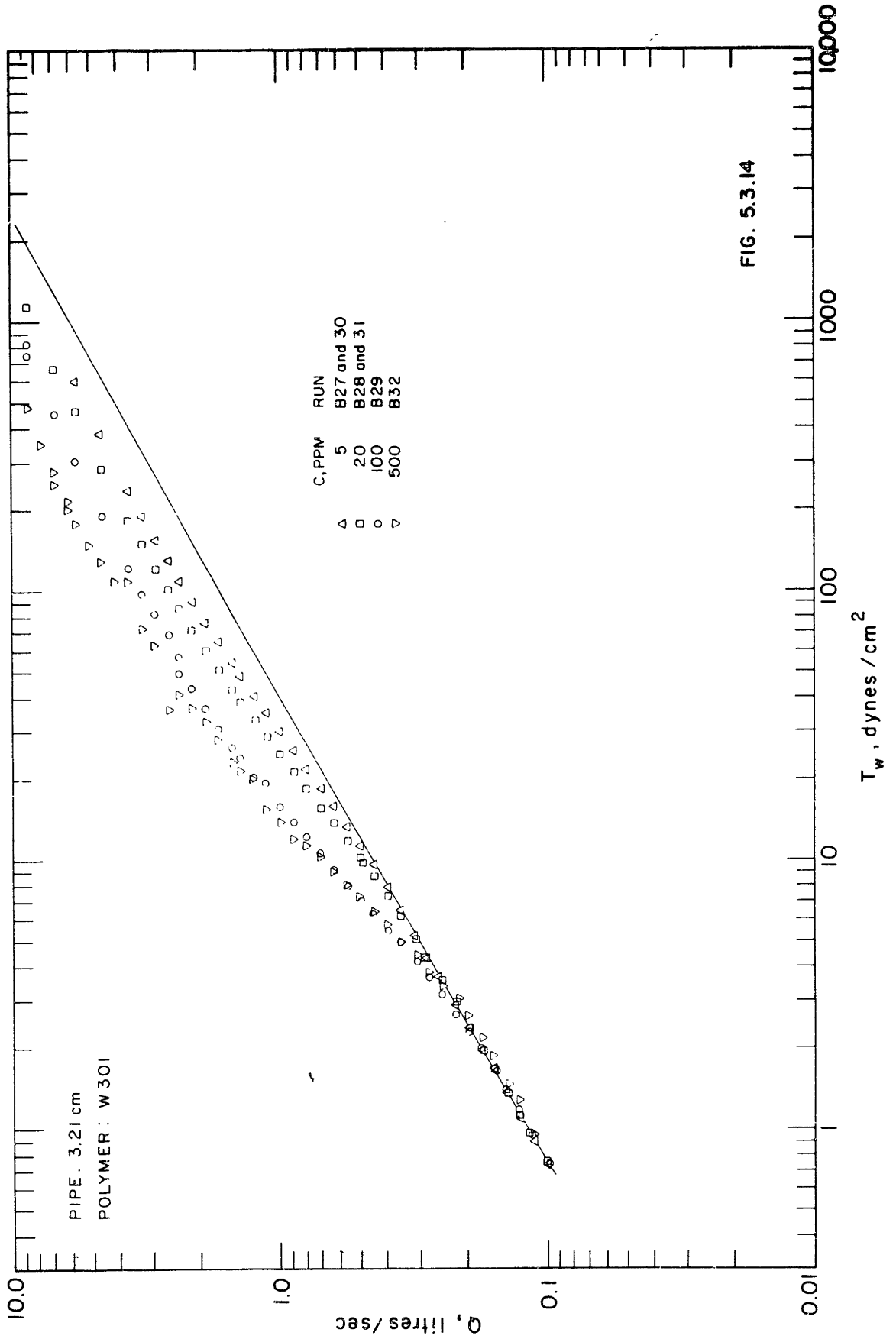


FIG. 5.3.14

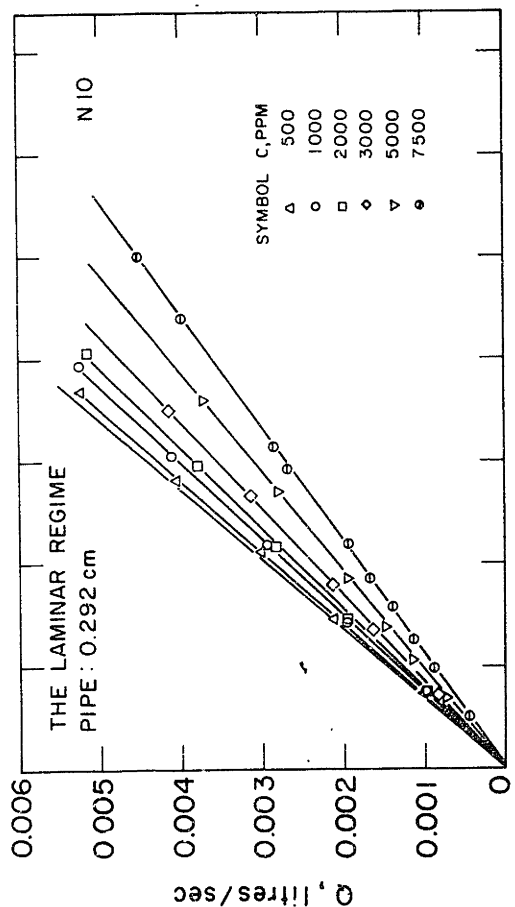
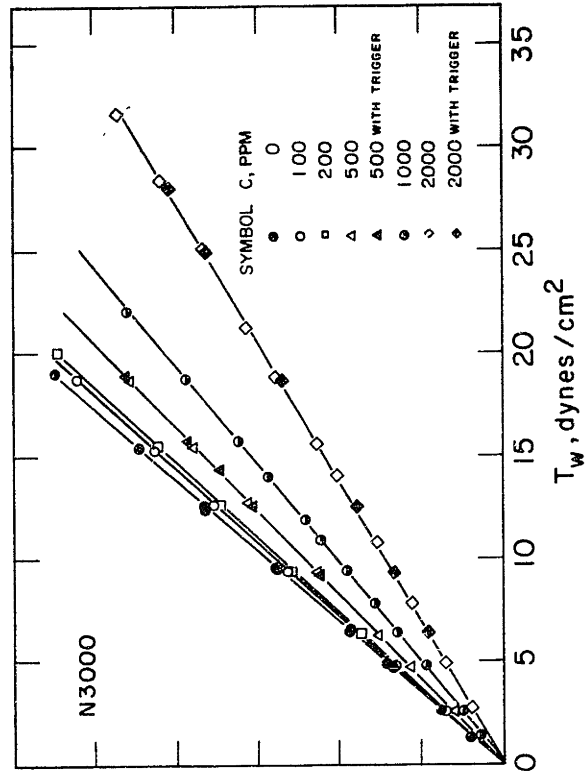
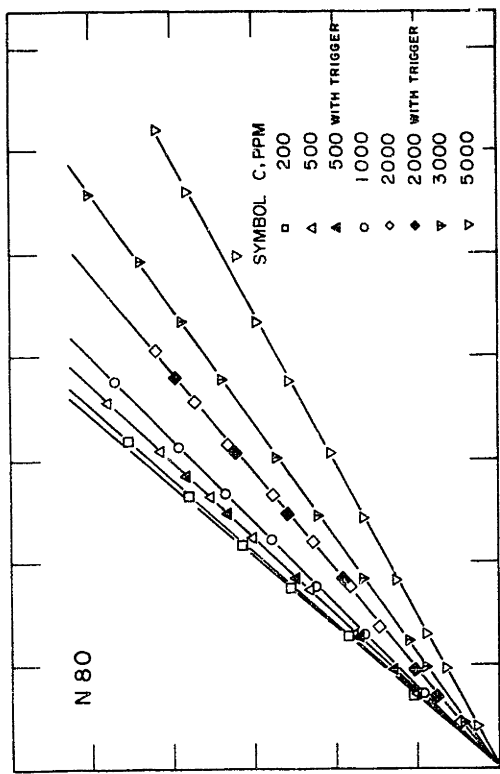
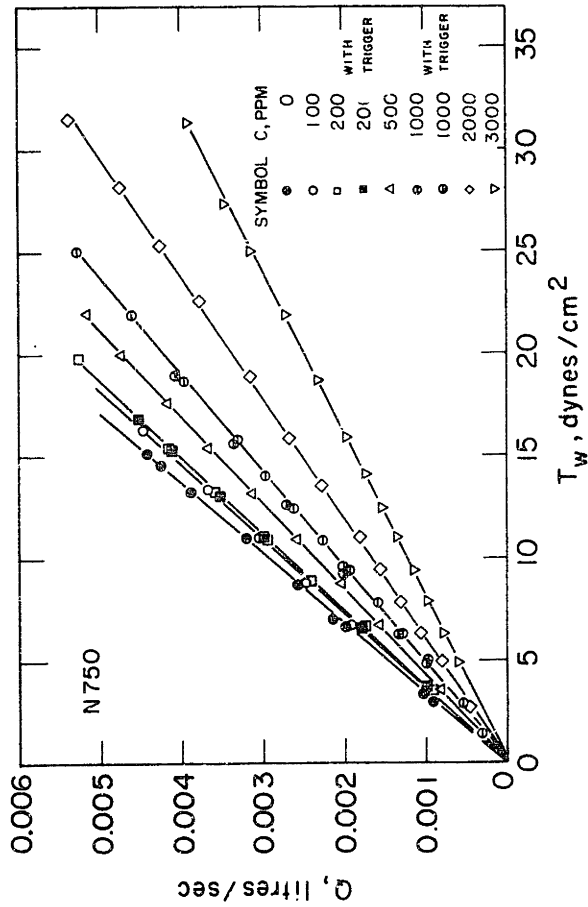


FIG. 5.3.15



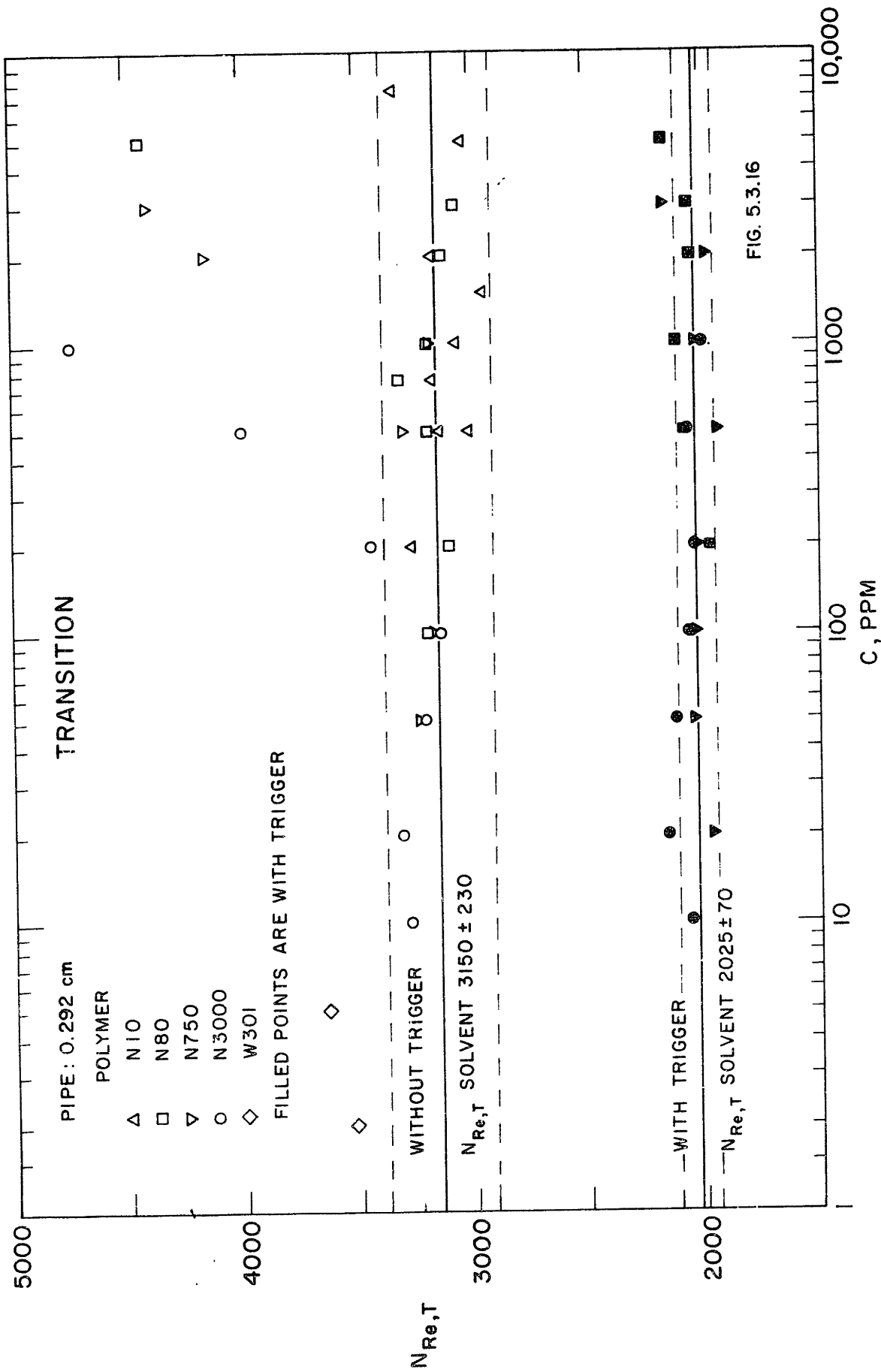
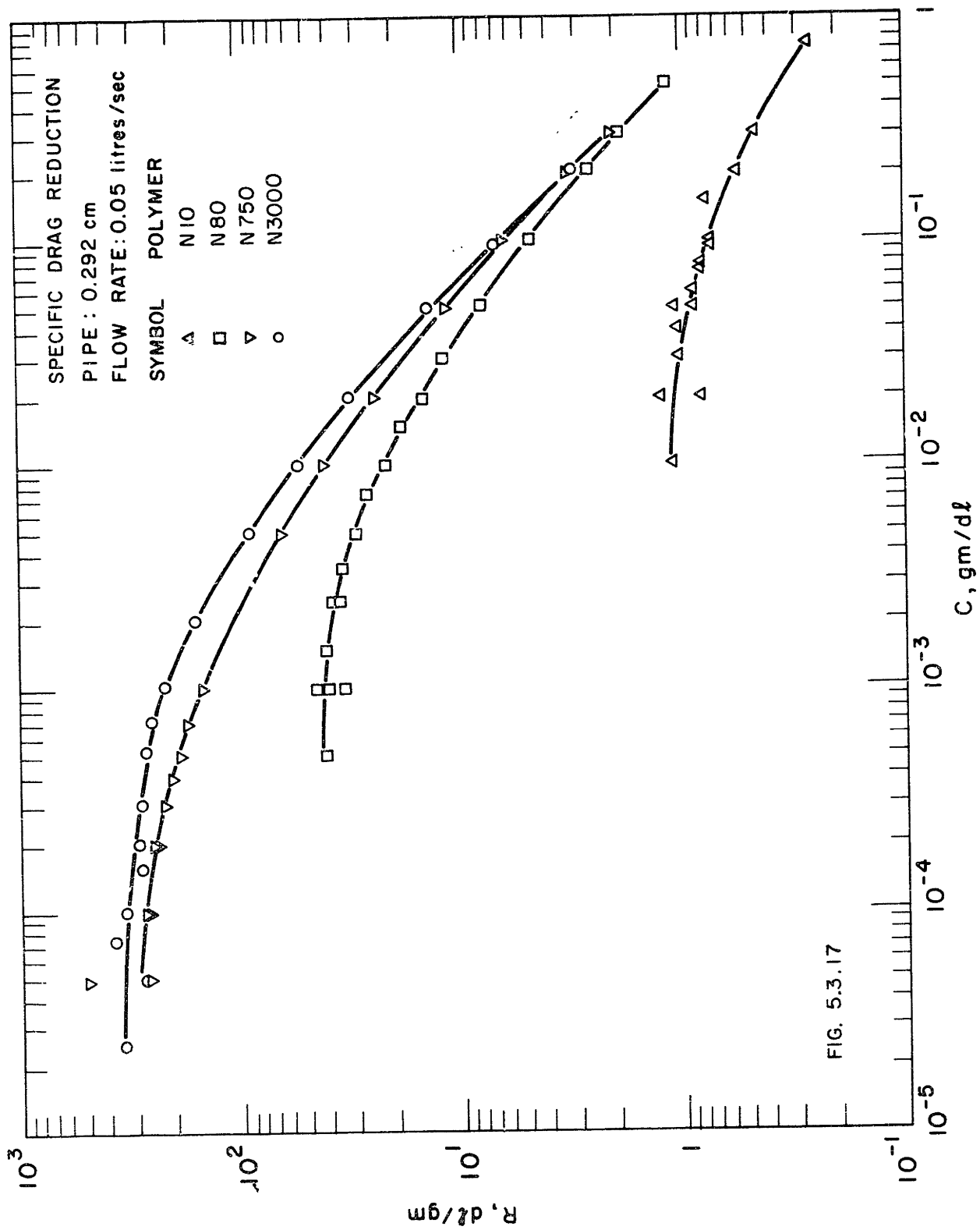


FIG. 5.3.16





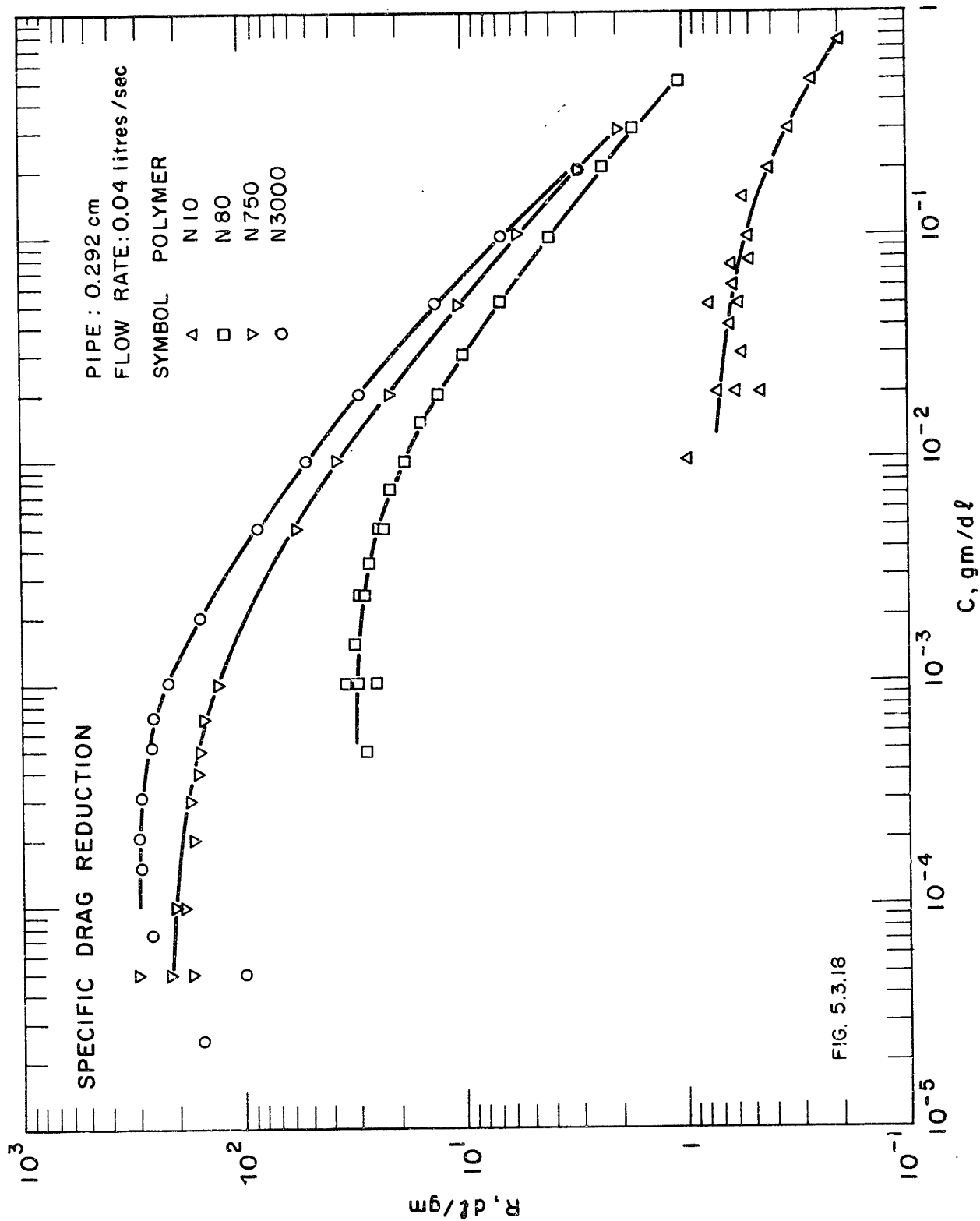


FIG. 5.3.18

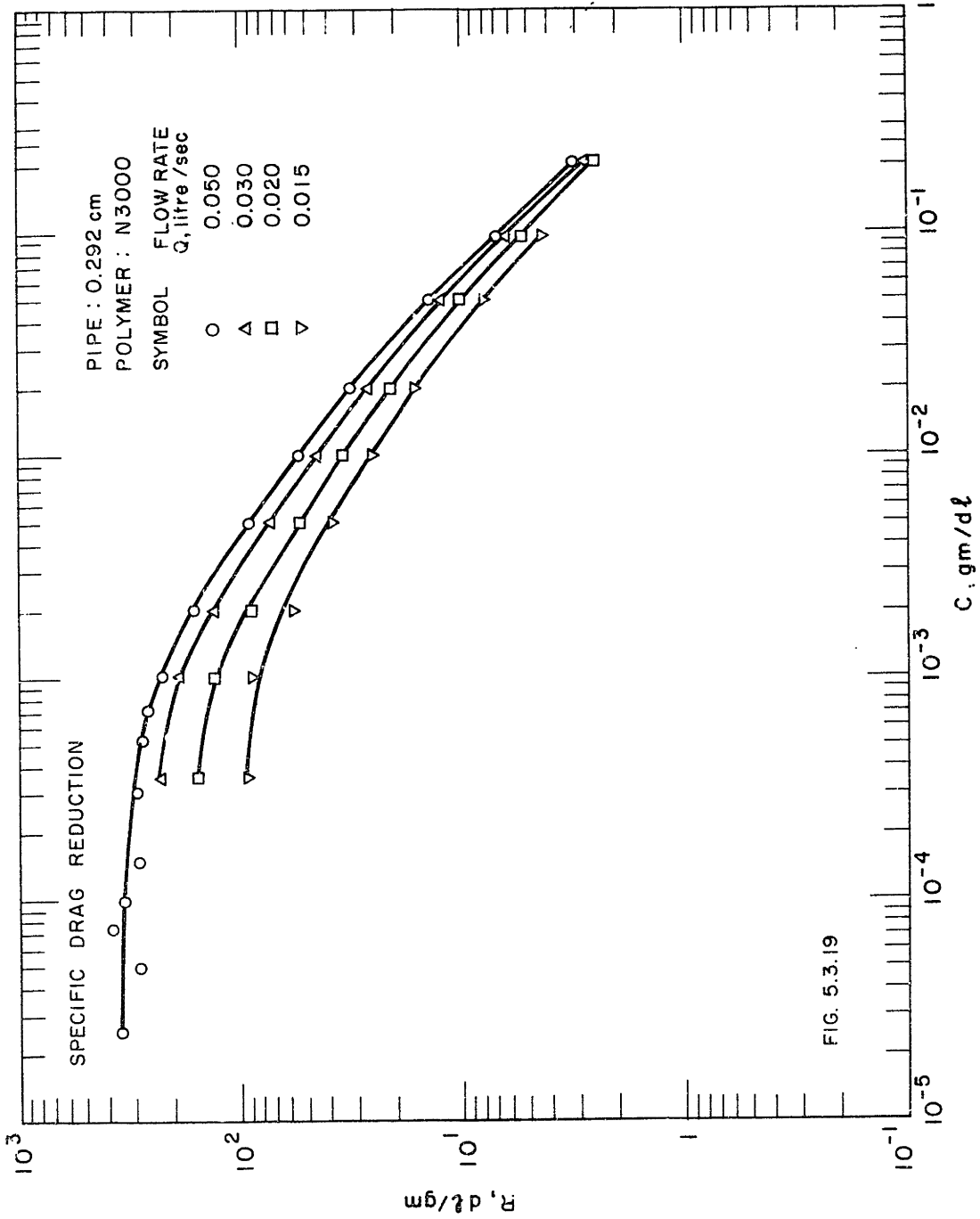


FIG. 5.3.19

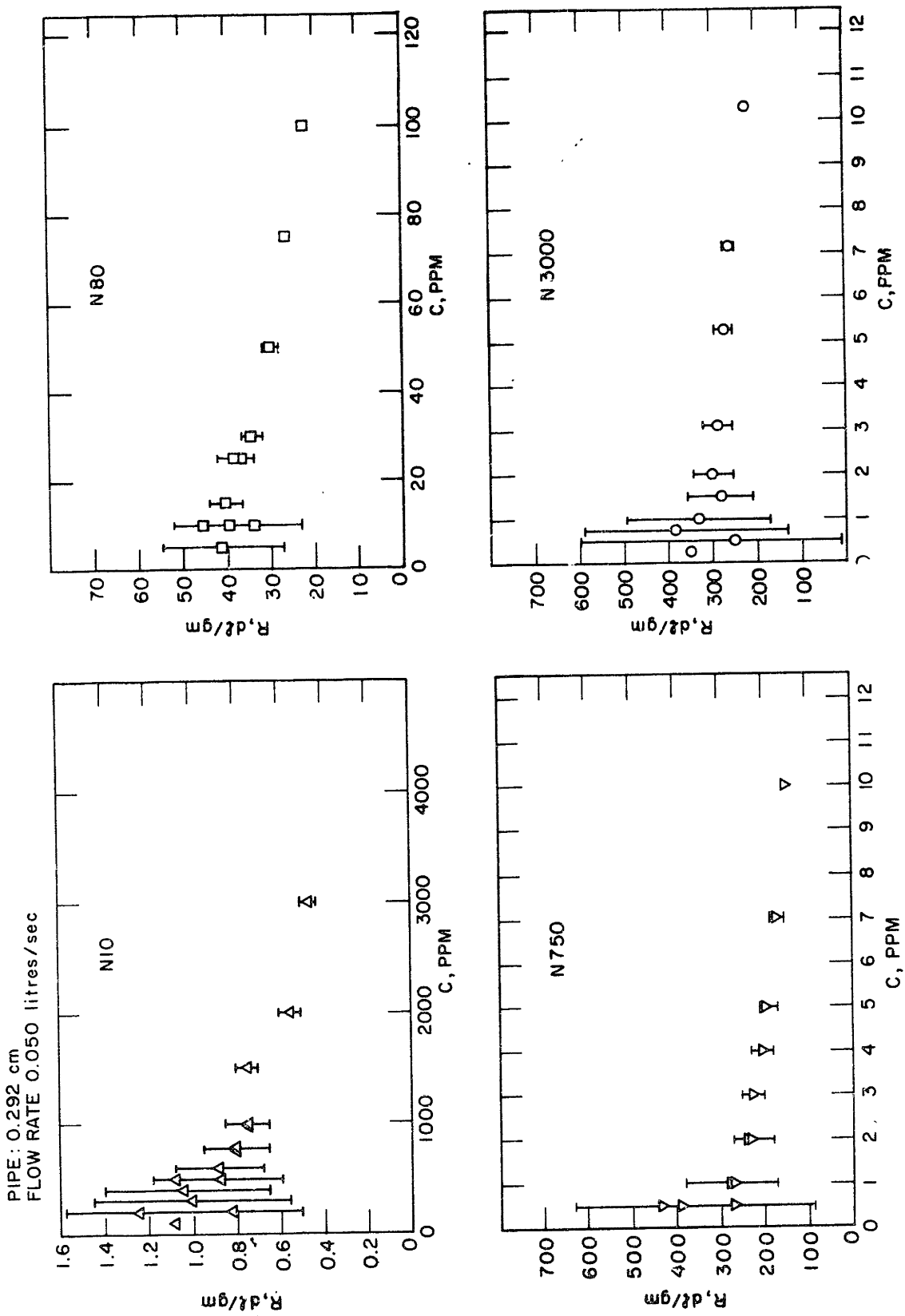


FIG. 5.3.20 SPECIFIC DRAG REDUCTION, C → O; 99% CONFIDENCE LIMITS

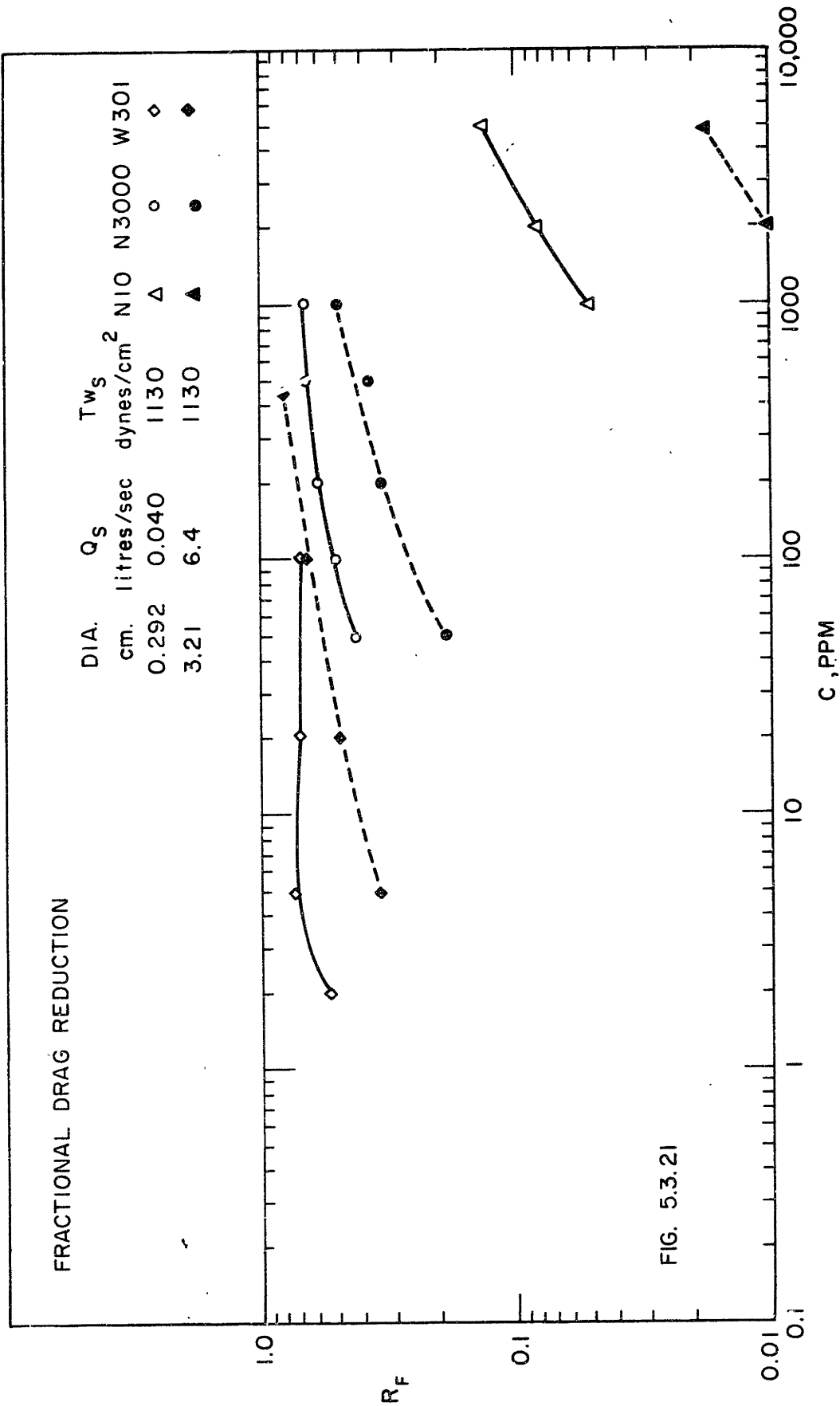


FIG. 5.3.21

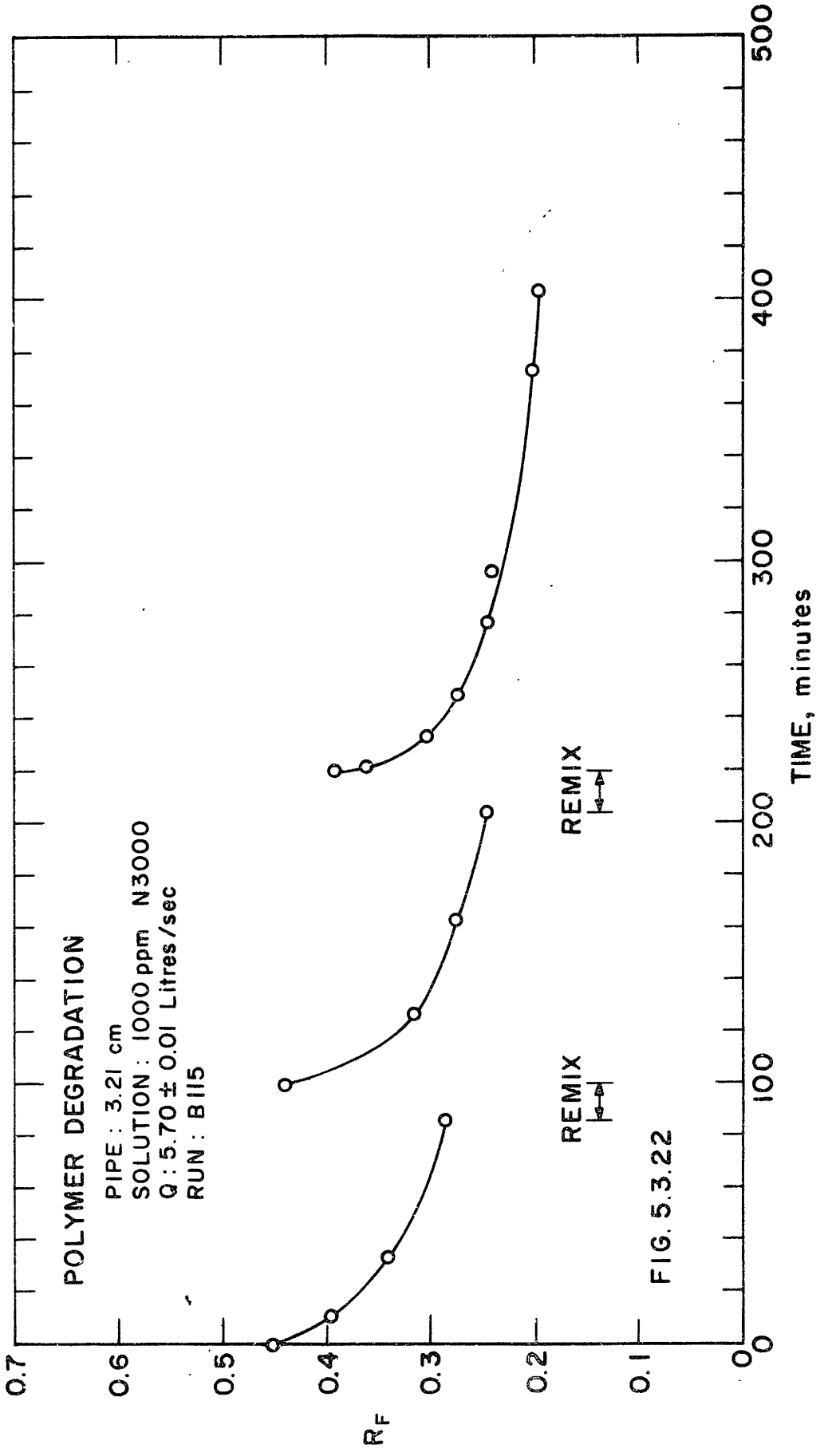
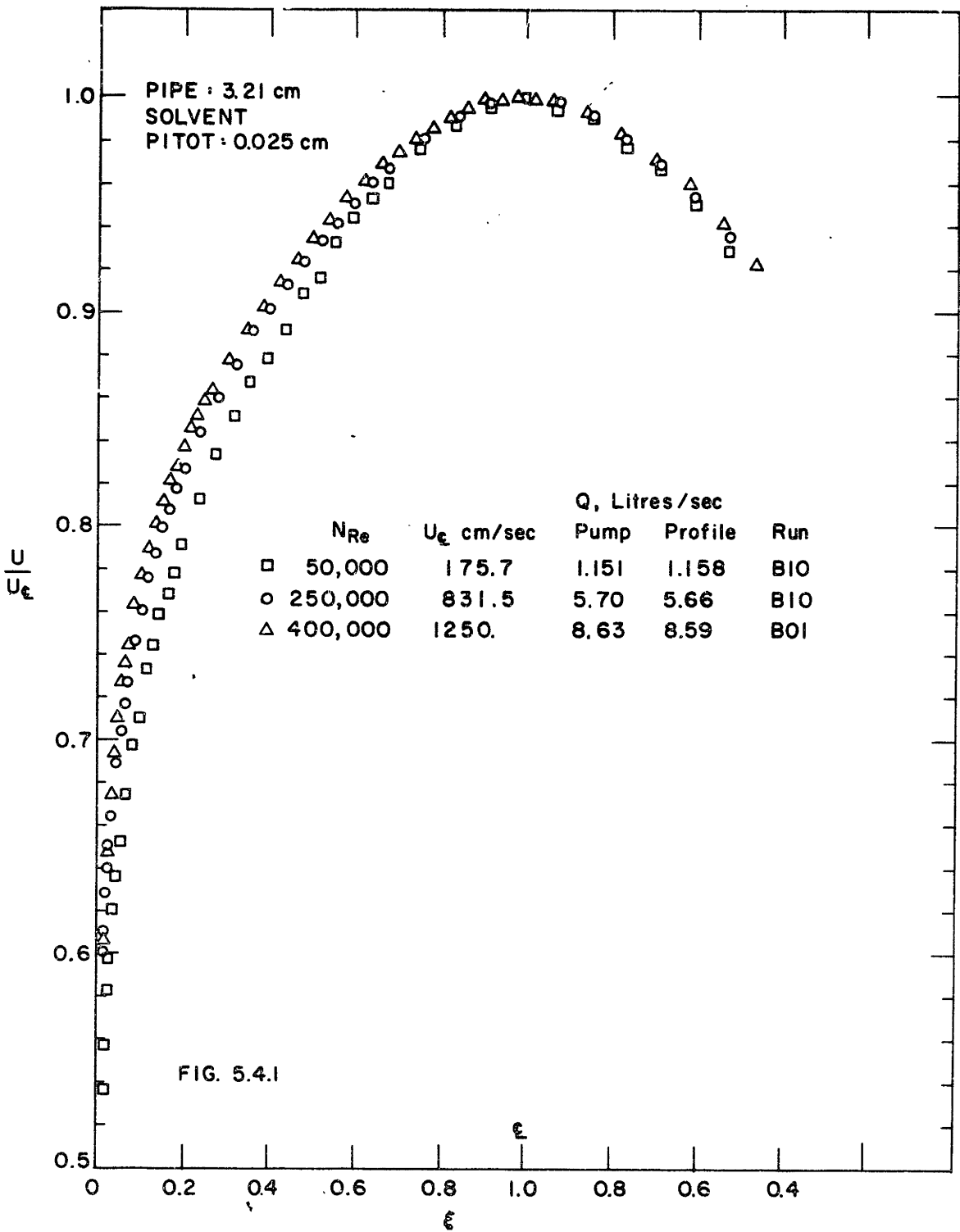
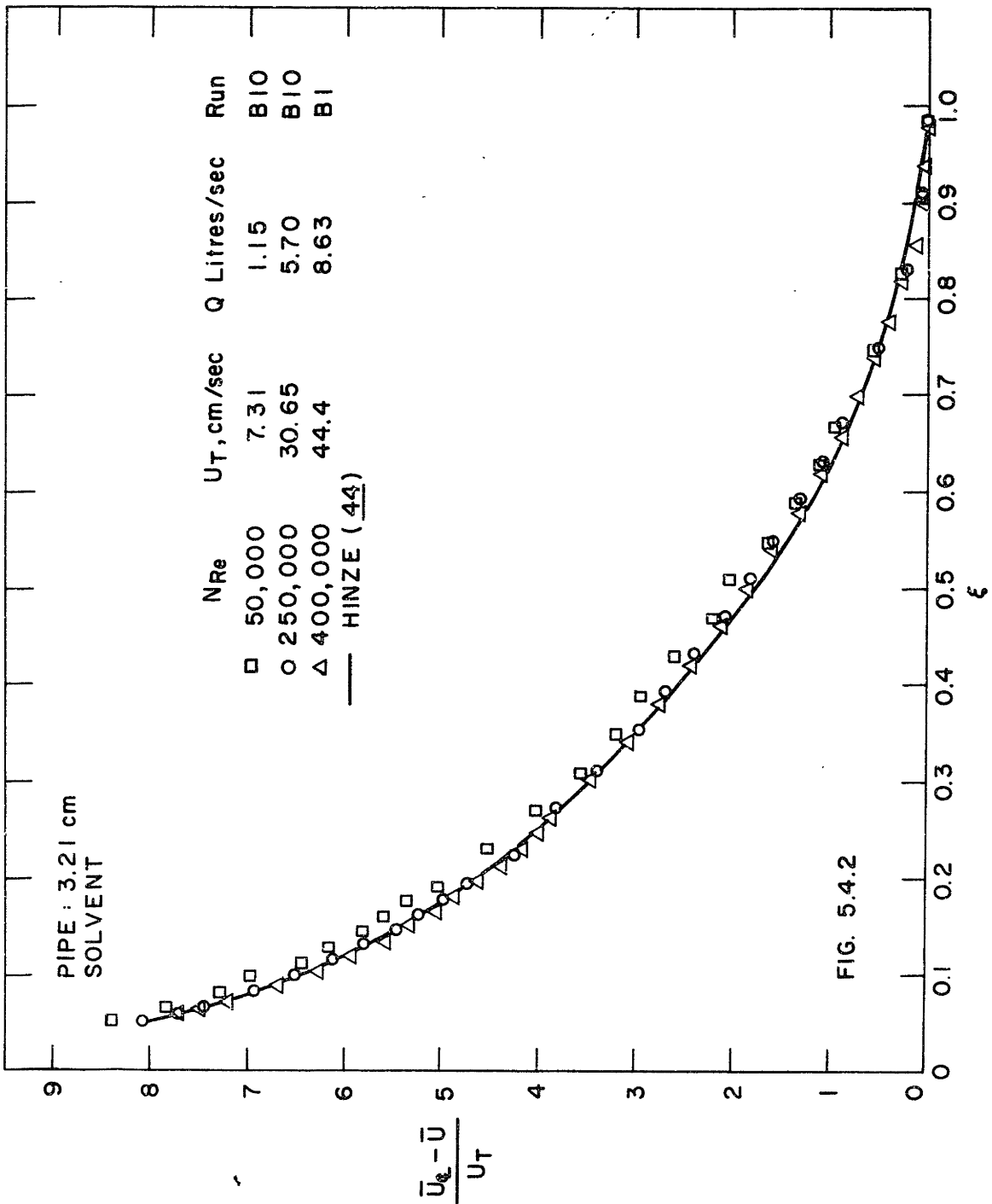
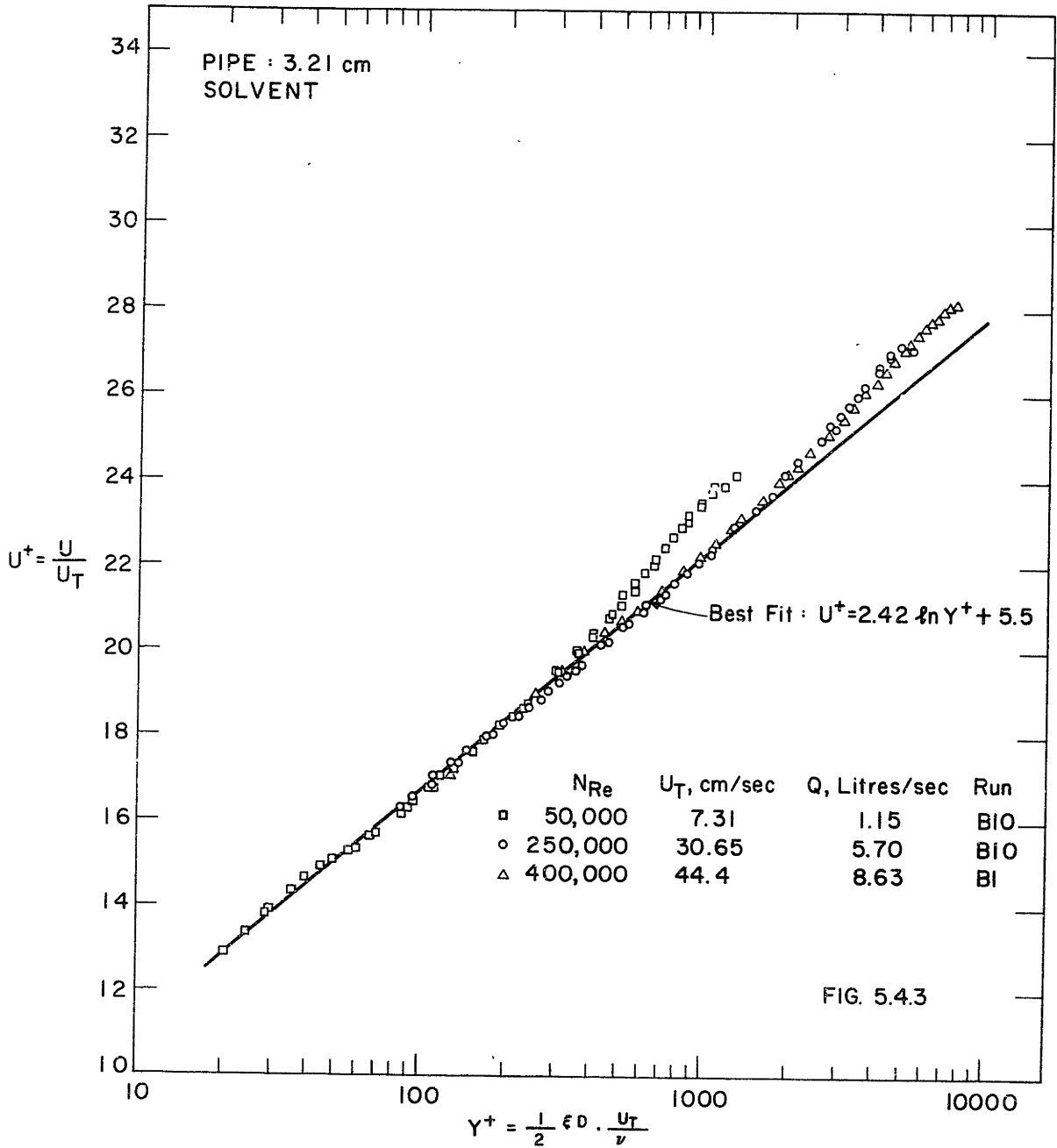


FIG. 5.3.22









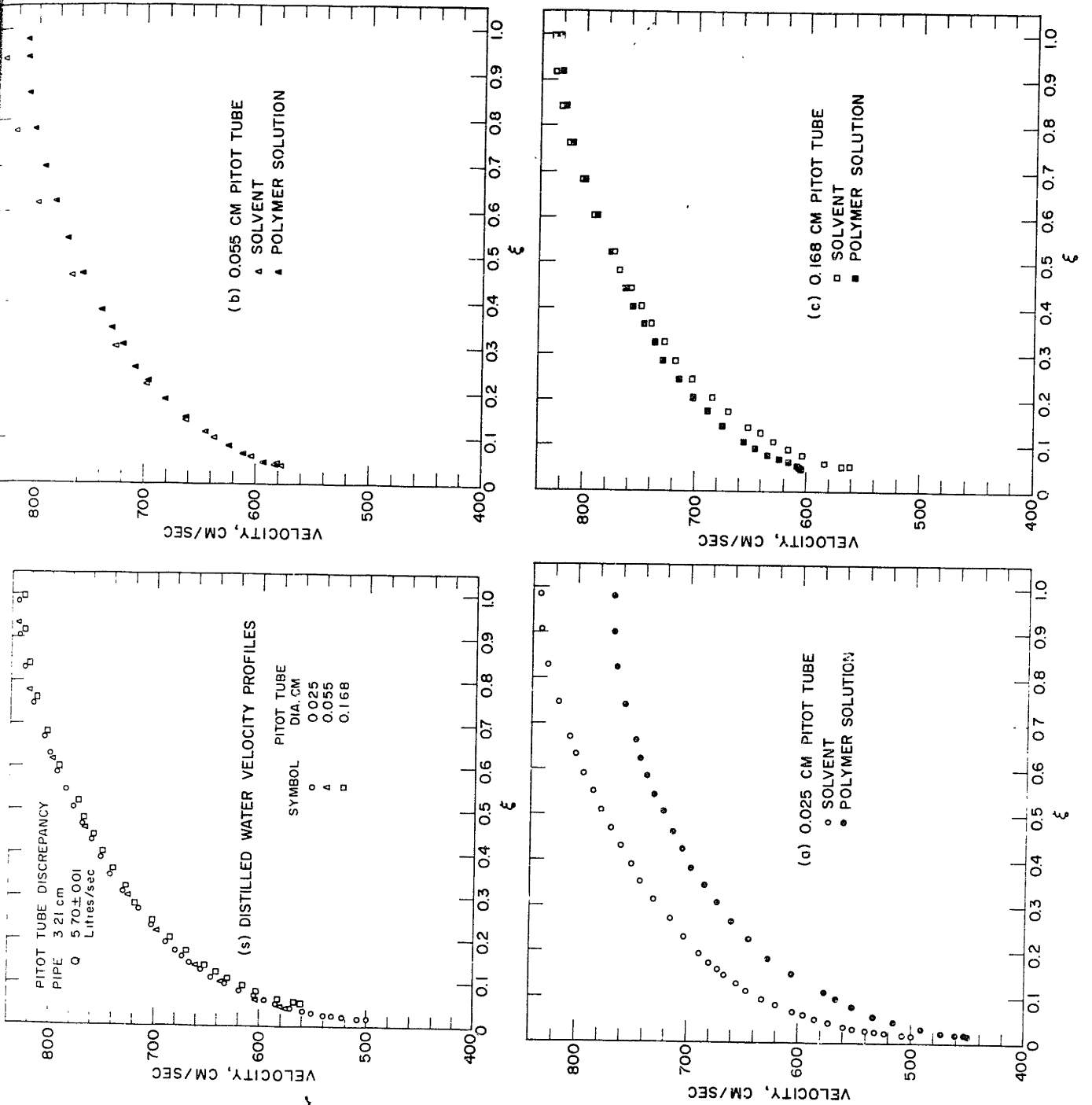
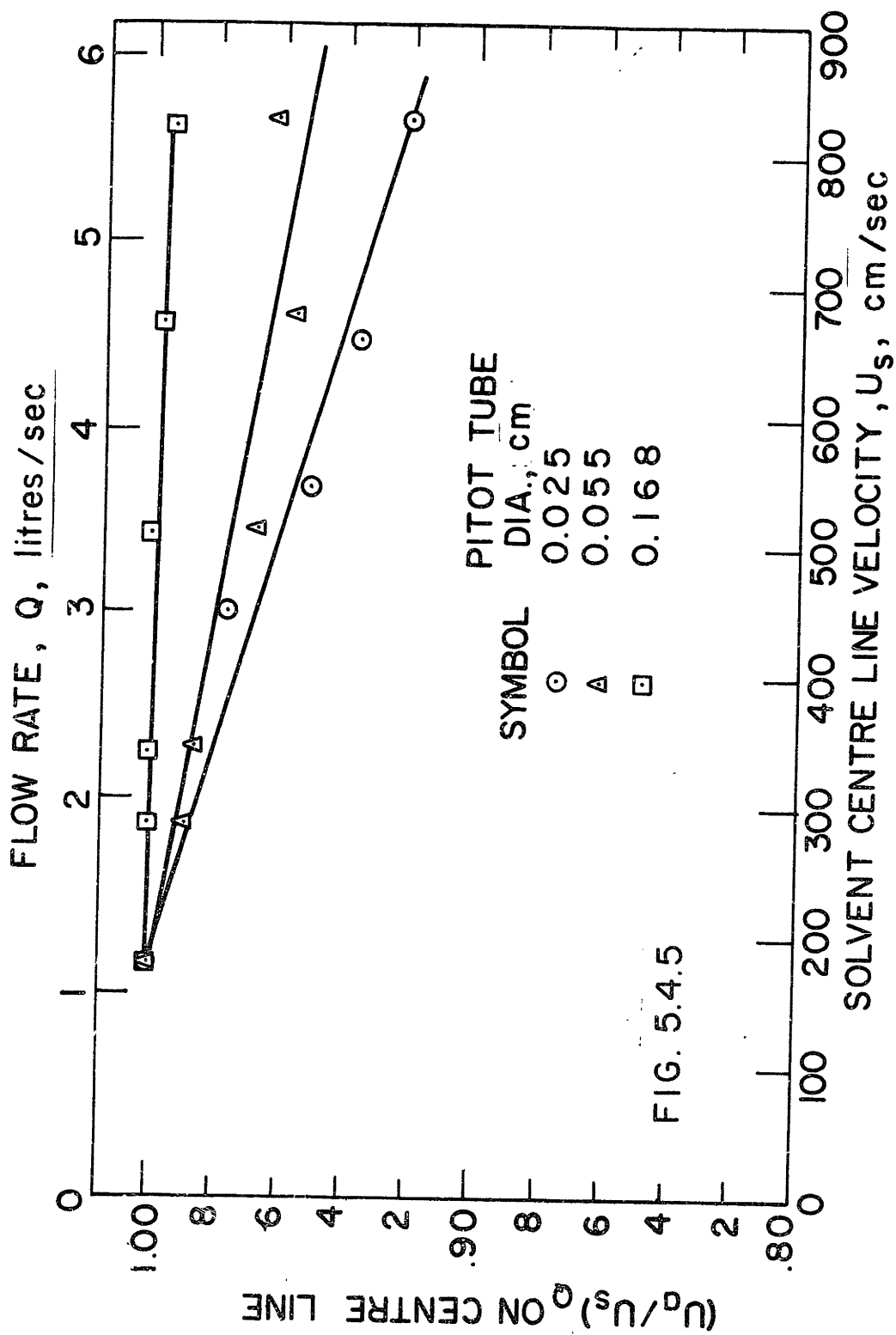
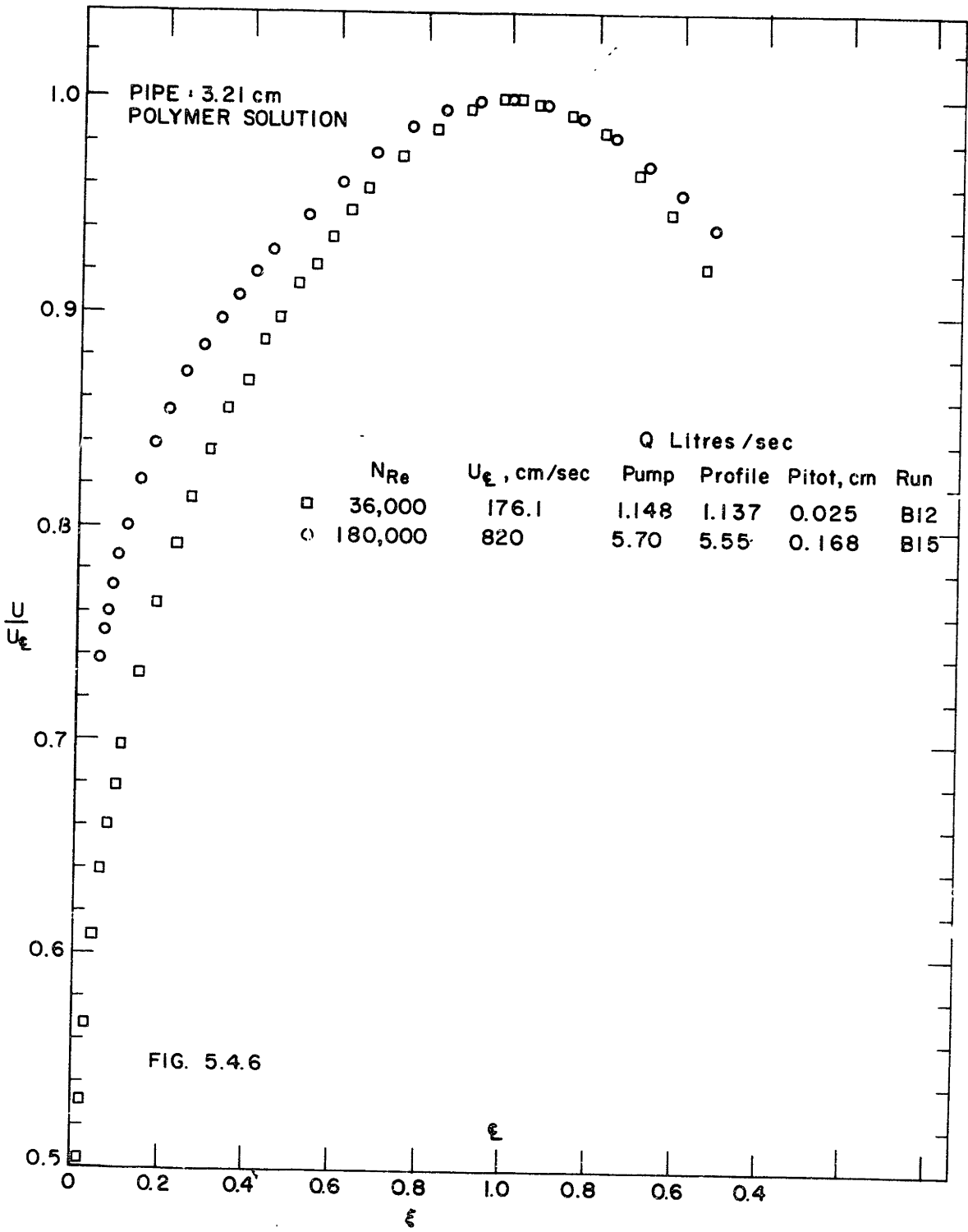


FIG 5.4.4



CENTRE LINE VELOCITIES AT EQUAL FLOW RATES IN POLYMER SOLUTION AND SOLVENT



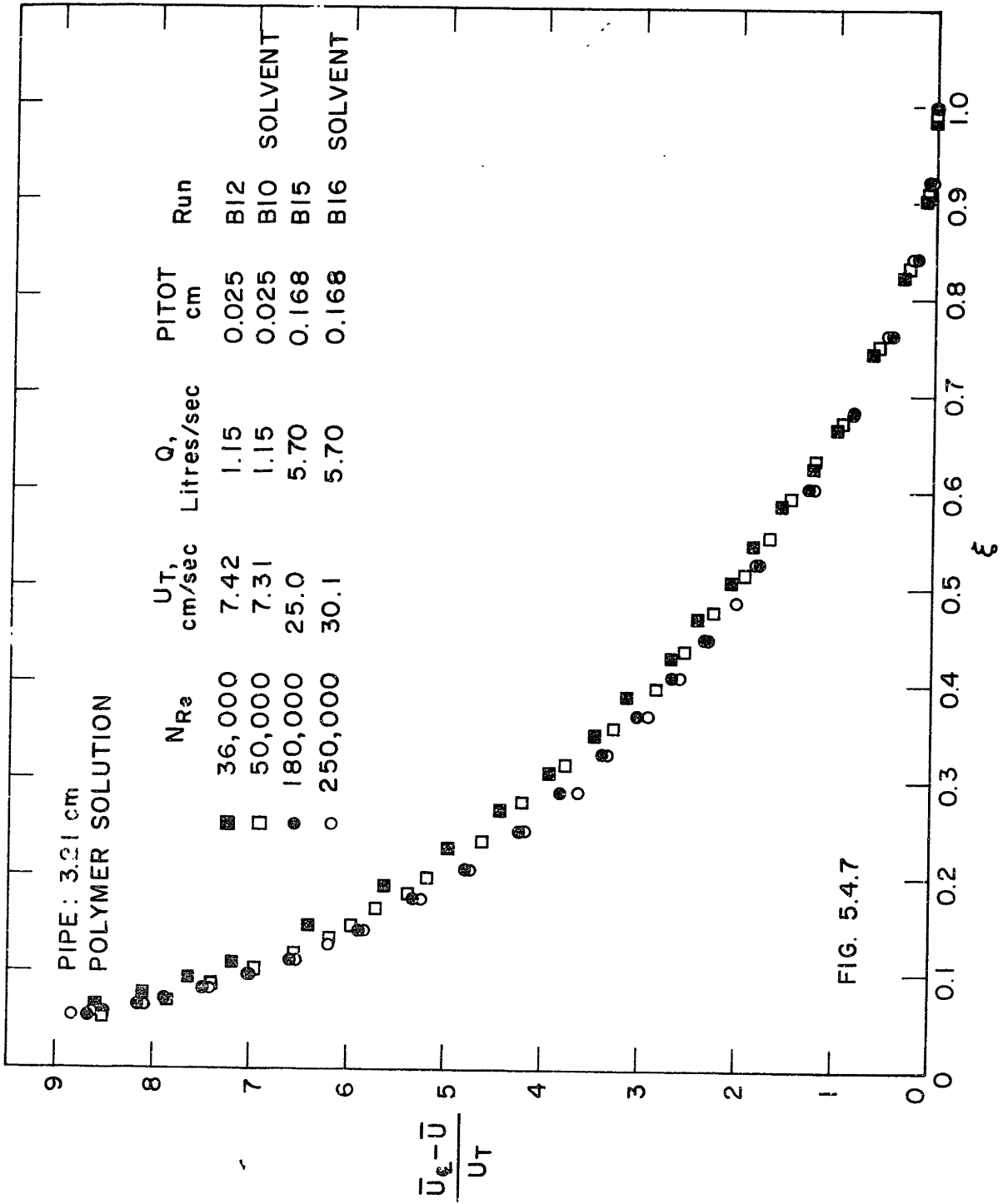
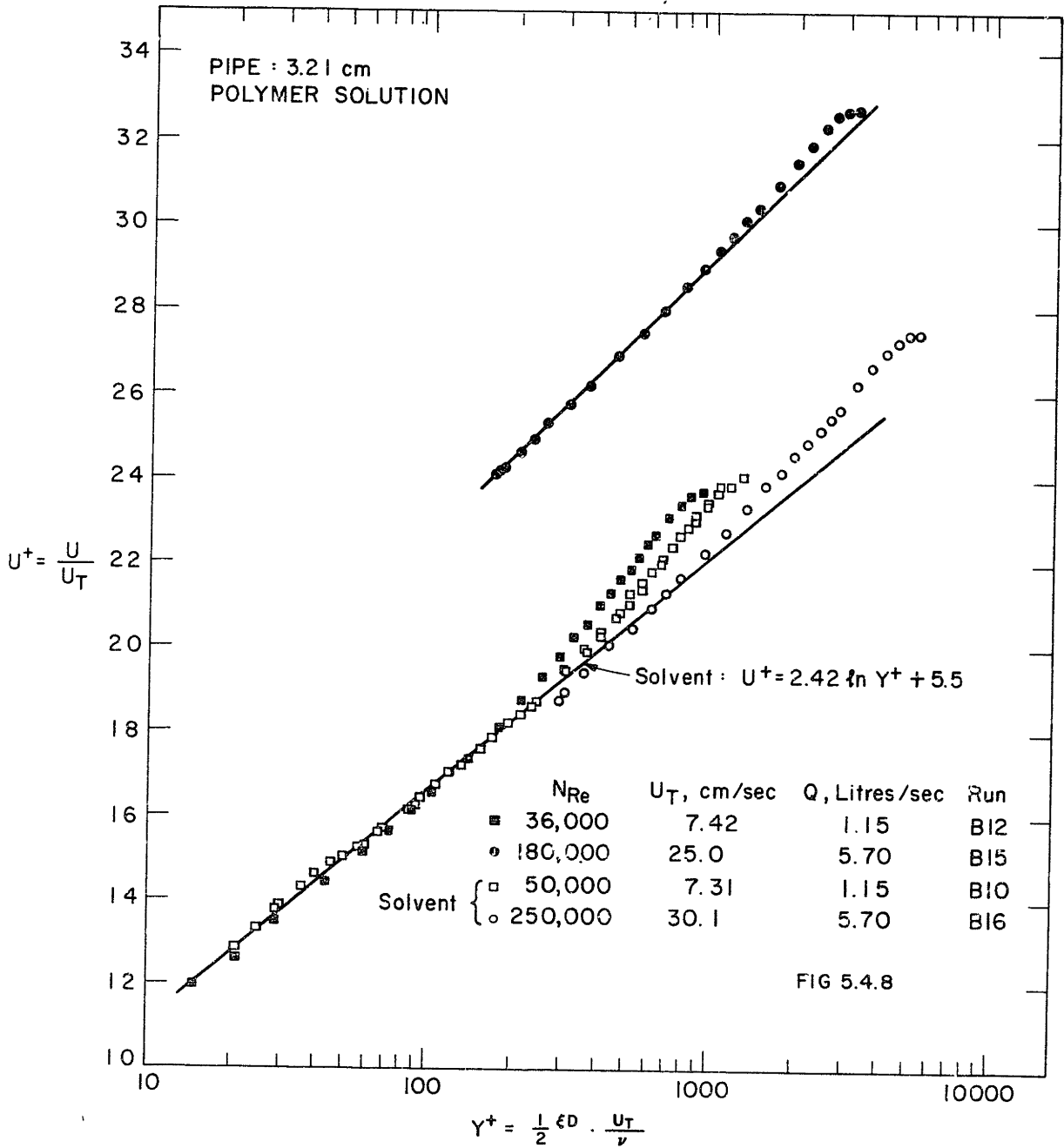
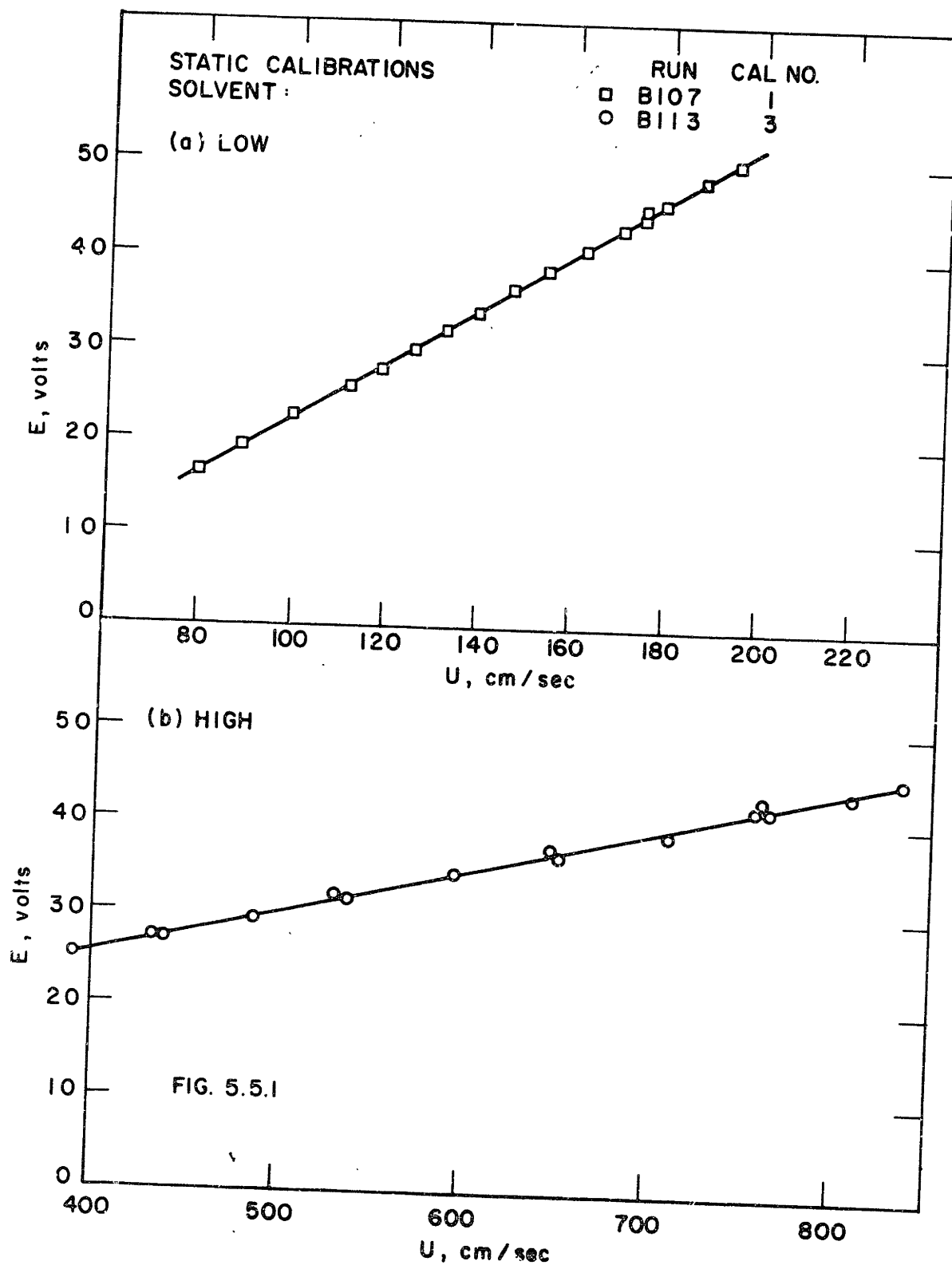
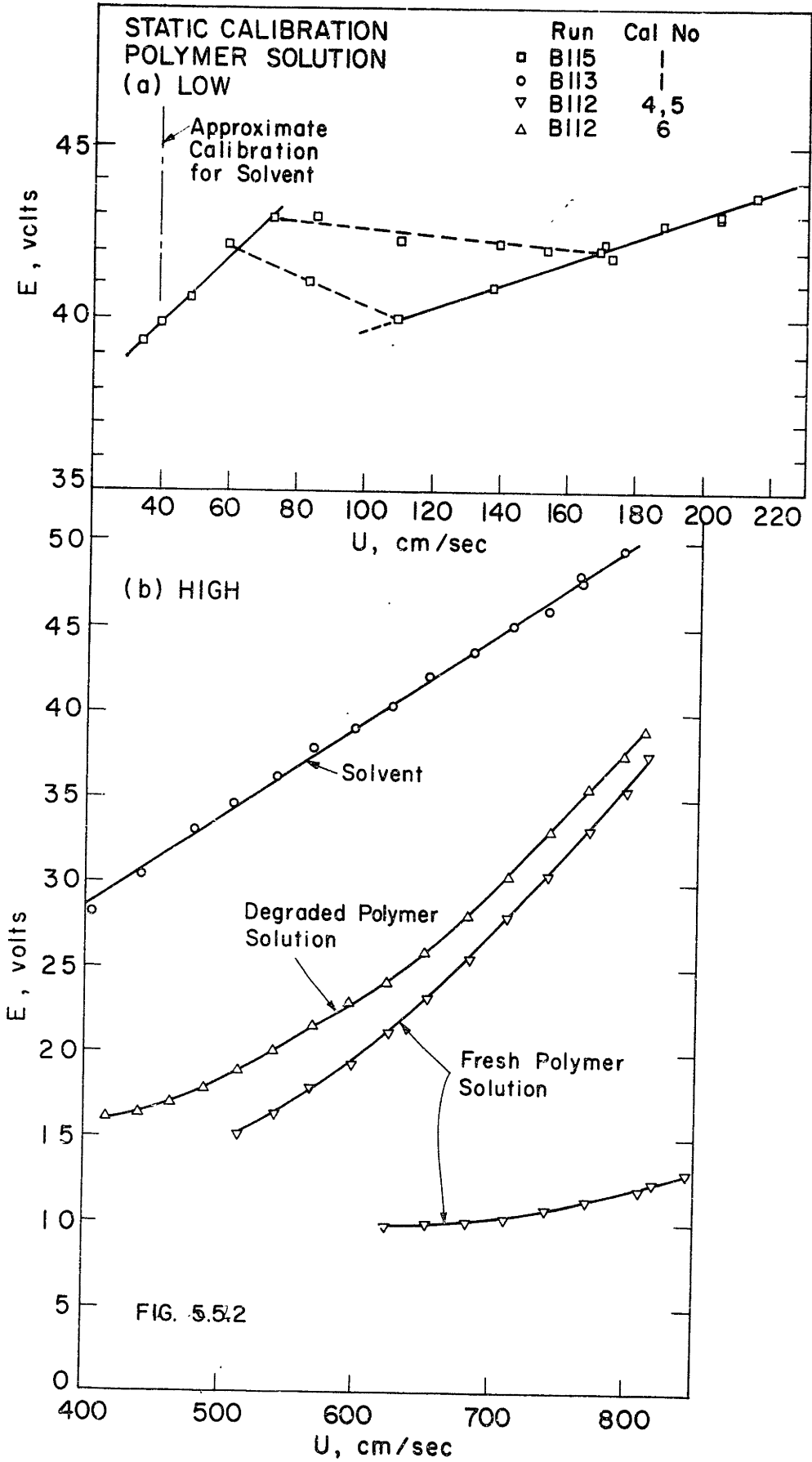


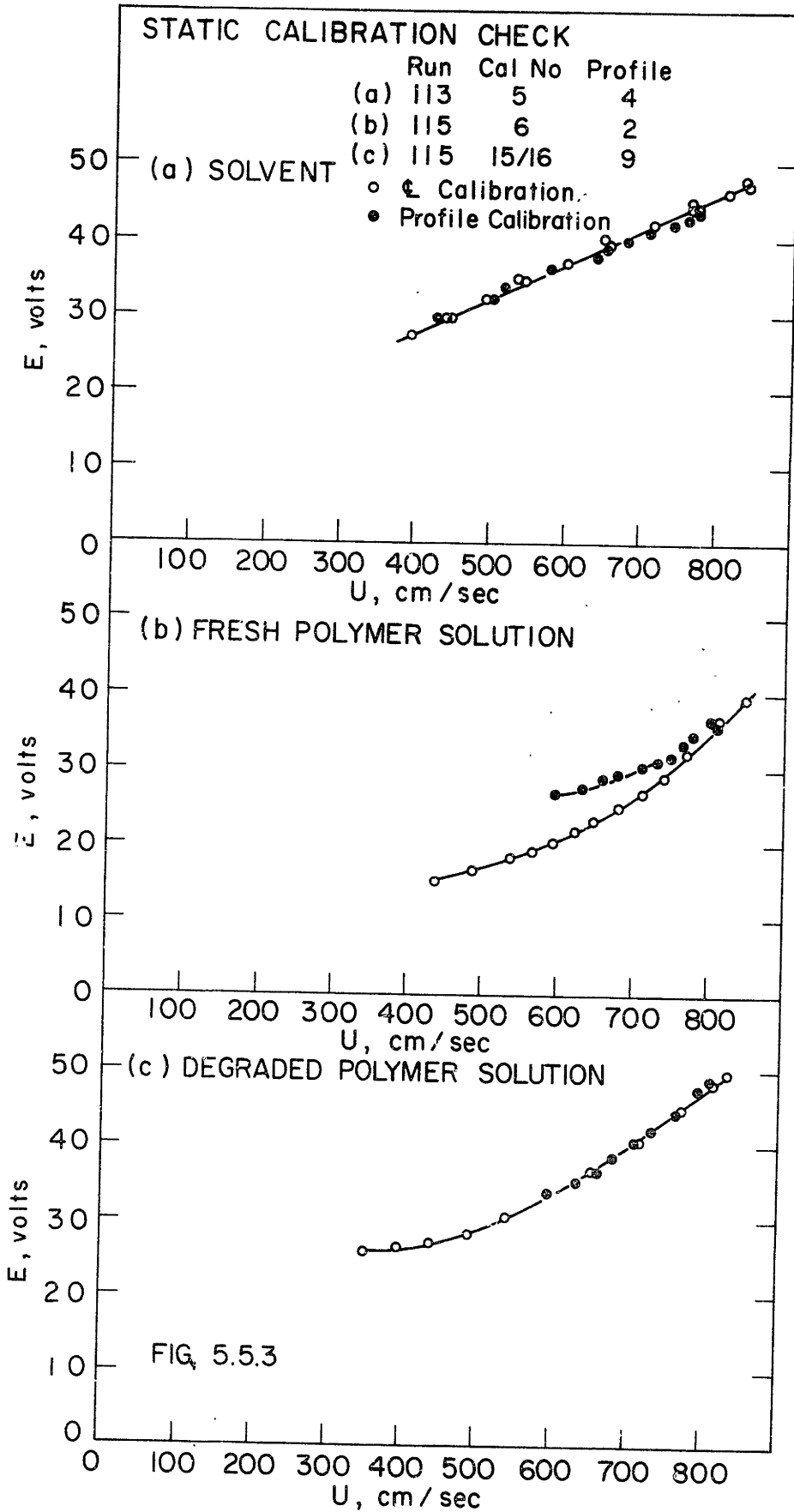
FIG. 5.4.7

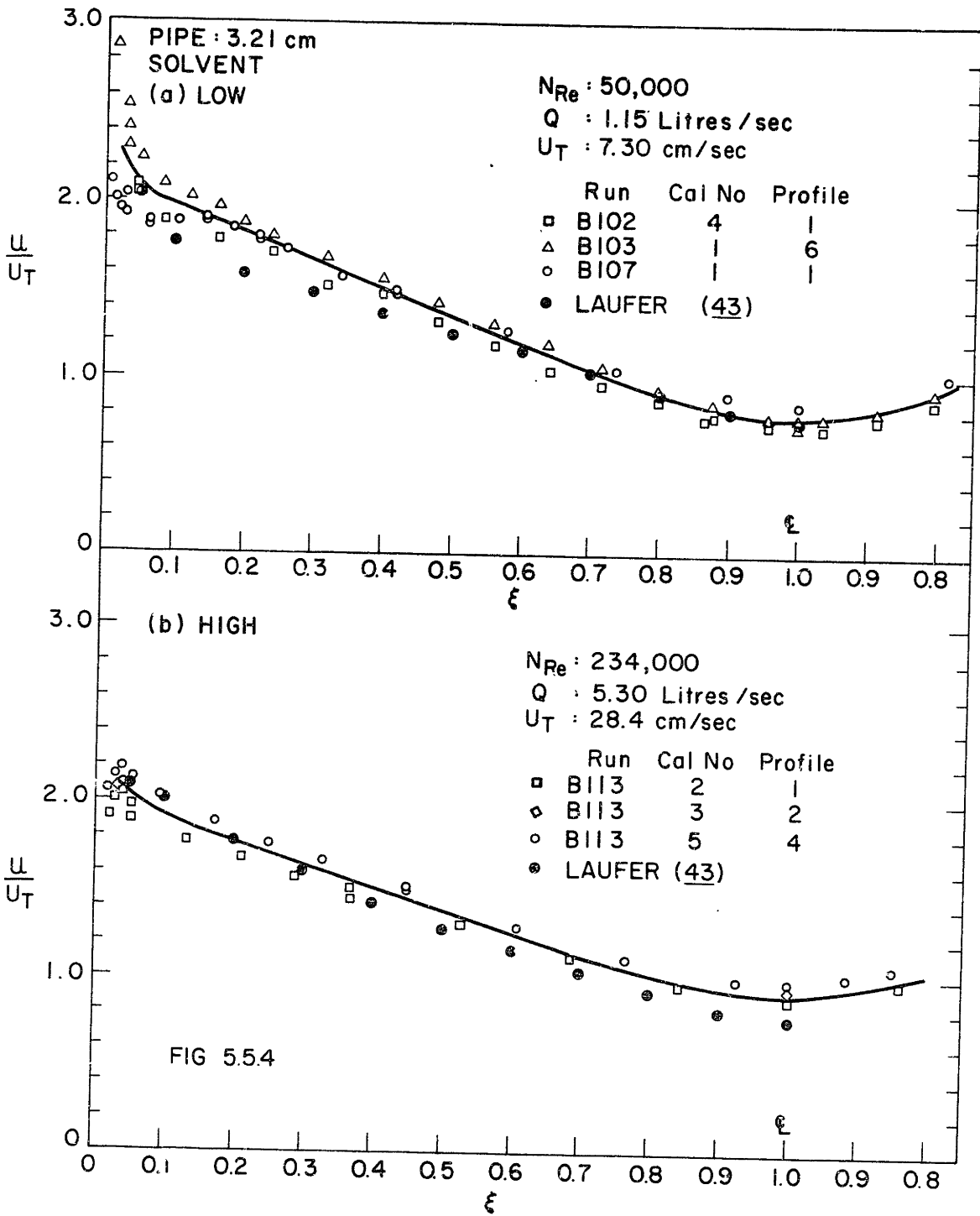


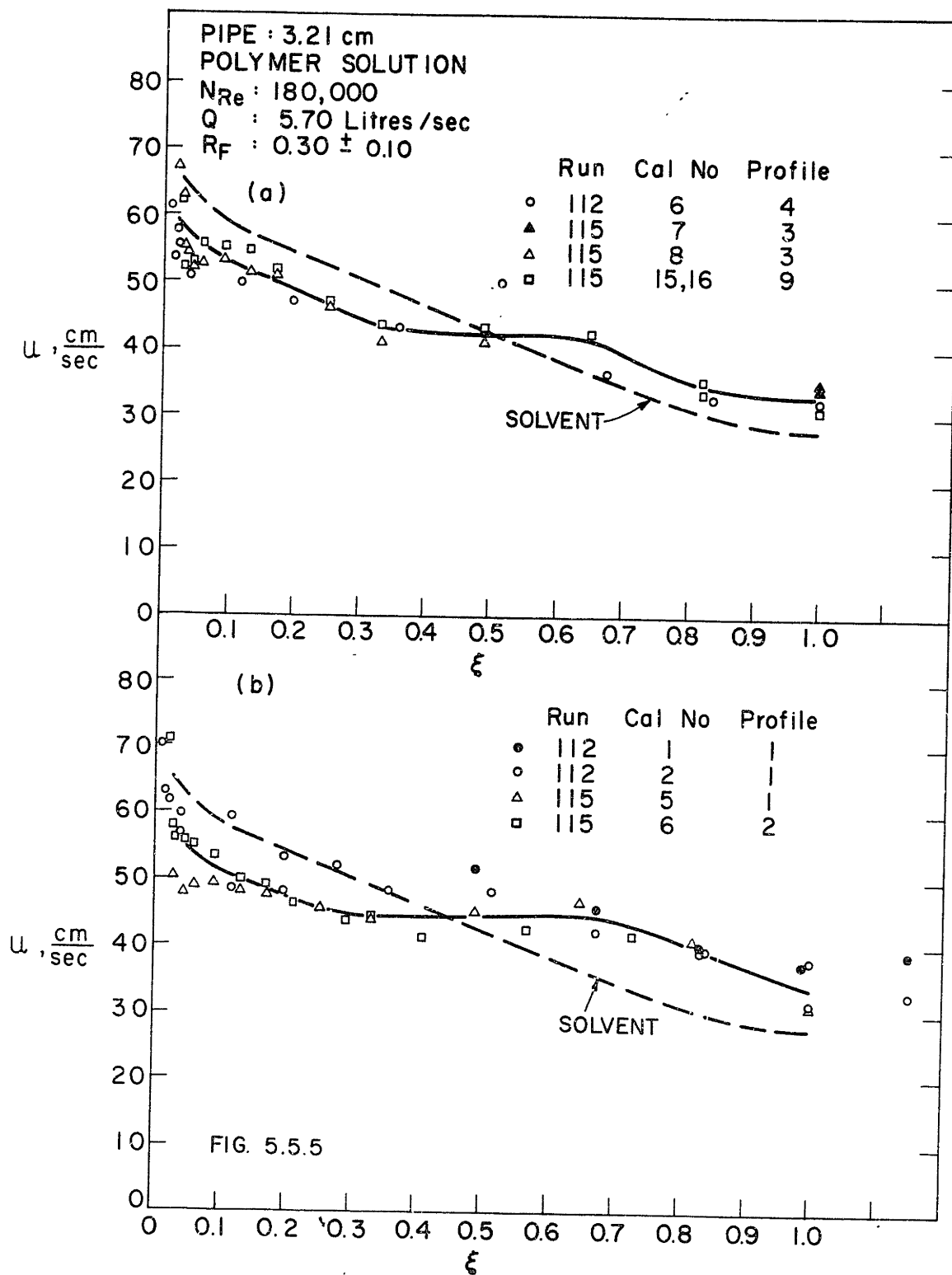


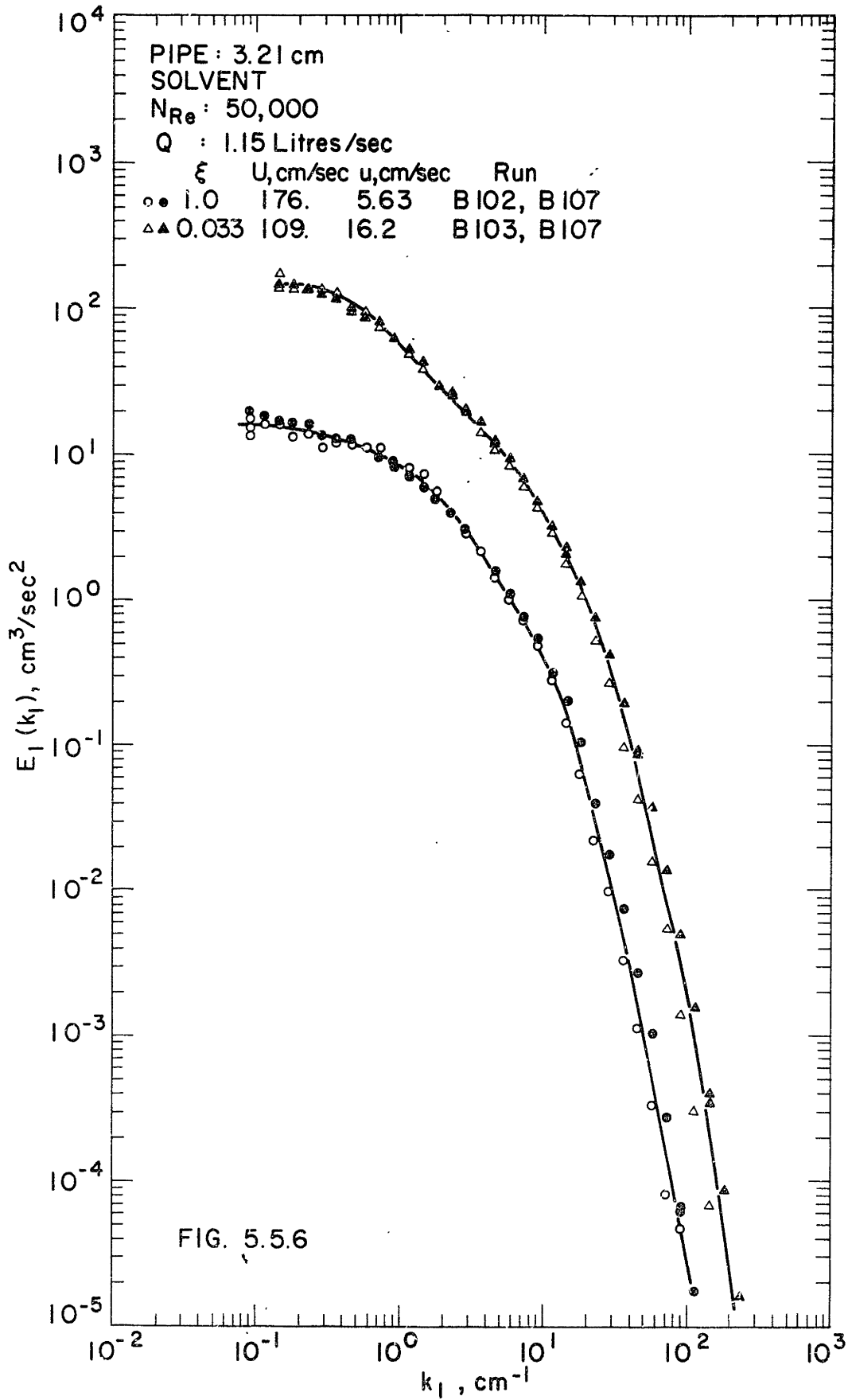


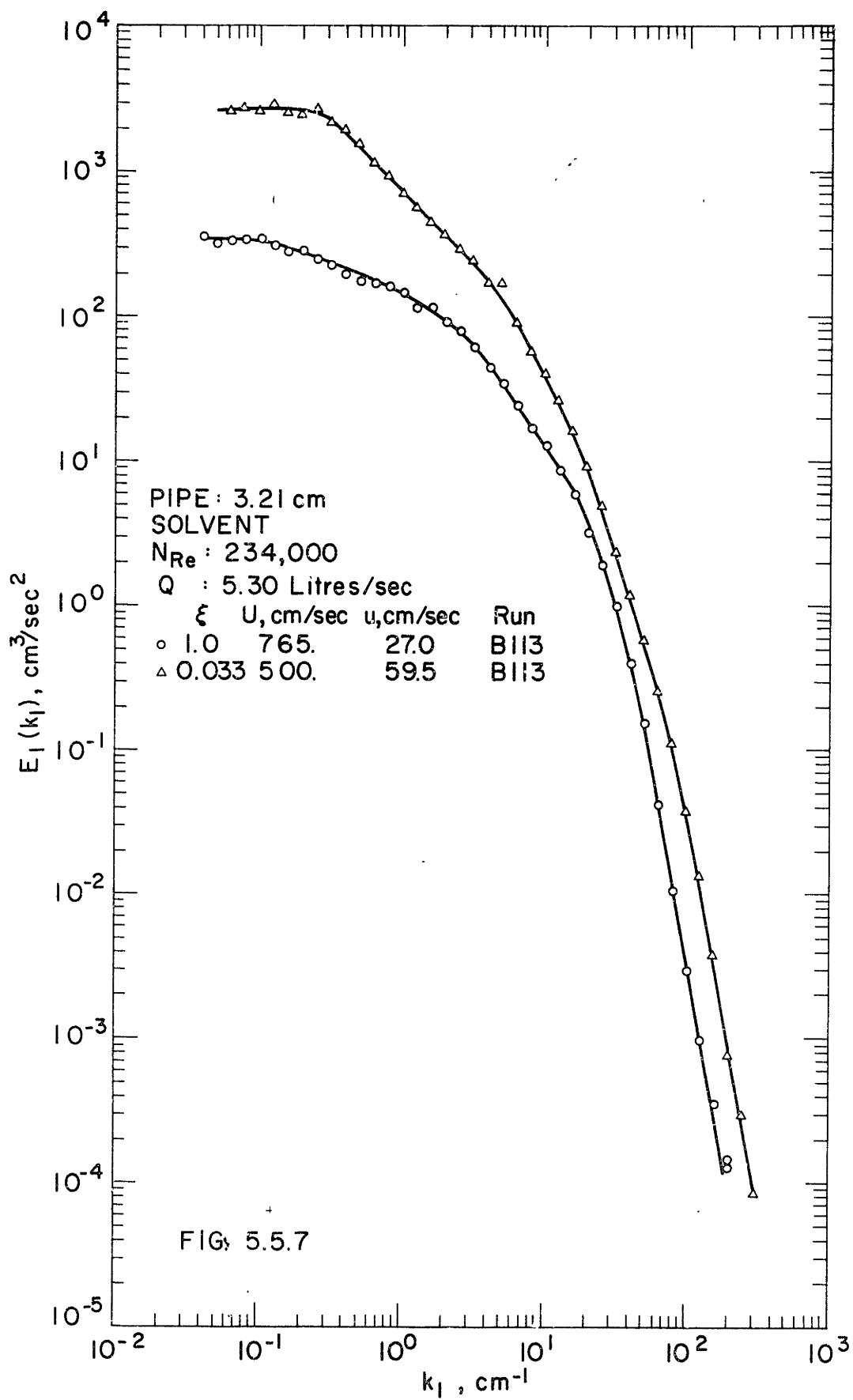


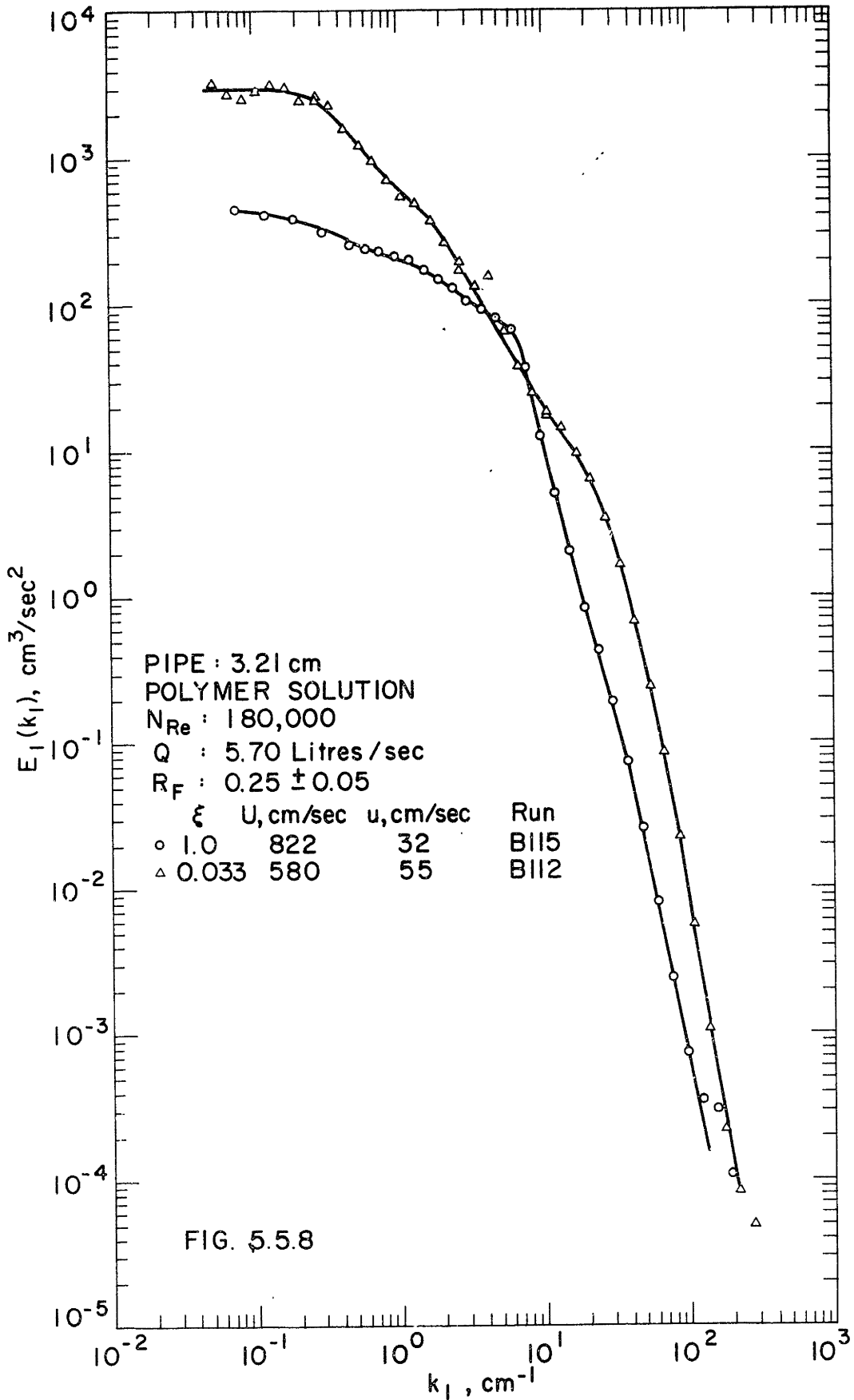












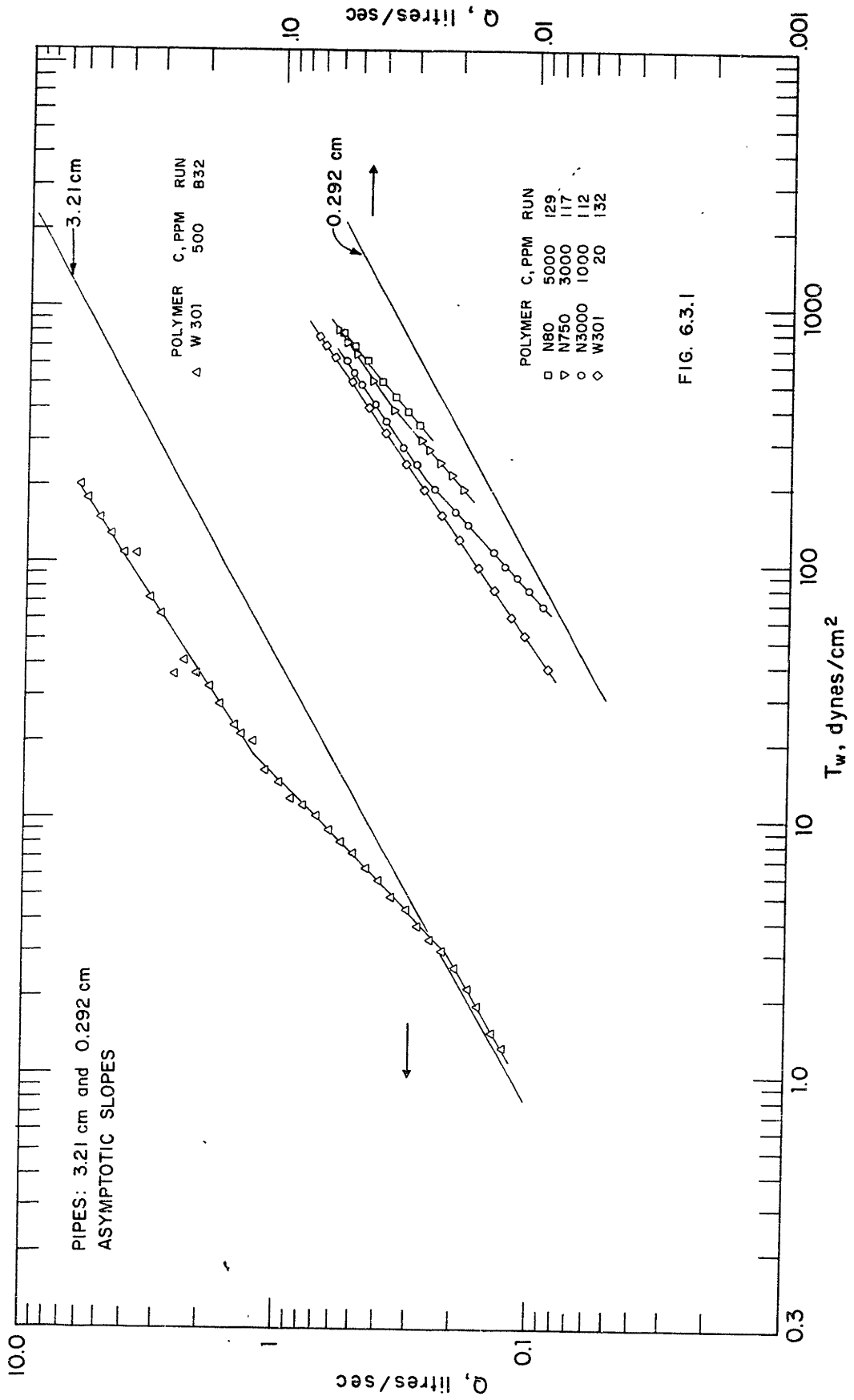
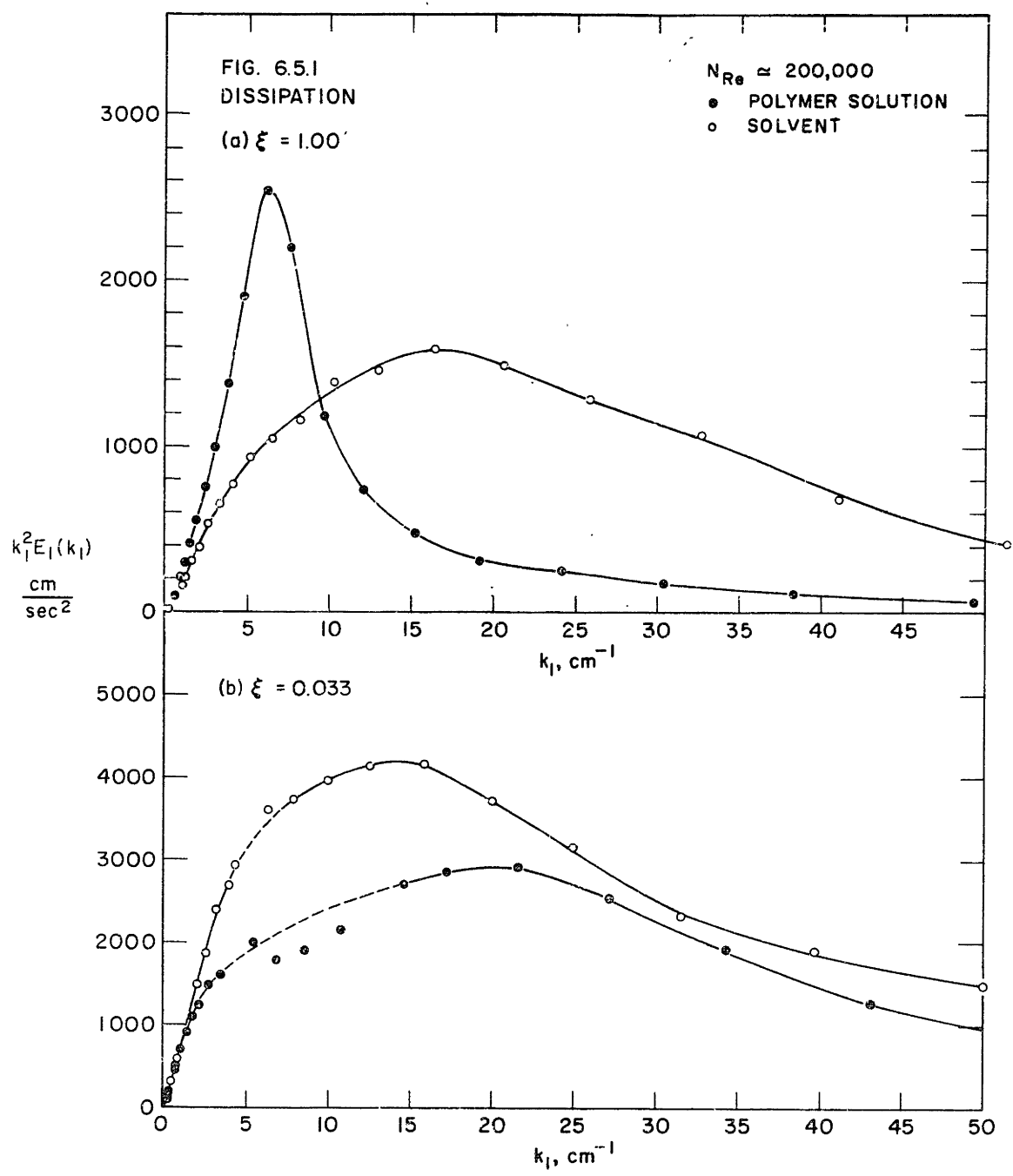
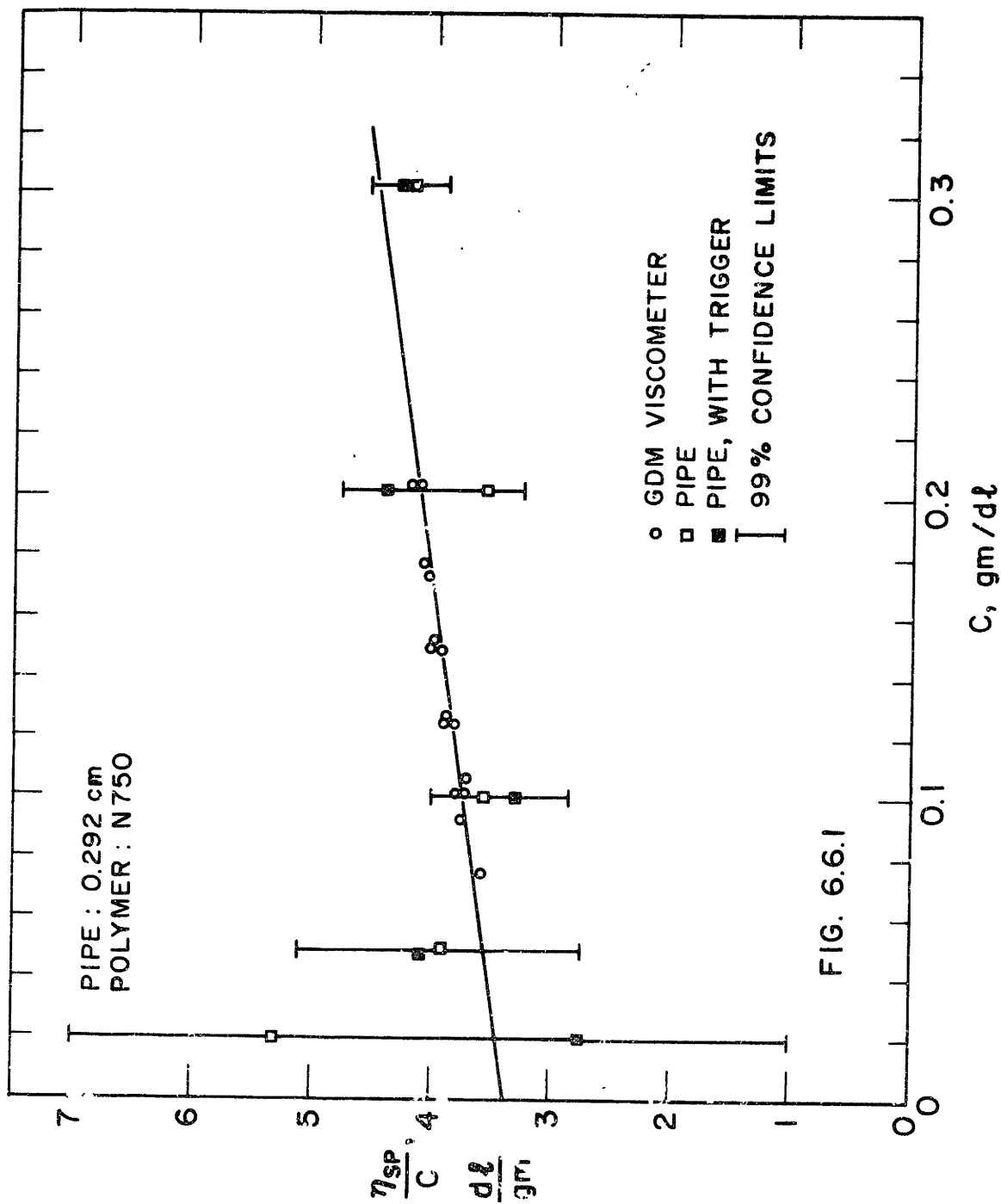
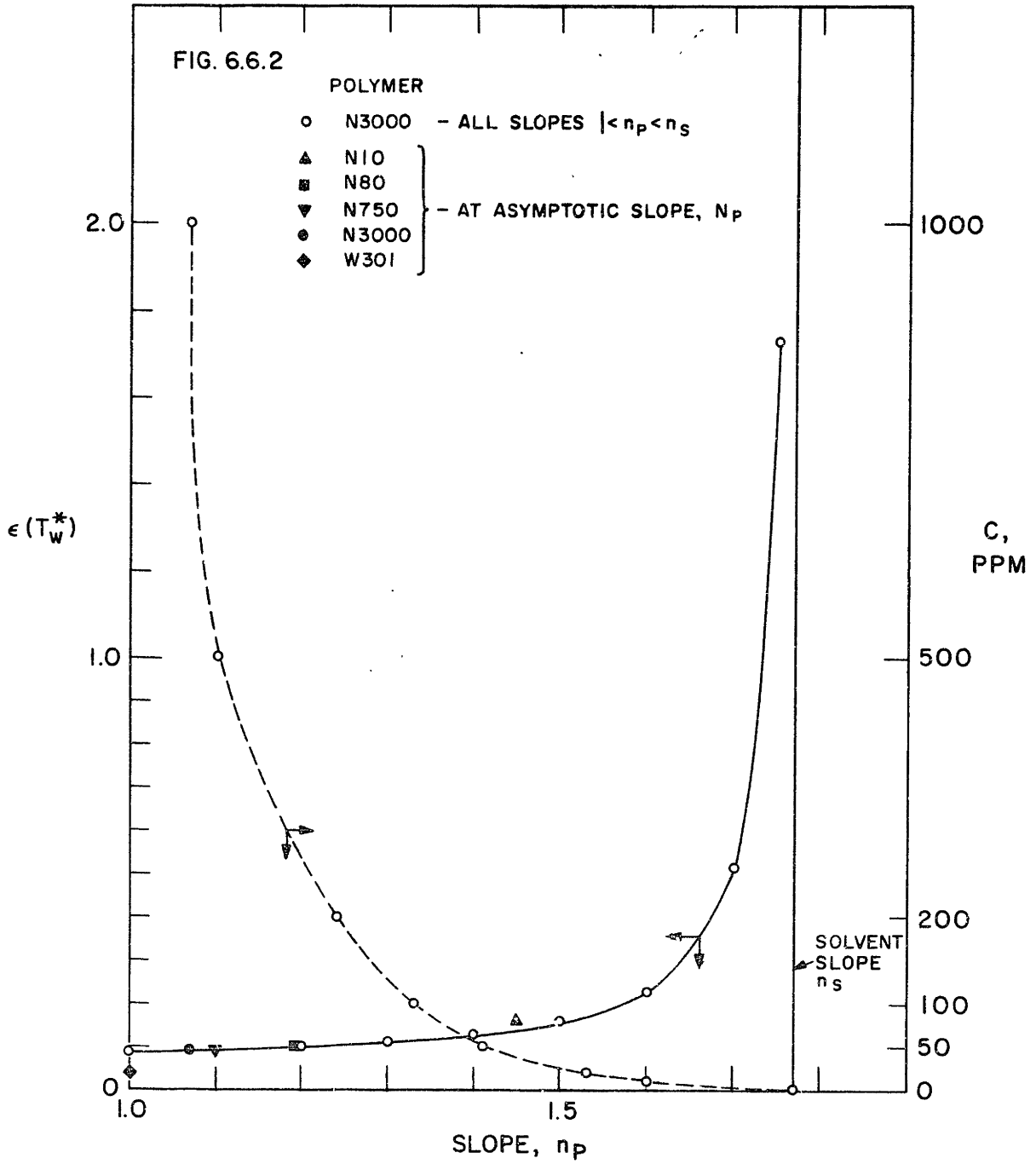


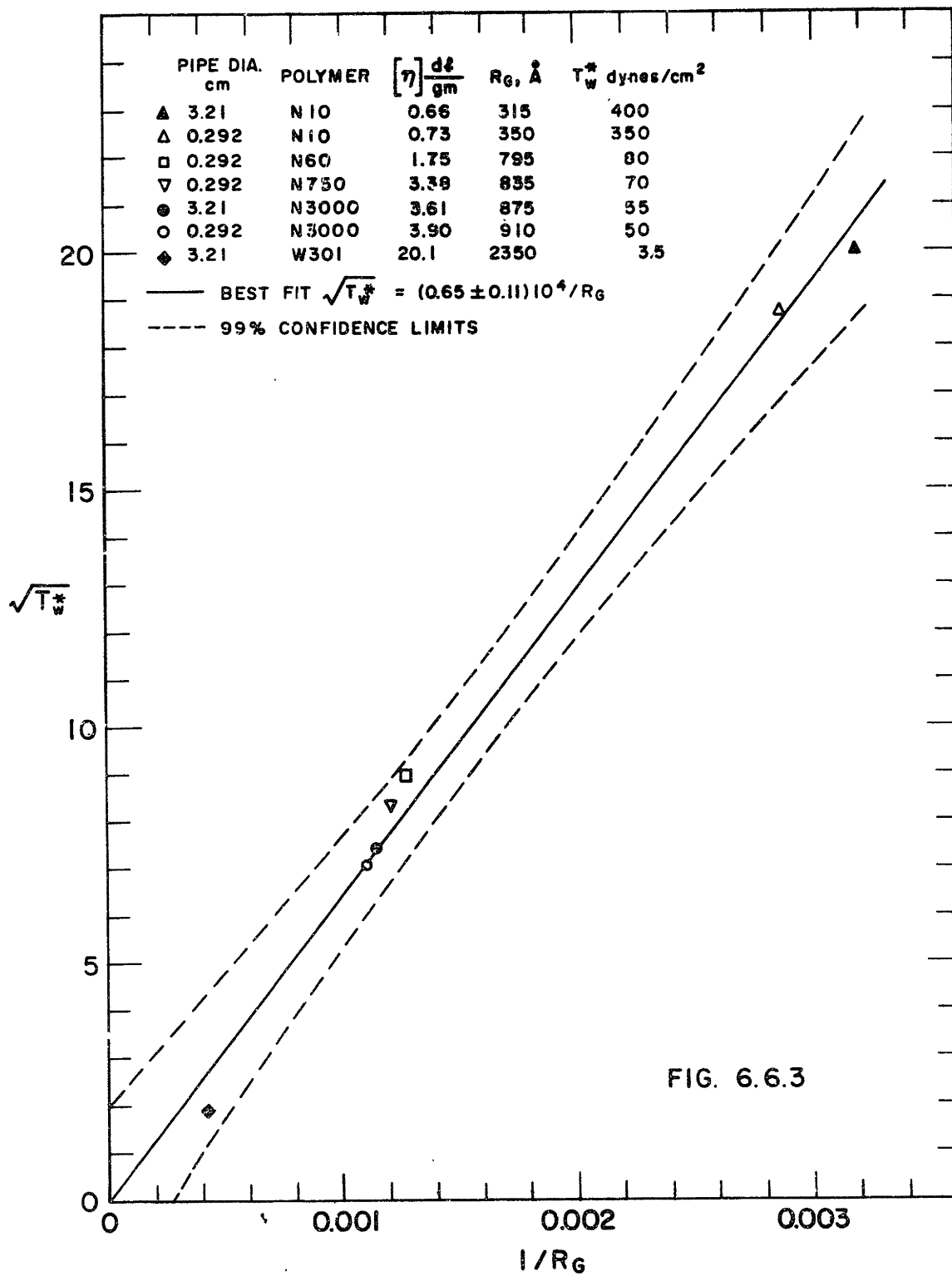
FIG. 6.3.1

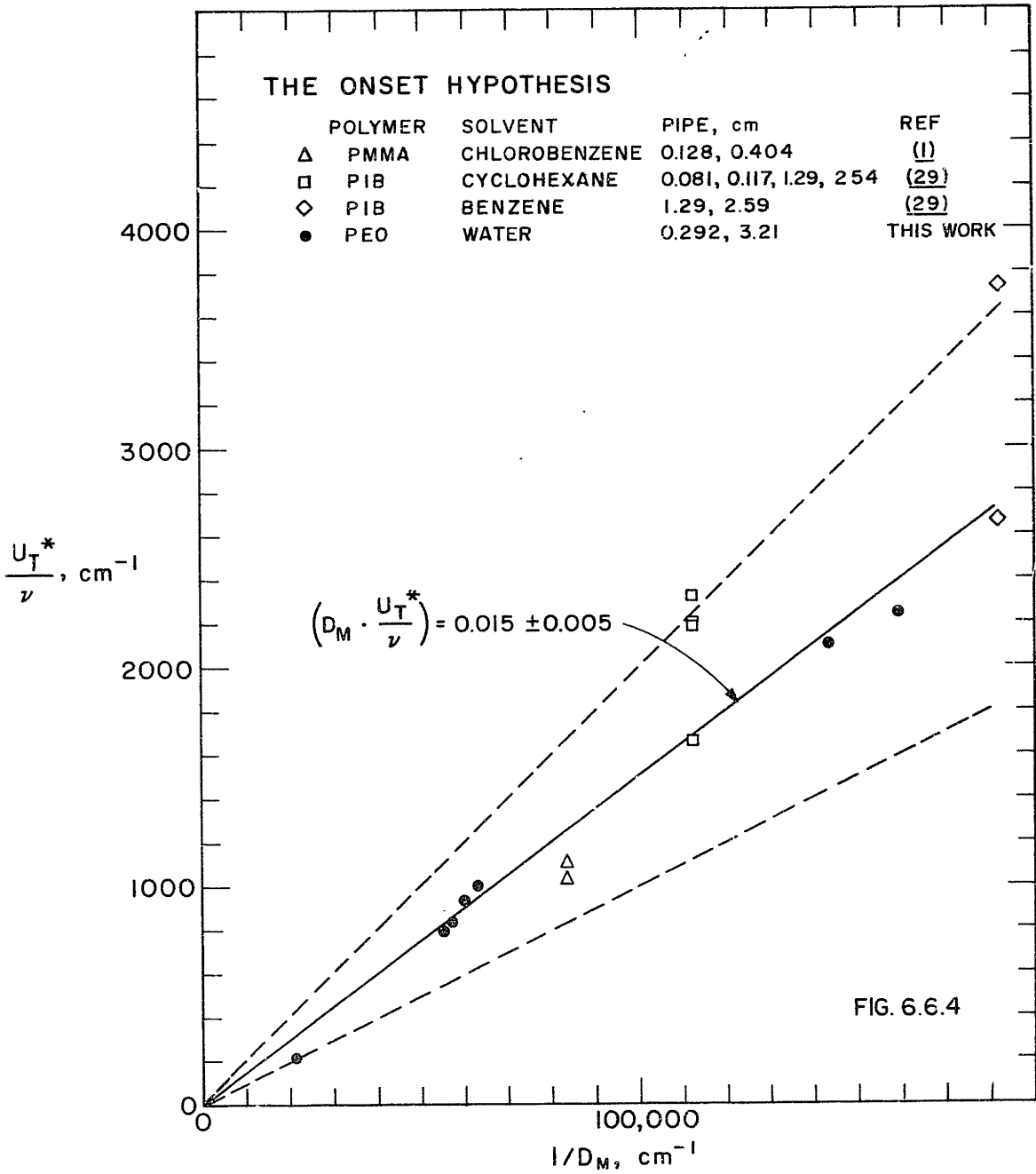


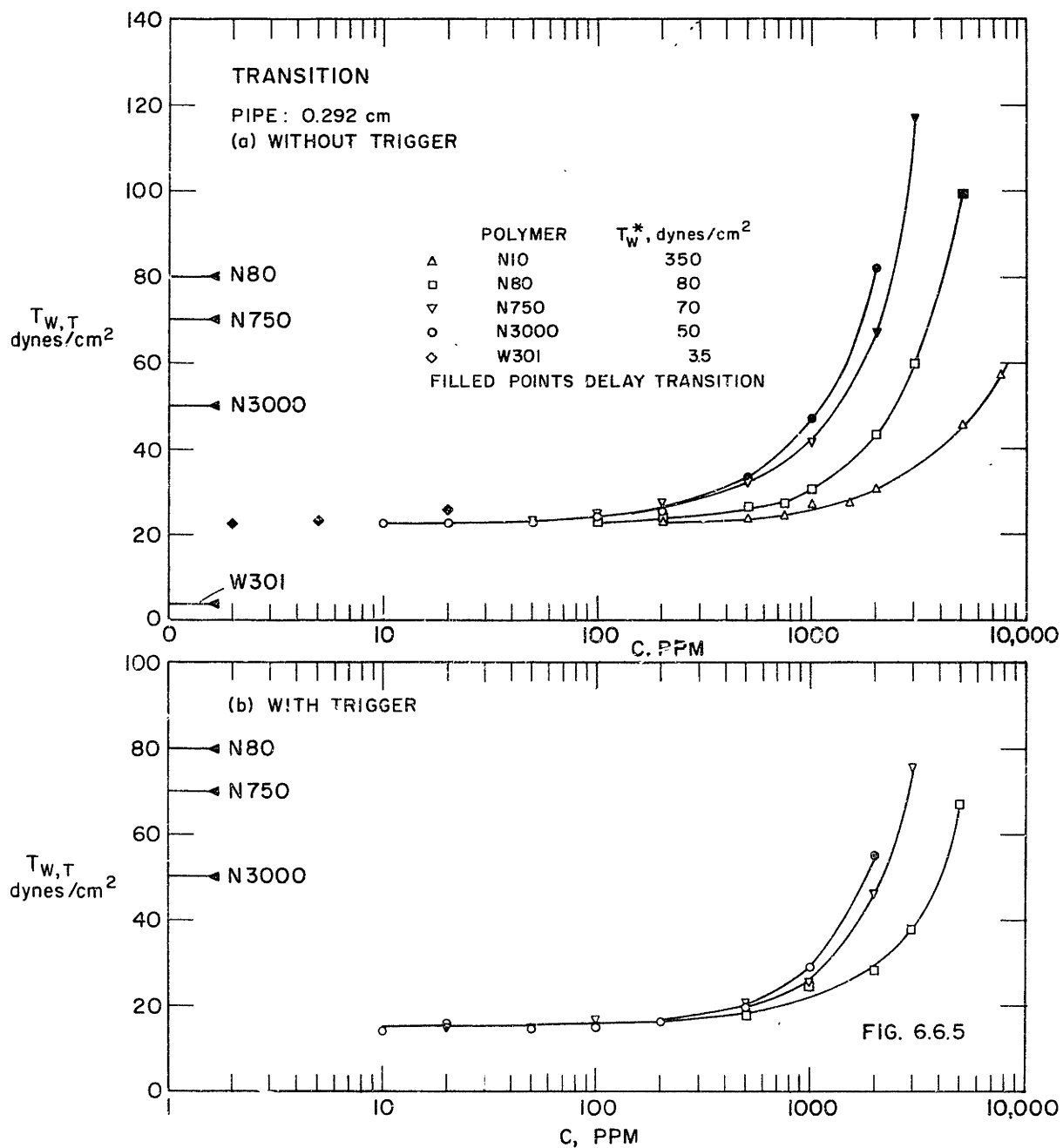






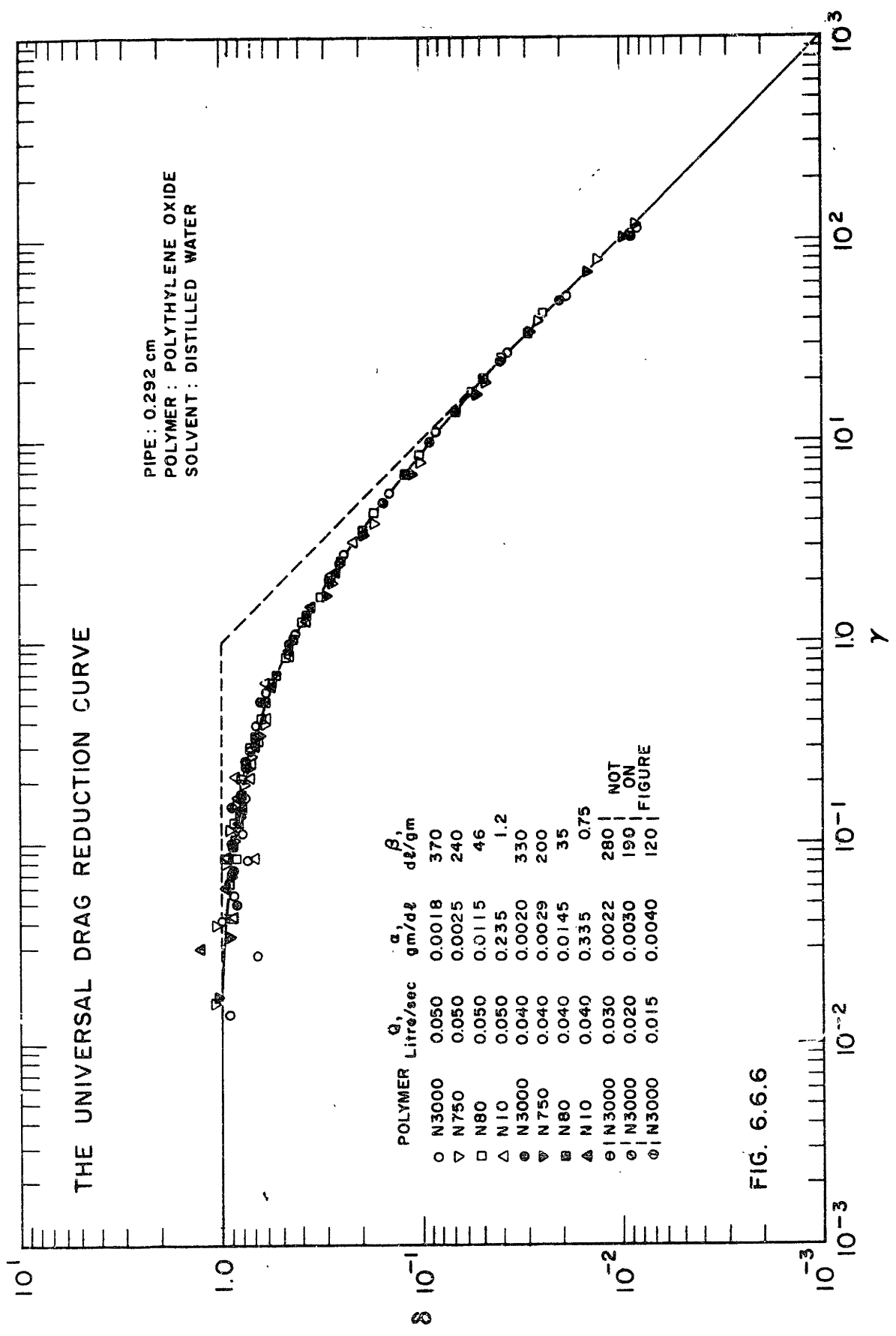






THE UNIVERSAL DRAG REDUCTION CURVE

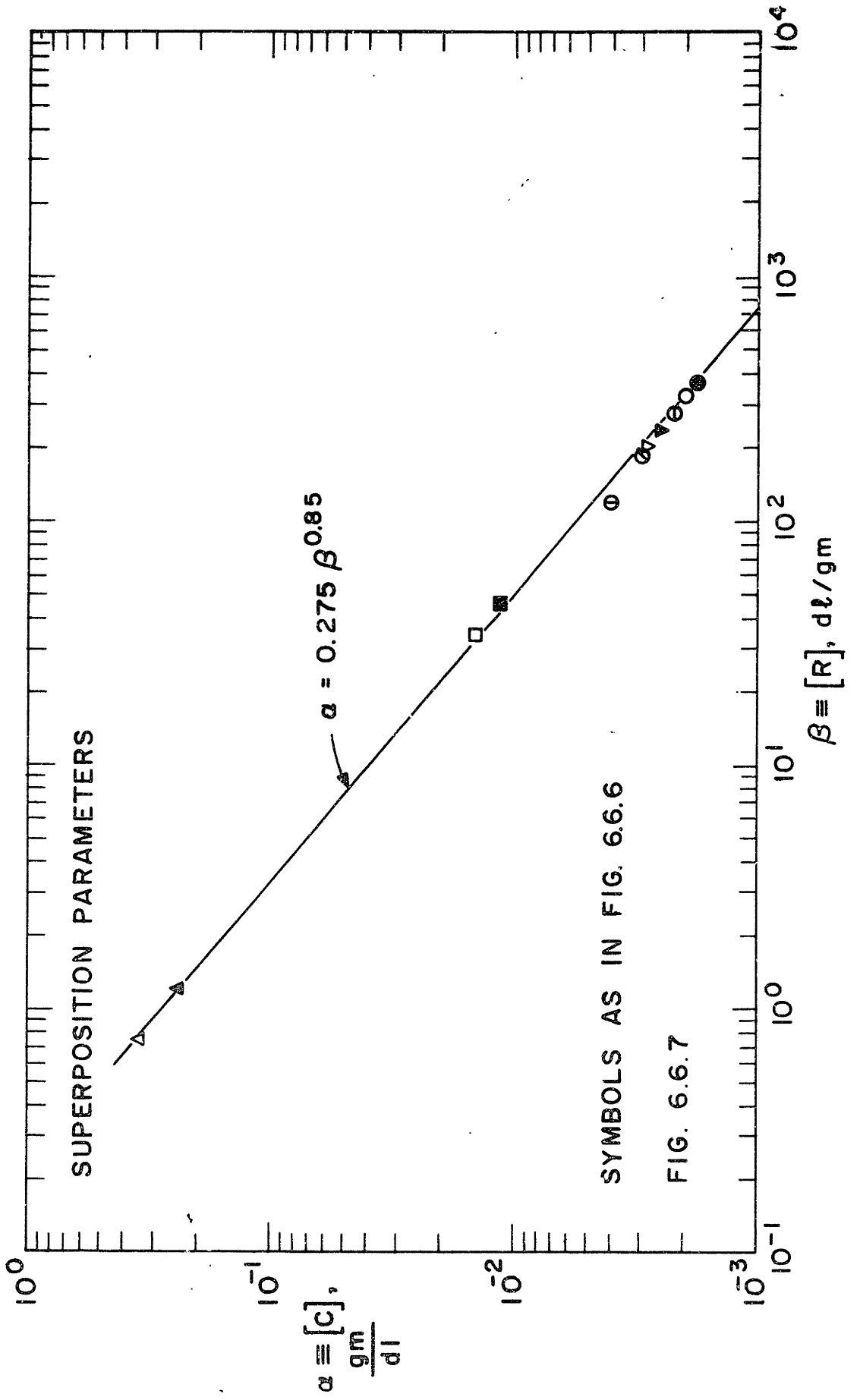
PIPE : 0.292 cm  
 POLYMER : POLYETHYLENE OXIDE  
 SOLVENT : DISTILLED WATER

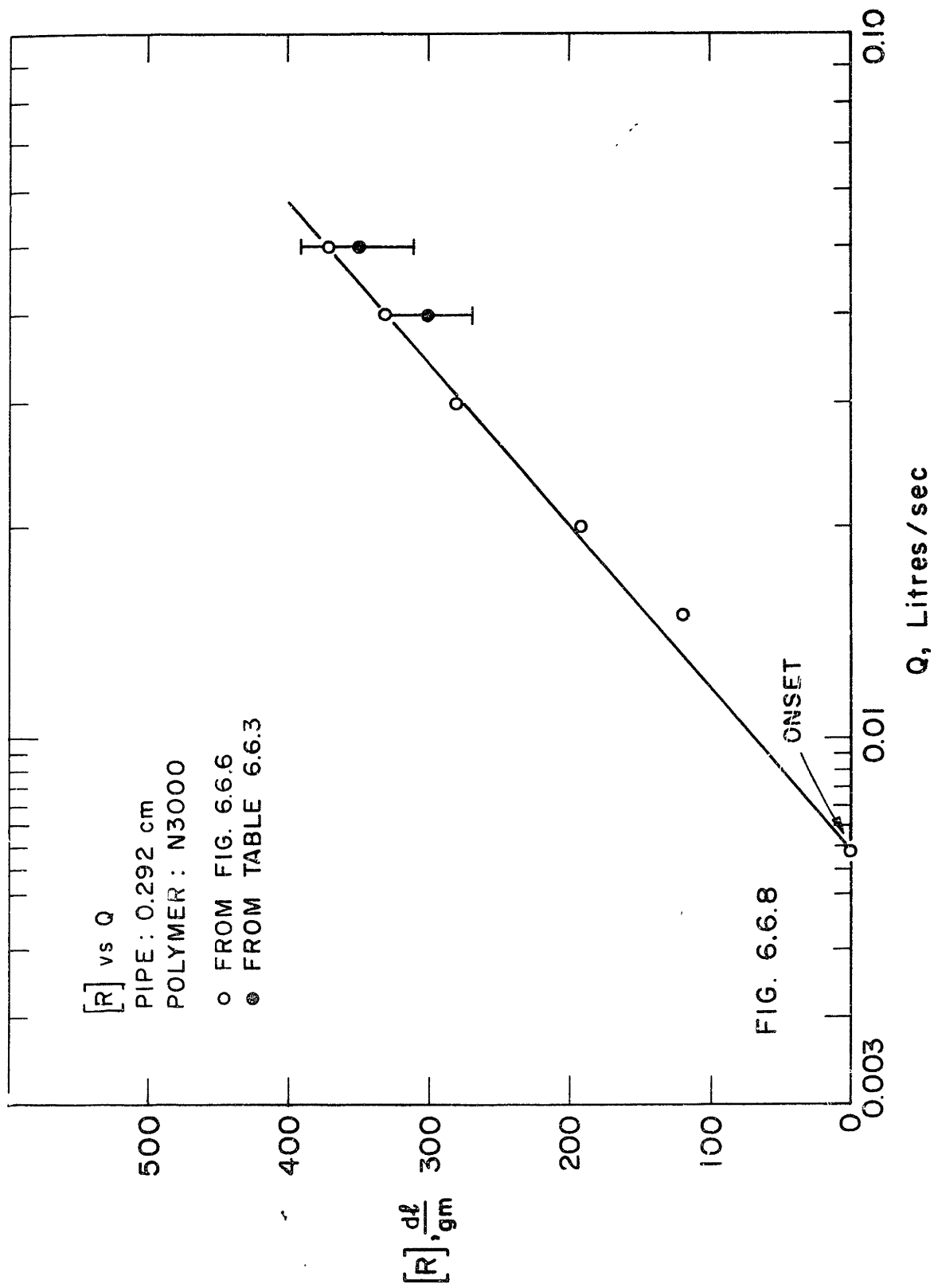


POLYMER	$Q$ , Litre/sec	$a$ , gm/dl	$\beta$ , dl/gm
○ N3000	0.050	0.0018	370
▽ N750	0.050	0.0025	240
□ N80	0.050	0.0115	46
△ N10	0.050	0.235	1.2
⊙ N3000	0.040	0.0020	330
⊖ N750	0.040	0.0029	200
⊗ N80	0.040	0.0145	35
▲ N10	0.040	0.335	0.75
⊕ N3000	0.030	0.0022	280
⊘ N3000	0.020	0.0030	190
⊙ N3000	0.015	0.0040	120

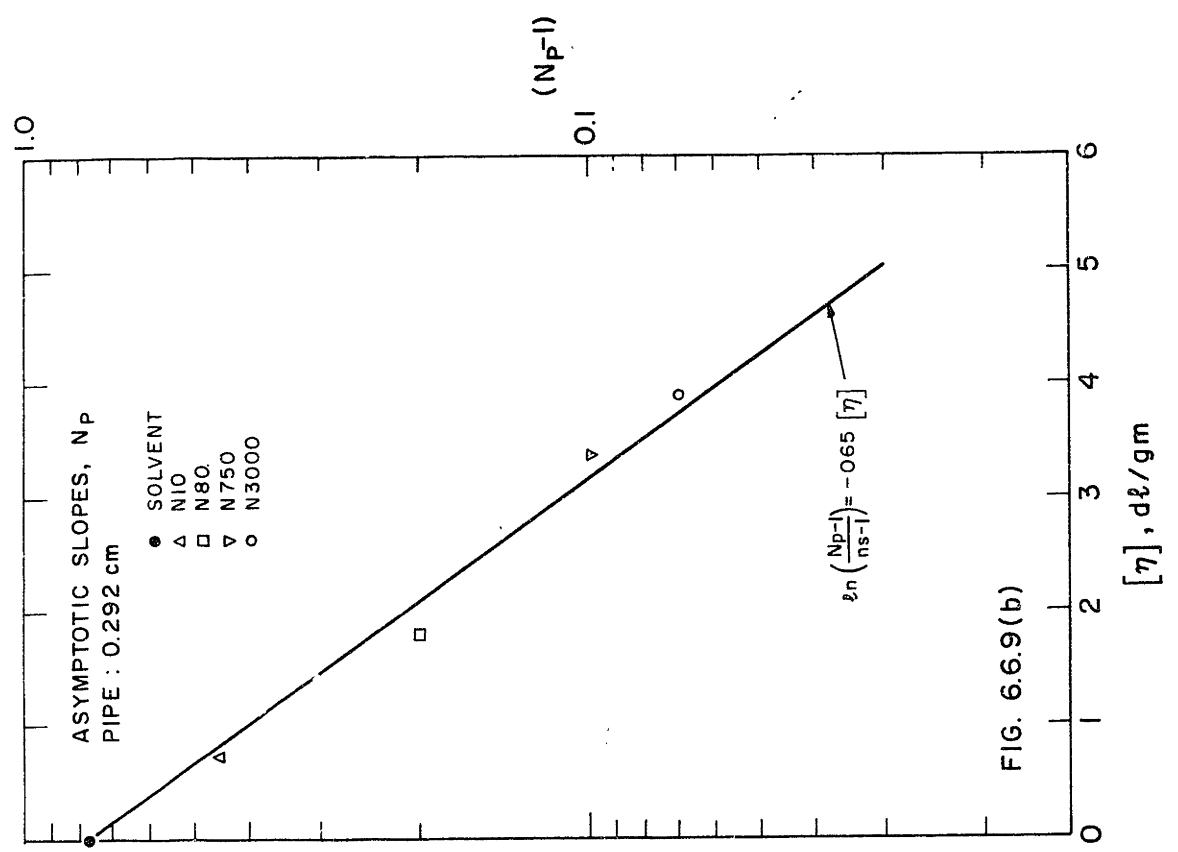
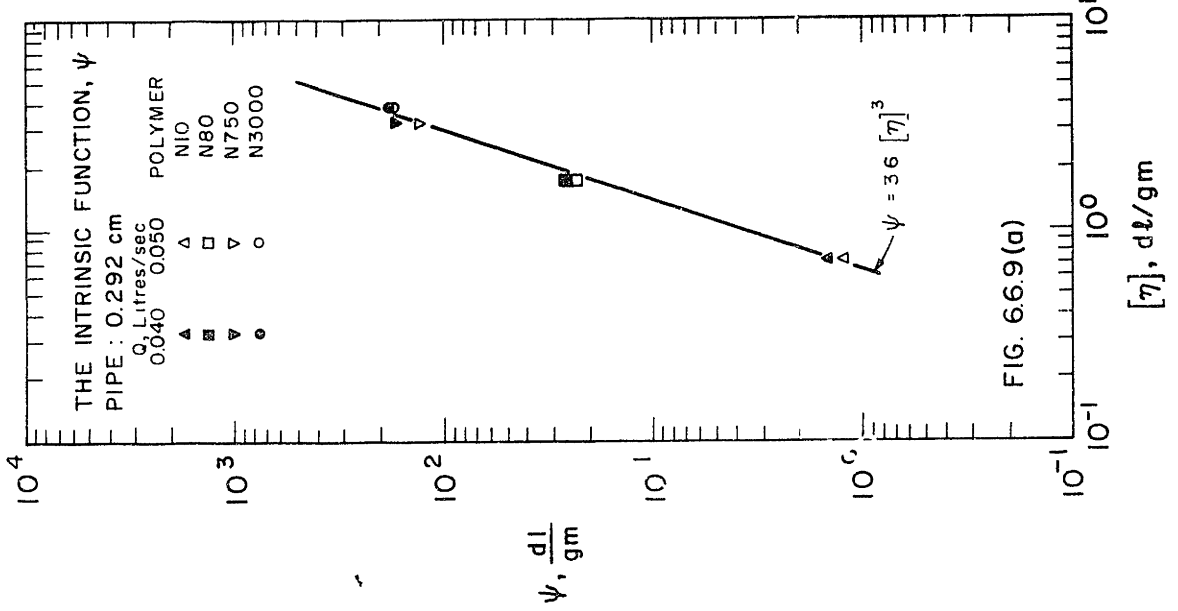
NOT  
ON  
FIGURE

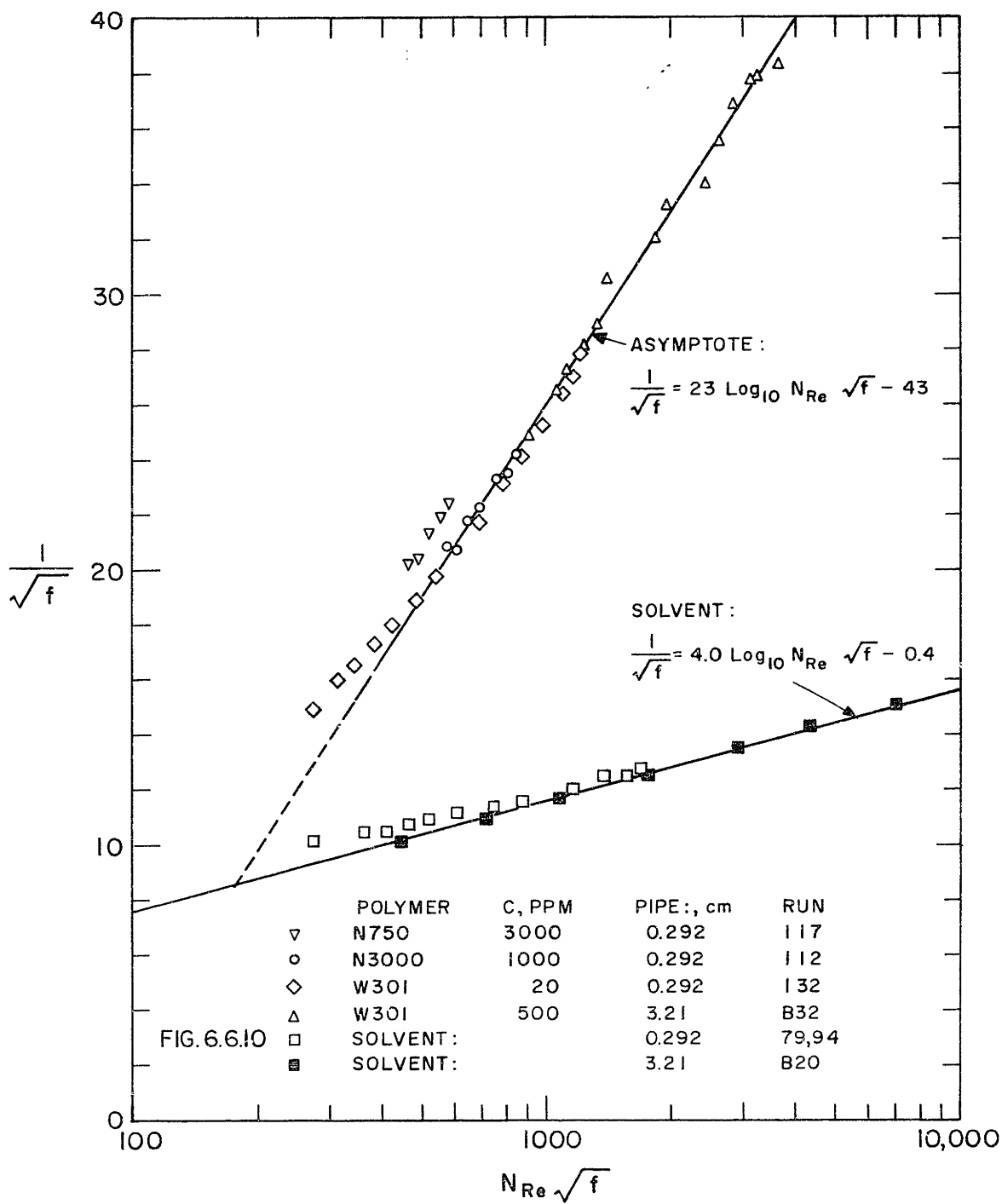
FIG. 6.6.6

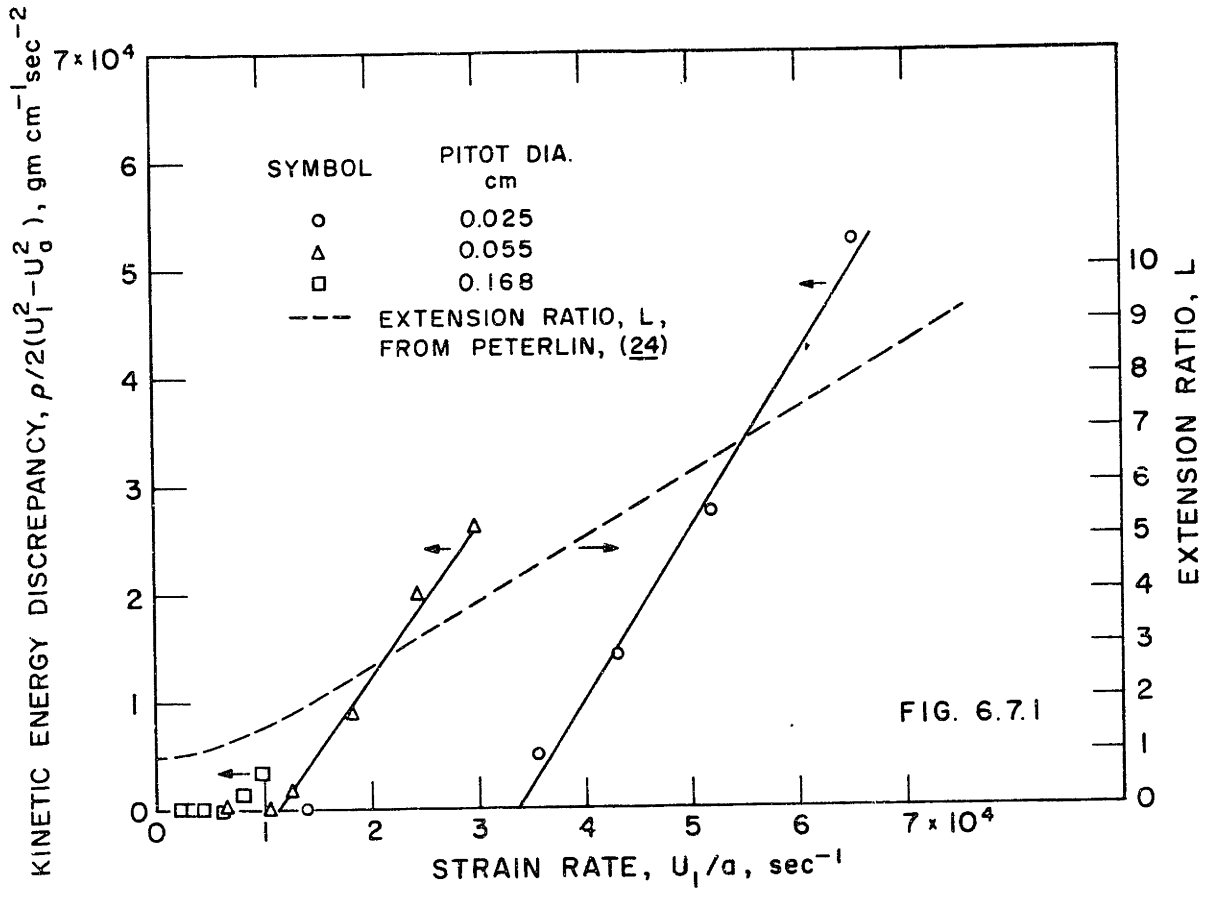


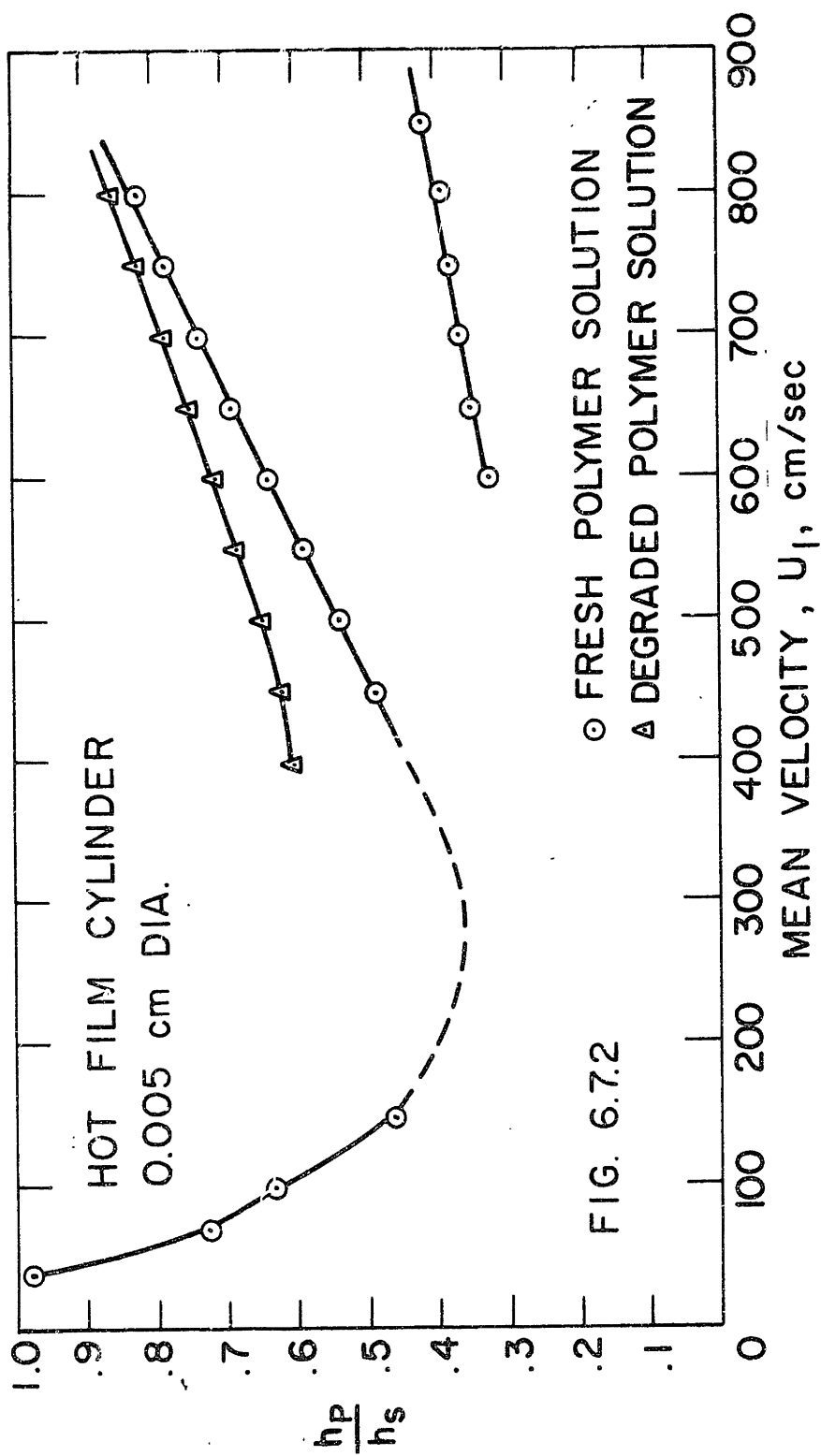












## THE "EFFECTIVE SLIP" MODEL

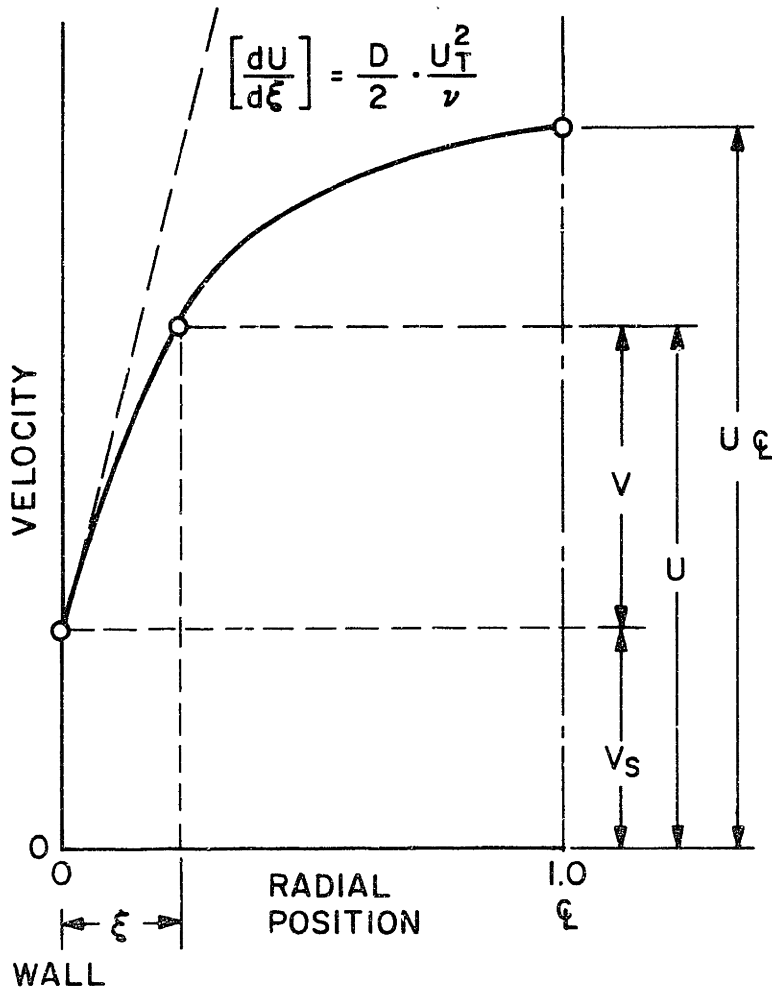
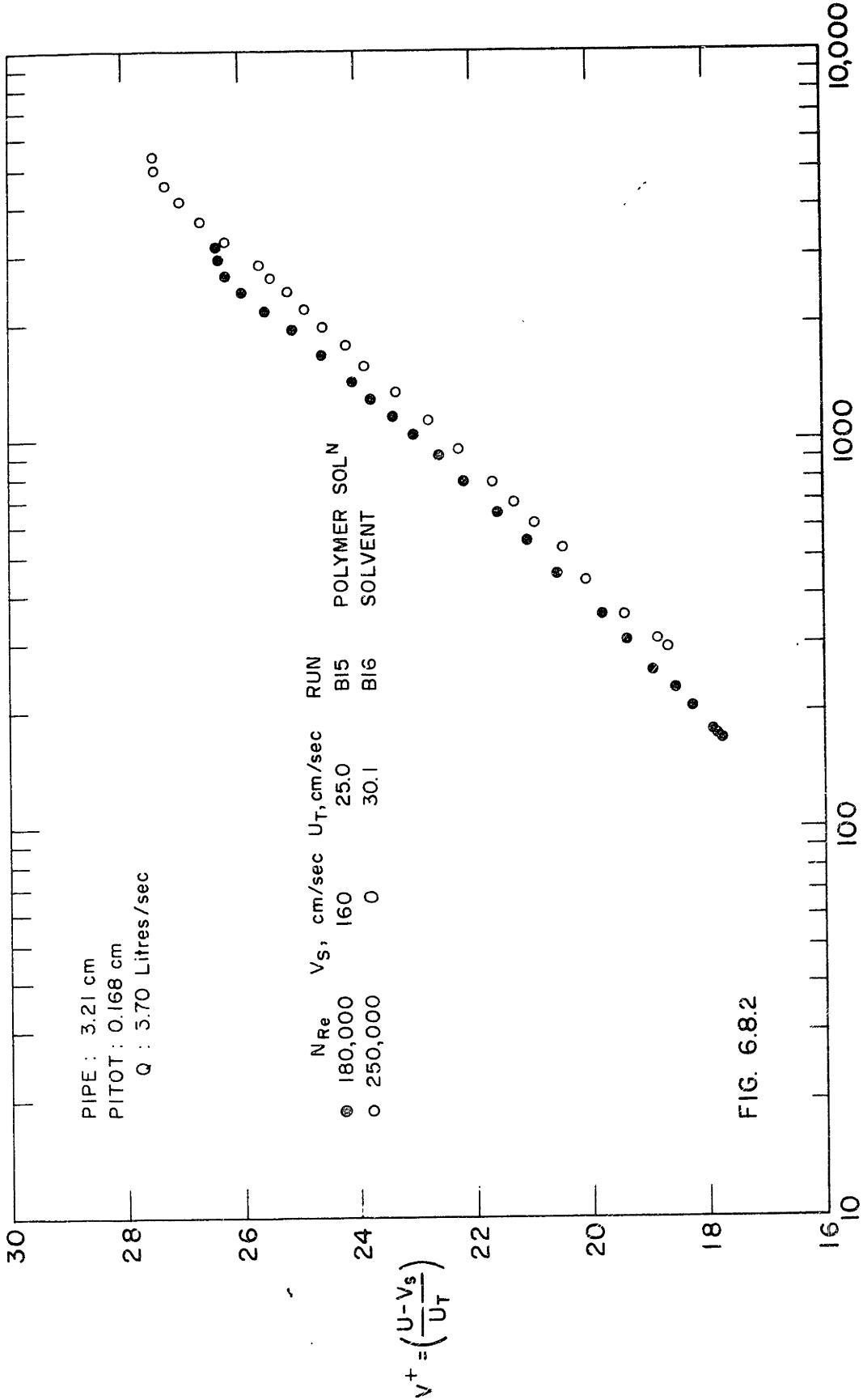
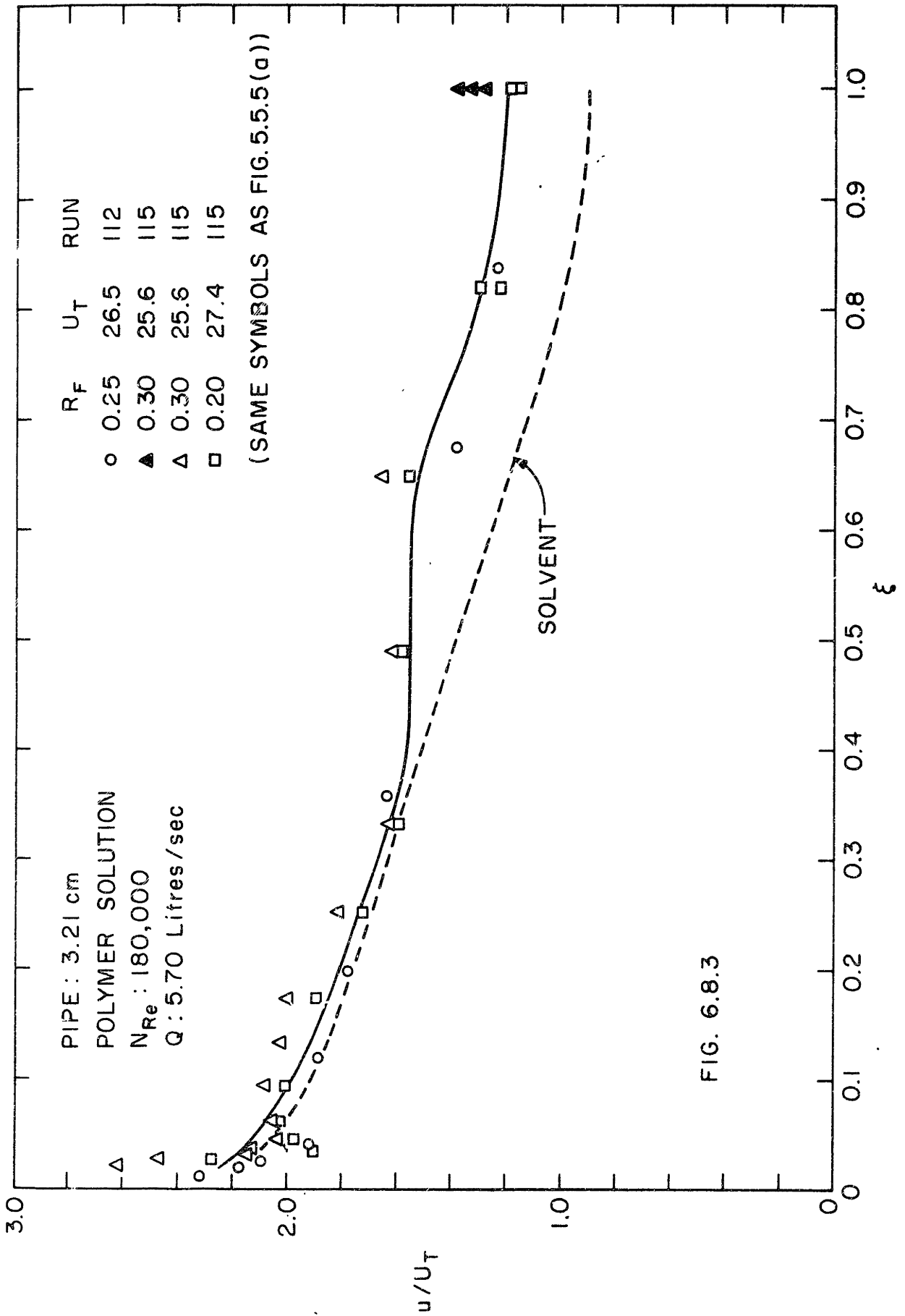
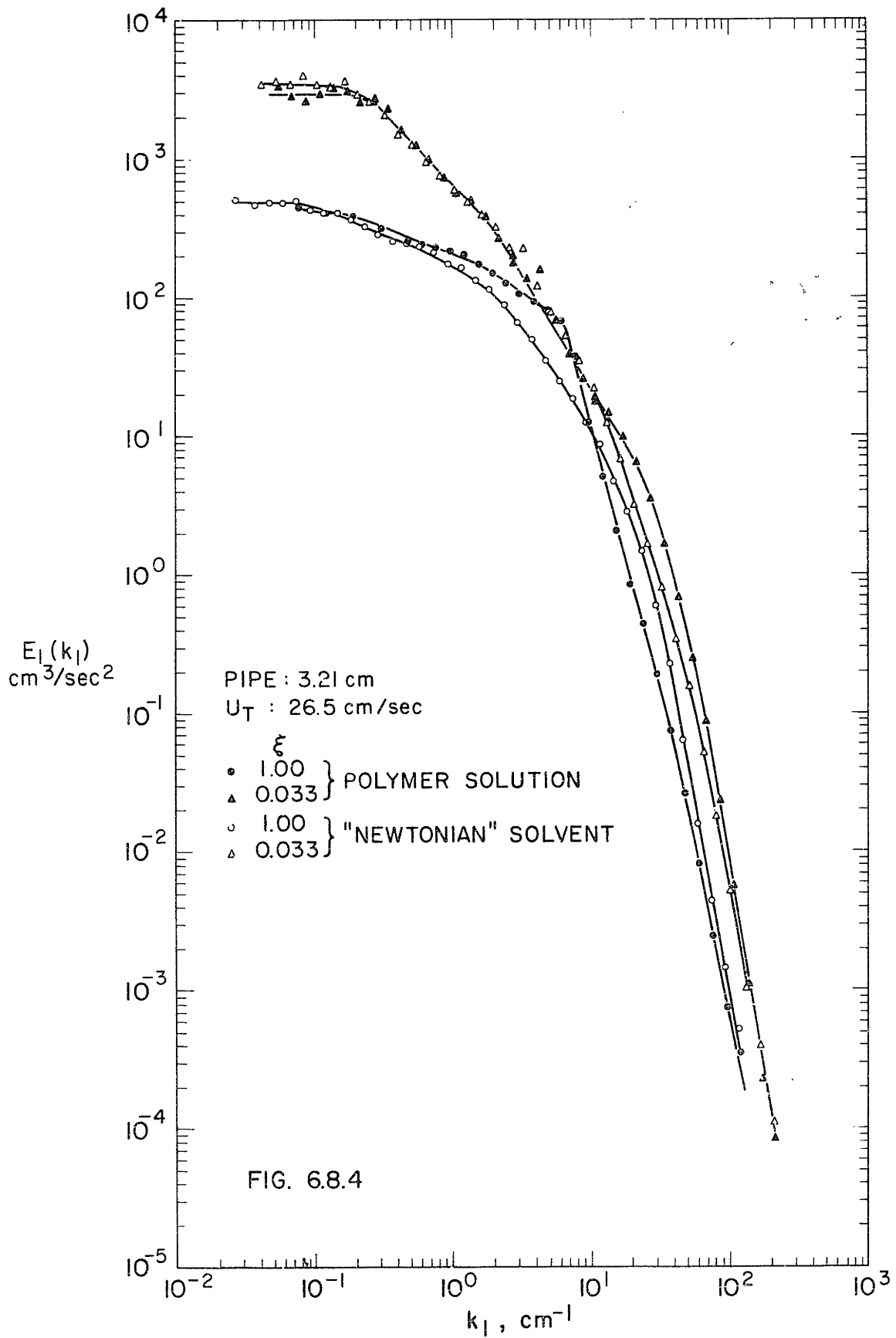


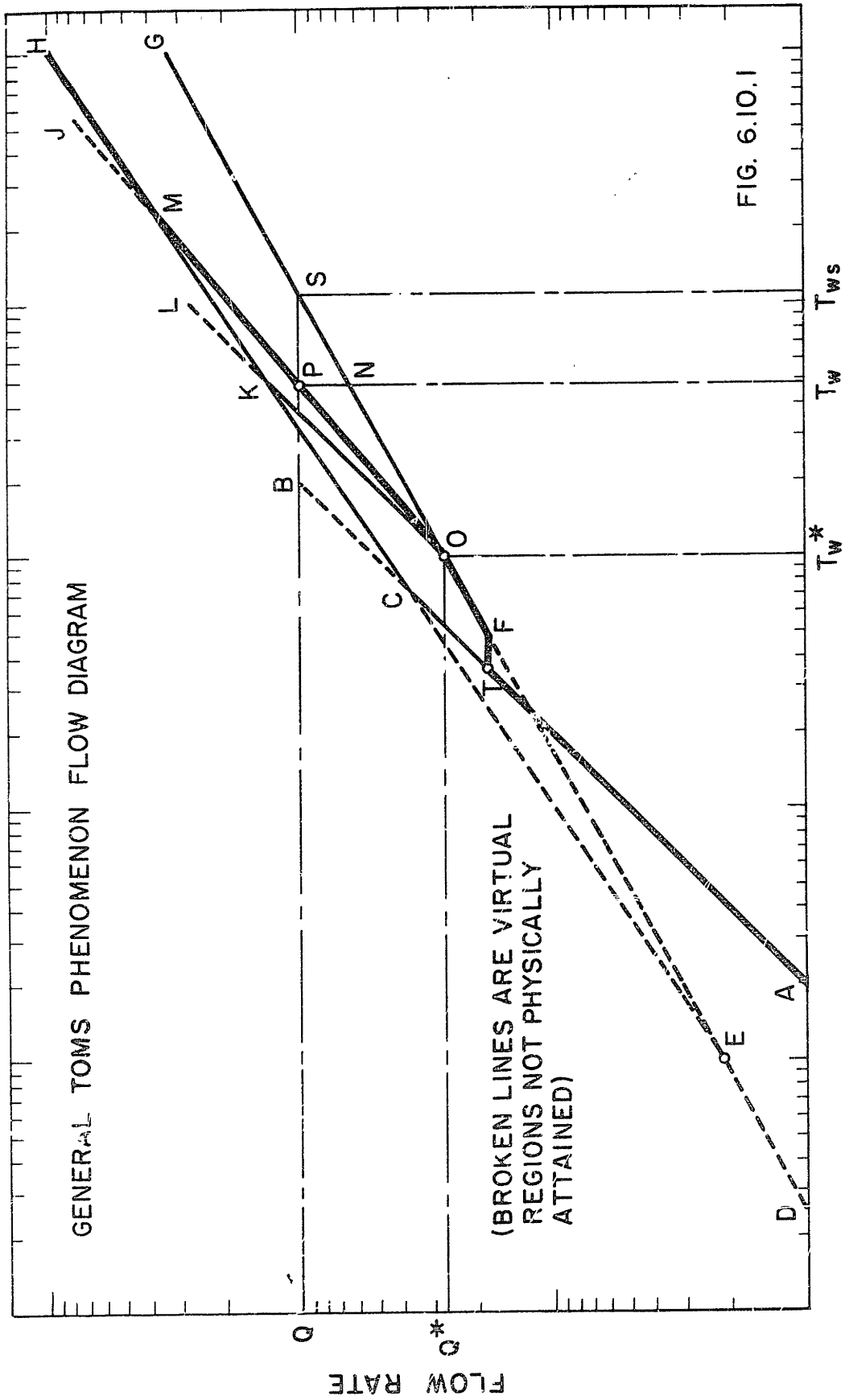
FIG. 6.8.1











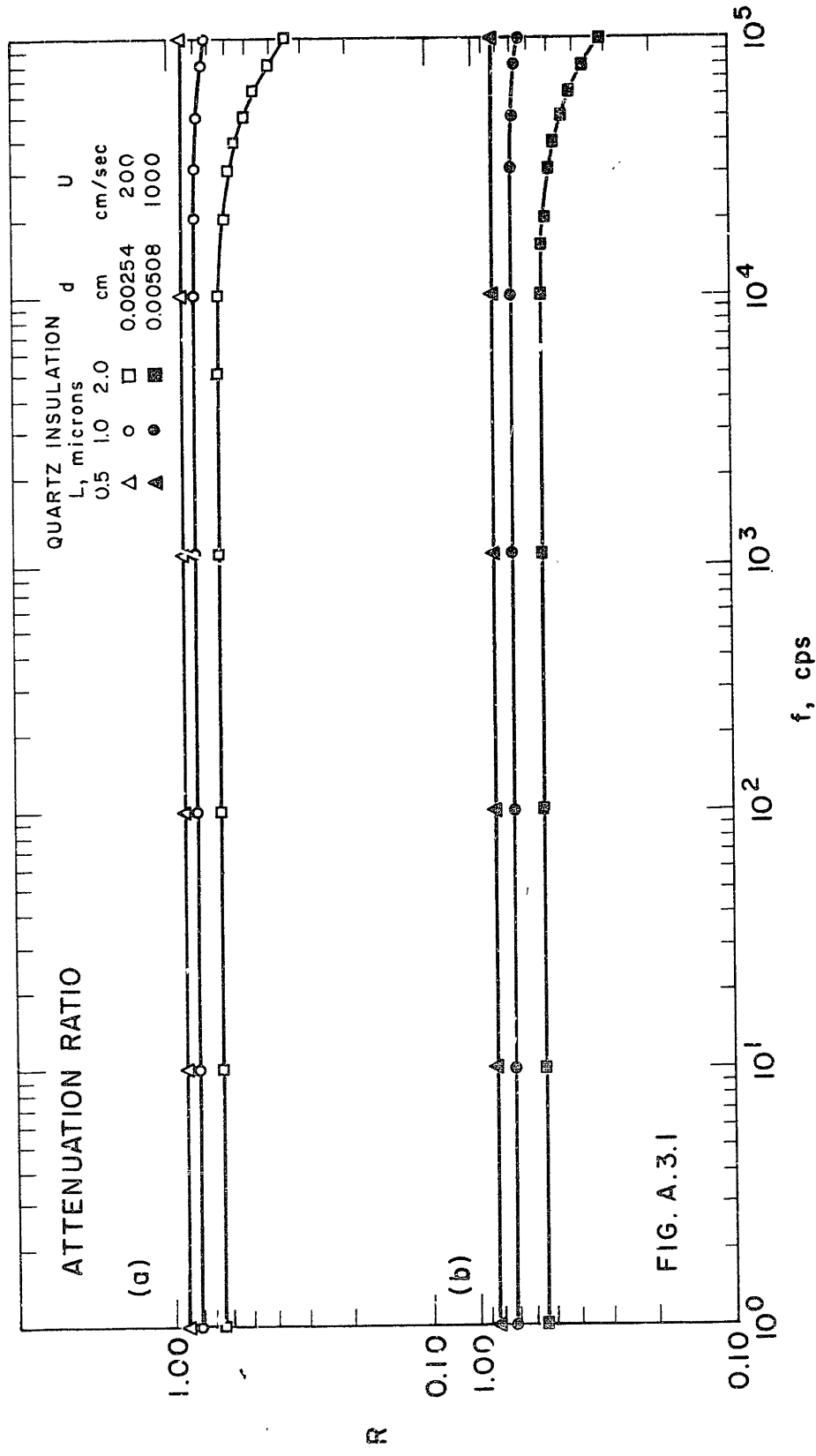
GENERAL TOMS PHENOMENON FLOW DIAGRAM

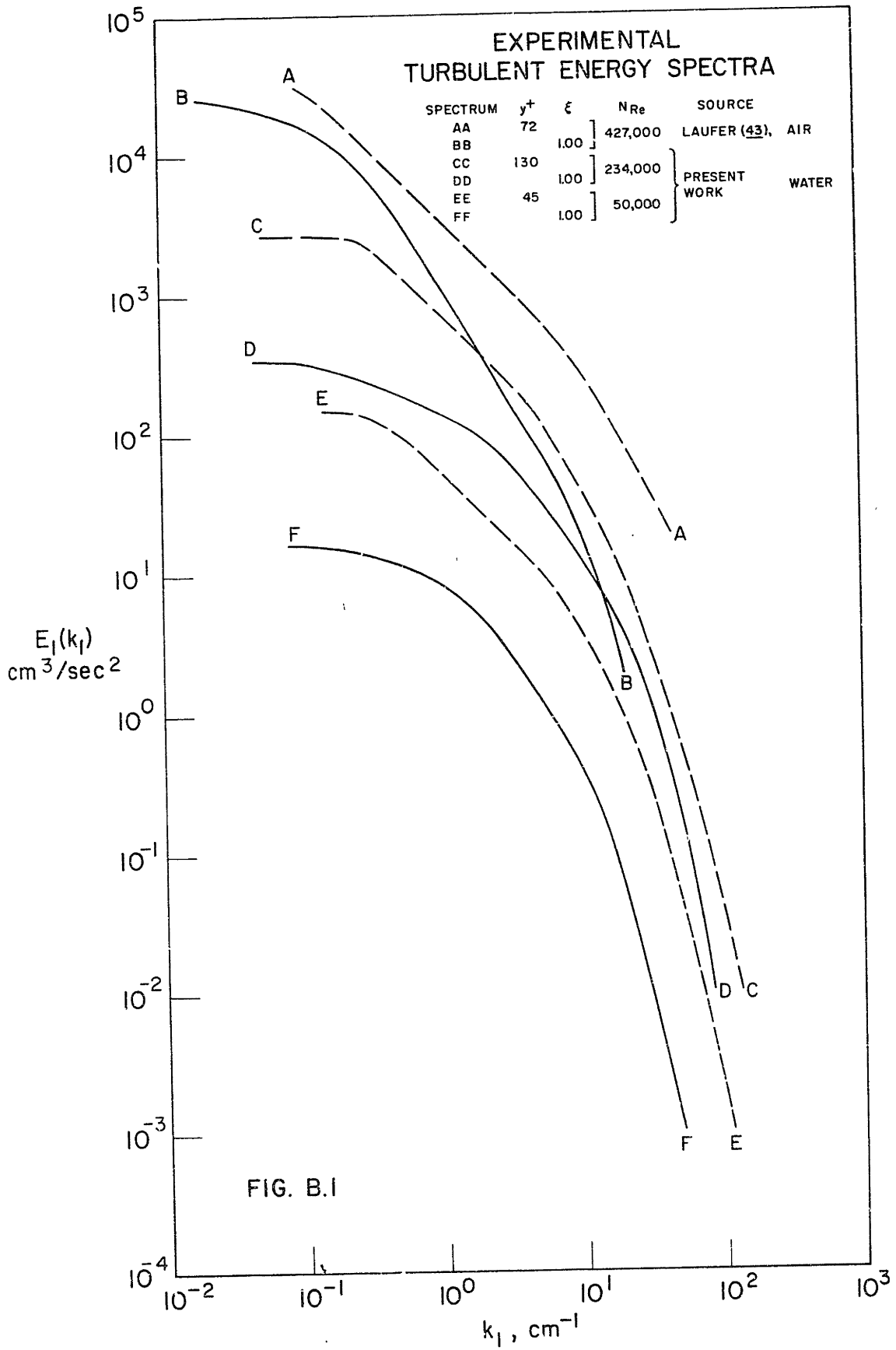
FIG. 6.10.1

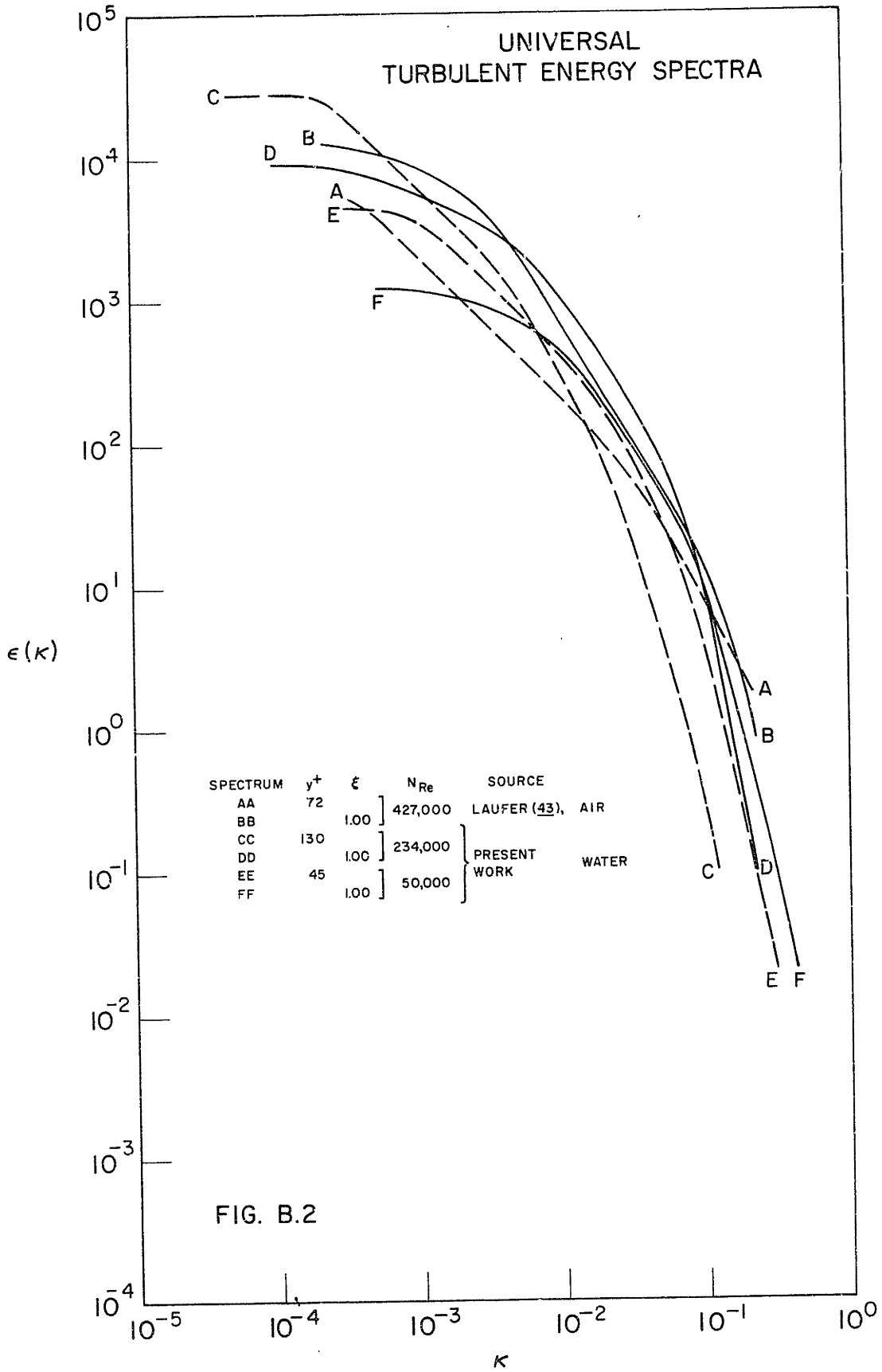
(BROKEN LINES ARE VIRTUAL  
REGIONS NOT PHYSICALLY  
ATTAINED)

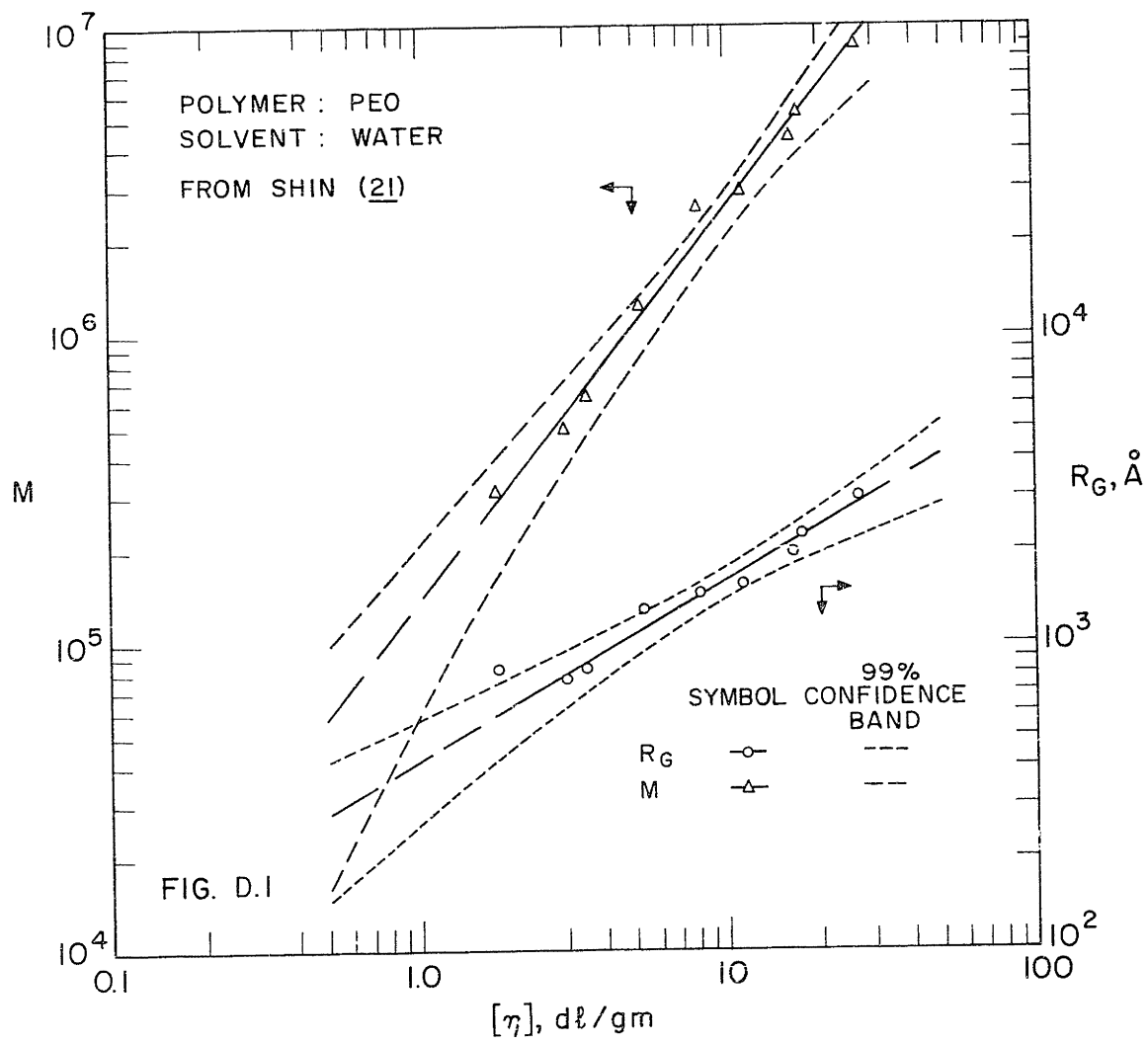
WALL SHEAR STRESS

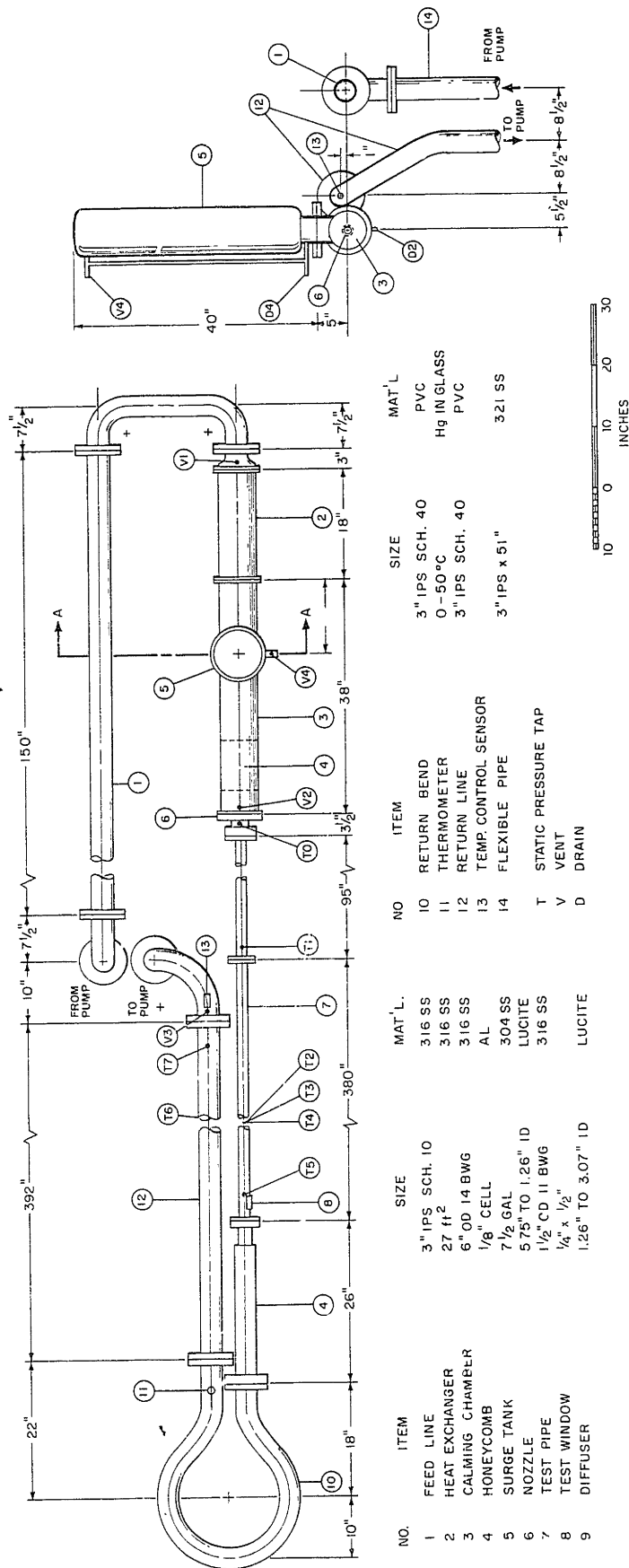
FLOW RATE







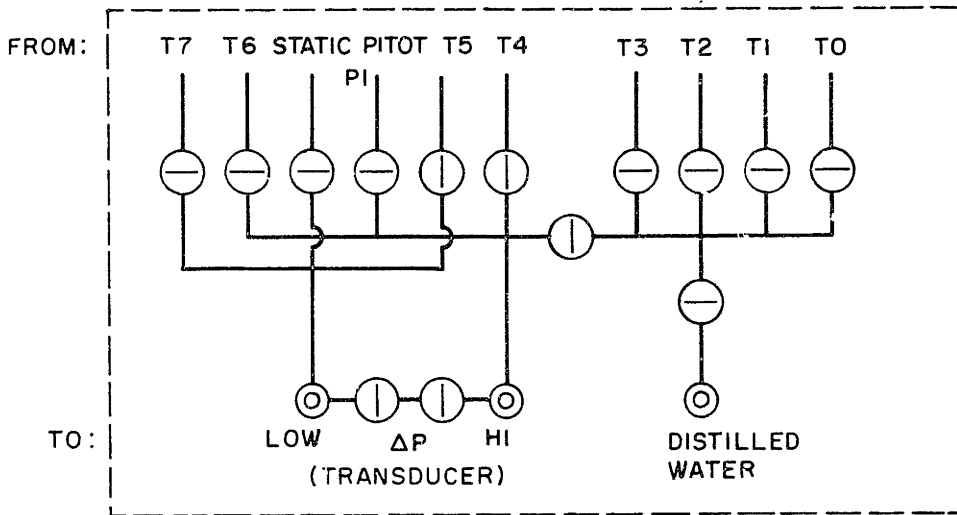







SECTION AT A-A

FIG. E.2.1 PLAN OF 3.21cm SYSTEM LOOP

CONTROL PANELS  
(a) TEST SECTION



NOTE: ALL TOP ROW BALL VALVES HAVE ASSOCIATED PURGE VALVE

-  BALL VALVE
-  NEEDLE VALVE
-  QUICK CONNECT

(b) PUMP END

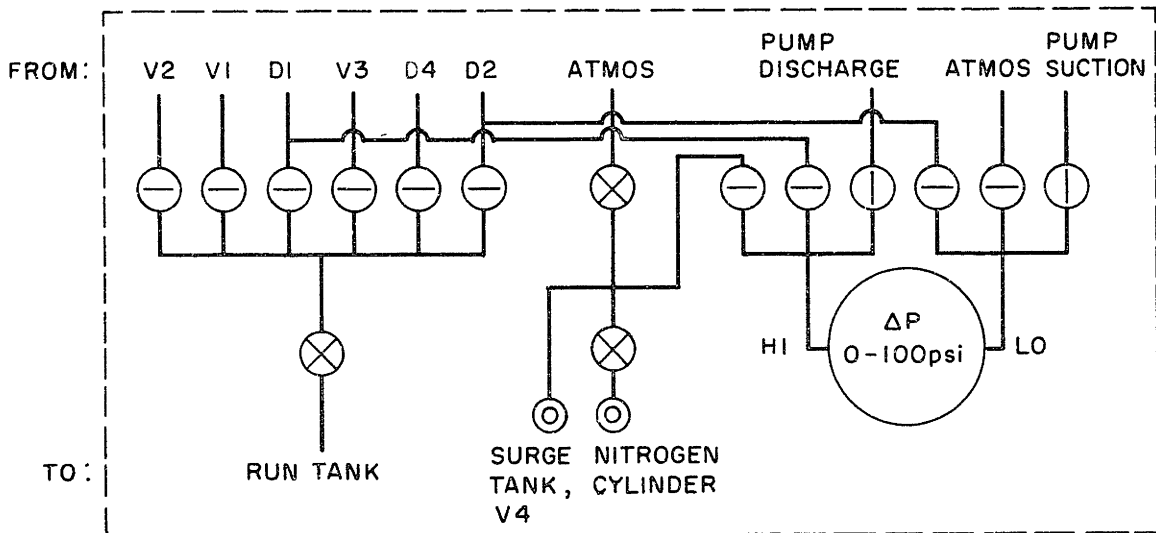
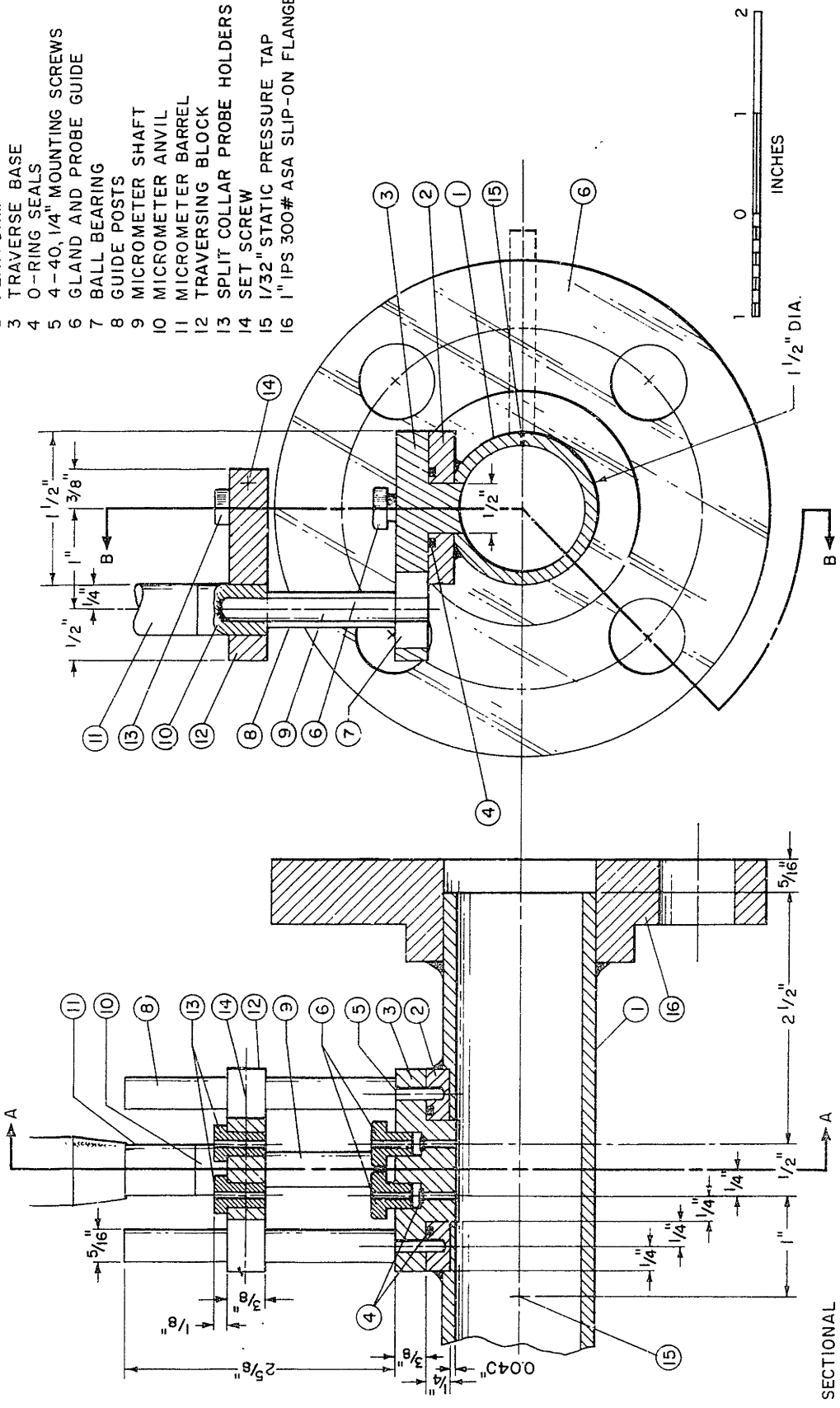


FIG. E.2.2

- No ITEM
- 1 TEST PIPE, 1/2" OD, 11 BWG
  - 2 PLATFORM
  - 3 TRAVERSE BASE
  - 4 O-RING SEALS
  - 5 4-40, 1/4" MOUNTING SCREWS
  - 6 GLAND AND PROBE GUIDE
  - 7 BALL BEARING
  - 8 GUIDE POSTS
  - 9 MICROMETER SHAFT
  - 10 MICROMETER ANVIL
  - 11 MICROMETER BARREL
  - 12 TRAVERSING BLOCK
  - 13 SPLIT COLLAR PROBE HOLDERS
  - 14 SET SCREW
  - 15 1/32" STATIC PRESSURE TAP
  - 16 1" IPS 300# ASA SLIP-ON FLANGE

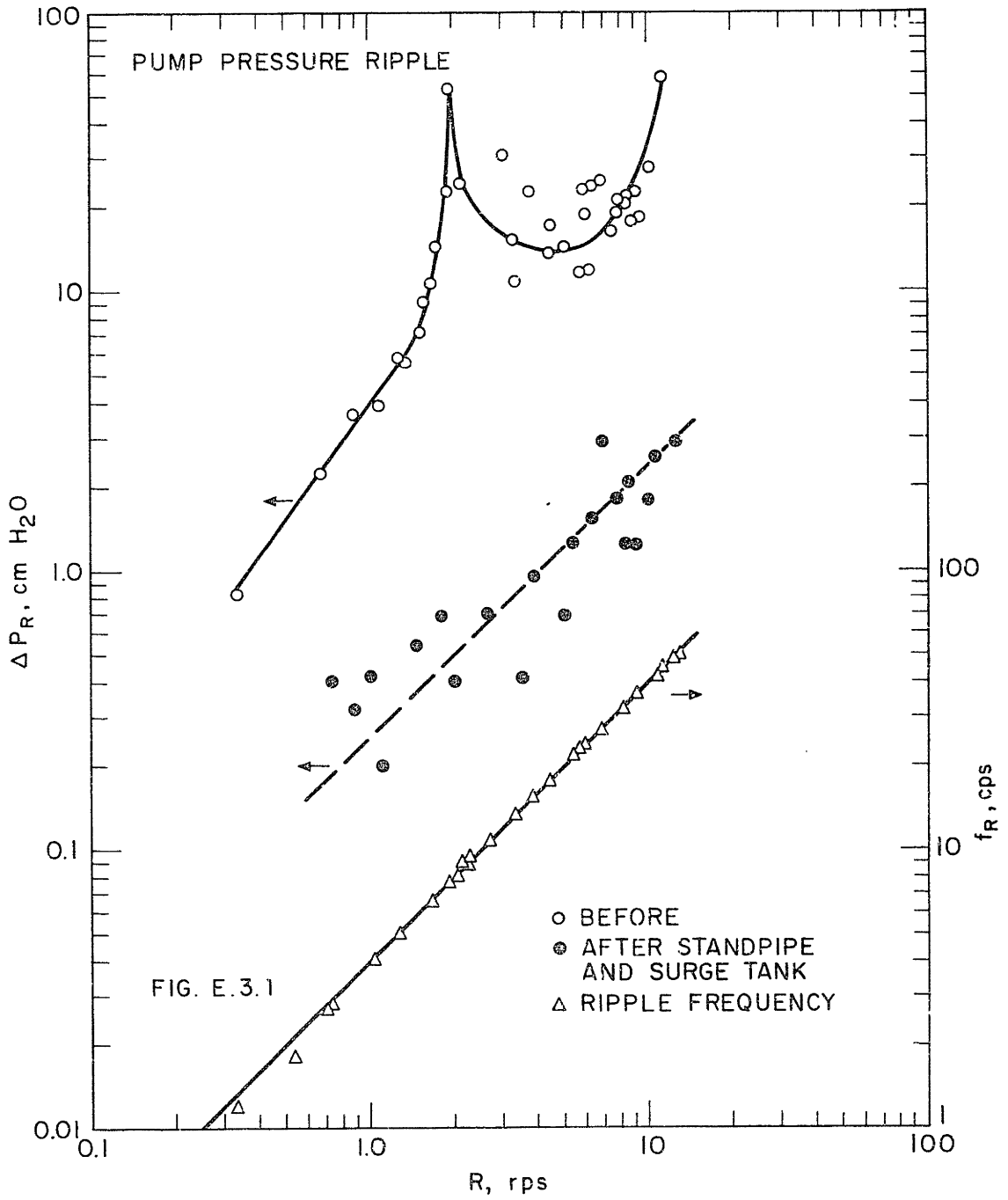


SECTION AT A-A

SECTIONAL ELEVATION AT B-B

FIG. E.2.3





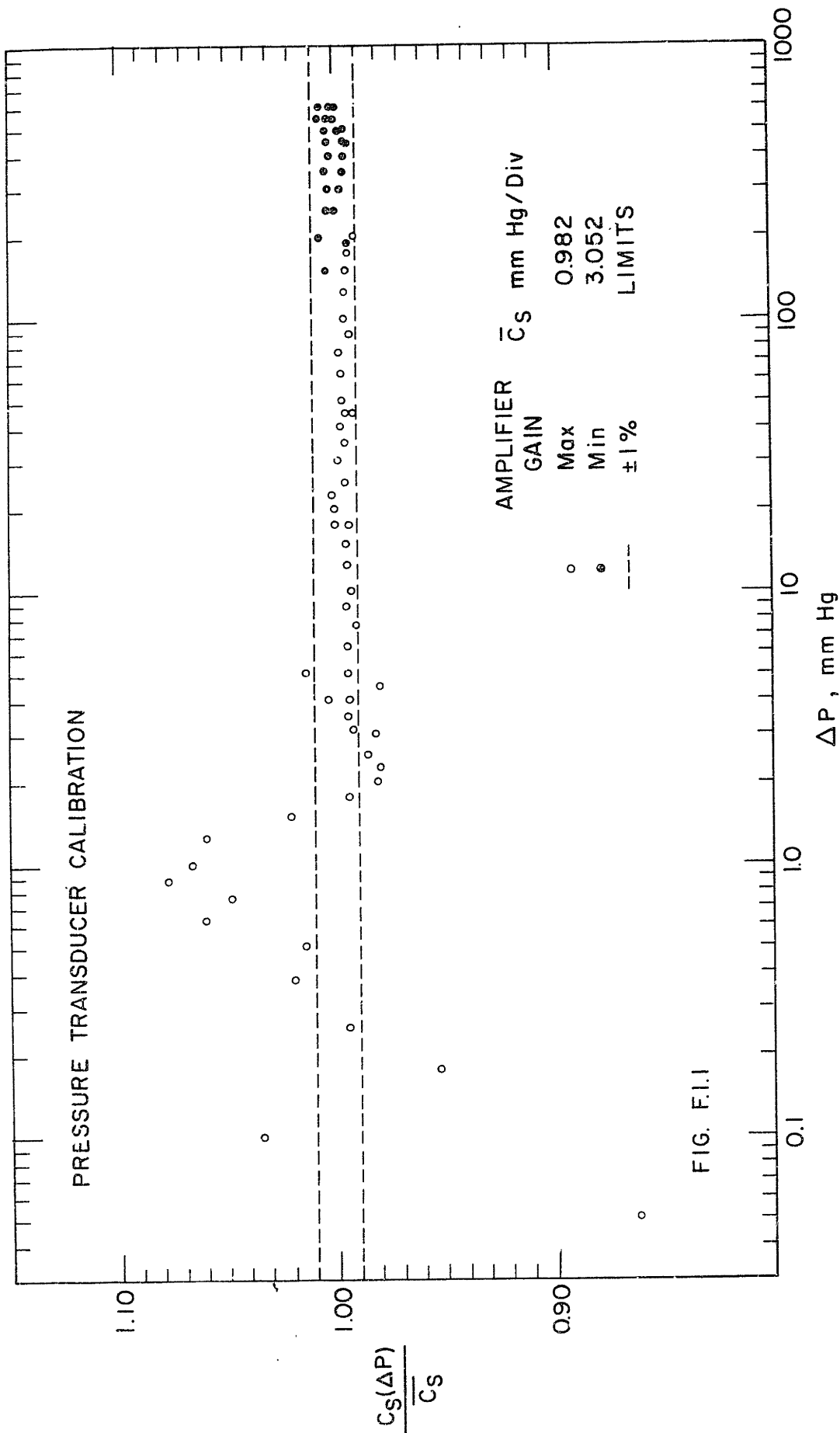


FIG. F.1.1

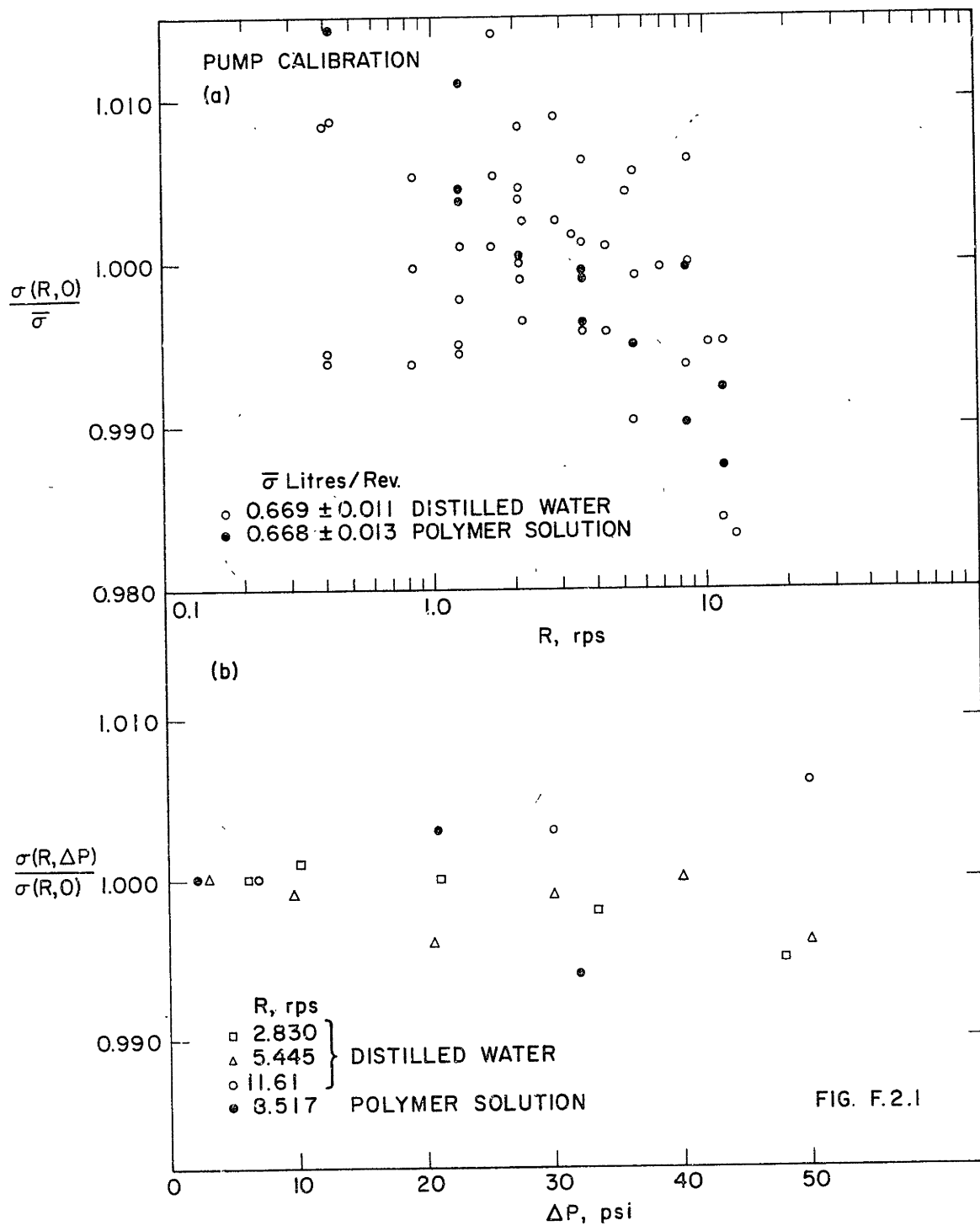
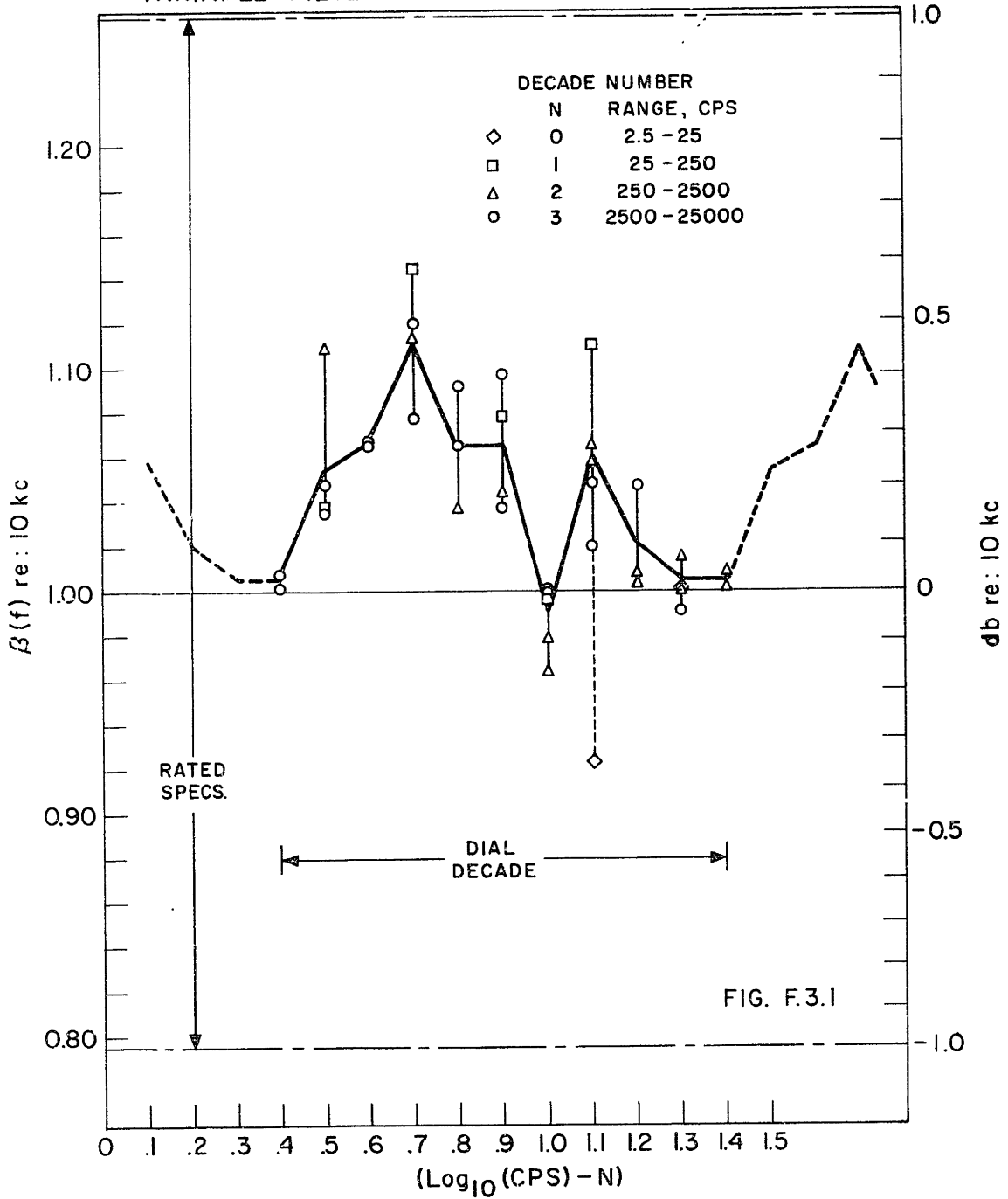


FIG. F.2.1

VARIABLE FILTER CALIBRATION

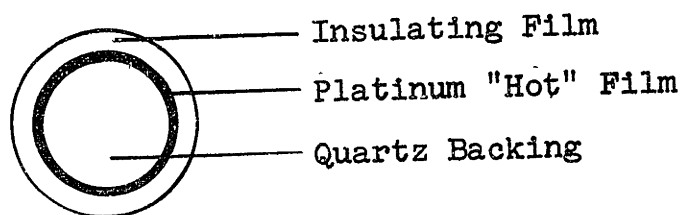


Chapter IX

APPENDICES

## A. Filmed Hot Film Analysis

In the present work, quartz-coated hot film sensors were used for turbulence measurements. It is of interest to know how the quartz coating, or, in general, any insulating film, affects the transient response of the hot film sensor. A cross section of the filmed hot film sensor is:



### A.1 Assumptions

(1) The thickness,  $L$ , of the insulation film is small compared to sensor diameter,  $d$ .

(2) The platinum "hot" film is of negligible thickness and is operated at constant temperature,  $T_p$ , by suitable feedback. This means the sensor resistance,  $r_p$ , is constant.

(3) Ambient fluid is at constant temperature,  $T_{\infty}$ .

(4) The turbulent intensity is small.

(5) The same overheat ratio is employed. This means that filmed hot film response will be compared to the unfilmed case, assuming that the platinum film temperature,  $T_p$ , is the same.

#### A.1.1 Note of Nomenclature

For this appendix only, the following nomenclature rules apply:

(1) For time varying quantities, subscript  $i$  denotes the instantaneous value, upper case the mean and lower case the fluctuating components. For example, for the velocity,

$$U_i = U + u \quad (A.1.1)$$

(2) All symbols are defined at first appearance.

(3) Subscripts used are:

- $i$  - instantaneous value
- $f$  - filmed hot film
- (none) - unfilmed hot film
- $p$  - at platinum film position
- $x$  - at position  $x = x$
- $0$  - at  $x = 0$
- $L$  - at  $x = L$

## A.2 The Simplified Model

The objective is to find the instantaneous heat flux,  $Q_i$ , at the platinum film; this is what determines the anemometer electrical signal,  $E_i$ , by

$$Q_i = E_i^2 / Jr_p \quad (\text{A.2.1})$$

or, on expansion,

$$Q + q = (E^2 + 2Ee + e^2) / Jr_p \quad (\text{A.2.2})$$

where  $J$  is a conversion factor for heat to electrical units,  $r_p$  is constant, assumption (2), and  $e^2$  can be neglected, being second order, assumption (4). Also from assumption (4), the heat transfer coefficient from sensor to fluid is

$$H_i = H + Gu \quad (\text{A.2.3})$$

where  $H$  and  $G$  are constants, directly related to mean velocity,  $U$ , and cylinder diameter,  $d$ , by standard, cross flow, heat transfer relations, e.g., in Eckert and Drake (55). If we let

$$u = u' \sin(\omega t) \quad (\text{A.2.4})$$

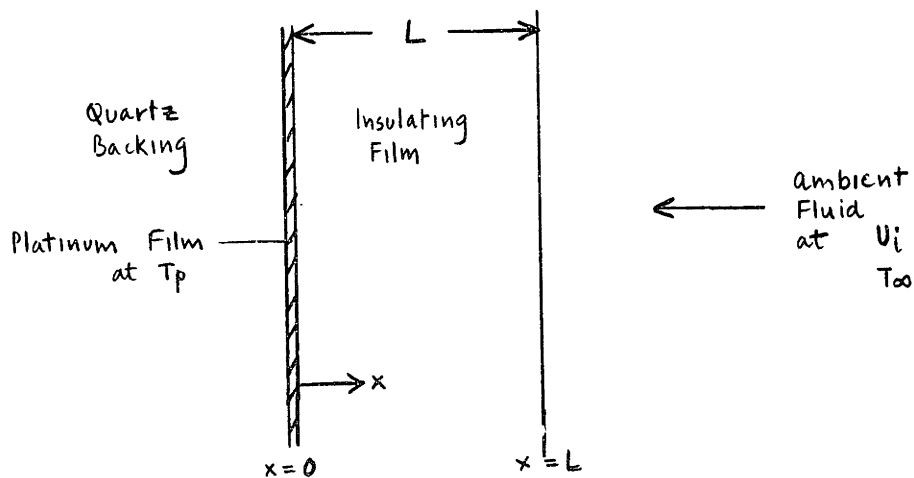
then



$$H_i = H + h \sin(\omega t); h = (Gu') \quad (\text{A.2.5})$$

where the constant  $h$  might be considered the varying heat transfer coefficient amplitude,  $\omega$  is frequency and  $t$  denotes time.

The simplified model of the filmed hot film, sketched below, becomes, from all of the foregoing, that of a parallel slab,  $0 < x < L$ , with boundary conditions of constant temperature,  $T_p$ , at  $x = 0$ , and a varying heat transfer coefficient, (A.2.5), at  $x = L$ .



If  $k$  is the thermal conductivity and  $\alpha$  the thermal diffusivity of the insulation, the temperature field,  $T_1(x,t)$ , in the slab is governed by:

- (1) the conduction equation,

$$\alpha \left( \partial^2 T_1 / \partial x^2 \right) = \left( \partial T_1 / \partial t \right), \quad 0 \leq x \leq L \quad (\text{A.2.6})$$

- (2) boundary conditions,

(a)  $T_1(0,t) = T_p$ , constant

(b)  $H_1(L,t) = H + h \sin(\omega t)$ , so

$$-k \left( \partial T_1(L,t) / \partial x \right) = \quad (\text{A.2.7})$$

$$(H + h \sin(\omega t))(T_1(L,t) - T_\infty)$$

We will solve (A.2.6) and (A.2.7) for two cases,

- (1) static,  $\omega = 0$   
 (2) dynamic,  $\omega \neq 0$

#### A.2.1 Static Analysis

This is essentially the steady state case. The unit heat flux is:

$$Q_i = H_i(T_p - T_{\infty}), \text{ unfilmed} \quad (\text{A.2.8})$$

$$Q_{if} = (H_i^{-1} + Lk^{-1})^{-1}(T_p - T_{\infty}), \text{ filmed}$$

From this, using assumption (5), equating mean and fluctuating components separately in (A.2.2) and letting  $w \rightarrow 0$  in (A.2.5) gives the ratio of filmed to unfilmed hot film signals:

$$\begin{aligned} (E_f/E) &= (1+B)^{-\frac{1}{2}}, \text{ mean} \\ (e_f/e) &= (1+B)^{-\frac{3}{2}}, \text{ turbulent} \end{aligned} \quad (\text{A.2.9})$$

where  $B$  is the Biot Number,  $(HL/k)$ .

Also, the steady temperature field is

$$Z(x) = T_p - (x/L)(T_p - T_{\infty})B/(1+B), \quad 0 \leq x \leq L \quad (\text{A.2.10})$$

### A.2.2 Dynamic Analysis

In this case we assume that the steady solution has been in effect for a long time,  $-\infty < t < 0$ , and at  $t = 0$  and thereafter the heat transfer coefficient is permitted to vary according to (A.2.5). This gives the convenient initial condition,

$$T_1(x,0) = Z(x) \quad (\text{A.2.11})$$

which is known from (A.2.10).

The solution of the problem defined by (A.2.6, 7 and 11),  $Z_1(x,t)$ , is assumed to consist of a steady and a time varying part, so

$$Z_1(x,t) = Z(x) + z(x,t) \quad (\text{A.2.12})$$

which, upon substitution and subtraction of the steady part, yields:

(1) the conduction equation,

$$\alpha(\partial^2 z / \partial x^2) = (\partial z / \partial t), \quad 0 \leq x \leq L \quad (\text{A.2.13})$$

(2) initial condition,

$$z(x,0) = 0 \quad (\text{A.2.14})$$

(3) boundary conditions,

$$(a) \quad z(0,t) = 0 \quad (\text{A.2.15})$$

$$(b) \quad -k(\partial z(L,t) / \partial x) = \\ (H + h \sin(\omega t))(Z(L) + z(L,t) - T_\infty) \\ - H(Z(L) - T_\infty) \quad (\text{A.2.16})$$

Linearization of the  $x = L$  boundary condition holds the key.

Expansion of the RHS in (A.2.16) gives:

$$Hz(L,t) + h\sin(\omega t)(Z(L) - T_{\infty}) + h\sin(\omega t)z(L,t)$$

in which the third term is second order from assumption (4).

Substituting for  $Z(L)$  from (A.2.10) gives the final form:

$$-k(\partial z(L,t)/\partial x) = Hz(L,t) + h(T_p - T_{\infty})(1+B)^{-1} \sin(\omega t) \quad (\text{A.2.16})$$

The solution of (A.2.13, 14, 15 and 16) is a horrendous algebraic task which will not be presented in detail. The steps involved are:

(1) Laplace transformation into an ordinary differential equation. With  $\bar{z}$  and  $p$  as complex temperature and time, respectively, this reads:

(1) transformed conduction equation,

$$(\frac{d^2 \bar{z}}{dx^2}) - (p/\alpha)\bar{z} = 0 \quad (\text{A.2.17})$$

(2) boundary conditions,

$$(a) \quad \bar{z}(0) = 0 \quad (\text{A.2.18})$$

$$(b) \quad -k(\frac{d\bar{z}(L)}{dx}) = h\bar{z}(L) + h(T_p - T_{\infty})(1+B)^{-1}w/(w^2 + p^2)$$

(ii) The solution of (A.2.17 and 18) reads:

$$\bar{z}(x,p) = - \frac{h(T_p - T_\infty)w \sinh(xP)}{(1+B)(w^2 + p^2)(kP \cosh(LP) + H \sinh(LP))} \quad (\text{A.2.19})$$

where  $P = (p/\alpha)^{1/2}$ .

(iii) Inversion of  $\bar{z}$  by Cauchy's theorem gives the temperature time field of interest, which is:

$$z(x,t) = - h(T_p - T_\infty)(1+B)^{-1} A \sin(\omega t + \psi) + \left[ \frac{2h(T_p - T_\infty)w\alpha}{(1+B)kL} \right] \left[ \sum_{n=1}^{\infty} \frac{\beta_n \sin(\beta_n x/L) \exp(-\alpha \beta_n^2 t/L^2)}{(w^2 + \alpha^2 \beta_n^4/L^4)((1-B)\cos(\beta_n) - \beta_n \sin(\beta_n))} \right] \quad (\text{A.2.20})$$

where

$\beta_n$  are the nth roots of  $\beta \cot(\beta) + B = 0$

$$A = (\theta_x^2 + \pi_x^2) / (\xi^2 + \Delta^2)$$

$$\psi = \tan^{-1} \left[ (\pi_x \xi - \theta_x \Delta) / (\theta_x \xi + \pi_x \Delta) \right]$$

and if  $j$  is a dummy variable,

$$\theta_j = \sinh(\phi_j) \cos(\phi_j)$$

$$\pi_j = \cosh(\phi_j) \sin(\phi_j)$$

(A.2.21)

$$\Gamma_j = \cosh(\phi_j) \cos(\phi_j)$$

$$\eta_j = \sinh(\phi_j) \sin(\phi_j)$$

and

$$\xi = (k\phi(\Gamma_L - \eta_L) + H\theta_L)$$

$$\Delta = (k\phi(\Gamma_L + \eta_L) - H\pi_L)$$

where

$$\phi = (w/2\alpha)^{1/2}$$

Now it is apparent that the second term on the RHS of (A.2.20) decays rapidly with time, through the term

$\exp(-\alpha \beta_n^2 t/L^2)$ . Physically, this represents an initial transient that occurs due to the initial conditions chosen and is of no interest here. The steady, time varying, solution of interest is, therefore,

$$z(x,t) = -h(T_p - T_{\infty})(1+B)^{-1} A \sin(\omega t + \psi) \quad (\text{A.2.22})$$

(iv) We require the heat flux,  $q_f$ , at  $x = 0$ , where

$$q_f = -k(\partial z(0,t)/\partial x) \quad (\text{A.2.23})$$

From (A.2.22), after another algebraic battle,

$$q_f = h(T_p - T_{\infty})(1-B)^{-1} \chi \sin(\omega t + \psi_0) \quad (\text{A.2.24})$$

where the amplitude function,  $\chi$ , is

$$\chi = \left[ (\Gamma_L^2 + \eta_L^2) + (B/F)(\theta_L(\Gamma_L - \eta_L) + \pi_L(\Gamma_L + \eta_L)) + (B/F)^2 \frac{1}{2}(\theta_L^2 + \pi_L^2) \right]^{-\frac{1}{2}} \quad (\text{A.2.25})$$

and the phase lag,  $\psi_0$ , is (from  $\psi$  defined in (A.2.21))

$$\psi_0 = \tan^{-1} (\theta_L - \pi_L - 2\eta_L(k\phi/H)) / (\theta_L + \pi_L + 2\Gamma_L(k\phi/H)) \quad (\text{A.2.26})$$



and  $F$  is the dimensionless frequency,

$$F = \phi L \quad (\text{A.2.27})$$

For the unfiled case, it is apparent that

$$q = h(T_p - T_\infty) \sin(\omega t) \quad (\text{A.2.28})$$

and from (A.2.2),

$$(q_f/q) = (e_f/e)(E_f/E) \quad , \quad (\text{A.2.29})$$

of which the mean response ratio is given in (A.2.9).

Therefore, combining (A.2.9, 24, 28 and 29) gives the ratio of filmed to unfiled turbulent signal amplitudes,

$$(e_f/e) = \chi (1 + B)^{-\frac{1}{2}} \quad (\text{A.2.30})$$

$(e_f/e)$  will be termed the Attenuation Ratio and denoted by  $R (= R(B, F))$  in what follows.

First, note that as  $\omega \rightarrow 0$ ,  $F \rightarrow 0$  and, from (A.2.25),  $\chi \rightarrow (1 + B)^{-1}$ , so that

$$R = (e_f/e) = (1 + B)^{-\frac{3}{2}}, \quad F \rightarrow 0 \quad (\text{A.2.31})$$

which is precisely the static result, (A.2.9).

Second, as  $B \rightarrow 0$ ,  $\chi \rightarrow (\Gamma_L^2 + \eta_L^2)^{-\frac{1}{2}}$ , so

$$R = ((\text{Cosh}(F)\text{Cos}(F))^2 + (\text{Sinh}(F)\text{Sin}(F))^2)^{-\frac{1}{2}} \quad (\text{A.2.32})$$

from which, if  $F$  is large,

$$R = 2 \exp(-F) \quad (\text{A.2.33})$$

Values of  $R(B,F)$  for  $10^{-4} < B < 10^2$  and  $10^{-2} < F < 10^2$  are presented in Table A.2.1.

TABLE A.2.1  
TURBULENT SIGNAL ATTENUATION RATIO, R

B	1.000E-04	1.000E-03	1.000E-02	1.000E-01	.100E 01	.100E 02	.100E 03
.100E-01	1.000E 00	.999E 00	.985E 00	.867E 00	.354E 00	.274E-01	.985E-03
.126E-01	1.000E 00	.999E 00	.985E 00	.867E 00	.354E 00	.274E-01	.985E-03
.158E-01	1.000E 00	.999E 00	.985E 00	.867E 00	.354E 00	.274E-01	.985E-03
.200E-01	1.000E 00	.999E 00	.985E 00	.867E 00	.354E 00	.274E-01	.985E-03
.251E-01	1.000E 00	.999E 00	.985E 00	.867E 00	.354E 00	.274E-01	.985E-03
.316E-01	1.000E 00	.999E 00	.985E 00	.867E 00	.354E 00	.274E-01	.985E-03
.398E-01	1.000E 00	.999E 00	.985E 00	.867E 00	.354E 00	.274E-01	.985E-03
.501E-01	1.000E 00	.998E 00	.985E 00	.867E 00	.354E 00	.274E-01	.985E-03
.631E-01	1.000E 00	.998E 00	.985E 00	.867E 00	.354E 00	.274E-01	.985E-03
.794E-01	1.000E 00	.998E 00	.985E 00	.867E 00	.354E 00	.274E-01	.985E-03
.100E 00	1.000E 00	.998E 00	.985E 00	.867E 00	.354E 00	.274E-01	.985E-03
.126E 00	1.000E 00	.998E 00	.985E 00	.867E 00	.354E 00	.274E-01	.985E-03
.158E 00	1.000E 00	.998E 00	.985E 00	.867E 00	.354E 00	.274E-01	.985E-03
.200E 00	.999E 00	.998E 00	.985E 00	.866E 00	.353E 00	.274E-01	.985E-03
.251E 00	.999E 00	.997E 00	.984E 00	.866E 00	.353E 00	.274E-01	.985E-03
.316E 00	.997E 00	.995E 00	.982E 00	.864E 00	.353E 00	.274E-01	.985E-03
.398E 00	.992E 00	.990E 00	.977E 00	.861E 00	.352E 00	.274E-01	.985E-03
.501E 00	.979E 00	.978E 00	.965E 00	.852E 00	.351E 00	.274E-01	.984E-03
.631E 00	.951E 00	.950E 00	.938E 00	.830E 00	.347E 00	.273E-01	.982E-03
.794E 00	.888E 00	.887E 00	.877E 00	.782E 00	.337E 00	.271E-01	.976E-03
.100E 01	.773E 00	.772E 00	.764E 00	.690E 00	.317E 00	.266E-01	.963E-03
.126E 01	.607E 00	.606E 00	.601E 00	.551E 00	.277E 00	.254E-01	.932E-03
.158E 01	.428E 00	.428E 00	.424E 00	.394E 00	.218E 00	.230E-01	.865E-03
.200E 01	.275E 00	.275E 00	.273E 00	.256E 00	.152E 00	.190E-01	.740E-03
.251E 01	.162E 00	.162E 00	.161E 00	.151E 00	.944E-01	.137E-01	.560E-03
.316E 01	.845E-01	.845E-01	.840E-01	.793E-01	.512E-01	.844E-02	.366E-03
.398E 01	.373E-01	.373E-01	.371E-01	.352E-01	.233E-01	.436E-02	.201E-03
.501E 01	.133E-01	.133E-01	.132E-01	.126E-01	.853E-02	.180E-02	.893E-04
.631E 01	.364E-02	.364E-02	.362E-02	.344E-02	.238E-02	.560E-03	.303E-04
.794E 01	.710E-03	.710E-03	.706E-03	.673E-03	.472E-03	.123E-03	.733E-05
1.000E 01	.908E-04	.908E-04	.903E-04	.861E-04	.611E-04	.173E-04	.116E-05
.126E 02	.682E-05	.681E-05	.678E-05	.647E-05	.463E-05	.142E-05	.107E-06
.158E 02	.262E-06	.262E-06	.260E-06	.249E-06	.179E-06	.583E-07	.499E-08
.200E 02	.432E-08	.432E-08	.430E-08	.411E-08	.298E-08	.102E-08	.998E-10
.251E 02	.247E-10	.247E-10	.245E-10	.235E-10	.171E-10	.612E-11	.683E-12
.316E 02	.369E-13	.369E-13	.367E-13	.352E-13	.257E-13	.953E-14	.121E-14
.398E 02	.103E-16	.103E-16	.102E-16	.978E-17	.717E-17	.273E-17	.396E-18
.501E 02	.000E 00	.000E 00	.000E 00	.000E 00	.000E 00	.000E 00	.000E 00

NOTE:  $B = (HL/k)$   
 $F = L(\omega/2\alpha)^{1/2}$   
 $R = e_r/e$

### A.3 Practical Applications

The parameter  $R$  is generally useful in evaluating filmed hot film operation. A convenient engineering approach is to consider the response in terms of:

- (1) The static attenuation,  $R_0$ ,

$$R_0 = R(B, 0) = (1 + B)^{-\frac{3}{2}} \quad (\text{A.3.1})$$

- (2) The cutoff frequency,  $F_0$ , defined by

$$R(B, F_0)/R_0 = (1 - D) \quad (\text{A.3.2})$$

where  $D$  is some acceptable fractional "distortion".

Within reasonable limits, say  $R_0 > 0.1$ , the value of  $R_0$  is immaterial since, in hot wire practice, absolute values are always established from a static calibration. The cutoff frequency,  $F_0$ , is of greater significance because, for  $F > F_0$ , frequencies are attenuated by different amounts which results in a distorted turbulent signal, especially serious for turbulent energy spectrum measurements. Typically, for a 0.1 db acceptable distortion, with reference to  $F = 0$ , the value of  $D$  in (A.3.2) is 0.022.

Putting  $R_0 = 0.10$  and  $D = 0.022$  shows, from (A.3.1), (A.3.2) and Table A.2.1, that filmed hot film operation is

feasible roughly within the following dimensionless limits:

$$\begin{aligned} B &< 5 \\ F &< 0.5 \end{aligned} \quad (A.3.3)$$

With reference to the present work, consider Fig. A.3.1 which is a plot of the attenuation ratio,  $R$ , vs. frequency,  $f$  cps, for quartz coated hot film sensors operating in distilled water at  $25^{\circ}\text{C}$ . The two cases, (a) and (b), represent operation at the highest mean velocities encountered at the two flow rates studied in the 3.21 cm pipe (see Chapter V of text). Values of insulation thickness,  $L$ , are based around the nominal 1 micron quoted, informally, by the manufacturers (59). Quartz physical properties are:

$$\begin{aligned} k &- 0.0026 \text{ cal/sec cm } ^{\circ}\text{C} \\ \rho &- 2.65 \text{ gm/cm}^3 \\ C_p &- 0.182 \text{ cal/gm } ^{\circ}\text{C} \\ \alpha &- 0.00539 \text{ cm}^2/\text{sec} \end{aligned}$$

It can be observed that in both cases (a) and (b),

(1) The static attenuation is within reasonable limits.

(2) More important, the frequency response is flat up to  $10^4$  cps or a little beyond, depending on  $L$ .

This shows that, in the present case, hot film operation was not adversely affected by the quartz coating.

## B. Spectrum Scaling Rules

The aim of this appendix is to derive rules by which measured turbulent energy spectra,  $E(k)$  vs.  $k$ , may be made universal,  $\epsilon(K)$  vs.  $K$ , and thereby used to predict spectra at other than the measured conditions,  $E'(k')$  vs.  $k'$ . Of particular interest is the region of the spectrum responsible for the energy dissipation, i.e., the higher wave numbers.

### B.1 Assumptions

(1) The Reynolds number is high enough for the "universal equilibrium" to exist at the higher wave numbers. In this case, for isotropic turbulence, the dissipation,  $\epsilon$ , and the kinematic viscosity,  $\nu$ , are the controlling parameters, Hinze (44), and spectra would be universal when normalized by them.

(2) Anisotropic turbulence, as in a pipe flow, tends to isotropy at the high wave numbers. It is assumed that the wave numbers of interest are high enough to be isotropic.

(3) From Laufer (43), all turbulent energy rates are unique functions of radial position when suitably normalized. We are particularly interested in the dissipation rate,  $\epsilon$ , for which:

(a) Near the pipe wall,  $(\epsilon\nu/u_\tau^4)$ , is a function only of  $y^+$ .

(b) In the central core of the pipe,  $(\varepsilon D/2u_\tau^3)$  is a function only of  $\xi$ ;  $D$  is pipe diameter.

(4) In the wall region, the turbulent energy production rate,  $\Gamma$ , is roughly equal to the dissipation rate,  $\varepsilon$ . Thus the normalized dissipation in (3a) above can be estimated from known normalized production,  $(\Gamma\nu/u_\tau^4)$ , vs.  $y^+$  curves.

## B.2 Universal Spectral Coordinates

From the controlling parameters,  $\nu$  and  $\varepsilon$ , length and time scales can be derived:

$$\begin{aligned} L &= (\nu^3/\varepsilon)^{1/4}, \quad \text{length} \\ T &= (\nu/\varepsilon)^{1/2}, \quad \text{time} \end{aligned} \tag{B.2.1}$$

Assume we have a measured spectrum,  $E(k)$  vs.  $k$ . From the dimensions of its coordinates, the nondimensional coordinates of the universal spectrum will be:

$$\begin{aligned} \kappa &= kL \\ E(\kappa) &= E(k)T^2/L^3 \end{aligned} \tag{B.2.2}$$

### B.2.1 The Wall Region

From assumption (3b),

$$\varepsilon = A(u_\tau^4/\nu) \tag{B.2.3}$$

where  $A$ , dimensionless, is a function only of  $y^+$ . By

invoking assumption (4), values of A are available from Laufer, Fig. 17. Substituting (B.2.3) into (B.2.1) gives:

$$\begin{aligned} L &= A^{-\frac{1}{4}} (u_{\tau}/\nu)^{-1} \\ T &= A^{-\frac{1}{2}} (u_{\tau}^2/\nu)^{-1} \end{aligned} \quad (\text{B.2.4})$$

from which substitution into (B.2.2) yields:

$$\begin{aligned} K &= k/(A^{\frac{1}{4}})(u_{\tau}/\nu) \\ \epsilon(K) &= E(k)/(A^{1/4})(\nu u_{\tau}) \end{aligned} \quad (\text{B.2.5})$$

(B.2.5) permits a universal spectrum to be obtained from a measured spectrum at a given radial position,  $y^+$ , knowing fluid properties,  $\nu$ , and gross flow conditions,  $u_{\tau}$ , in the pipe.

### B.2.2 The Central Core

From assumption (3b),

$$\xi = B(2u_{\tau}^3/D) \quad (\text{B.2.6})$$

where B, dimensionless, is a function only of  $\xi$ , available from Laufer, Figs. 18 and 20. Length and time scales are

$$\begin{aligned} L &= (2B)^{-\frac{1}{4}} (Du_{\tau}/\nu)^{\frac{1}{4}} (u_{\tau}/\nu)^{-1} \\ T &= (2B)^{-\frac{1}{2}} (Du_{\tau}/\nu)^{\frac{1}{4}} (u_{\tau}^2/\nu)^{-1} \end{aligned} \quad (\text{B.2.7})$$

which yield the universal coordinates in the central core,



$$K = k/(2B)^{\frac{1}{4}} (Du_{\tau}/\gamma)^{-\frac{1}{4}} (u_{\tau}/\gamma)$$

$$\epsilon(K) = E(k)/(2B)^{\frac{1}{4}} (Du_{\tau}/\gamma)^{-\frac{1}{4}} (\gamma u_{\tau})$$
(B.2.8)

### B.3 Testing of Universal Coordinates

Distilled water (solvent) spectra obtained in the present work at each of two radial positions and two flow rates, Figs. 5.5.6 and 5.5.7, will be compared with the spectra of Laufer in air to test the rules derived in B.2. Figure B.1 is a plot of all the spectra,  $E_1(k_1)$  vs.  $k_1$ , as measured; Table B.1 is a summary of prevailing conditions in each case, values of the constants A and B are from Laufer. Figure B.2,  $\epsilon(K)$  vs.  $K$ , shows the results of universalization of all the spectra on Fig. B.1, with the parameters on Table B.1, by the direct use of relations (B.2.5) for "wall" spectra, AA, CC and EE, and (B.2.8) for "axis" spectra, BB, DD, and FF. Consider each group separately first; this eliminates, in essence, the role of the position constants A and B. For the higher wave numbers, the agreement between universal "axis" spectra is particularly good. For the "wall" spectra, the agreement is not so good, even though the universal spectra are bunched much closer together than the measured ones. This latter is very like due to a breakdown of assumption (2) - high wave number isotropy - close to the wall. Next,

Table B.1  
 Prevailing Conditions for  
 Experimental Spectra on Fig. B.1

Spectrum and Source	Radial Position		Constants		$N_{Re, Av.}$	D cm	$u_{\tau}$ cm/sec	$\gamma$ cm <sup>2</sup> /sec
	$y^+$	$\frac{z}{\delta}$	$\frac{1}{(A)} \sqrt{\frac{1}{4}}$	$\frac{1}{(2B)} \sqrt{\frac{1}{4}}$				
AA Laufer	72		0.40		427,000	24.7	107	0.15
BB		1.00		1.45				
CC Fig. 5.5.7	130		0.37		234,000	3.21	28.4	0.0089
DD		1.00		1.45				
EE Fig. 5.5.6	45		0.50		50,000	3.21	7.3	0.0089
FF		1.00		1.45				

consider all of the spectra together. Comparison of Figs. B.1 and B.2 shows that, considering the orders of magnitude scaled, significant progress is made towards over-all universality at the higher wave numbers. This establishes some confidence in the rules developed.

#### B.4 The Scaling Rules

The universal spectra on Fig. B.2 were, within an order of magnitude, independent of radial position. In this section we will restrict ourselves to scaling at a particular radial position,  $y^+$  or  $\xi$ , which, hopefully, would result in enhanced accuracy. This eliminates the need for values of the position constants, A and B.

Consider a point,  $(k, E(k))$ , on a measured spectrum at known conditions and let  $(k', E'(k'))$  be the point corresponding to it at some other condition. If both conditions satisfy the assumptions of B.1, then, in the wall region, for example

$$K = k/(A^{1/4})(u_\tau/\nu) = k'/(A'^{1/4})(u'_\tau/\nu')$$

$$E(K) = E(k)/(A^{1/4})(\nu u_\tau) = E'(k')/(A'^{1/4})(\nu' u'_\tau)$$

(B.2.5)

Because we are at the same radial position,  $y^+$ , in both cases (same A), we need not revert to the universal coordinates and can scale directly from  $(k, E(k))$  to  $(k', E'(k'))$  using the second equality above. Thus the scaling rules are:

In the wall region, at same  $y^+$ ,

$$\begin{aligned} k' &= k \left[ (u'_\tau / \nu') / (u_\tau / \nu) \right] \\ E'(k') &= E(k) \left[ (\nu' u'_\tau) / (\nu u_\tau) \right] \end{aligned} \tag{B.4.1}$$

Similarly, in the central core of the pipe, at the same  $\xi$ ,

$$\begin{aligned} k' &= k \left[ (u'_\tau / \nu') (u_\tau / \nu) \right] \left[ (D' u'_\tau / \nu') / (D u_\tau / \nu) \right]^{-\frac{1}{4}} \\ E'(k') &= E(k) \left[ (\nu' u'_\tau) / (\nu u_\tau) \right] \left[ (D' u'_\tau / \nu') / (D u_\tau / \nu) \right]^{-\frac{1}{4}} \end{aligned} \tag{B.4.2}$$

### B.5 Scaling Rules for $k_d$

The dissipation wave number,  $k_d$ , was defined in connection with the Onset Hypothesis, Section 6.6.2. By definition, it depends only upon the shape of the high end of the spectrum, which region can reasonably be universalized by the rules developed. Thus

$$K_d = k_d / (A^{1/4}) (u_\tau / \nu) \quad (\text{B.5.1})$$

where  $K_d$  is the universal dissipation wave number. Once the value of  $K_d$  is established,  $k_d$  can be obtained for any flow conditions. Presently available data are listed in Table B.2. All that can be said is that  $K_d$  is of order  $10^{-1}$ ; the uncertainty is due, in part, to measured spectra having dissipation curves,  $k^2 E(k)$  vs.  $k$ , with flat maxima which make it difficult to obtain  $k_d$  precisely.

(B.5.1) can be put in the form

$$k_d = K(u_\tau / \nu); \quad K = (K_d A^{1/4}) \quad (\text{B.5.2})$$

where  $K$  is a function only of  $y^+$ . This is equation (6.6.5) in the text. For the purposes of the Onset Hypothesis, Section 6.6.2,  $K$  has to be obtained at  $y^+ \simeq 10$ , where the dissipation rate is a maximum. At this position, the value of  $A^{1/4}$  ( $\simeq 0.71$ ) can be obtained from Laufer with considerable confidence, but no measured spectra are available, so

a good value of  $K_d$  is not available. As an approximation,  $K_d$  from Laufer's spectrum at  $y^+ = 72$  may be used, so

$$K = (0.22)(0.71) \approx 0.2 \quad (\text{B.5.3})$$

0.2 is the value used for  $K$ , with stated reservations, in Section 6.6.2.

Table B.2

Universal Dissipation Wave Numbers and Frequencies

Spectrum	$y^+$	$k_d \text{ cm}^{-1}$	$K_d$	$\omega_d \text{ sec}^{-1}$	$\Omega_d$
AA Laufer	72	60	0.22	104,000	8.6
CC Fig. 5.5.7	130	16	0.014	8,000	0.63
EE Fig. 5.5.6	45	14.5	0.036	1,580	1.1

On entirely analogous grounds, scaling rules for the dissipation frequency,  $\omega_d$ , used in "time" based onset hypotheses may be derived. From the time scales,

$$\Omega_d = \omega_d / (A^2) (u_\tau^2 / \nu) \quad (\text{B.5.4})$$

where  $\Omega_d$  is the universal dissipation frequency. Relevant frequency data are also listed on Table B.2; it will be

recalled that frequency and wave number are related through the mean velocity,  $U$ , by

$$\omega = kU \quad (\text{B.5.5})$$

The universal dissipation frequency is, from Table B.2, of order  $10^0$  to  $10^1$ . Re-arranging (B.5.4) gives

$$\omega_d = W(u_r^2/\gamma) ; \quad W = (\Omega_d A^{\frac{1}{2}}) \quad (\text{B.5.6})$$

which is equation (6.6.18), Section 6.6.23, in the text.

From Laufer's  $y^+ = 72$  spectrum, the value of  $W$  is about 4 at  $y^+ \simeq 10$ .

## B.6 Further Comparison of Water Data

It was seen in Section B.3 that the present water spectra compared reasonably with Laufer's spectra in air, particularly on the pipe axis. Two other spectrum-derived quantities can be compared:

- (a) the macroscale,  $\Lambda_f$ , and
- (b) the dissipation integral,  $\int_0^{\infty} k_1^2 E_1(k_1) dk_1$

Comparison is possible only for spectra on the pipe axis, because Laufer's "wall" spectrum does not cover the range required.

(a) Macroscales, characteristic of the larger, energy containing eddies, should be governed by the pipe dimensions;  $\Lambda_f/D$  is typically around 1/4.

(b) The normalized "dissipation" obtained from the second moments of the experimental spectra, assuming isotropy should be equal. This is  $(15 \nu \int_0^{\infty} k_1 E_1(k_1) dk_1) / (2u_r^3/D)$ .

Table B.3 indicates that both (a) and (b) are reasonably similar for our spectra and Laufer's. Thus considerable confidence can be placed in the present measured spectra.



Table B.3  
Comparison of Macroscales and Dissipation Integrals

Spectrum	$\gamma$	$\Lambda_f$ cm	$\Lambda_f/D$	$\int_0^{\infty} k_1^2 E_1(k_1) dk_1$ sec <sup>-2</sup>	$(15 \gamma \int_0^{\infty} k_1^2 E_1(k_1) dk_1) / (2u_f^3/D)$
BB Laufer	1.00	7.0	0.28	870,000	0.80
DD Fig. 5.5.7	1.00	0.73	0.24	605,000	0.60
FF Fig. 5.5.6	1.00	0.82	0.26	925	0.51

## C. Currently Available Onset of Drag Reduction Data

Table C.1

## Summary of Experimental Onset of Drag Reduction Data

No.	Solvent	Polymer	$[\eta]$ dl/gm	Pipe Dia. cm	$R_G$	$\frac{u_T^*}{\nu_s}$ $\text{cm}^{-1}$	$C'$	Ref.
1	MCB	PMMA	3.9	0.128	600	1030	0.0124	1
2	MCB	PMMA	3.9	0.404	600	1100	0.0132	1
3	CYC	PIB	3.44	0.081	445	2190	0.0195	29
4	CYC	PIB	3.44	0.117	445	2200	0.0196	29
5	CYC	PIB	3.44	1.29	445	2320	0.0206	29
6	CYC	PIB	3.44	2.54	445	1660	0.0148	29
7	BEN	PIB	0.82	1.29	275	3740	0.0206	29
8	BEN	PIB	0.82	2.54	275	2640	0.0145	29
9	Water	PEO	0.66	3.21	315	2240	0.0141	Present work
10	Water	PEO	0.73	0.292	350	2100	0.0147	
11	Water	PEO	1.75	0.292	795	1000	0.0159	
12	Water	PEO	3.38	0.292	835	940	0.0157	
13	Water	PEO	3.61	3.21	875	830	0.0145	
14	Water	PEO	3.90	0.292	910	790	0.0144	
15	Water	PEO	20.1	3.21	2350	210	0.0099	
16	Water	Guar	7.0	2.20	200	2000	0.0080	26
17	Water	Guar	7.0	5.02	200	1980	0.0079	26
18	Water	Guar	19.0	1.65	400	1090	0.0087	28
19	Water	Guar	19.0	3.63	400	1480	0.0118	28
20	Water	PEO	2.7	1.02	740	1750	0.0259	17
21	Water	PEO	4.3	1.02	960	1220	0.0234	17

Table C.1 (Cont.)

No.	Solvent	Polymer	$[\eta]$ dl/gm	Pipe Dia. cm	$R_G$ Å	$u_T^*/\gamma_s$ cm <sup>-1</sup>	$c'$	Ref.
22	Water	CMC	10	2.29	500	1060	0.0106	27
23	Water	CMC?	--	2.54	-	2140	--	8
24	Water	CMC?	--	3.33	-	2100	--	8
25	Water	CMC?	--	4.80	-	2090	--	8
26	Water	CMC?	--	2.54	-	1520	--	8
27	Water	CMC?	--	3.33	-	1520	--	8
28	Water	CMC?	--	4.80	-	1920	--	8
29	Water	PVP?	--	2.54	-	790	--	8
30	Water	PVP?	--	3.33	-	850	--	8
31	Water	PVP?	--	4.80	-	960	--	8

## Notes:

(1) Abbreviations used are:

- MCB - Monochlorobenzene  
 CYC - Cyclohexane  
 BEN - Benzene  
 PMMA - Polymethylmethacrylate  
 PIB - Polyisobutylene  
 PEO - Polyethylene oxide  
 Guar - Guar gum  
 CMC - Carboxymethylcellulose  
 PVP - Polyvinylpyrrolidone  
 ? - Indicates uncertainty about polymer used.

## Table C.1 Notes (Cont.)

- (2)  $\gamma_s$  is for solvent in all cases
- (3)  $C'$  is the onset constant, dimensionless, from equation (6.6.6).
- (4) Estimates of  $R_G$  for synthetic and natural "gums", CMC and Guar, are extremely uncertain, say  $\pm 100\%$ .
- (5) In cases 20 and 21, from Fabula (17),  $u_T^*$  was obtained by back extrapolation to solvent line; accuracy estimated  $\pm 100\%$ .

C.2 Estimation of  $R_G$ 

Experimental values of  $R_G$  for the PEO-Water system are given in Appendix D. In all other cases,  $R_G$  was estimated from intrinsic viscosity - molecular weight relationships using the "equivalent sphere" model and Flory's universal constant,  $\bar{\Phi}$ . The exact procedure has been detailed by Kurata and Stockmeyer (51), and can easily be derived from Chapter 12 in Flory (42), so it will not be elaborated on. The accuracy of the  $R_G$  estimates is about  $\pm 20\%$  for cases 1 through 8 on Table C.1 and about  $\pm 100\%$  for the remaining, non-PEO, cases.

## D. Polyethylene Oxide - Water Data of Shin (21)

Table D.1

 $[\eta]$  vs. M and  $R_G$  with Best Fit Constants

Shin Designation	$[\eta]$ , dl/gm	M	$R_G^{\circ}$ , Å	Present Designation
LS-6	1.80	302,000	810	N80
LS-9	3.00	492,000	755	N750
LS-5	3.50	622,000	820	N3000
LS-4	5.35	1,226,000	1280	-
LS-1	8.20	2,580,000	1440	-
LS-7	11.40	2,820,000	1510	-
LS-2	16.50	4,270,000	1940	-
LS-3	17.60	5,180,000	2220	W301
LS-8	27.00	8,450,000	2920	-
Best Fits:				
$M = (0.136 \pm 0.076) 10^6 [\eta] (1.265 \pm 0.242)$				
$R_G = (0.418 \pm 0.158) 10^3 [\eta] (0.574 \pm 0.163)$				

## Notes:

(1) Polymer N80 (LS-6) is excluded from the fittings because  $R_G$  lies outside the 99% confidence belt, Fig. D.1.

(2) All error limits are for 99% confidence.

(3) Present designations, column 5, are for closest corresponding polymers. Commercial batches with same name, e.g., N750, typically vary  $\pm 20\%$  in  $[\eta]$ .

(4) All values in distilled water at 25.0°C.

Experimental values and best fit lines with confidence envelopes, derived from Table D.1, are plotted on Fig. D.1.

## E. Equipment Details

This appendix is in five sections:

E.1 The Small System

E.2 The Big System

E.3 The Pump

E.4 The Constant Temperature Hot  
Film Anemometer

E.5 List of Commercial Equipment Vendors  
and Manufacturers.

### E.1 The Small System

Adequately detailed descriptions of this system were given in Chapter III.

### E.2 The Big System

Scale drawings of the following are presented:

Fig. E.2.1 System layout

Fig. E.2.2 Control panel connections

Fig. E.2.3 Test station and micrometer traverse

### E.3 The Pump

The pump was a Moyno type 2L10 SSQ with a chrome plated stainless steel rotor and a Buna-N stator. It had a nominal capacity of 140 gpm at 750 rpm and 75 psi differential between suction and discharge.

#### E.3.1 Drive

The prime mover was a constant speed, 1725 rpm, 10 hp, 3 phase a-c motor. The motor was an integral part of a variable speed, eddy-current coupled, magnetic drive. A 36 pole a-c generator-tachometer, part of the electronic drive speed control, was mounted integrally on the drive output shaft. The output speed could be varied from 1670 to 100 rpm; its precise value,  $R_d$  rps, was obtained from the frequency,  $f$  cps, of the tachometer signal. The relation is

$$R_d = (f/18) \quad (E.3.1)$$

An electronic counter was used to measure  $f$ . The speed control was tested to be better than  $\pm 5$  rpm for steady load (flow) conditions. The drive output was coupled to the input shaft of a gear box by a timing belt arrangement that effected a (26/84) speed reduction. The gear box had six speed ratios, Table E.3.1, and its output was direct-coupled to the pump rotor. The pump rotor speed,  $R$  rps,

at any gear ratio,  $G(N)$ , is directly related to the drive speed,  $R_d$ , from which, in terms of tachometer frequency,  $f$ ,

$$R = F(N)f \quad , \quad F(N) = (26/84)(1/G(N))(1/18) \quad (E.3.2)$$

Values of  $F(N)$  are also listed in Table E.3.1. By this arrangement pump speed could be varied from 0.14 to 12.5 rps and measured very precisely. The lower speed limit was set by the drive, while the upper limit was recommended by the pump manufacturers for mechanical reasons.

Table E.3.1  
Drive Gear Ratios

Gear	Input/Output	Frequency Factor
<u>N</u>	<u>G(N)</u>	<u>F(N) (rps/cps)</u>
1	4.11/1	0.004179
2	2.48/1	0.007069
3	1.58/1	0.01089
4	1/1	0.01720
5	1/1.69	0.02906
6	1/2.60	Not used



### E.3.2 Pumping Characteristics

Specific displacement vs. pump speed and pressure differential data for the pump are given in Appendix F.2 - Pump Calibration. In addition, the pump appears to "pulse" slightly; this is described with reference to the big system.

#### E.3.21 Pressure Ripple

Initial operation of the 3.21 cm system, without the surge tank or the standpipe, indicated sinusoidal pressure fluctuations, termed "ripple". Measurements taken across pressure taps T<sup>4</sup>-T<sup>5</sup> are shown on Fig. E.3.1 on which the rms amplitude of the pressure ripple,  $\Delta P_R$  cm H<sub>2</sub>O, and ripple frequency,  $f_R$ , are plotted vs. pump speed, R rps. It can be observed that:

- (1)  $f_R \simeq 4R$
- (2)  $\Delta P_R$  has a sharp maximum at  $R \simeq 2$  rps where  $f_R \simeq 8$  cps.

The distance around the loop from pump discharge to suction is about 100 ft., and the speed of sound in water about 5000 fps so the "natural frequency" of the system is roughly  $((5000)/(2\pi)(100)) = 7.95$  cps, which is very close to the observed maximum ripple frequency. This shows that the ripple is caused by shock waves emanating from the pump.

The solid points on Fig. E.3.1 show results after

installation of the standpipe and surge tank in the system; it is seen that the ripple amplitude was attenuated from 10 to 200 fold. Also, no distinct ripple frequency could be detected, though this may, partly, have been due to the ripple signal being so weak that it bordered on the noise band of the transducer.

The source of this ripple appears to lie in the eccentric movement of the two ends of the pump rotor, in particular the drive end which is at the same axial position as the suction port. Curiously, the ripple appeared not to affect the mean flow in the pipe; a few gross flow and mean velocity measurements (not reported) taken initially were practically identical with those taken after the ripple was eliminated.

### E.4 The Constant Temperature Hot Film Anemometer

The hot film anemometer has two major components: the filmed hot sensor and the electronic control unit which maintains it at constant temperature. Of these, the former has been adequately described and analysed (Chapter III and Appendix A), so only the latter will be considered.

#### E.4.1 The Electronic Control Unit

This has been described in great detail by its designer, Ling (41). It consists of:

- (1) a proportional controller
- (2) a "linearizer" .

(1) The proportional controller consists of a d-c bridge, of which the sensor is one leg, an amplifier and a feedback system. By means of this the sensor platinum "hot" film is maintained at constant temperature,  $T_p$ , above the ambient,  $T_\infty$ , and the bridge current  $i_b$ , required to do this reflects the instantaneous heat transfer coefficient,  $H_1$ , from the sensor to the fluid, which, in turn, is characteristic of the instantaneous flow velocity,  $U_1$ , past the sensor. The platinum film resistance,  $r_p = r(T_p)$ , is a unique function of its temperature; the ratio  $r(T_p)/r(T_\infty)$ , termed the "overheat", sets the (constant) operating value of  $(T_p - T_\infty)$ . Thus

$$q_1 = i_b^2 r_p = H_1 A (T_p - T_\infty) \quad (\text{E.4.1})$$

where  $q_1$  is the instantaneous heat flux and  $A$  is sensor area. From standard heat transfer relations for cylinders in cross-flow,

$$H_1 = a_1 + a_2 U_1^{1/2} \quad (\text{E.4.2})$$

so

$$i_b = (a_3 + a_4 (U_1)^{\frac{1}{2}})^{\frac{1}{2}} \quad (\text{E.4.3})$$

where all  $a$ 's are constants.

(2) An ideal linearizer would operate on the bridge current, given by (E.4.3), to yield a final anemometer signal,  $E_1$ , that was linear in the instantaneous velocity,  $U_1$ . In the Ling unit, the linearizer is a pentode that performs a roughly 4th power operation, so

$$E_1 \approx a_5 i_b^4 \quad (\text{E.4.4})$$

If  $a_3$  is small compared to  $a_4 U_1^{1/2}$  in (E.4.3), then the operation of (E.4.4) will give an anemometer signal roughly linear in  $U_1$ ; static calibrations (Figs. 5.5.1(a) and (b)) show that this is so over limited ranges of mean velocity.

#### E.4.2 Modifications

The control unit was modified by the manufacturer to accept 5 to 10 ohm sensors (it was designed for 15 to 25 ohms). Also, the standard 3/4-turn overheat and d-c balance potentiometers were replaced by 10-turn ones for finer adjustments.

#### E.4.3 Operational Points

(1) The d-c balance - i.e., the reference voltage supplied to the differential amplifier - drifted considerably during an initial 4 hour warmup period. This drift did not affect the slope of the static calibrations (mean signal vs. mean velocity), but resulted in parallel displacements which, if unknown, would lead to erroneous apparent calibrations. After 4 hours the drift was small, but required constant checking.

(2) For a given sensor and overheat ratio, the control unit became unstable beyond a certain mean velocity. The maximum velocity for stable operation increased as the overheat ratio was decreased as shown on Table E.4.1. For this reason, 0.001 in. sensors were operated at an overheat of 1.05 and 0.002 in. sensors at 1.025.

Table E.4.1

Overheat vs. Mean Velocity for Instability

Sensor OD, in. Overheat Ratio	0.001	0.002
1.03		> 1000
1.035		550
1.04		370
1.05		230
1.06		150
1.07		100
1.08		75
1.10	> 800	50

Velocities in cm/sec

(3) The operating point (gain) of the linearizer was set by a 10 turn "meter set" potentiometer, settings  $0 \leq G \leq 1000$ . At a given mean velocity,  $U$ , mean signal values,  $E$ , were roughly related to gain setting,  $G$ , by

$$\ln(E(G_1)/E(G_2)) = (0.0155 \pm 0.0005)(G_1 - G_2) \quad (E.4.5)$$

E.5 List of Equipment Vendors and Manufacturers

(i) Small System

- |              |                             |   |
|--------------|-----------------------------|---|
| 1. Tank      | 5 gal syrup                 | O. G. Kelley Co., Quincy, Mass.                   |
| 2. Test pipe | 0.187 OD x<br>0.036 ID wall | Nuclear Metals, Inc.,<br>Somerville, Mass.        |
| 3. Fittings  | "Swagelok"                  | Cambridge Valve and<br>Fitting, Framingham, Mass. |
| 4. Stirrer   | Lightnin F                  | Mixing Equipment Co.,<br>Rochester, New York      |

(ii) Big System

- |                   |                           |  |
|-------------------|---------------------------|--|
| 1. Pump           | 2L10 SSQ                  | Robbins and Myers,<br>Springfield, Ohio                    |
| 2. Drive          | V S, 10 hp                | Reliance Electrical and<br>Engineering, Cleveland,<br>Ohio |
| 3. Gear Box       | 10116-107RR               | Turner Unidrive, Kansas<br>City, Missouri                  |
| 4. Heat Exchanger | SSF 602YH-1P              | Young Radiator Co.,<br>Racine, Wisconsin                   |
| 5. Surge Tank     | 7 $\frac{1}{2}$ gal syrup | O. G. Kelley, Co., Quincy,<br>Mass.                        |

E.5 (Cont.)

6.	Filter	CMC-60S	Filterite, Timonium, Md.
7.	Mixer	Lightnin ND-1, EVS	Mixing Equipment Co., Rochester, New York
8.	Honeycomb	1/8 in. cell, A1	Hexcell Products, Havre de Grace, Maryland
9.	Temperature Control	M7023A1000 Q455C1011	Honeywell, Allston, Mass. (Motorized Valve)
10.	Stainless pipe and fittings, Type 316	1 1/2 in. OD, 11BWG 3 in. IPS, Sch 10 6 in. OD, 14 BWG	Stainless Pipe and Fittings, Cambridge, Massachusetts
11.	PVC pipe	3 in. IPS, Sch 40	Glover Coating Co., Malden, Massachusetts
12.	Flexible pipe	321 stainless	J.G. Shelley Co., Wellesley, Mass.
		Rubber	Greene Rubber Co., Cambridge, Massachusetts
(iii) Instruments			
1.	Pressure Transducer	267 BC	Sanborn Co., Waltham, Mass.
2.	Transducer Amplifier-Indicator	411 T	Sanborn Co., Waltham, Mass.



E.5 (Cont.)

- 3. Strip Chart Recorder VOM-5  
Bausch and Lomb,  
Rochester, New York
- 4. Hot Film Anemometer 40 W  
Lintronic Labs, Silver  
Springs, Maryland
- 5. Sensors QS 20 N  
Thermo-Systems Inc.,  
Minneapolis, Minnesota
- 6. RMS Random Signal  
Voltmeter 12 A 1  
Flow Corporation,  
Cambridge, Massachusetts
- 7. Variable Filter 1564 A  
General Radio Co., Concord,  
Massachusetts
- 8. Frequency Counter 5211 B  
Hewlett-Packard, Palo Alto,  
California
- 9. VTVM 412 AR  
Hewlett-Packard, Palo Alto,  
California
- 10. Oscilloscope 502 A  
Tektronix Inc., Portland,  
Oregon
- 11. Pitot tubes  
United Sensor and Control,  
Watertown, Massachusetts

## F. Calibrations

### F.1 Differential Pressure Transducer

The low pressure side of the transducer was connected to a static mercury reservoir and its high pressure side to a mercury reservoir mounted on a 14 in. micrometer traverse. The two reservoirs themselves could be connected or isolated by a stop cock. Differential pressures known to 0.0005 in. Hg could be applied to the transducer over a range of 0 to 12 in. Hg. For the range 10 to 30 in. Hg, the mercury differential was read to  $\pm 0.02$  in. on the arms of a U-tube manometer.

The pressure transducer + transducer amplifier-indicator + recorder combination was used and calibrated as a unit. Amplifier and recorder full scales were synchronized with a voltage divider. One transducer "division",  $D$ , is defined as the amplifier attenuator setting,  $A$ , times the fractional full scale deflection,  $F$ , on the indicator:

$$D = AF \quad (\text{F.1.1})$$

At a given amplifier gain ("sensitivity"),  $S$ , the calibration constant of the instrument combination,  $C_s(\Delta P)$ , is

$$C_s(\Delta P) = \Delta P/D \quad (\text{F.1.2})$$

where  $\Delta P$  is the applied differential pressure, and D is the corresponding transducer divisions. Only extreme amplifier gains, maximum or minimum, were employed; intermediate values were less reproducible.

A typical calibration is shown on Fig. F.1.1, with coordinates  $(C_s(\Delta P)/\bar{C}_s)$  vs.  $\Delta P$ , values of  $C_s(\Delta P)$  being normalized by their average,  $\bar{C}_s$ , at that sensitivity. For the three higher decades of  $\Delta P$ , the calibration is constant within  $\pm 1\%$ .

## F.2 Pump

The Moyno pump was calibrated, both with distilled water and fresh, 1000 ppm N3000 polymer solution, using the traditional bucket and stop watch method. At worst, liquid weight was known to  $\pm 1/4\%$ , time to  $\pm 1/2\%$  and pump speed, derived from the gear ratio and drive generator-tachometer frequency, to  $\pm 1/4\%$ . The pressure differential across the pump, known to  $\pm 0.5$  psi, was varied from 0 to 50 psi by throttling the discharge end with a diaphragm valve. All calibrations were performed with the liquid at  $25.0 \pm 1.0^\circ\text{C}$ .

The specific displacement,  $\sigma(R, \Delta P)$  litres/revolution, is defined by

$$\sigma(R, \Delta P) = (Q/R) \quad (\text{F.2.1})$$

where Q litres/sec is the flow rate at pump speed R revolutions/sec and pressure differential  $\Delta P$  psi across the pump.

Calibrations are presented on Fig. F.2.1 in two parts:

(a) Specific displacement vs. pump speed at (essentially) zero pressure differential across the pump.

(b) Specific displacement vs. pressure differential at constant pump speeds.

On Fig. F.2.1(a), values of  $\sigma(R,0)$  are normalized by the respective average value,  $\bar{\sigma}$ , for each set; in the legend, error limits on  $\bar{\sigma}$  are for 99% confidence. It is observed that:

(1) The calibration is constant to about  $\pm 1\%$  over the whole speed range and

(2) There is no significant difference between calibrations with distilled water and polymer solution

At the extreme high speeds,  $R > 11$  rps, slight cavitation was noticed during calibration. This was due to the NPSH provided by the calibration setup being inadequate at those speeds. Cavitation did not occur during actual operation of the big system in which adequate NPSH was provided.

On Fig. F.2.1(b),  $\sigma(R,\Delta P)$  values are normalized by the corresponding  $\sigma(R,0)$  at the same speed. It is seen that for both distilled water and polymer solution, the specific displacement is independent of differential pressure up to 50 psi.

Finally, one noteworthy point. The Moyno pump used has a Buna-N rubber stator and thermal expansion of the stator alters the specific displacement. As a result, the calibration is quite sensitive to temperature, e.g.,  $\bar{\sigma}(35^{\circ}\text{C})/\bar{\sigma}(25^{\circ}\text{C}) \approx 0.975$ .

### F.3 Variable Filter

A constant signal from a white noise generator, power spectrum flat  $\pm 0.2$  db from 20 cps to 20 kc, was fed through the proportional bandwidth, 2.5 cps to 25 kc variable filter into a true rms random signal voltmeter, response  $\pm 0.2$  db from 2 cps to 250 kc and time constants 60 sec for  $< 100$  cps and 15 sec for  $> 100$  cps. Ideally, the mean square voltmeter reading,  $V^2(f)$ , should be proportional to the filter frequency,  $f$ . In practice,

$$V^2(f) = \alpha(f)f \quad (\text{F.3.1})$$

where the filter calibration constant,  $\alpha(f)$ , is, in general, a function of frequency. With reference to an arbitrary frequency,  $f_R$ , the calibration curve for the filter is obtained from

$$\beta(f)_{\text{re:}f_R} = (\alpha(f)/\alpha(f_R)) = (V^2(f)/f)(V^2(f_R)/f_R) \quad (\text{F.3.2})$$

All calibrations, and later spectrum measurements, were performed with a (1/10) octave filter bandwidth at 10 logarithmically equi-spaced frequencies per decade.

Calibration results for each of the four frequency decades of the filter are shown on Fig. F.3.1, with

coordinates  $\beta(f)_{re:10\text{ kc}}$  vs.  $\text{Log}_{10}(f)$ . It can be observed that:

(a) The filter is well within its rated  $\pm 1$  db specifications.

(b) Roughly the same calibration pattern is repeated in each decade.

The high scatter in calibrations is due to the test instruments, the noise generator and the rms voltmeter, being good only to  $\pm 0.2$  db each, which, combined, is of the order of magnitude of the rated  $\pm 1$  db for the filter.

## G. Summary of Data and Calculated Values

Experimental results are tabulated in seven sections:

- G.1 intrinsic viscosity measurements,
- G.2 0.292 cm system gross flow data,
- G.3 3.21 cm system gross flow data,
- G.4 mean velocity profiles,
- G.5 hot film static calibrations,
- G.6 rms turbulent intensity profiles,
- G.7 turbulent energy spectra.

### Notes:

(1) Table G.1. The first digit of master batch number indicates polymer used:

- |   |       |
|---|-------|
| 1 | N10   |
| 2 | N80   |
| 3 | N750  |
| 4 | N3000 |
| 5 | W301  |

(2) Sections G.2 to G.7 inclusive. On computer print-out, the nomenclature is:

<u>On Printout</u>	<u>In Text</u>	<u>Units</u>
C	c	weight ppm
DIA	d	cm
E(K)	E(k)	cm <sup>3</sup> /sec <sup>2</sup>
F	f	cps
K	k	cm <sup>-1</sup>
Q	Q	litres/sec
QI	Q <sub>i</sub>	litres/sec
R	R	dl/gm
RE,T	N <sub>Re,T</sub>	
TEMP	T	°C
TW	T <sub>w</sub>	dynes/cm <sup>2</sup>
u	u	cm/sec
U	U	cm/sec
UCL	U <sub>CL</sub>	cm/sec
UT	u <sub>T</sub>	cm/sec
η <sub>R</sub>	η <sub>r</sub>	
NU	ν	cm <sup>2</sup> /sec
XI	ξ	

.4998E 02 indicates  $0.4998 \times 10^2$

(3) Table G.2.1. T in first column denotes runs with trigger. Batch refers to listing on Table G.1. Concentrations are  $\pm 0.5\%$ .  $\eta_r$  is reported only where derived from experimental laminar flow data.

(4) Table G.2.2 is compiled from pressure differentials



measured across taps T1-T4 (Fig. 3.3.1); Table G.2.3 from across T1-T3. The latter gives slightly superior accuracy at the highest flow rates since it prevents transducer overloading.

(5) On all  $Q$  vs.  $T_w$  listings, please disregard numbers in excess of 4 significant figures.

(6) All runs on Tables G.3 to G.7 are referred to with prefix B in text.

(7) Table G.3.1. Batch refers to listing on Table G.1. Concentrations are  $\pm 5\%$ .  $\eta_r$  values are initial, measured on the low shear GDM viscometer.

(8) Table G.4. In polymer solution,  $u_r$  value is the average for the duration of profile; typical variation of 5% occurred from beginning to end.

(9) Table G.5. All calibrations were taken on pipe centre line. DIA refers to hot film cylinder sensor. OVHT is the overheat ratio. GAIN refers to operating point for linearizer (Section E.4.3(3)).

(10) Tables G.6 and G.7. All values of  $\xi$  (XI) are nominal - obtained from cathetometer readings during probe installation. At "low" flow rate (1.15 litres/sec) these are identical with actual values - obtained from noting when sensor touched pipe wall. At "high" flow rate (5.3 or 5.7 litres/sec) sensor was  $0.005 \pm 0.001$  in. closer to wall than nominal due to probe deflection. Thus

$$\gamma_{\text{actual}} = \gamma_{\text{nominal}} - 0.01$$

Also, in polymer solution, initial, low shear, values of  $\gamma$  (NU) are reported without accounting for polymer degradation: actual values are, at worst, 10% lower than reported. Values of  $u_{\tau}$  are average for duration of profile or spectrum.

Table G.1  
Polymer Master Batch Intrinsic Viscosities

Batch	$c$ gm/dl	$[\eta]_s$ dl/gm	$\pm$	$k'$	$[\eta]_r$ dl/gm	$\pm$	$k''$	$[\eta]$ dl/gm	$\pm$
100	5.350	0.796	0.061	0.325	0.792	0.048	-0.157	0.794	0.055
101	7.230	0.734	0.106	0.404	0.736	0.059	-0.125	0.735	0.083
101	7.230	0.730	0.001	0.385	0.732	0.015	-0.133	0.731	0.008
105	6.061	0.704	0.069	0.415	0.708	0.039	-0.123	0.706	0.054
111	7.452	0.658	0.014	0.400	0.661	0.009	-0.128	0.659	0.011
201	2.913	1.77	0.13	0.349	1.77	0.09	-0.147	1.77	0.11
202	3.705	1.73	0.03	0.363	1.73	0.02	-0.141	1.73	0.02
202	3.705	1.78	0.08	0.306	1.77	0.05	-0.164	1.77	0.06
203	9.270	1.78	0.25	0.383	1.79	0.16	-0.135	1.78	0.21
301	1.631	3.42	0.08	0.314	3.40	0.05	-0.162	3.41	0.07
301	1.631	3.35	0.23	0.326	3.33	0.13	-0.156	3.34	0.18
402	1.072	3.91	0.36	0.359	3.90	0.19	-0.141	3.91	0.28
402	1.072	3.89	0.11	0.377	3.89	0.07	-0.136	3.89	0.09
403	2.497	3.96	0.33	0.296	3.91	0.16	-0.165	3.94	0.25
411	2.710	3.72	0.42	0.297	3.69	0.29	-0.171	3.71	0.35
415	1.711	3.52	0.28	0.411	3.54	0.18	-0.124	3.53	0.23
501	0.301	18.8	1.2	0.408	18.9	0.6	-0.126	18.8	0.9
511	0.806	20.1	0.5	0.339	20.0	0.3	-0.149	20.1	0.4

Notes:  $[\eta]_s$  - from  $\text{Lim}_c \rightarrow 0 (\eta_{sp}/c)$

$[\eta]_r$  - from  $\text{Lim}_c \rightarrow 0 (\ln \eta_r/c)$

$\pm$  - 99% confidence Limits

$k', k''$  - Flory-Huggins Constants

TABLE G.2.1 INDEX OF 0.292 CM SYSTEM RUNS

RUN	BATCH	C	TEMP	R	RE•T	RUN	BATCH	C	TEMP	R	RE•T
						T 124	203	.1014E 04	25.6	1.29	2105
2	0	.0000E 00	27.0			T 125	203	.2032E 04	25.3	1.39	2040
7	0	.0000E 00	24.0	.98	3210	44	202	.2075E 04	25.1	1.38	3120
8	0	.0000E 00	25.0			128	203	.3048E 04	25.4	1.62	3060
13	0	.0000E 00	24.7	.98	3270	T 126	203	.3051E 04	25.4	1.61	2050
21	0	.0000E 00	24.8	1.00	3060	129	203	.5076E 04	25.5	2.09	4430
31	0	.0000E 00	24.8			T 127	203	.5085E 04	25.3	2.14	2165
35	0	.0000E 00	24.5			57	301	.4998E 00	25.0		
46	0	.0000E 00	25.1			58	301	.9995E 00	25.0		
T 55	0	.0000E 00	25.0		2042	59	301	.9995E 00	25.0		
56	0	.0000E 00	24.9			60	301	.1999E 01	25.0		
61	0	.0000E 00	25.0		3200	62	301	.1999E 01	25.7		
77	0	.0000E 00	26.0			63	301	.2999E 01	25.4		
78	0	.0000E 00	25.4	.99	3040	64	301	.4001E 01	25.3		
79	0	.0000E 00	25.1	1.00	3140	65	301	.4997E 01	25.1		
80	0	.0000E 00	25.3			66	301	.6997E 01	25.1		
T 94	0	.0000E 00	24.5	1.00	2010	67	301	.9996E 01	25.0		
102	0	.0000E 00	24.8		3003	T 70	301	.1999E 02	25.0	1.03	1970
111	0	.0000E 00	25.0		3265	T 71	301	.4997E 02	25.1	1.01	2040
130	0	.0000E 00	24.8	1.01	3115	75	301	.4998E 02	25.3	1.02	3230
103	105	.1011E 03	25.2			T 69	301	.9841E 02	25.0	1.07	2020
18	101	.1990E 03	25.0	.99	3270	68	301	.9996E 02	25.0	1.05	3180
104	105	.2003E 03	25.1			T 72	301	.1999E 03	25.3	1.06	2020
105	105	.3001E 03	25.0			74	301	.1999E 03	25.3	1.11	3140
106	105	.4036E 03	25.1			T 73	301	.4814E 03	24.6	1.20	1925
20	101	.4994E 03	25.6	1.02	3140	76	301	.4998E 03	25.1	1.20	3300
22	101	.5000E 03	25.3	1.07		115	302	.1013E 04	25.6	1.36	3190
107	105	.5006E 03	24.9			T 118	302	.1013E 04	25.3	1.33	2020
14	100	.5009E 03	24.7	1.03	3010	116	302	.2027E 04	25.6	1.72	4150
108	105	.6019E 03	24.9			T 119	302	.2029E 04	25.3	1.79	1975
24	101	.7485E 03	24.9	1.01	3170	T 120	302	.3028E 04	25.5	2.30	2160
109	105	.7793E 03	24.8			117	302	.3035E 04	25.3	2.27	4400
110	105	.9883E 03	24.8			81	402	.2565E 00	25.2		
17	101	.9950E 03	25.4	1.09	3065	82	402	.5042E 00	24.9		
15	100	.1503E 04	24.5	1.09	2940	83	402	.7522E 00	24.7		
19	101	.1998E 04	25.3	1.15	3170	84	402	.1003E 01	25.0		
23	101	.2991E 04	24.9	1.21		85	402	.1502E 01	24.9		
16	101	.5087E 04	25.4	1.41	3030	86	402	.2049E 01	25.0		
114	105	.7496E 04	24.8	1.58	3330	87	402	.3090E 01	25.1		
47	202	.4998E 01	25.5			88	402	.5242E 01	25.3		
36	202	.1001E 02	24.8			89	402	.7149E 01	25.2		
48	202	.1001E 02	25.3			T 95	402	.9999E 01	24.4	.98	2055
49	202	.1503E 02	25.3			891	402	.1029E 02	25.5	.99	3280
37	202	.2498E 02	24.7			90	402	.1998E 02	25.1	.99	3310
50	202	.2500E 02	25.6			T 96	402	.2000E 02	24.4	1.05	2155
51	202	.3496E 02	25.1			91	402	.4988E 02	24.8	.99	3210
38	202	.4999E 02	24.8			T 97	402	.4999E 02	24.4	.99	2120
54	202	.5001E 02	25.3			892	402	.9989E 02	25.3	1.03	3140
39	202	.5006E 02	24.7			T 98	402	.9998E 02	24.6	1.02	2060
40	202	.7498E 02	24.8			92	402	.1997E 03	24.6	1.05	3440
41	202	.9998E 02	25.0			T 99	402	.2000E 03	24.9	1.05	2025
29	201	.1001E 03	24.8	.98	3190	93	402	.4987E 03	24.6	1.16	3760
42	202	.1498E 03	25.0			T 100	402	.5000E 03	24.7	1.16	2065
53	202	.2000E 03	25.3	1.02	3100	112	403	.9952E 03	25.3	1.37	4740
T 122	203	.2037E 03	26.1	1.05	1970	T 101	402	.9998E 03	24.7	1.41	2000
43	202	.2998E 03	25.0			113	403	.2079E 04	24.9	1.90	
T 123	203	.5080E 03	25.7	1.09	2075	T 121	403	.2080E 04	25.3	1.95	
45	202	.5185E 03	24.9	1.08	3180	133	501	.2000E 01	25.1	.99	3525
52	202	.1000E 04	25.1	1.15	3190	131	501	.5000E 01	25.3	1.01	3640
						132	501	.2000E 02	25.3	1.06	
						134	501	.1000E 03	28.8		













45	46	47	48	49	50
Q	TW	C	TW	Q	TW
.04033	736.04	.C3750	1068.50	.03593	965.14
.04400	923.57	.C4610	1132.40	.03993	1065.38
.04953	966.66	.C4273	1259.19	.04100	1159.99
.05233	1038.16	.C4520	1297.50	.04293	1251.54
.05497	1123.96	.C4825	1547.33	.04490	1351.78
		.C5057	1679.88	.04573	1449.15
				.04865	1546.52
				.05020	1618.12
				.05040	1646.76
				.05103	1715.49

51	52	53	54	55	56
Q	TW	Q	TW	Q	TW
.03833	953.01	.04200	702.89	.03833	781.13
.04040	1030.75	.04587	789.09	.04405	862.84
.04243	1117.12	.04920	859.38	.04680	1055.09
.04460	1220.77			.04980	1155.99
.04677	1310.03			.05240	1242.47
.04867	1405.04			.04927	1377.90
.05055	1468.38			.05153	1484.70
.05060	1491.42			.05340	1565.55
.05450	1669.93				

57	58	59	60	61	62
Q	TW	Q	TW	C	TW
.03630	934.06	.03640	939.59	.03637	938.54
.03853	1032.08	.03860	1042.71	.03863	1036.72
.04050	1132.98	.04070	1122.92	.04065	1129.13
.04247	1233.88	.04250	1165.89	.04260	1224.43
.04515	1378.02	.04250	1234.64	.04457	1328.39
.04805	1527.93	.04435	1317.71	.04645	1426.57
.04977	1611.54	.04635	1412.25	.04820	1516.10
.05120	1689.38	.04810	1515.37	.04980	1605.62
.05330	1755.68	.04967	1601.31	.05140	1683.59
		.05165	1687.25	.05320	1750.01
		.05335	1761.73		

48	49	50
Q	TW	Q
.03923	1058.70	.03470
.04140	1153.90	.03775
.04343	1256.41	.03953
.04705	1442.38	.04150
.04873	1549.11	.04210
.05073	1621.23	.04367
.05240	1725.08	.04543
		.04753
		.04950
		.05100
		.05280

54	55	56
Q	TW	C
.03640	945.59	.03643
.03867	1049.37	.03950
.04040	1130.10	.04227
.04243	1236.76	.04523
.04455	1334.78	.04807
.04607	1421.27	.05027
.04790	1516.40	.05307
.04957	1602.89	
.05137	1689.38	
.05315	1758.57	

57	58	59
Q	TW	Q
.03640	945.59	.03643
.03867	1049.37	.03950
.04040	1130.10	.04227
.04243	1236.76	.04523
.04455	1334.78	.04807
.04607	1421.27	.05027
.04790	1516.40	.05307
.04957	1602.89	
.05137	1689.38	
.05315	1758.57	

57	58	59	60	61	62
Q	TW	Q	TW	Q	TW
.03640	945.59	.03643	942.71	.03643	942.71
.03867	1049.37	.03950	1075.32	.03950	1075.32
.04040	1130.10	.04227	1233.88	.04227	1233.88
.04243	1236.76	.04523	1372.26	.04523	1372.26
.04455	1334.78	.04807	1519.29	.04807	1519.29
.04607	1421.27	.05027	1640.37	.05027	1640.37
.04790	1516.40	.05307	1758.57	.05307	1758.57





TABLE G.2.4 SPECIFIC DRAG REDUCTION

NOTE  
± LIMITS FOR R ARE 99PC CONFIDENCE

Q = .0400

POLYMER	C	N10	R	±	C	N80	R	±	C	N750	R	±	C	N3000	R	±
.1011E 03		.971E 00	.140E 01	.4998E 01	.212E 02	.123E 02	.4998E 00	.218E 03	.2565E 00	.415E 02	.824E 03					
.1990E 03		.436E 00	.608E 00	.1001E 02	.342E 02	.627E 01	.4998E 00	.300E 03	.5042E 00	.722E 02	.388E 03					
.2003E 03		.574E 00	.603E 00	.1001E 02	.285E 02	.611E 01	.4998E 00	.313E 03	.7522E 00	.221E 03	.265E 03					
.3001E 03		.501E 00	.451E 00	.1001E 02	.225E 02	.684E 01	.9895E 00	.187E 03	.1003E 01	.240E 03	.158E 03					
.4036E 03		.621E 00	.331E 00	.1001E 02	.249E 02	.141E 02	.9995E 00	.207E 03	.1532E 01	.286E 03	.618E 02					
.4994E 03		.949E 00	.513E 00	.1503E 02	.318E 02	.314E 01	.1999E 01	.170E 03	.2049E 01	.300E 03	.352E 02					
.5006E 03		.574E 00	.262E 00	.2498E 02	.282E 02	.297E 01	.1999E 01	.166E 03	.3090E 01	.290E 03	.285E 02					
.6019E 03		.772E 00	.133E 00	.2500E 02	.287E 02	.296E 01	.2999E 01	.174E 03	.5242E 02	.253E 03	.153E 02					
.7485E 03		.604E 00	.178E 00	.3496E 02	.270E 02	.235E 01	.4001E 01	.158E 03	.7149E 01	.255E 03	.117E 02					
.793E 03		.695E 00	.107E 00	.4999E 02	.247E 02	.141E 01	.6997E 01	.157E 03	.1029E 02	.216E 03	.144E 02					
.9883E 03		.513E 00	.161E 00	.5001E 02	.243E 02	.127E 01	.6997E 01	.150E 03	.1998E 02	.152E 03	.405E 01					
.9950E 03		.498E 00	.116E 00	.5001E 02	.243E 02	.115E 01	.9996E 01	.127E 03	.4988E 02	.855E 02	.213E 01					
.1503E 04		.548E 00	.455E-01	.5006E 02	.239E 02	.124E 01	.4998E 02	.577E 02	.333E 01	.9989E 02	.506E 02					
.1998E 04		.403E 00	.633E-01	.7498E 02	.215E 02	.759E 00	.9996E 02	.372E 02	.445E 00	.1997E 03	.296E 02					
.2991E 04		.331E 00	.258E-01	.9998E 02	.184E 02	.430E 00	.1999E 03	.219E 02	.305E 00	.4987E 03	.133E 02					
.5087E 04		.262E 00	.251E-01	.1001E 03	.120E 02	.445E 01	.4998E 03	.106E 02	.302E 00	.9952E 03	.569E 01					
.7496E 04		.192E 00	.272E-01	.1498E 03	.177E 02	.600E 01	.1013E 04	.577E 01	.631E-01	.2079E 04	.294E 01					
				.2000E 03	.129E 02	.209E 00	.2827E 04	.294E 01	.514E-01							
				.2998E 03	.101E 02	.116E 00	.3035E 04	.196E 01	.199E-01							
				.5185E 03	.687E 01	.170E 00										
				.1000E 04	.412E 01	.650E-01										
				.2075E 04	.230E 01	.187E-01										
				.3048E 04	.172E 01	.733E-01										
				.5076E 04	.108E 01	.119E-01										

Q = .0500

.1011E 03		.108E 01	.167E 01	.4998E 01	.413E 02	.134E 02	.4998E 00	.429E 03	.200E 03	.366E 03	.657E 03
.1990E 03		.808E 00	.93E 00	.1001E 02	.455E 02	.648E 01	.4998E 00	.266E 03	.188E 03	.255E 03	.371E 03
.2003E 03		.122E 01	.704E 00	.1001E 02	.391E 02	.613E 01	.4998E 00	.385E 03	.204E 03	.378E 03	.252E 03
.3001E 03		.101E 01	.453E 00	.1001E 02	.394E 02	.732E 01	.9995E 00	.325E 03	.104E 03	.103E 01	.152E 03
.4036E 03		.102E 01	.369E 00	.1001E 02	.339E 02	.114E 02	.9995E 00	.323E 03	.950E 02	.281E 03	.741E 02
.4994E 03		.643E 00	.263E 00	.1503E 02	.404E 02	.386E 01	.1999E 01	.237E 03	.369E 02	.1502E 01	.438E 02
.5006E 03		.875E 00	.288E 00	.2498E 02	.385E 02	.347E 01	.1999E 01	.245E 03	.615E 02	.2049E 01	.325E 02
.5009E 03		.106E 01	.145E 00	.2500E 02	.369E 02	.285E 01	.2999E 01	.222E 03	.239E 02	.3090E 01	.325E 02
.5019E 03		.879E 00	.196E 00	.3496E 02	.344E 02	.198E 01	.4001E 01	.208E 03	.183E 02	.5242E 01	.138E 02
.7485E 03		.793E 00	.111E 00	.4999E 02	.304E 02	.116E 01	.4001E 01	.208E 03	.183E 02	.7149E 01	.259E 03
.7793E 03		.798E 00	.171E 00	.5001E 02	.295E 02	.112E 01	.6997E 01	.188E 03	.163E 02	.1029E 02	.135E 02
.9883E 03		.748E 00	.120E 00	.5001E 02	.289E 02	.110E 01	.9997E 01	.171E 03	.880E 01	.1998E 02	.160E 03
.9950E 03		.741E 00	.757E-01	.5006E 02	.299E 02	.110E 01	.9996E 01	.148E 03	.530E 01	.4988E 02	.905E 01
.1503E 04		.755E 00	.537E-01	.7498E 02	.263E 02	.707E 00	.4998E 02	.652E 02	.164E 01	.9989E 02	.537E 02
.1998E 04		.557E 00	.518E-01	.9998E 02	.221E 02	.422E 00	.9996E 02	.613E 02	.339E 00	.1997E 03	.314E 02
.2991E 04		.459E 00	.238E-01	.1001E 03	.197E 02	.360E 01	.4999E 03	.242E 02	.175E 00	.4987E 03	.138E 02
.5087E 04		.350E 00	.357E-01	.1498E 03	.185E 02	.304E 01	.1999E 03	.115E 02	.169E 03	.9952E 03	.690E 01
.7496E 04		.268E 00	.597E-01	.2000E 03	.149E 02	.204E 00	.1013E 04	.627E 01	.483E-01	.2079E 04	.306E 01
				.2998E 03	.116E 02	.116E 00	.3035E 04	.205E 01	.159E-01		
				.5185E 03	.787E 01	1.000E-01					
				.1000E 04	.669E 01	.694E-01					
				.2075E 04	.257E 01	.152E-01					
				.3048E 04	.191E 01	.199E-01					
				.5076E 04	.118E 01	.102E-01					

TABLE G.3.1 INDEX OF 3.21 CM SYSTEM RUNS

RUN	BATCH	C	TEMP	R
10	0	.0000E 00	25.1	1.
16	0	.0000E 00	25.2	1.
17	0	.0000E 00	25.3	1.
20	0	.0000E 00	25.2	1.
102	0	.0000E 00	24.8	1.
103	0	.0000E 00	25.2	1.
107	0	.0000E 00	25.0	1.
113	0	.0000E 00	25.2	1.
21	111	.9500E 03	25.0	1.07
22	111	.1920E 04	25.1	1.14
23	111	.4760E 04	25.0	1.35
24	111	.4760E 04	25.2	1.35
25	415	.5000E 02	24.9	1.02
26	415	.2000E 03	24.8	1.07
11	411	.5000E 03	25.0	1.20
12	411	.1000E 04	25.3	1.42
112	412	.1000E 04	25.1	1.42
13	412	.1015E 04	25.2	1.42
14	413	.1015E 04	25.3	1.42
15	413	.1015E 04	25.3	1.42
115	412	.1050E 04	25.3	1.43
27	511	.5000E 01	25.0	1.01
30	511	.5000E 01	25.3	1.01
28	511	.2000E 02	25.1	1.04
31	511	.2000E 02	25.1	1.04
29	511	.1000E 03	25.2	1.22
32	511	.4500E 03	25.1	2.19















## H. Sample Calculations

### H.1 Gross Flow

(a) Wall Shear Stress,  $T_w$ .

$$T_w = 0.25D(-dP/dx) \quad (6.3.1)$$

System: 0.292 cm

Run 79

Point 21

Pressure Taps T1 - T4

Pipe inside diameter,

$$D = 0.292 \pm 0.002 \text{ cm}$$

Distance between taps,

$$\Delta x = 30.48 \pm 0.02 \text{ cm}$$

Pressure differential,

$$\begin{aligned} \Delta P &= 63.4 \text{ transducer divisions at max. gain} \\ &= 82600 \pm 500 \text{ dynes/cm}^2 \end{aligned}$$

whence

$$T_w = 198 \pm 2 \text{ dynes/cm}^2$$

(b) Flow Rate,  $Q$ .

$$Q = \bar{\sigma} R \quad (F.2.1)$$

$$R = F(N)f \quad (E.3.2)$$

System: 3.21 cm  
 Run B10  
 Point 19  
 Gear,  $N = 2$   
 Tachometer frequency,  $f = 399.6 \pm 0.3$  cps  
 Conversion factor,  $F(2) = 0.007068$  (Table E.3.1)  
 Pump speed,  $R = 2.824$  rps  
 Specific displacement,  $\bar{\sigma} = 0.669 \pm 0.011$   
 litres/rev

whence

$$Q = 1.892 \pm 0.031$$

litres/sec

H.2 Radial Position,  $\xi$ .

$$\xi = (1 - (2r/D)) \quad (\text{Definition})$$

System: 3.21 cm

$$D = 1.261 \pm 0.001 \text{ in. at test section}$$

Run B10

Pitot 0.025 cm

Profile 1

Point 16

Micrometer 1.300 in.

(a) From cathetometer measurements, Pitot axis coincides with pipe axis at micrometer reading 0.793 in. (increasing micrometer readings indicate probe traversing towards far wall).

$$\begin{aligned} \text{Radial coordinate, } r &= 1.300 - 0.793 = 0.507 \\ \text{so } \xi &= (1 - (2(0.507)/(1.261))) \\ &= 0.197. \end{aligned}$$

(b) From experimental observation that Pitot rests on pipe wall at micrometer reading 1.414 in.

$$\begin{aligned} \text{Pitot shaft dia.} &= 0.020 \text{ in.} \\ \text{Radial coordinate, } r &= (1.261/2) - (1.414 - \\ &\quad 1.300 + 0.010) \\ &= 0.507 \text{ in.} \\ \text{so } \xi &= 0.197. \end{aligned}$$

### H.3 Mean Velocity, U.

$$U = (2(P_s - P)/\rho)^{1/2} \quad (\text{Bernoulli's Theorem})$$

where  $P_s$  is stagnation pressure and  $P$  the static pressure.

Run B10

Profile 1

Point 16

Pressure Taps P1 - T5 (Fig. 3.1.2)

T5 is 0.875 in. upstream of Pitot face, so

$$(P_s - P) = (P1 - T5) + (T4 - T5)(0.875/93) \quad (\text{H.3.1})$$

where the second term on the RHS accounts for the static pressure drop in the test section between axial locations T5 and P1.

$$(P1 - T5) = 7.26 \text{ transducer divisions} \\ \text{at max. gain}$$

$$(T4 - T5) = 12.04 \text{ transducer divisions} \\ \text{at max. gain}$$

$$\text{so } (P_s - P) = 7.26 + 0.113 = 7.373 \\ \text{transducer divisions} \\ = 9610 \pm 60 \text{ dynes/cm}^2$$

$$\text{water density, } \rho = 0.997 \text{ gm/cm}^3$$

$$\text{so } U = 138.7 \pm 0.5 \text{ cm/sec}$$

H.4 Integrated Flow Rate,  $Q_1$ .

$$Q_1 = (\pi D^2/4) \int_0^1 U d(1 - \xi)^2 \quad (6.8.5)$$

For a mean velocity profile with  $n$  points,  $U$  vs.  $\xi$ , the integration was performed on a computer by the summation:

$$Q_1 = (\pi D^2/4) \sum_{k=0}^n \frac{1}{2} (U_{k+1} + U_k) \left[ (1 - \xi_{k+1})^2 - (1 - \xi_k)^2 \right] \\ (\text{H.4.1})$$



where

$$U_0 = U_{CL}$$

$$\xi_0 = 1.00$$

$$U_{n+1} = 0.0$$

$$\xi_{n+1} = 0.0$$

and  $\xi_n = (d_{\text{Pitot}}/D_{\text{pipe}})$

Note that  $U$  is assumed linear in  $(1 - \xi)^2$  between the  $n^{\text{th}}$  point (closest to the wall) and the wall. For a Newtonian flow, it is easy to show that as long as  $\xi_n$  is outside the laminar sublayer, the assumed variation of  $U$  will cause a truncation error leading to lower than actual values of  $Q_1$ ; this error will increase with increasing  $(d/D)$ . In the present case, with water, the error is less than 1% with the 0.025 cm Pitot and about 2% with the 0.168 cm Pitot.

H.5 rms Turbulent Velocity,  $u$ .

$$u' = (dU/dE)_U e' \quad (6.7.6)$$

so the rms value is

$$u = \overline{(u'u')}^{\frac{1}{2}} = (dU/dE)_U e \quad (H.5.1)$$

(a) in solvent

Run B113

Profile 2 (Fig. 5.5.4(b))

Calibration 3 (Fig. 5.5.1(b))

Point 2

rms anemometer signal

$$e = 2.69 \pm 0.05 \text{ volts, rms}$$

Calibration slope

$$\begin{aligned} (dU/dE) &= 22.08 \pm 1.06 \text{ cm/sec volt} \\ &\text{(99\% confidence error limits)} \end{aligned}$$

$$\text{so } u = 59.4 \pm 4.7 \text{ cm/sec, rms.}$$

(b) in polymer solution

Run B112

Profile 4 (Fig. 5.5.5(a))

Calibration 6 (Fig. 5.5.2(b))

Point 5

Mean anemometer signal

$$E = 25.5 \text{ volts}$$

rms anemometer signal

$$e = 3.20 \pm 0.06 \text{ volts, rms}$$

Mean velocity, (from Cal 6)

$$U = 645 \text{ cm/sec}$$

Calibration slope

$$(dU/dE)_U = 15.8 \pm 2.5 \text{ cm/sec volt}$$

(estimated error limits)

so  $u = 50.5 \pm 8 \text{ cm/sec}$

(c) Radial Position,  $\xi$ .

Hot film sensor radial position was located similar to the Pitot tube - Section H.2.

### H.6 Turbulent Energy Spectra, $k$ vs. $E(k)$

$$k = 2\pi f/U \quad (\text{definition})$$

$$\int_0^{\infty} E(k) dk = \int_0^{\infty} E(f) df = u^2 \quad (\text{definition})$$

Run B113

$\xi$  0.033

Spectrum 1

$U$  500  $\pm$  10 cm/sec

$u$  59.5  $\pm$  5 cm/sec rms

Point 27

All pass signal  $S = 1.02$  volts, rms

Frequency  $f = 1995 \pm 40$  cps

Filtered signal  $s(f) = 0.0557$  volts, rms

Filter calibration  $\beta(f) = 1.02$  (Fig. F.3.1)

From definition,

$$\text{Wave number, } k = 2\pi(1995 \pm 40)/(500 \pm 10) = 25.1 \pm 1.0 \text{ cm}^{-1}$$

It can be shown that the energy density,  $E(f)$ , at frequency  $f$  is

$$E(f) = C(s(f)/S)^2/(f\beta(f)) \quad (\text{H.6.1})$$

where  $C$  is a proportionality constant, which, from the definition above, is given by

$$C = u^2 / \left( \int_0^{\infty} (s(f)/S)^2 df/f\beta(f) \right) \quad (\text{H.6.2})$$

For our case,

$$(s(f)/S)^2/f\beta(f) = (0.1465 \pm 0.003) \times 10^{-5} \text{ (cps)}^{-1}$$

$$u^2 = 3540 \pm 600 \text{ (cm/sec)}^2$$

$$\int_0^{\infty} (s(f)/S)^2 df/f\beta(f) = 0.08245 \pm 0.002 \text{ (from computer integration)}$$

so frequency energy density,

$$E(f) = 0.0629 \pm 0.012 \text{ cm}^2/\text{sec}^2 \text{ cps}$$

and wave number energy density,

$$E(k) = E(f) U/2\pi = 5.01 \pm 1.05 \text{ cm}^3/\text{sec}^2$$

## I. Location of Data

All laboratory notebooks and experimental records are located in Room 12-144 of the Chemical Engineering Department, Massachusetts Institute of Technology, Cambridge, Massachusetts 02139.

## J. Nomenclature

<u>Symbol</u>	<u>Meaning</u>	<u>Units and/or defining equation</u>
a	radius	cm
A	constant	
B	constant	
c	concentration	gm/dl or wppm
[c]	concentration, intrinsic	gm/dl
C, C', C''	constants, onset	(6.6.2, 6, 7)
C <sub>t</sub> , C' <sub>t</sub> , C'' <sub>t</sub>	constants, onset, "time" based	(6.6.16, 19, 20)
d	diameter, cylinder outside	cm
D	diameter, pipe inside	cm
D <sub>M</sub>	diameter, macromolecule effective	cm or Å
e'	anemometer signal, turbulent	volts
e	anemometer signal, turbulent, rms, $(\overline{e'e'})^{1/2}$	volts
E	anemometer signal, mean	volts
E	macromolecule elastic energy	ergs/molecule
E(k)	turbulent energy density at k	cm <sup>3</sup> /sec <sup>2</sup>

f	frequency, circular	cps
f	Fanning friction factor ( $2T_w/\rho U_{Av}^2$ )	
G	shear rate	sec <sup>-1</sup>
h	heat transfer coefficient	cal/cm <sup>2</sup> sec °C
$h(\xi)$	wake correction in defect law (44)	
I	intercept	(6.6.12)
k	wave number ( $2\pi f/U$ )	cm <sup>-1</sup>
$k_e$	wave number, dissipation	(6.6.15)
k	constant, Boltzmann ( $1.38)(10)^{-16}$ )	ergs/molecule °C
$k', k''$	constant, Flory-Huggins ( $k'' = k' - 0.5$ )	
K	constant, spectrum scaling, $\approx 0.2$	(6.6.5)
L	macromolecule extension ratio	(6.6.13)
m	concentration, molecular	molecules/cm <sup>3</sup>
M	molecular weight	

$n, N$	exponents	
$N_A$	number, Avogadro's (6.023)(10) <sup>23</sup>	molecules/gm mole
$N_{Pr}$	number, Prandtl	
$N_{Re}$	number, Reynold's ( $DU_{AV}/\gamma$ or $dU_1/\gamma$ )	
$P$	pressure	dynes/cm <sup>2</sup>
$\Delta P$	pressure, differential	dynes/cm <sup>2</sup>
$Q$	volumetric flow rate	litres/sec
$r$	radial coordinate	cm
$r_e$	macromolecule rms end- to-end distance	cm
$R$	drag reduction, specific (6.6.28)	dl/gm
$[R]$	drag reduction, intrinsic (6.6.29)	dl/gm
$R_F$	drag reduction, fractional	(6.6.26)
$R_{FN}$	$R_F$ based on Newtonian solvent	(6.6.45)
$R_G$	macromolecule rms radius of gyration	cm or Å
$S$	slip, specific ( $S_F/c$ )	dl/gm
$[S]$	slip, intrinsic, $\text{Lim}_{c \rightarrow 0}(S)$	dl/gm
$S_F$	slip, fractional	(6.8.10)



t	time	sec
T	temperature	$^{\circ}\text{C}$ or $^{\circ}\text{K}$
$T_w$	wall shear stress	dynes/cm <sup>2</sup>
$u^+$	$(U/u_{\tau})$	
$u'$	velocity, axial turbulent	cm/sec
u	velocity, axial turbulent, rms $(\overline{u'u'})^{1/2}$	cm/sec
$u_{\tau}$	velocity, friction $(T_w/\rho)^{1/2}$	cm/sec
U	velocity, axial mean	cm/sec
$v'$	velocity, radial turbulent	cm/sec
V	velocity, axial mean in Newtonian plug	cm/sec
$v^+$	$(V/u_{\tau})$	
V(X)	variance of X	
W	constant, spectrum scaling $\approx 4$	(6.6.18)
x	axial coordinate	cm
$x_v$	volume fraction	
$y^+$	$(\int Du_{\tau}/2\gamma)$	

Greek

$\alpha$  }  
 $\beta$  }

multipliers for log-log scaling

$\beta_0$	Peterlin parameter	(6.6.13)
$\gamma$	$(c/[C])$ universal drag reduction	(6.6.31)
$\delta$	$(R/[R])$ coordinates	
$\Gamma$	turbulent energy rate, production	$\text{cm}^2/\text{sec}^3$
$\varepsilon$	turbulent energy rate, dissipation	$\text{cm}^2/\text{sec}^3$
$\varepsilon(X)$	standard error in X, $(V(X)/X^2)^{1/2}$	
$\eta$	viscosity	$\text{gm}/\text{cm sec}$
$[\eta]$	viscosity, intrinsic, of polymer	$\text{dl}/\text{gm}$
$\nu$	viscosity, kinematic	$\text{cm}^2/\text{sec}$
$\lambda_f$	microscale (6.8.13)	$\text{cm}$
$\Lambda_f$	macroscale (6.8.12)	$\text{cm}$
$\pi$	3.14159 etc.	
$\pi$	postulated polymeric group	
$\rho$	density	$\text{gm}/\text{cm}^3$
$\tau_M$	macromolecule relaxation time	$\text{sec}$
$\tau_1$	macromolecule relaxation time, terminal	$\text{sec}$
$\Phi$	Flory's universal con- stant, $(2.1)(10)^{21}$	

$\xi$	radial coordinate $(1-(2r/D))$	
$\psi$	polymeric intrinsic parameter	dl/gm
	(6.6.35)	
$\omega$	frequency	sec <sup>-1</sup>

### Subscripts (sometimes suffixes)

a	apparent
	on an asymptote
	on pipe axis
Av	average
c	critical, for macromolecular
	touching
d	dissipation, at maximum $k^2 E(k)$
,d	based on diameter
i	integrated
m	on maximum drag reduction asymptote
N	in Newtonian plug
p	in polymer solution
s	in solvent
sp	specific
S	"effective slip"
r	relative to solvent
,T	at transition
w	at (or near) pipe wall

o	unperturbed
1	in axial direction
2	on Pitot face
$\xi$	at radial position $\xi$

### Superscripts

*	at the onset of drag reduction
'	at some different condition
—	time averaged

Note: In Appendices, all symbols are defined at first appearance; where possible, these are consistent with the text. On figures, nomenclature is consistent with context; in some cases  $U_T$  denotes  $u_T$ .

## K. Literature Citations

1. Toms, B. A., "Some Observations on the Flow of Linear Polymer Solutions through Straight Tubes at Large Reynolds Numbers," Proc. 1st Intl. Congress on Rheology, Vol. II, pp. 135-141, North Holland Pub. Co. (1948).
2. Oldroyd, J. G., "A Suggested Method of Detecting Wall Effects in Turbulent Flow through Pipes," Proc. 1st Intl. Congress on Rheology, Vol. II, pp. 130-134, North Holland Pub. Co. (1948).
3. Agoston, G. A. et al., "Flow of Gasoline Thickened by Napalm," Ind. Eng. Chem., 46, 1017 (1954).
4. Shaver, R. G. and E. W. Merrill, "Turbulent Flow of Pseudoplastic Polymer Solutions in Straight Cylindrical Tubes," A. I. Ch. E. Journal, 5, No. 2, 181 (1959).
5. Dodge, D. W. and A. B. Metzner, "Turbulent Flow of Non-Newtonian Systems," A.I.Ch.E. Journal, 5, No. 2, 189 (1959).
6. Metzner, A. B. and J. C. Reed, "Flow of Non-Newtonian Fluids - Correlation of the Laminar, Transition and Turbulent-Flow Regions," A.I.Ch.E. Journal, 1, No. 4, 434 (1955).
7. Shaver, R. G., "Turbulent Flow of Pseudoplastic Fluids in Straight, Cylindrical Tubes," Sc.D. Thesis, M.I.T., Cambridge, Mass. (1957).

8. Savins, J. G., "Drag Reduction Characteristics of Solutions of Macromolecules in Turbulent Pipe Flow," Symposium on Non-Newtonian Fluid Mechanics, 56th Annual A.I.Ch.E. Meeting, Houston, Texas (1963).
9. Sproull, W. T., "Viscosity of Dusty Gases," *Nature* 190, 976 (1961).
10. Lapple, C. E. and H. J. Kamack, "Performance of Wet Dust Scrubbers," *Chem. Eng. Prog.* 51, No. 3, 110 (1955).
11. Saffman, P. G., "On the Stability of Laminar Flow of a Dusty Gas," *J. Fluid Mech.* 13, 120 (1962).
12. Michaels, D. H., "The Stability of Plane Poiseuille Flow of a Dusty Gas," *J. Fluid Mech.* 13, 19 (1964).
13. Eissenberg, D. M., "Measurement and Correlation of Turbulent Friction Factors of Thoria Suspensions at Elevated Temperatures," *A.I.Ch.E. Journal* 10, No. 3, 403 (1964).
14. Elata, C. and A. T. Ippen, "The Dynamics of Open Channel Flow with Suspensions of Neutrally Buoyant Particles," M.I.T. Hydrodynamics Lab., Technical Report No. 45 (1960).
15. Daily, J. W. and G. Bugliarello, "Basic Data for Dilute Fiber Suspensions in Uniform Flow with Shear," *TAPPI* 44, No. 7, 497 (1961).

16. Ryan, N. W. and M. M. Johnson, "Transition from Laminar to Turbulent Flow in Pipes," A.I.Ch.E. Journal 5, No. 4, 433 (1959).
17. Fabula, A. G., "The Toms Phenomenon in the Turbulent Flow of Very Dilute Polymer Solutions," 4th Intl. Congress on Rheology, Brown U., Providence, Rhode Island (1963).
18. Merrill, E. W., H. S. Mickley and A. Ram, "Degradation of Polymers in Solution Induced by Turbulence and Droplet Formation," J. Poly. Sci. 62, S109 (1962).
19. Meter, D. M., "Studies on the Turbulent Flow and Visco-elastic Properties of Dilute Non-Newtonian Polymer Solutions," Ph.D. Thesis, U. of Wisconsin, Madison, Wisconsin (1964).
20. Metzner, A. B. and M. G. Park, "Turbulent Flow Characteristics of Visco-elastic Fluids," J. Fluid Mech. 20, 291 (1964).
21. Shin, H., "Reduction of Drag in Turbulence by Dilute Polymer Solutions," Sc.D. Thesis, M.I.T., Cambridge, Mass. (1965).
22. Rouse, P. E., "A Theory of the Linear Visco-elastic Properties of Dilute Solutions of Random Coiling Polymers," J. Chem. Phys. 21, 1272 (1953).
23. Lee, T. S., "Turbulent Flow of Dilute Polymer Solutions - Studies in Couette Flow," Sc.D. Thesis, M.I.T., Cambridge, Mass. (1966).

24. Peterlin, A., "Gradient Dependence of Intrinsic Viscosity of Freely Flexible Linear Macromolecules," J. Chem. Phys. 33, 1799 (1960).
25. Virk, P. S., E. W. Merrill, H. S. Mickley, and K. A. Smith, "The Critical Wall Shear Stress for Reduction of Turbulent Drag in Pipe Flow," in "Modern Developments in the Mechanics of Continuum," S. Eskanazi, Ed., Academic Press, New York (in press).
26. Elata, C. and J. Tirosh, "Frictional Drag Reduction," Israel Inst. of Tech. Informal report on Contract 62558-4093 for Office of Naval Research (1965).
27. Ripken, J. F. and M. Pilch, "Studies of the Reduction of Pipe Friction with the Non-Newtonian Additive CMC," St. Anthony Falls Hydraulic Lab., U. of Minnesota, Technical Paper No. 42, Series B (1963).
28. Wells, C. S., "On the Turbulent Shear Flow of an Elastico-Viscous Fluid," Preprint 64-36, A.I.A.A. Meeting, New York, New York (1964).
29. Hershey, H. C. and J. L. Zakin, "A Study of Turbulent Drag Reduction of Solutions of High Polymers in Organic Solvents," Preprint 21B, Symposium on Mechanics of Visco-elastic Fluids, Part II, 58th Meeting, A.I.Ch.E., Philadelphia, Pa. (1965).
30. Zimm, B. H., "Dynamics of Polymer Molecules in Dilute Solutions: Viscoelasticity, Flow Birefringence and Dielectric Loss," J. Chem. Phys. 24, 264 (1956).



31. Boggs, F. W. and J. Thompsen, "Flow Properties of Dilute Solutions of Polymers," Part I, Final Report. Office of Naval Research Contract No. Nonr-3120(00), (1966).
32. Spriggs, T. W. and R. B. Bird, "Some Nonlinear Viscoelastic Models with Inclusion of Results from Molecular Theory," Ind. Eng. Chem. Fundamentals 5, No. 2, 182 (1965).
33. Ernst, W. D., "Investigation of the Turbulent Shear Flow of Dilute Aqueous CMC Solutions," A.I.Ch.E. Journal 12, No. 3, 581 (1966).
34. Astarita, G. and L. Nicodemo, "Velocity Distributions and Normal Stresses in Viscoelastic Turbulent Pipe Flow," A.I.Ch.E. Journal 12, No. 3, 478 (1966).
35. Smith, K. A., E. W. Merrill, H. S. Mickley and P. S. Virk, "Anomalous Pitot Tube and Hot Film Measurements in Dilute Polymer Solutions." Chem. Eng. Sci. (in press).
36. Savins, J. G., "A Pitot Tube Method for Measuring the First Normal Stress Difference and its Influence on Laminar Velocity Profile Determinations," A.I.Ch.E. Journal 11, No. 4, 673 (1965).
37. Giles, W. B., "Note on Visco-elastic Stability and Flow Noise," AIAA Torpedo Propulsion Conference, J. G. Waugh, Chairman (July 1963).

38. Astarita, G. and L. Nicodemo, "Flow of Viscoelastic Liquids through Sudden Enlargements," *Ind. Eng. Chem. Fundamentals* 5, No. 2, 237 (1966).
39. Lindgren, E. R., "Friction Reduction Effects on Turbulent Flows of Water in Rough Pipes by Dilute Additive of High Molecular Weight Polymer," Report No. 1, Contract Nonr 2595(05), Bureau of Ships Research Program S-R009 01 01, David Taylor Model Basin, Washington, D. C. (1965).
40. Hoyt, J. W. and A. G. Fabula, "The Effect of Additives on Fluid Friction," 5th Symposium on Naval Hydrodynamics, Bergen, Norway (1964).
41. Ling, S. C., "Measurement of Flow Characteristics by the Hot-Film Technique," Ph.D. Thesis, State U. of Iowa, Iowa (1955).
42. Flory, P. J., "Principles of Polymer Chemistry," Cornell U. Press, Ithaca, New York (1953).
43. Laufer, J., "The Structure of Turbulence in Fully Developed Pipe Flow," NACA Report No. 1174 (1954).
44. Hinze, J. O., "Turbulence," McGraw-Hill, New York (1959).
45. Batchelor, G. K., "The Theory of Homogeneous Turbulence," Cambridge U. Press (1960).

46. Gilinson, P. J., C. R. Dauwalter, and E. W. Merrill, "A Rotational Viscometer using an A.C. Torque to Balance Loop and Air Bearing," *Trans. Soc. Rheology* 27, 303 (1963).
47. Schlichting, H., "Boundary Layer Theory," 4th Ed., McGraw-Hill, New York (1960).
48. Roshko, A., "On the Development of Turbulent Wakes from Vortex Streets," NACA Report 1191 (1953).
49. Tanford, C., "The Physical Chemistry of Macromolecules," John Wiley and Sons, New York (1961).
50. Townsend, A. A., "The Structure of Turbulent Shear Flow," Cambridge U. Press (1956).
51. Kurata, M. and W. H. Stockmeyer, "Intrinsic Viscosities and Unperturbed Dimensions of Long Chain Molecules," *Fortschr. Hochpolym. Forsh.* 3, 192 (1963).
52. Fabula, A. G., J. L. Lumley, and W. D. Taylor, "Some Interpretations of the Toms Effect," in "Modern Developments in the Mechanics of Continuum," S. Eskinazi, Ed., Academic Press, New York (in press).
53. Levinthal, C. and P. F. Davidson, "Degradation of Deoxyribonucleic Acid Under Hydrodynamic Shearing Forces," *J. Mol. Biol.* 3, 674 (1961).
54. Smith, K. A. Personal Communication, M.I.T. (1966).
55. Eckert, E. R. G. and J. M. Drake, "Heat and Mass Transfer," 2nd Ed., McGraw-Hill, New York (1959).

56. Korchak, E. I., "Fluid Flow in Packed Beds," Sc.D. Thesis, M.I.T., Cambridge, Mass. (1964).
57. Clauser, F. H., "The Turbulent Boundary Layer," in "Advances in Applied Mechanics," H. L. Dryden and Th. von Karman, Ed., Vol. IV, p. 1, Academic Press, New York (1956).
58. Smith, K. A., "The Transpired Turbulent Boundary Layer," Sc.D. Thesis, M.I.T., Cambridge, Mass. (1962).
59. Fingerson, L. M. Personal Communication. Thermo Systems, Inc., Minneapolis, Minn. (May 1965).

## L. Biographical Note

The author was born in Faridkot, India, on March 25, 1942. He has since been through the educational grind - the Welham and Doon Schools, Dehra Dun, 1948 to 1958, the Indian Institute of Technology, Kharagpur, 1958 to 1962, and the Massachusetts Institute of Technology, Cambridge, 1962 to 1966 - the impact of which has been cushioned considerably by:

a happy childhood - 1942 to 1948 inclusive and intermittent periods thereafter,

extra curricular activities - free-flight model aircraft, trekking in the Himalayas,

marriage - to the former Usha Rao in 1964,

relaxation - the years spent at this thesis,  
and finally

the birth of a son - Kanad Singh Virk in 1966.